https://doi.org/10.15388/vu.thesis.134
https://orcid.org/0000-0002-8238-8445

VILNIUS UNIVERSITY
CENTER FOR NATURAL SCIENCES AND TECHNOLOGY

Rosvaldas
ŠUMINAS

# Femtosecond filamentation in media with competing quadratic and cubic nonlinearities

**DOCTORAL DISSERTATION**

Natural Sciences
Physics (N 002)

VILNIUS 2021

This dissertation was written between 2016 and 2020 at Laser Research Center, Vilnius University. The research was supported by the Research Council of Lithuania.

**Academic supervisor:**
**prof. habil. dr. Audrius Dubietis** [Vilnius University, Natural Sciences, Physics, N 002]

**Dissertation Defense Panel:**

**Chairman – prof. dr. Aidas Matijošius** [Vilnius University, Natural Sciences, Physics, N 002]

**Members:**
**assoc. prof. dr. Rytis Butkus** [Vilnius University, Natural Sciences, Physics, N 002]
**dr. Audrius Pugžlys** [Vienna University of Technology, Natural Sciences, Physics, N 002]
**prof. habil. dr. Kęstutis Staliūnas** [Vilnius University & ICREA, Natural Sciences, Physics, N 002]
**dr. Arūnas Varanavičius** [Vilnius University, Natural Sciences, Physics, N 002]

The dissertation shall be defended at a public meeting of the Dissertation Defense Panel at 13:00 on 29 January 2021 in Room 306 of the Laser Research Center.
Address: Saulėtekio al. 10, Laser Research Center, Room 306, Vilnius, Lithuania.
Tel. +370 5 236 6005;

The text of this dissertation can be accessed at the Vilnius University Library, as well as on the website of Vilnius University:
https://www.vu.lt/naujienos/ivykiu-kalendorius

https://doi.org/10.15388/vu.thesis.134
https://orcid.org/0000-0002-8238-8445

VILNIAUS UNIVERSITETAS
FIZINIŲ IR TECHNOLOGIJOS MOKSLŲ CENTRAS

Rosvaldas
ŠUMINAS

# Femtosekundinių šviesos impulsų saviveika medžiagose su konkuruojančiais kvadratiniu ir kubiniu netiesiškumais

**DAKTARO DISERTACIJA**

Gamtos mokslai
Fizika (N 002)

VILNIUS 2021

Disertacija rengta 2016–2020 metais Lazerinių tyrimų centre, Vilniaus universitete. Mokslinius tyrimus rėmė Lietuvos mokslo taryba.

**Mokslinis vadovas:**
**prof. habil. dr. Audrius Dubietis** [Vilniaus universitetas, gamtos mokslai, fizika, N 002]

**Gynimo taryba:**

**Pirmininkas – prof. dr. Aidas Matijošius** [Vilniaus universitetas, gamtos mokslai, fizika, N 002]

**Nariai:**
**doc. dr. Rytis Butkus** [Vilniaus universitetas, gamtos mokslai, fizika, N 002]
**dr. Audrius Pugžlys** [Vienos technikos universitetas, gamtos mokslai, fizika, N 002]
**prof. habil. dr. Kęstutis Staliūnas** [Vilniaus universitetas ir ICREA, gamtos mokslai, fizika, N 002]
**dr. Arūnas Varanavičius** [Vilniaus universitetas, gamtos mokslai, fizika, N 002]

Disertacija ginama viešame Gynimo tarybos posėdyje 2021 m. Sausio mėn. 29 d. 13:00 val. Fizikos fakulteto Lazerinių tyrimų centro 306 auditorijoje. Adresas: Saulėtekio al. 10, Lazerinių tyrimų centras, 306 aud., Vilnius, Lietuva. Tel. +370 5 236 6005;

Disertaciją galima peržiūrėti Vilniaus universiteto bibliotekoje ir VU interneto svetainėje adresu: https://www.vu.lt/naujienos/ivykiu-kalendorius

# CONTENTS

# LIST OF ABBREVIATIONS

| | |
|---|---|
| $\beta$-BBO | Beta barium borate, $\beta$-$BaB_2O_4$ |
| CE | Conical emission, |
| CCD | Charge-coupled device |
| CMOS | Complementary metal–oxide–semiconductor |
| DFG | Difference frequency generation |
| FROG | Frequency resolved optical gating |
| FWHM | Full width at half maximum |
| GVD | Group velocity dispersion |
| IR | Infrared |
| KTA | Potassium titanyl arsenate, $KTiOAsO_4$ |
| MBC | Micro-bolometric camera |
| MPA | Multiphoton absorption |
| OPA | Optical parametric amplification |
| OPCPA | Optical parametric chirped-pulse amplification |
| RQPM | Random quasi-phase matching |
| SBN | Strontium barium niobate, $Sr_xBa_{1-x}Nb_2O_6$ for $0.32 \leq x \leq 0.82$ |
| SC | Supercontinuum |
| SFG | Sum frequency generation |
| SH | Second harmonic |
| SPM | Self-phase modulation |
| SPS | Scanning prism spectrometer |
| TH | Third harmonic |
| ZnS | Zinc sulfide |
| ZnSe | Zinc selenide |
| ZnTe | Zinc telluride |

# INTRODUCTION

The nonlinear propagation of intense ultrashort light pulses in transparent media gives rise to one of the most spectacular nonlinear optical phenomena, during which the incident pulse undergoes a remarkable spatiotemporal transformation accompanied by large scale spectral broadening, termed supercontinuum (SC) generation. Today, the physical picture of SC generation is fairly well understood in the framework of femtosecond filamentation [1].

Couairon et al. has defined filament as "a dynamic structure with an intense core, that is able to propagate over extended distances much larger than the typical diffraction length while keeping a narrow beam size without the help of any external guiding mechanism" [2]. The formation of filament is typically accompanied by two distinct types of radiation: 1) low divergence, spatially and temporally coherent extremely broadband radiation termed SC generation and 2) high divergence colored radiation emitted in a concentric pattern termed conical emission (CE). Each of these processes are closely intertwined and form a complex interplay between temporal and spatial effects such as self-focusing, self-phase-modulation (SPM), multiphoton absorption (MPA) and group velocity dispersion (GVD). In what follows we will briefly describe these effects and their influence on filamentation and SC generation.

Self focusing is a process, which occurs due to intrinsic cubic (Kerr) nonlinearity imposing an intensity dependence on the linear refractive index of the material: $n = n_0 + n_2 I$, where $n_0$ is the linear refractive index, $n_2$ is the nonlinear refractive index and I is the intensity. For a cylindrically symmetrical Gaussian beam in a nonlinear medium with a positive nonlinear refractive index ($n_2 > 0$) this leads to the peripheral parts of the beam travelling at a faster phase velocity with respect to the central part of the beam. Similar to the effect of a convex lens the beam phase-front curvature enforces the beam to self-focus. The input beam power required to perfectly balance out the diffractive spread of the beam is called the critical power for self-focusing:

$$P_{cr} = \frac{3.77\lambda^2}{8\pi n_o n_2}, \tag{1}$$

where $\lambda$ is the input wavelength.

If the input beam power $P$ is not only equal but exceeds the critical power for self-focusing $P_{cr}$, the effect of diffractive spreading is overcome and the beam will self-focus at a distance $z_{sf}$, which can be estimated using a well known empirical formula devised by Marburger et al. [3]:

$$z_{\mathrm{sf}} = \frac{0.367\ z_R}{\sqrt{[(P/P_{\mathrm{cr}})^{1/2} - 0.852]^2 - 0.0219}}, \tag{2}$$

where $z_R = \pi n_0 \omega_0^2/\lambda$ is the Rayleigh length for a Gaussian input beam and $\omega_o$ is the beam radius at $1/e^2$.

It should be fairly evident that the beam cannot collapse (become infinitesimally small) under real experimental conditions, therefore some physical mechanism must be present to stop the beam from collapsing. The collapse at the nonlinear focus is arrested due to nonlinear losses from MPA and the subsequent generation of free-electron plasma, which not only absorbs, but due to the intrinsic nature of free-electron plasma possessing a negative nonlinear refractive index, defocuses the beam. As a result the high intensity central part of the filament is attenuated and clamped at a certain level, which is highly dependent on the MPA order $K$ and can be estimated as the integer part of $(E_g/\hbar\omega_p)+1$, where $E_g$ is the bandgap of the material and $\omega_p$ is the fundamental frequency [4, 5]. For high input beam powers multiple self-focusing/defocusing cycles may occur. In the spatial domain, this process is intuitively described by the dynamic spatial replenishment model [6]. The following steps outline the main idea: 1) an input beam with an input peak power $P > P_{cr}$ will initially self-focus due to the Kerr effect; 2) the central part of the beam is attenuated due to MPA; 3) free-electron plasma generated near the nonlinear focus facilitates the defocusing of the central part of the beam; 4) if the peak power of the central part still exceeds $P_{cr}$ the process repeats itself. Therefore, it is clear that filamentation is initiated by self-focusing, which is a link that has been long established by demonstrating that SC generation threshold in various media is within 10% of the critical power for self-focusing [5].

In the temporal domain, cubic nonlinearity induced SPM imparts a large temporal phase variation, which gives rise to generation of new frequencies: [2]:

$$\omega(t) = -\frac{\partial \phi}{\partial t} \propto \omega_p - \frac{n_2 \omega_p}{c} z \frac{\partial I(r,t)}{\partial t}, \tag{3}$$

where $z$ is the propagation distance and c is the speed of light. Therefore, the bandwidth of the phase modulated pulse is determined by the magnitude of the slope of the pulse $\frac{\partial I(r,t)}{\partial t}$, the nonlinear refractive index $n_2$ and the propagation length $z$. The sign of the nonlinear refractive index and the slope of the pulse determines whether the acquired frequency modulation at the trailing and leading front of the pulse contains the blue-shifted or red-shifted frequency components. Most nonlinear media possess positive nonlinear refractive index values, therefore the leading front of the pulse contains the red-shifted frequency components, whereas the trailing front contains the blue-ones. The extremely high intensities reached during self-focusing strengthen the SPM process leading to an extreme spectral broadening at the nonlinear focus. In fact, it was demonstrated that for multiphoton orders $K < 3$, SC generation cannot occur due to the low value of clamping intensity, which limits the effect of SPM [4].

Chromatic dispersion, and in particular GVD defined as $k'' = \partial^2 k/\partial\omega^2|_{\omega_p}$,

where $k = \omega_p n_0/c$ is the wavenumber, also plays an important role in the filamentation and SC generation process [7, 8]. In the normal GVD range ($k'' > 0$), the lower frequency components travel faster than the high frequency ones. In the anomalous GVD range ($k'' < 0$), the opposite of this is true. With regard to filamentation and SC generation this leads to unique spatiotemporal features observable in each of these regimes.

In the range of normal GVD, the incident pulse undergoes asymmetrical pulse-splitting at the nonlinear focus producing two sub-pulses with shifted carrier frequencies moving in the opposite directions with respect to the initial pulse. Pulse-splitting was demonstrated numerically [9–11] and experimentally [12, 13] at first for self-focusing and later with regards to filamentation and SC generation [14, 15]. The spectral features were shown to be directly related to the pulse-splitting dynamics. In particular, the steep trailing intensity slope of the trailing sub-pulse as opposed to the leading front of the leading sub-pulse, was shown to produce the typically highly asymmetrical SC spectrum featuring a blue-pedestal [5, 16, 17].

In the range of anomalous GVD the input wave packet undergoes simultaneous self-compression in spatial and temporal domains. This leads to a qualitatively new filamentation regime, producing self-compressed spatiotemporal light bullets, which exhibit quasi-stationary, sub-dispersive and sub-diffractive propagation over extended distances in the nonlinear medium [18–21], possess exceptional robustness against perturbations [22], maintain stable carrier envelope phase [23], and give rise to generation of ultrabroadband, several octave spanning SC [24–27].

The zero GVD range combines the features of both the normal and anomalous GVD featuring extremely broadband SC spectra in combination with pulse-splitting [28].

The development of the effective three-wave mixing model, which views SC generation as occuring due to scattering of the incident field from a material-wave representing a nonlinear perturbation, provided a full spatiotemporal picture of SC generation [7, 8]. By taking into account the chromatic dispersion of the material one may acquire an angular map of the scattered frequencies, which includes both the SC radiation and CE [29]. This in turn paved the way for interpreting SC generation in the normal and anomalous GVD regimes as occurring due to spontaneous transformation of the input wave packet into nonlinear X- [30] and O-waves [20], respectively.

To this day, SC generation was observed in a variety of wide bandgap solid state media and with input pulse wavelengths ranging from the ultraviolet to the mid-IR [24–27, 31–34] and found numerous applications in metrology [35], spectroscopy [36] and as a seed in OPA [37] and OPCPA systems [38, 39]. However, the rapidly growing field of applications requires methods for achieving broadband SC radiation with desired spectral and temporal properties.

For isotropic media, possessing only cubic nonlinearity, the relevant parameters for SC generation, such as the linear and the nonlinear refractive indices, are usually fixed for a specific input wavelength, thereby requiring complex methods in which the input pulse shape [40, 41], polarization [42], chirp [43], phase [44, 45] or the focusing conditions [46] are varied, in order to obtain a certain level of control. On the other hand, the use of anisotropic media, possessing both cubic and quadratic nonlinearities, presents a viable alternative. In such media, second-order cascading effects are exploited by the use of phase-mismatched second harmonic (SH) generation, which leads to a reccurrent energy exchange between the fundamental and the SH waves. This introduces a phase delay between the back-converted and the non-converted fundamental waves, therefore the pulse travels at a slower or faster effective phase velocity [47, 48]. The effect may be described similarly to the optical Kerr effect by the use of the cascaded nonlinear index of refraction, which, unlike the Kerr-one, may be varied in sign and magnitude by setting an appropriate phase mismatch $\Delta k = k_{2\omega} - 2k_{\omega}$, where $k_{\omega,2\omega}$ are the fundamental and SH wavenumbers, respectively. Thus, the competition between the Kerr-like cascaded-quadratic and cubic nonlinearities, allows us to readily enhance or supress the nonlinear effects [49, 50] and to access different regimes of SC generation and filamentation.

A different outlook on the problem is provided by the necessity of broadband spectral sources e.g. for the detection of various substances and pollutants via vibrational spectroscopy in the so called molecular fingerprint region [51], leading to a growing demand in search of suitable nonlinear materials for ultrabroadband multi-octave SC generation in the mid-IR spectral range [1]. Of particular interest, are quadratic disordered polydomain or polycrystalline media, which due to the random nature (size, orientation, shape) of the constituent parts (crystallites, ferroelectric domains) possess greatly relaxed phase matching conditions allowing for extremely broadband and fairly efficient three-wave nonlinear interactions [52]. The generation of multiple second and higher order harmonics, which accompany SC generation in such media [53], greatly enhances the SC spectral bandwidth and opens new avenues for studies of extreme light-matter interactions [54–56].

## The objective of the thesis

The objective of this dissertation is investigation of filamentation and SC generation in ordered monocrystalline and disordered polydomain or polycrystalline nonlinear media, possessing both, the intrinsic-cubic and quadratic second-order nonlinearity, by use of femtosecond infrared laser sources with wavelengths, which fall into the normal, zero and anomalous GVD regions of the materials.

The main tasks of the thesis

- Investigation and spatio-temporal characterization of filamentation and SC generation in media with competing cascaded-quadratic and cubic nonlinearities, namely $\beta$-BBO crystal, in the regimes of normal and anomalous GVD.

- Demonstration of energy-scalable filamentation-free self-compression mid-infrared pulses with competing cubic and cascaded-quadratic nonlinearities.

- Study of random quasi-phase matching and its effect on filamentation and SC generation in disordered polycrystalline zinc-blende (ZnSe, ZnS) and polydomain (SBN) media in the regimes of normal, zero and anomalous GVD.

- The estimation of the nonlinear refractive index in a polydomain SBN crystal by the use of filament traces produced by planar second harmonic generation.

Practical and scientific novelty

- The competition between cascaded-quadratic and intrinsic cubic nonlinearities in a $\beta$-BBO crystal is exploited in order to achieve controllable nonlinear interactions in both, normal and anomalous GVD regimes. Controllable radiation polarized along the ordinary and the extraordinary axis of the nonlinear crystal is observed and attributed to SC and self-phase matched second harmonic generation, respectively. The control of the blue-shifted cut-off of the SC is shown to be facilitated by the complex interplay between the self-phase matched second harmonic generation and the self-steepening induced by competing cubic and quadratic nonlinear response. Meanwhile the observable phase mismatch dependent second harmonic spectral shifts are explained as occurring due to a certain range of SC spectral components satisfying the second harmonic self-phase matching conditions.

- Media possessing competing cascaded-quadratic and intrinsic cubic nonlinearities, namely $\beta$-BBO crystal, is shown to exhibit very similar features as to those reported in isotropic dieletric media in both normal and anomalous GVD. In particular, in the normal GVD range, pulse splitting and with further propagation axial pulse reconstruction is observed, whereas, in the anomalous GVD range, the formation of spatially and temporally compressed light bullets is confirmed.

- Favorable interplay between SPM facilitated by phase mismatch dependent effective nonlinear refractive index and anomalous GVD is exploited in a $\beta$-BBO crystal in order to demonstrate virtually lossless filamentation-free energy-scalable more than three-fold (sub-30 fs) pulse self-compression using incident pulses of 2.1 $\mu$m.

- Efficient generation of SC accompanied by multiple even and odd harmonics is observed in polycrystalline zinc-blende media (ZnS and ZnSe) as obtained using mid-infrared femtosecond laser pulses. More specifically, using 60 fs, 3.6 $\mu$m and 100 fs, 4.6 $\mu$m incident pulses, almost uniform harmonics enhanced SC radiation in polycrystalline ZnS and ZnSe is demonstrated spanning the spectral ranges of 0.4–5 $\mu$m and 0.5–5 $\mu$m, respectively. In the first case, up to 7th and 6th, and in the second case, up to 10th and 8th order harmonic radiation is observed.

- Evidence is provided that efficient second and higher harmonic generation in polycrystalline zinc-blende media stems from the random quasi-phase matched three-wave mixing processes facilitated by the filamentation of the input beam. In particular, we demonstrate that the generated harmonics 1) possess broadband spectral features, which replicate the fundamental harmonic in the frequency scale; 2) are randomly polarized; 3) have a linear generation efficiency dependence on the number of crystallites ("grains") in the polycrystalline sample.

- We show that polydomain SBN serves as an excellent nonlinear medium for SC generation in the infrared spectral range producing 0.8 - 1.81 $\mu$m, 1.04 - 2.5 $\mu$m and 1.0 - 3.32 $\mu$m SC spectra using pump pulses with carrier wavelengths of 1.2 $\mu$m, 2.0 $\mu$m and 2.4 $\mu$m falling into the normal, zero and anomalous GVD range of the material, respectively. The SC generation is accompanied by broadband planar second harmonic radiation facilitated by the random quasi-phase matching process and input beam filamentation. The planar radiation was shown to precisely map the intensity distribution along the filament of light allowing us to visualize filamentation dynamics. This feature was exploited in order to determine the nonlinear refractive indices of the material at 1.2 $\mu$m, 2.0 $\mu$m and 2.4 $\mu$m.

Statements to be defended

1. Filamentation in nonlinear media, during type-I phase-mismatched second harmonic generation in cases where the incident wavelength falls into either, normal or anomalous group velocity dispersion regions, is accompanied by ordinarily polarized controllable supercontinuum generation along with extraordinarily polarized phase-mismatched second harmonic

at a fixed wavelength, and self-phase matched second harmonic with a tunable wavelength.

2. In the normal group velocity dispersion region supercontinuum generation in birefringent media with competing cascaded quadratic and cubic nonlinearities results in incident pulse splitting into two sub-pulses, whereas in the anomalous group velocity dispersion region it transforms into a spatially and temporally compressed wave packet - light bullet.

3. Filamentation-free high-energy throughput mid-infrared pulse self-compression can be achieved in the anomalous group velocity dispersion region by exploiting the control of phase mismatch dependent effective nonlinear refractive index in birefringent media with competing cascaded quadratic and cubic nonlinearities.

4. Supercontinuum generation in polycrystalline zinc-blende media is accompanied by random quasi-phase matching induced multiple broadband even and odd harmonic generation limited by the short-wavelength transparency edge of the material.

5. Polydomain SBN serves as an excellent nonlinear medium for SC generation in the infrared spectral range producing more than octave spanning spectra using incident wavelengths which fall into the normal, zero and anomalous group velocity dispersion ranges. Supercontinuum generation is accompanied by planar random quasi-phase matching induced second harmonic generation, which closely follows the intensity dynamics of the light filament and can be exploited in order to determine the nonlinear refractive index of the material.

Contribution of the author

In no particular order, the main co-authors of the research results presented in the thesis are PhD student A. Šuminienė (Marcinkevičiūtė), dr. Nail Garejev, dr. Gintaras Tamošauskas, prof. habil. dr. Gintaras Valiulis, dr. Vytautas Jukna, prof. dr. Arnaud Couairon and prof. habil. dr. Audrius Dubietis. For more detailed aknowledgements please see the *Aknowledgements* section. Contribution of the author is noted below for each publication on which this thesis is based on.

Performed the evaluation of the nonlinear refractive indices in articles [**A1, A2, A4**], conducted all of the experimental measurements and the subsequent data analysis and visualization, as well as prepared the initial draft of articles [**A1-A6**].

# LIST OF PUBLICATIONS

On the dissertation topic


[A1] **R. Šuminas**, G. Tamošauskas, G. Valiulis, A. Dubietis, Spatiotemporal light bullets and supercontinuum generation in $\beta$-BBO crystal with competing quadratic and cubic nonlinearities, Opt. Lett. **41**, 2097–2100 (2016).

[A2] **R. Šuminas**, G. Tamošauskas, G. Valiulis, V. Jukna, A. Couairon, A. Dubietis, Second-order cascading-assisted filamentation and controllable supercontinuum generation in birefringent crystals, Opt. Express **25**, 6746–6756 (2017).

[A3] **R. Šuminas**, G. Tamošauskas, G. Valiulis, V. Jukna, A. Couairon, A. Dubietis, Multi-octave spanning nonlinear interactions induced by femtosecond filamentation in polycrystalline ZnSe, Appl. Phys. Lett. **110**, 241106 (2017).

[A4] **R. Šuminas**, G. Tamošauskas, A. Dubietis, Filamentation-free self-compression of mid-infrared pulses in birefringent crystal with second-order cascading-enhanced self-focusing nonlinearity, Opt. Lett. **43**, 235–238 (2018).

[A5] **R. Šuminas**, A. Marcinkevičiūtė, G. Tamošauskas, A. Dubietis, Even and odd harmonics-enhanced supercontinuum generation in zinc-blende semiconductors, J. Opt. Soc. Am. B **36**, A22–A27 (2019).

[A6] **R. Šuminas**, N. Garejev, A. Šuminienė, V. Jukna, G. Tamošauskas, A. Dubietis, Femtosecond filamentation, supercontinuum generation and determination of $n_2$ in polycrystalline SBN, J. Opt. Soc. Am. B **37**, 1530–1534 (2020).

Other publications

[A7] I. Gražulevičiūtė, **R. Šuminas**, G. Tamošauskas, A. Couairon, A. Dubietis, Carrier-envelope phase-stable spatiotemporal light bullets, Opt. Lett. **40**, 3719–3722 (2015).

[A8] N. Garejev, V. Jukna, G. Tamošauskas, M. Veličkė, **R. Šuminas**, A. Couairon, A. Dubietis, Odd harmonics-enhanced supercontinuum in bulk solid-state dielectric medium, Opt. Express **24**, 17060–17068 (2016).

[A9] A. Dubietis, G. Tamošauskas, **R. Šuminas**, V. Jukna, A. Couairon, Ultrafast supercontinuum generation in bulk condensed media (Invited Review), Lith. J. Phys. **57**, 113–157 (2017).

[A10] A. Marcinkevičiūtė, N. Garejev, **R. Šuminas**, G. Tamošauskas, A. Dubietis, A compact, self-compression-based sub-3 optical cycle source in the 3-4 $\mu$m spectral range, J. Opt. **19**, 105505 (2017).

[A11] A. Marcinkevičiūtė, V. Jukna, **R. Šuminas**, N. Garejev, G. Tamošauskas, A. Dubietis, Supercontinuum generation in the absence and in the presence of color centers in NaCl and KBr, Results Phys. **14**, 102396 (2019).

[A12] A. Marcinkevičiūtė, V. Jukna, **R. Šuminas**, N. Garejev, G. Tamošauskas, A. Dubietis, Femtosecond filamentation and supercontinuum generation in bulk silicon, Opt. Lett. **44**, 1343–1346 (2019).

[A13] A. Šuminienė, V. Jukna, **R. Šuminas**, G. Tamošauskas, M. Vengris, A. Dubietis, LiSAF: an efficient and durable nonlinear material for supercontinuum generation in the ultraviolet, Lith. J. Phys. **60**, 217–224 (2020).

Conference presentations

[C1] I. Gražulevičiūtė, **R. Šuminas**, D. Majus, G. Tamošauskas, N. Garejev, V. Jukna, A. Couairon, D. Faccio, A. Dubietis, Carrier-envelope phase-stable spatiotemporal light bullets, Naujametė fizikos konferencija LT$\phi$, Vilnius, Lithuania, 2015.

[C2] **R. Šuminas**, G. Tamošauskas, A. Dubietis, Supercontinuum generation in BBO crystal with competing quadratic and cubic nonlinearities, 41st Lithuanian National Conference on Physics, Vilnius, Lithuania, 2015.

[C3] I. Gražulevičiūtė, **R. Šuminas**, N. Garejev, G. Tamošauskas, A. Couairon, D. Faccio, A. Dubietis, Versatile spatiotemporal light bullets, 41st Lithuanian National Conference on Physics, Vilnius, Lithuania, 2015.

[C4] **R. Šuminas**, G. Tamošauskas, G. Valiulis, A. Dubietis, Three-dimensional self-focusing and control of supercontinuum generation in BBO crystal with competing quadratic and cubic nonlinearities, 59th Scientific Conference for Students of Physics and Natural Sciences Open Readings, Vilnius, Lithuania, 2016.

[C5] N. Garejev, V. Jukna, G. Tamošauskas, M. Veličkė, **R. Šuminas**, A. Couairon, A. Dubietis, Multioctave odd-harmonics-enhanced supercontinuum from plasma-dominated filamentation in solid state medium, Europhoton, Vienna, Austria 2016.

[C6] **R. Šuminas**, G. Tamošauskas, V. Jukna, A. Couairon, A. Dubietis, Second-order cascading assisted controllable supercontinuum generation in birefringent media, CLEO Europe/EQEC, Munich, Germany, 2017.

[C7] J. Lukošiūnas, **R. Šuminas**, N. Garejev, G. Tamošauskas, A. Dubietis, Multi-octave spanning nonlinear interactions induced by femtosecond filamentation in polycrystalline ZnSe, 60th Scientific Conference for Students of Physics and Natural Sciences Open Readings, Vilnius, Lithuania, 2017.

[C8] A. Marcinkevičiūtė, N. Garejev, **R. Šuminas**, G. Tamošauskas, A. Dubietis, Generation and compression of few optical cycle pulses in the 3–4 $\mu$m spectral range, 42nd Lithuanian National Conference on Physics, Vilnius, Lithuania, 2017.

[C9] **R. Šuminas**, G. Tamošauskas, G. Valiulis, V. Jukna, A. Couairon, A. Dubietis, Multi-octave supercontinuum and harmonic generation induced by femtosecond filamentation in polycrystalline ZnSe, 42nd Lithuanian National Conference on Physics, Vilnius, Lithuania, 2017.

[C10] A. Marcinkevičiūtė, V. Jukna, **R. Šuminas**, S. Balandytė, G. Tamošauskas, A. Dubietis, Femtosecond filamentation of mid-infrared pulses in bulk silicon, 8th EPS-QEOD Europhoton Conference "Solid State, Fibre, and Waveguide Coherent Light Sources", Barcelona, Spain, 2018.

[C11] **R. Šuminas**, J. Lukošiūnas, A. Marcinkevičiūtė, G. Tamošauskas, A. Dubietis, Filamentation induced ultrabroadband nonlinear interactions in polycrystalline zinc-blende semiconductors, 8th EPS-QEOD Europhoton Conference "Solid State, Fibre, and Waveguide Coherent Light Sources", Barcelona, Spain, 2018.

[C12] A. Marcinkevičiūtė, V. Jukna, **R. Šuminas**, S. Balandytė, G. Tamošauskas, A. Dubietis, Filamentation of femtosecond mid-infrared pulses in crystalline silicon, 11th International Conference on Photo-Excited Processes and Applications, Vilnius, Lithuania, 2018.

[C13] **R. Šuminas**, J. Lukošiūnas, A. Marcinkevičiūtė, G. Tamošauskas, A. Dubietis, Simultaneous ultrabroadband nonlinear interactions in polycrystalline ZnS and ZnSe, 11th International Conference on Photo-Excited Processes and Applications, Vilnius, Lithuania, 2018.

[C14] A. Marcinkevičiūtė, V. Jukna, **R. Šuminas**, N. Garejev, G. Tamošauskas, A. Dubietis, Influence of color centers on filamentation and supercontinuum generation in alkali metal halides NaCl and KBr, Ultrafast Optics UFO XII, Bol, Croatia 2019.

[C15] **R. Šuminas**, N. Garejev, A. Marcinkevičiūtė, V. Jukna, G. Tamošauskas, A. Dubietis, Filamentation and supercontinuum generation in polycrystalline strontium barium niobate (SBN) using infrared femtosecond laser pulses, Ultrafast Optics XII, Bol, Croatia, 2019.

# EXPERIMENTAL METHODS

This chapter aims to provide a brief introduction for the equipment and the practical methods used in the experiments. For more details please refer to the reprinted articles in the *Copies of Publications* chapter.

## LIGHT SOURCES

- Ti:sapphire laser system (Spitfire-PRO, Newport-Spectra Physics). Produces 800 nm, 120 fs pulses with an energy of up to 3 mJ at a repetition rate of up to 1 kHz. Used as a pump source in section 1.1. In the remaining sections used as a pump source for the commercial collinear and non-collinear OPAs.

- Commercial non-collinear OPA (TOPAS-White, Light Conversion Ltd.). Generates 530 – 720 nm, down to 20 fs pulses with an energy of up to 30 $\mu$J. Used as a reference pulse for spatiotemporal and temporal measurements in chapter 1.

- Commercial collinear OPA (TOPAS-PRIME, Light Conversion Ltd.). Generates 1200 - 2600 nm, 85 – 125 fs pulses with energy of up to 100 $\mu$J. Used as a pump source in sections 1.2, 1.3, 2.1 and 2.3. In section 2.2 the signal and idler waves were used for difference frequency generation.

- Difference frequency generation in a 1 mm long KTA crystal cut for type-II phase matching ($\theta = 43°$, $\phi = 0°$) between suitably predelayed signal and idler outputs of the collinear commercial OPA. Produces 3 – 5 $\mu$m, 60 – 100 fs pulses with an energy of up to 10 $\mu$J. Used in section 2.2.

## MEASUREMENT EQUIPMENT

- Home-built scanning prism spectrometer (SPS). At the output slit equipped with neutral density filter wheel of varying transmittance and up to two detectors performing simultaneous measurements. This, in addition to a choice of four different (Si, Ge, PbSe and InAsSb) photodetectors allowed us to perform high dynamic range measurements in the 0.3 – 5.8 $\mu$m spectral range. Used for spectral measurements in sections 1.1, 1.3 and throughout chapter 2.

- Commercial fiber spectrometer (AvaSpec-NIR256-2.5, Avantes) operating in the 1000 – 2500 nm wavelength range. Used for spectral measurements in section 1.2.

- Commercial fiber spectrometer (AvaSpec-2048, Avantes) operating in the 200 – 1100 nm wavelength range. Used for spectral measurements in section 1.2 and for SFG-FROG measurements in section 1.3.

- Commercial fiber spectrometer (QE65000, Ocean Optics) with an on-board thermoelectric cooler operating in the 200 – 1000 nm wavelength range. Used for luminescence trace measurements in section 2.2 and planar SH spectral measurements in section 2.3.

- Consumer CMOS camera (Nikon D7200). Used with 1.0x magnification lens for imaging planar SH radiation inside of the SBN crystal in section 2.3.

- Industrial CCD camera (Grasshopper 2, Point Grey), pixel size 4.4 µm, 14-bit dynamic range. Used for three dimensional mapping in section 1.2.

- Industrial CCD camera (COHU-6612 with Spiricon Inc. frame grabber), pixel size 9.9 µm, 10-bit dynamic range. Used for beam measurements in section 2.1.

- Industrial micro-bolometric camera (MBC) (DataRay WinCamD-FIR2-16-HR), pixel size 17 µm, 14-bit dynamic range. Used for beam measurements in section 2.1.

## MEASUREMENTS OF SPECTRAL DYNAMICS

Most of the spectral measurements with only small variations were performed in the following way. The input beam of appropriate wavelength was focused using a plano-convex lens into the front face of the nonlinear medium. The focal length of the lens was chosen so as to maintain a loose focusing condition in order to achieve efficient SC generation [46, 57]. The input pulse energy was adjusted using a rectangular continuously variable metallic neutral density filter (NDL-25C-2, Thorlabs Inc.) mounted on a vertically moving translation stage. The output beam was imaged onto the entrance slit of the home built SPS or a fiber tip using a 4f imaging system with a magnification of 4x consisting of a pair of silver coated parabolic mirrors.

A small exception to this formula is section 1.2. In this case the spectra were recorded using two calibrated fiber spectrometers (AvaSpec-2048 and AvaSpec-NIR256-2.5) and analyzed in polarization using a broadband dielectric polarizer. This deviation from the standard measurement setup arose due to the simple fact that the home-built SPS system was not yet developed.

Please refer to Tables 1 and 2 for a brief summary of the input beam parameters and material samples used throughout the experiments.

## TEMPORAL AND SPATIAL PULSE CHARACTERIZATION

A wide array of temporal and spatial characterization techniques were used throughout this work.

In section 1.1 an intensity cross-correlation setup was employed in order to investigate SC generation in the temporal domain. More precisely, the axial cross-correlation functions were measured by sampling the output pulse with a short, 25-fs gating pulse at 700 nm from the noncollinear optical parametric amplifier via sum-frequency generation in a thin (20 $\mu$m) BBO crystal.

In section 1.2 a three-dimensional imaging technique commonly known as three dimensional (3D) mapping [58] was used in order to verify the formation of spatiotemporally compressed light bullets. The main idea of the method is described in the following. The reconstruction of the spatiotemporal intensity distribution of an unknown wave packet is acquired by collection of a series of cross-correlation images with a CCD camera. Each of the images is shifted in time with respect to a short probe pulse, which acts as a time gate in a noncollinear sum-frequency generation setup. It is important to note that a thin enough nonlinear crystal must be chosen so as not to limit the spatio-temporal resolution of the maps due to the finite sum-frequency generation bandwidth. In our case, the spatially resolved cross-correlation function was recorded by sum-frequency generation in a thin (20 $\mu$m) $\beta$-BBO crystal using a short (20 fs) gating pulse at 685 nm produced by the noncollinear OPA system.

In section 1.3 the temporal intensity profiles were retrieved using the sum-frequency generation-based frequency-resolved optical gating (SFG-FROG) [59]. The measurements were performed using 19 fs, 707 nm reference pulses from the SH-pumped noncollinear optical parametric amplifier. Commercial FROG trace retrieval software (FROG version 3.2.4, Femtosoft Technologies) was used in order to retrieve the spectral and temporal properties of the self-compressed pulse.

For input pulse duration measurements a simple home-built intensity autocorrelator setup equipped with a thin (20 $\mu$m) $\beta$-BBO crystal was used in most cases.

For input beam measurements and output beam spatial characterization a variety of CCD and MBC cameras were used throughout the chapters.

## EXPERIMENTAL PARAMETER SUMMARY

The following tables and graphs provide a quick summary of the relevant experimental parameters and nonlinear media used in each of the following sections describing the experimental results.

Please refer to Table 1 for a summary of the input parameters and samples used in each of the sections. See Table 2 and Figure 1 for a summary of relevant linear and nonlinear parameters of the samples used in the experiments.

Table 1: Summary of relevant input beam/pulse and material parameters used in the experiments in each of the subsections. $\lambda_p$ is the pump wavelength, $\tau$ is the pulse width, $w_0$ is the $1/e^2$ radius of the focal spot at the crystal input and $d$ is the sample thickness.

| Section | $\lambda_p$, $\mu$m | $\tau$, fs | $w_0$, $\mu m$ | Sample(s) | $d$, mm |
|---|---|---|---|---|---|
| Section 1.1 | 0.8 | 120 | 21 | $\beta$-BBO[1] | 4.85 |
| Section 1.2 | 1.8 | 90 | 60 | $\beta$-BBO[2] | 5.5 |
| Section 1.3 | 2.1 | 68; 95 | 875; 1200 | $\beta$-BBO[2] | 5.5 |
| Section 2.1 | 2.4 | 100 | 43 | ZnSe | 5 |
| Section 2.2 | 3.6; 4.6 | 60; 100 | 71; 91 | ZnS | 2; 4 |
| | 3.6; 4.6 | 60; 100 | 71; 91 | ZnSe | 0.75; 2; 3 |
| | 3.6; 4.6 | 60; 100 | 71; 91 | ZnTe | 0.6; 1.2 |
| Section 2.3 | 1.2; 2.0; 2.4 | 85; 95; 125 | 36; 54; 53 | SBN:61 | 5 |

[1] Cut for type-I phase matching; $\theta = 37.4°$, $\phi = 90°$.
[2] Cut for type-I phase matching; $\theta = 24.3°$, $\phi = 90°$.

Table 2: Linear and nonlinear parameters of the samples used in the experiments. $E_g$ is the energy bandgap, $n_2$ is the nonlinear index of refraction, $d$ is the nonlinear optical coefficient, $\lambda_0$ is the zero GVD wavelength.

| Material | ZnS | ZnSe | ZnTe | SBN:61 | $\beta$-BBO |
|---|---|---|---|---|---|
| $E_g$, eV | 3.68[1] | 2.71[1] | 2.3[1] | 3.4[1] | 6.2[1] |
| Transparency range, $\mu$m | 0.4–12.5[1] | 0.5–20[1] | 0.55–25[1] | 0.45-5.5[1] | 0.19-3.5[1] |
| $n_2$, $\times 10^{-16}$ cm$^2$/W | 22[2] | 66[2] | 106[2] | 52.4[3] | 5.1[4] |
| $d$, pm/V | 8[5] | 30[5] | 52[5] | - | 2.2; 0.04[6] |
| $\lambda_0$, $\mu$m | 3.6[7] | 4.8[1] | 6.2[1] | 1.96[8] | 1.49[9] |

[1] The transparency range is defined at 10% transmission level of 1 mm thick sample as taken from [60].
[2] Evaluated at 3.6 $\mu$m using the formalism described in [61], with an updated dimensionless parameter $K = 7.33 \times 10^{-9}$ [62].
[3] Measured by Sheik-Bahae et al. [61] at 1.06 $\mu$m.
[4] Estimated by Bache et al. [63] at 0.8 $\mu$m.
[5] $d = d_{14} = d_{25} = d_{36}$ measured by Wagner et al. [64] at 1.321 $\mu$m.
[6] $|d_{22}| = 2.2$ pm/V, $|d_{31}| = 0.04$ pm/V measured by Shoji et al. [65] at 1.064 $\mu$m.
[7–9] Estimated using Sellmeier equations from [66–68].

Figure 1 shows the group velocity dispersion curves for each of the materials used in the experiments as calculated from the dispersion equations provided in [60, 66–68].

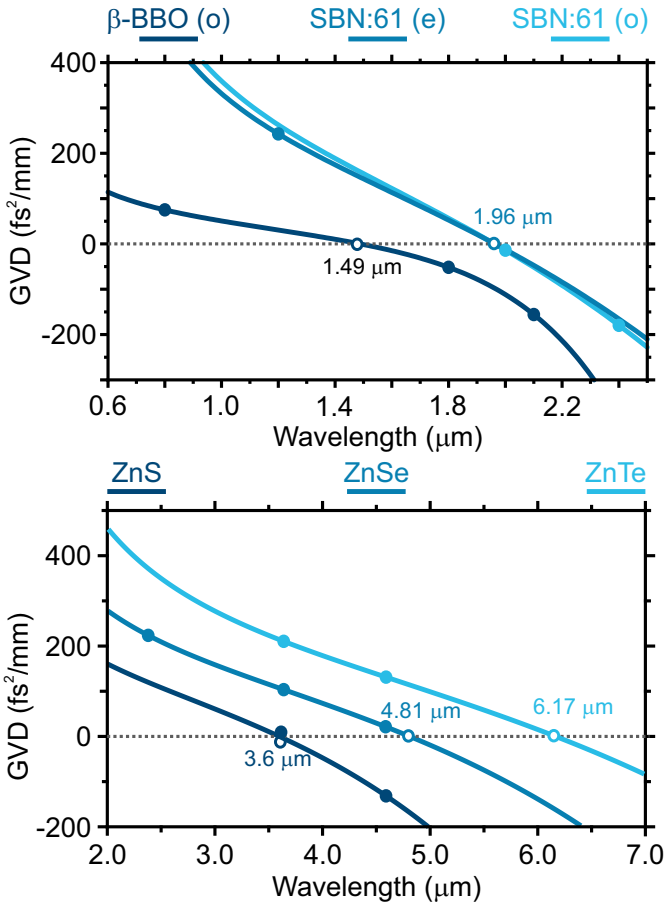


Figure 1: Group velocity dispersion curves for each of the nonlinear media used in the experiments. Empty and filled in circles mark the zero GVD and input wavelength points, respectively. Each material is attributed a single curve with the exception of SBN:61 which has two curves associated with the extraordinary (e) and ordinary (o) waves. Please see the legend above the figure for more details.

# EVALUATION OF THE CASCADED, KERR AND EFFECTIVE NONLINEAR REFRACTIVE INDICES

The estimation of the $\beta$-BBO effective (total) nonlinear refractive index serves as basis for the experiments performed throughout Chapter 1. Therefore, it is important to provide a detailed description of the procedure, which was followed in order to acquire it.

The first part of the calculation involves second-order cascaded nonlinearity, the nature of which can be explained intuitively in terms of Type-I phase-mismatched second-harmonic generation. During this process there is a recurrent energy exchange, commonly known as cascading, between the fundamental and second-harmonic waves [48]. The fundamental wave intensity follows a sinusoidal pattern along the length of the crystal, where a period of frequency up-conversion is followed by a period of frequency back-conversion, which occur after each odd and even number of coherence lengths $2\pi/|\Delta k|$, respectively. In case of strong phase mismatch ($\Delta kL \ll 2\pi$) this may happen hundreds of times and implies that the back-converted fundamental wave has a different phase as opposed to the unconverted fundamental wave. The resulting phase shift can be described by a higher-order nonlinear index in this work referred to as cascaded nonlinear refractive index [63]:

$$n_2^{\text{casc}} = -\frac{2\omega_p d_{\text{eff}}^2}{c^2\epsilon_0 n_o^2(\omega_p) n_{e,\theta}(2\omega_p)\Delta k}, \tag{4}$$

where $\omega_p$ is the fundamental frequency, $d_{eff}$ is the effective second-order nonlinear coefficient, $c$ is the speed of light, $\epsilon_0$ is the vacuum permittivity, $n_{o,e}$ is the linear refractive index for the ordinary and extraordinary waves, respectively and $\Delta k = k_{2\omega_p} - 2k_{\omega_p}$ is the phase mismatch.

The extraordinary refractive index for the second harmonic wave in a uniaxial crystal may be written as [69]:

$$n_{e,\theta}(2\omega) = \left[\frac{n_o^2(2\omega_p) n_e^2(2\omega_p)}{n_o^2(2\omega_p)\sin^2\theta + \mathrm{n_e^2(2\omega_p)}\cos^2\theta}\right]^{\frac{1}{2}} \tag{5}$$

where $\theta$ is the angle between the optical axis of the crystal and the pump-wave.

The following Sellmeier equations were used in order to acquire the linear refractive indices [68]:

$$
\begin{aligned}
n_o^2(\lambda) = 2.7359 + \frac{0.01878}{\lambda^2 - 0.01822} - 0.01471\lambda^2 \\
+0.0006081\lambda^4 - 0.00006740\lambda^6 \\
n_e^2(\lambda) = 2.3753 + \frac{0.01224}{\lambda^2 - 0.01667} - 0.01627\lambda^2 \\
+0.0005716\lambda^4 - 0.00006305\lambda^6
\end{aligned}
\tag{6}
$$

The effective second-order nonlinear coefficient $d_{\text{eff}}$ for Type-I phase matching interaction was estimated as [70]:

$$
d_{\text{eff}} = d_{31}\sin(\theta + \rho) - \mathrm{d}_{22}\cos(\theta + \rho)\sin(3\phi), \tag{7}
$$

where $\phi$ is the azimuthal angle between the optical axis of the crystal and the pump-wave, $\rho = \arctan\left[\frac{\mathrm{n}_{\mathrm{e},\theta}(2\omega)}{2}\left(\frac{1}{\mathrm{n}_{\mathrm{e}}^2(2\omega)} - \frac{1}{\mathrm{n}_{\mathrm{o}}^2(2\omega)}\right)\sin 2\theta\right]$ is the spatial walk-off angle for a negative uniaxial crystal [71].

The nonlinear coefficients $d_{22} = -2.2$ pm/V and $d_{31} = 0.04$ pm/V as measured by Shoji et al. [65] at 1064 nm were scaled to the appropriate wavelength before inserting into eq. (7) by the use of Miller's rule [65, 72]:

$$
\Delta_{\mathrm{ijk}} = \frac{d_{ijk}}{\chi_i^{(1)}(2\omega_p)\chi_j^{(1)}(\omega_p)\chi_k^{(1)}(\omega_p)} \tag{8}
$$

where $\chi_i^{(1)} = n_i^2 - 1$ and $d_{\mathrm{ijk}}$ are the appropriate linear susceptibilities and nonlinear coefficients, respectively.

The second part of the calculation involves the intrinsic cubic (Kerr) nonlinearity, which is responsible for the rise of an intensity dependent change in the refractive index $n = n_0 + n_2^{Kerr} I$ of the material, where $n_2^{Kerr}$ is the so called Kerr nonlinear refractive index and I is intensity of the fundamental wave. The value of $n_2^{Kerr}$ can be estimated as follows [63]:

$$
n_2^{\mathrm{Kerr}} = \frac{3c_{11}}{4n_o^2(\omega_p)\epsilon_0 c}, \tag{9}
$$

Throughout this work the nonlinear coefficient $c_{11}$ is estimated using the wavelength independant Miller's delta $\Delta_{1111} = 52.8 \times 10^{-24}$ m$^2$/V$^2$ [63] and the Miller's rule:

$$
c_{11} = \Delta_{1111} \times (\chi_1^{(1)}(\omega_p))^4 \tag{10}
$$

In the third and final part of the calculation we estimate the effective nonlinear refractive index, which is the result of the competition between the quadratic-cascaded and cubic (Kerr) nonlinearities:

$$
n_2^{\mathrm{eff}} = n_2^{\mathrm{casc}} + n_2^{\mathrm{Kerr}} \tag{11}
$$

# 1. SUPERCONTINUUM GENERATION AND PULSE SELF-COMPRESSION IN $\beta$-BBO CRYSTAL WITH COMPETING CASCADED-QUADRATIC AND CUBIC NONLINEARITIES

## Motivation

The rapidly expanding field of applications calls for achieving broadband radiation with desired temporal and spectral properties, which in turn require setting an efficient control of the filamentation process. Since the relevant parameters of an isotropic medium are generally fixed for a given input wavelength, a certain control of SC generation was demonstrated by tailoring the shape [40, 41] and the chirp [43] of the input pulse, by varying the polarization state [42], phase [44, 45] and the numerical aperture [46] of the input beam. More sophisticated methods are based on performing two color filamentation in collinear [73] and noncollinear [74] geometries.

However, the achieved degree of control of the SC spectrum is rather limited, and most of these methods require more or less complex technical implementation. In that regard, the use of birefringent nonlinear media, which possess both, quadratic and cubic nonlinearities, may provide a desired degree of freedom to perform the nonlinear interactions in a fully controlled fashion. The second-order cascading, which results from the phase-mismatched second harmonic (SH) generation [47, 48], produces a cascaded-quadratic Kerr-like nonlinearity, which contributes to the nonlinear index of refraction. Thus the light wave sees a material with an effective nonlinear index of refraction, $n_2^{\text{eff}} = n_2^{\text{Kerr}} + n_2^{\text{casc}}$, whose cascaded counterpart, $n_2^{\text{casc}} \propto -d_{\text{eff}}^2/\Delta k$, may be varied in sign and magnitude by setting an appropriate phase mismatch, $\Delta k = k_{2\omega} - 2k_{\omega}$. Therefore the interplay between the cascaded-quadratic and intrinsic cubic (Kerr) nonlinearities may be readily exploited to either enhance or suppress the nonlinear effects [49, 50] and to access qualitatively different regimes of nonlinear propagation.

The self-defocusing regime ($n_2^{\text{eff}} < 0$) is achieved within a certain range of positive phase mismatch. To this end, soliton compression was demonstrated, where negative effective nonlinearity imprints a frequency modulation that is compressible by the normal GVD of the medium [75–77]. Such soliton compression regime could be attained in a variety of nonlinear crystals [78] producing ultrabroadband supercontinuum [79] and allowing scaling of energy [80] and average power [81] of the self-compressed pulses. In contrast, the self-focusing regime ($n_2^{\text{eff}} > 0$) is achieved within a wide range of either positive or negative phase mismatch, which in the normal GVD region leads to SC generation via filamentation [82–84], large scale spectral broadening [85] and the ability

to control both the filamentation dynamics [86] and the spectral extent of supercontinuum [87]. More recent experiments in the anomalous GVD region demonstrate the feasibility of the self-focusing regime for spatial, spectral and temporal shaping of light within a wide input parameter space, ranging from picosecond [88] to few optical cycle pulses [89].

Furthermore, cascaded-quadratic nonlinearity may be used for a practical realization of a controllable anomalous GVD-induced self-compression regime, which relies upon using a shorter nonlinear medium and a larger input beam, extracting the self-compressed pulse before the catastrophic self-focusing and filamentation regime sets in. Numerical simulations suggest that filamentation-free self-compression could yield pulse widths approaching a single optical cycle and could be scaled in wavelength and energy, as long as one dimensional dynamics of the input pulse are maintained [90–95]. To date, soliton compression was experimentally demonstrated with microjoule [96] and millijoule [97] input pulse energies in the $3-4$ $\mu$m wavelength range, yielding self-compressed pulses with homogenous spatial profiles and durations of sub-three optical cycles.

This chapter is based on the research published in papers **[A1, A2, A4]** and presents a comprehensive study on filamentation and supercontinuum generation in a birefringent medium ($\beta$-BBO crystal) as pumped by 0.8 $\mu m$, 1.8 $\mu m$ and 2.1 $\mu m$ femtosecond pulses. The wavelenghts were chosen so as to fall into both the normal and anomalous GVD regions of the material. In the case of 2.1 $\mu m$ pulses, favorable conditions for controllable self-compression and energy scaling of the self-compressed pulses are demonstrated in the absence of self-focusing and filamentation of the input beam.

## 1.1. Supercontinuum generation in the normal group velocity dispersion region

The following section is dedicated to the investigation of SC generation in a $\beta$-BBO crystal using 0.8 $\mu$m, 120 fs pulses with the input wavelength chosen so as to fall into the normal GVD region of the material. For a brief summary of the experimental methods and measurement equipment used please see the *Experimental Methods* chapter. As for the following experiments, suffice it to say, the nonlinear sample was placed on a rotational stage allowing us to vary the phase delay $\Delta k$ between the incident fundamental wave and the generated second harmonic wave. In doing so, we were able to control the nonlinear refractive index of the material by simply changing the angle $\theta$ between the incident wave and the optical axis of the crystal. The latter effect facilitated by the phase mismatch dependent cascaded nonlinear refractive index variation was estimated using the standard cascading model briefly described in the *Evaluation of the Cascaded, Kerr and Effective Nonlinear Refractive Indices* chapter.

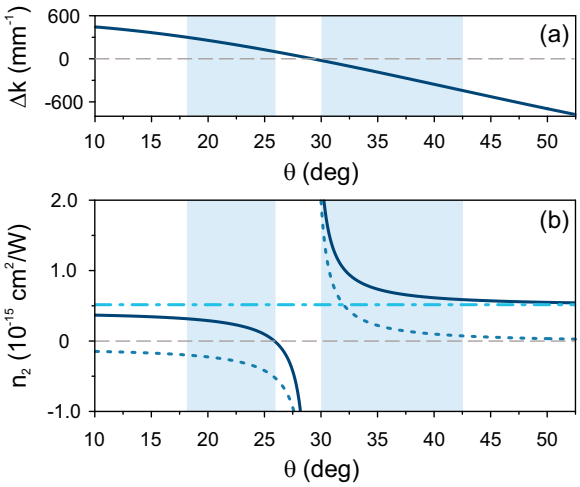


Figure 1.1: (a) Calculated phase mismatch parameter $\Delta k$ in $\beta$-BBO crystal for $\lambda_p = 800$ nm and $\lambda_{SH} = 400$ nm. (b) Nonlinear refractive indices: $n_2^{\text{Kerr}}$ (dash-dotted line), $n_2^{\text{casc}}$ (dotted curve) and $n_2^{\text{eff}}$ (solid curve) versus the angle $\theta$. The shaded areas mark the angle range where control of SC spectral extent was experimentally observed.

Figure 1.1 shows the evaluated phase mismatch parameter $\Delta k = k_{2\omega} - 2k_{\omega}$ and nonlinear refractive indices as functions of the angle $\theta$. Several regions of interest may be distinguished. In case of large positive phase mismatch, both defocusing and self-focusing regimes are available. This is due to the negative contribution of the cascaded nonlinearity, which depending on the magnitude either exceeds or contributes little to the intrinsic (Kerr) one. Also of interest is the angle marking the boundary between the two distinct regions, where the contributions of cascaded-quadratic and cubic nonlinearities are equal. The beam should experience neither self-focusing nor de-focusing at the so called zero focusing angle $\theta_{\text{zf}} = 25.9°$. For negative phase mismatch, cubic and cascaded-quadratic nonlinearities are of the same sign, thus leading to a large positive effective nonlinear index of refraction, where enhanced self-focusing is expected. As a final note, due to efficient SH generation the cascading approximation breaks down for small either positive or negative phase mismatch values ($|\Delta k L| \ll 2\pi$) therefore should not be used.

Figure 1.2 presents measurements of spectral broadening versus the angle $\theta$ for several input pulse energies mostly in the range of negative phase mismatch. The spectra consists of both, the ordinarily and extraordinarily polarized spectral components concentrated around the fundamental and SH wavelength, respectively. The spectral ranges for each of these polarizations are denoted with arrows labeled $o$ and $e$ in the figure. The measured dynamics immediately reveal a number of interesting features, associated with spectral broadenings at ordinary and extraordinary polarizations.

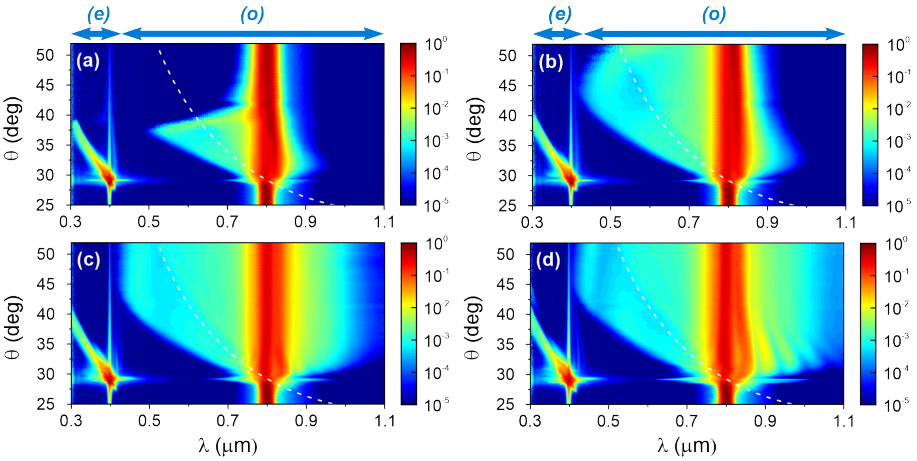


Figure 1.2: Experimentally measured spectra as functions of angle $\theta$ with various input pulse energies: (a) 160 nJ, (b) 190 nJ, (c) 280 nJ, (d) 410 nJ. Each plot is composed of 110 individual spectra. The logarithmic intensity scale is used to highlight fine spectral features. The solid and dashed curves depict the self-phase matching curve for an axial SH component and the corresponding wavelengths in the spectrally broadened fundamental pulse, respectively.

First of all, a considerable spectral broadening around the SH (400 nm) and fundamental (800 nm) wavelengths is captured at the phase matching angle for SH generation ($\theta_{SHG} = 29.2°$). The nature of this phenomenon may be explained by filamentation of the SH beam itself. We demonstrate this by considering the efficiency of SH generation and bearing in mind that the critical power for self-focusing is directly proportional to the input wavelength $P_{cr} \propto \lambda_0^2$. In fact, with 45% energy conversion (see Fig. 1.3), the peak power of the SH pulse even with the lowest input pulse energy of 160 nJ, exceeds the critical power for self focusing more than twofold $\frac{P}{P_{cr}} > 2$, where $P_{\mathrm{cr}} = 0.23$ MW was estimated using $n_2^{\mathrm{Kerr}} = 6.3 \times 10^{-16}$ cm$^2$/W at 400 nm [63]. Hence filamentation of the SH pulse leads to generation of the extraordinarily polarized SC, which spans from 300 to 610 nm and induces a considerable spectral broadening (from 650 nm to 1 $\mu$m) around the fundamental wavelength due to cross-phase modulation.

Secondly, a complex spectrum of the extraordinarily polarized SH consisting of two distinct peaks is observed. The narrow spectral peak centered at exactly 400 nm is attributed to the phase mismatched SH, whose intensity rapidly drops as the crystal is rotated out of phase matching. The second peak is broader and much more intense and is tunable in the $300 - 400$ nm range. Its occurrence is attributed to the so-called self-phase matching (solid curves in Fig. 1.2), which is inherent to SH generation by narrow light beams carrying broadband pulses [98], and which is accessed by a certain range of spectral components

(dashed curves in Fig. 1.2) present in a spectrally broadened fundamental pulse.

Figure 1.3 shows the energy conversion efficiency to SH as a function of the angle $\theta$ for the input pulse energies of 160 nJ and 280 nJ. Here the total energy was estimated by the integration of the spectra presented in Figs. 1.2(a) and 1.2(c) over the entire 300-1100 nm range, while the energy contained in the SH was estimated by the integration in the 300-450 nm range. At the vicinity of phase matching, the SH energy was estimated by the integration over wider 300-610 nm spectral range due to SC generation by the SH pulse. For $\theta > 32°$, we may readily distinguish between the energy conversions to self-phase-matched SH (tunable in wavelength) and phase-mismatched SH (at 400 nm), as shown in the inset.

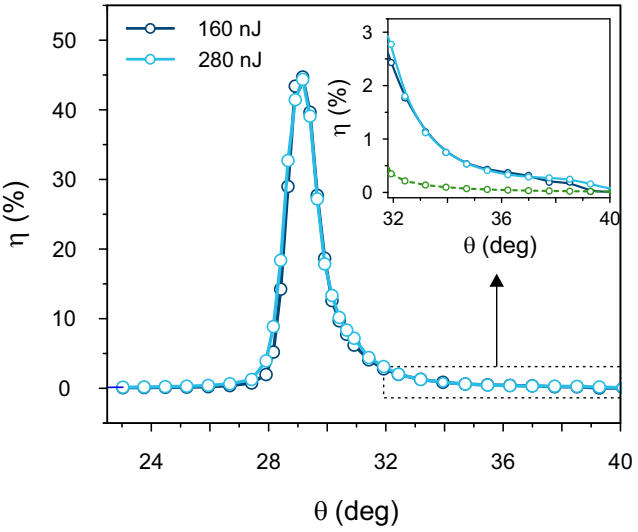


Figure 1.3: The total SH energy conversion efficiency as a function of the angle $\theta$ with the input pulse energies of 160 nJ (dark blue curve) and 280 nJ (light blue curve). The inset shows a magnified fraction of the graph, which distinguishes between the self-phase-matched and phase mismatched (green dashed curve) SH generation.

Thirdly, and most importantly, at the ordinary polarization, the spectral broadening around the carrier wavelength shows a qualitatively different behavior in the $\theta$ range above and below 42.5°. In the range of very large negative phase mismatch ($\theta > 42.5°$) and for relatively low input pulse energies the spectral broadening is almost absent [Fig. 1.2(a)] or unstable, as seen from the ragged blue-shifted edge of the SC spectrum in Fig. 1.2(b). At higher input pulse energies, a stable SC, which spans from 410 nm to 1.1 $\mu$m is generated, whose spectral extent remains constant irrespective of phase mismatch [Figs. 1.2(c) and 1.2(d)]. These results are rather obvious, since in this angle

range the contribution of the cascaded second-order nonlinearity to the effective nonlinear index of refraction quickly vanishes, as seen from Fig. 1.1(b). Therefore for input pulse energy of 160 nJ, its power just very slightly exceeds the critical power for self-focusing ($P \approx 1.04P_{cr}$) and the beam is not able to self-focus within the crystal. For input pulse energy of 190 nJ, the nonlinear focus is located very close to the output face of the crystal, resulting in unstable spectral broadening due to small fluctuations of laser pulse energy. Only with input energies of 280 nJ and 410 nJ a stable filamentation regime is achieved.

Finally, the most striking behavior of the spectral broadening is observed in the $\theta$ range of $30° - 42.5°$. Here the extension of the blue-shifted part of the SC spectrum shows a very strong dependence on the angle $\theta$, while the extent of the red-shifted part is almost constant over the entire angle range, especially with higher input pulse energies, as seen in Figs. 1.2(c) and 1.2(d). The most fascinating feature of the SC spectrum is that its blue-shifted cut-off gradually extends to shorter wavelengths while varying angle $\theta$ from 30° to 42.5°. Moreover, the cut-off wavelength is remarkably stable for a given crystal orientation and does not change with input pulse energy, suggesting a complete control of the blue-shifted spectral extent of the SC via phase mismatch. This is illustrated in more detail in Fig. 1.4, which shows the cut-off wavelength, defined at the $10^{-4}$ intensity level, as a function of the input pulse energy for several angles $\theta$.

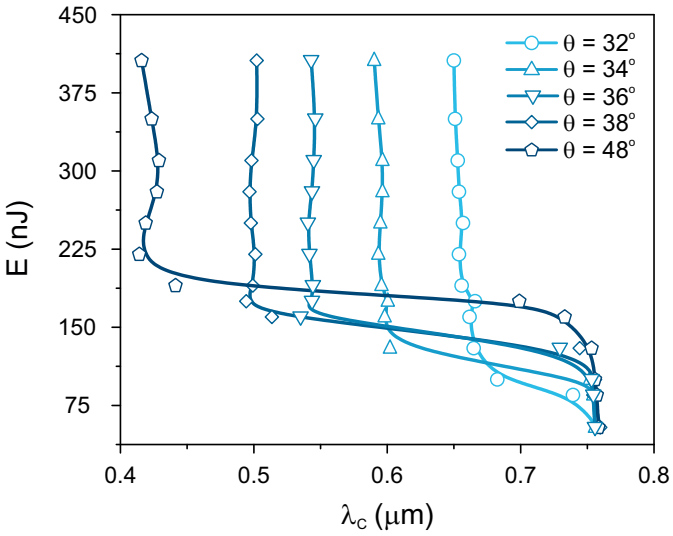


Figure 1.4: The blue-shifted cut-off of the SC spectrum as a function of the input pulse energy and angle $\theta$.

In order to get more insight into the underlying phenomena, we consider the effects of pulse splitting and self-steepening, which play a key role in producing spectral broadening in the filamentation regime [12, 15]. For that purpose we

have measured the axial cross-correlation functions of SC pulses generated at several crystal orientations, which yield SC spectra with different blue-shifted broadenings. The measurements were performed by employing a noncollinear sum-frequency generation setup using a short probe pulse in a thin BBO crystal. For more details please refer to the *Experimental Methods* chapter. The results presented in Fig. 1.5 confirm that pulse splitting is detected over the entire range of angles $\theta$, where spectral broadening takes place. For a fixed input pulse energy and different values of $\theta$, we capture the split sub-pulses at various stages of their evolution, in line with the whole evolution cycle of femtosecond filaments in the range of normal group velocity dispersion [99]. More precisely, as the pulse splitting event takes place at the nonlinear focus, a large part of the energy is expelled out of propagation axis, and thereafter with further propagation rebuilds the axial pulse at the center (at the zero delay). If its power exceeds the critical power for self-focusing, the reconstructed pulse undergoes another self-focusing cycle with subsequent secondary splitting event.

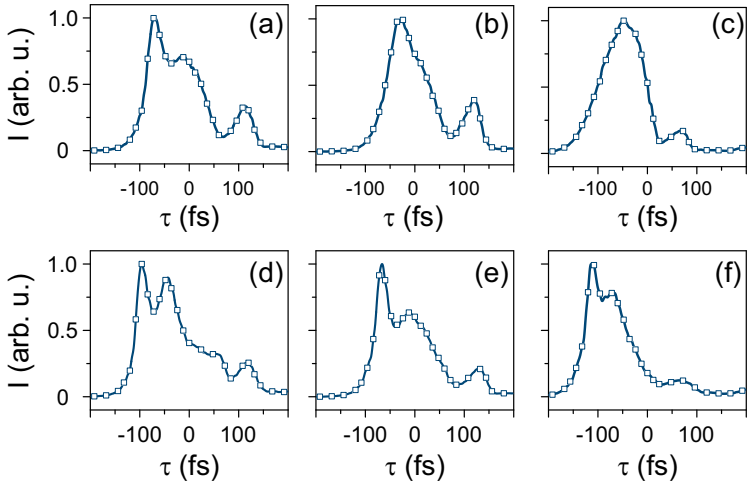


Figure 1.5: The axial cross-correlation functions measured with two input pulse energies: 190 nJ (top row) and 280 nJ (bottom row) and at various angles $\theta$: (a),(d) 32.4°, (b),(e) 37.5°, (c),(f) 42.6°.

The measured cross correlation functions confirm the above scenario in great detail, taking into account the inverse relationship between $n_2^{\text{eff}}$ and $\theta$ as shown in Fig. 1.1(b). As for the high values of $n_2^{\text{eff}}$, the nonlinear focus is located closer to the input face of the crystal, thus after the pulse splitting event, there remains a sufficient propagation distance to rebuild the axial pulse, as shown in Fig. 1.5(a). In contrast, for the lower values of $n_2^{\text{eff}}$, only split sub-pulses are detected, as pulse splitting takes place closer to the output face of the crystal [Figs. 1.5(b) and 1.5(c)]. Similar considerations apply to the results

shown in Figs. 1.5(d)-1.5(e). However, in this case due to higher input pulse energy the nonlinear focus and the inherent pulse splitting event is shifted even closer to the input face of the nonlinear crystal, therefore the reconstructed pulse is present in all measurements. For the highest value of $n_2^{\text{eff}}$, we capture the splitting of the reconstructed pulse after the secondary nonlinear focus, as shown in Fig. 1.5(d). The secondary splitting produces periodic modulation in the SC spectrum due to temporally separated pairs of the sub-pulses at the leading and trailing edges. This is barely seen in Fig. 1.2(c) but clearly emerges in Fig. 1.2(d).

On the other hand, the spectral superbroadening is a direct consequence of self-steepening, and the spectral blue shift is associated with the self-steepening of the trailing front of the trailing sub-pulse [15]. The earlier studies of spectral broadening in the absence of filamentation demonstrated that quadratic self-steepening due to second-order cascading has a nearly identical effect as cubic self-steepening, with the additional property of being inversely proportional to the phase mismatch parameter $\Delta k$, and hence controllable in sign and magnitude [100, 101]. More precisely, in the range of relatively small negative phase mismatch, the quadratic self-steepening is expected to amplify the effect of cubic self-steepening, giving rise to a considerable blue-shifted spectral broadening. However, our measurements presented in Fig. 1.2 show directly the opposite. Therefore, at this point we refer to the results of Fig. 1.3 and its inset in particular, which demonstrate that even at large phase mismatch, a still reasonable amount of the input pulse energy is converted into the self-phase-matched SH. More importantly, the blue-shift of the self-phase-matched SH wavelength suggests that it is generated only by the trailing sub-pulse, whose carrier frequency is blue-shifted [102].

In order to estimate the energy fraction carried by the trailing sub-pulse, we performed a numerical simulation using the standard filamentation model in media with cubic nonlinearity, which is based on solving the paraxial unidirectional propagation equation with cylindrical symmetry for the nonlinear pulse envelope coupled with an evolution equation for the electron density generated by the high-intensity pulse [103]. The model simulated filamention as if the second-order nonlinear effects were absent, corresponding to the experimental situation far away from the phase matching. The numerical data show that a light filament with a 5 $\mu$m FWHM diameter emerges after 1.5 mm of propagation, and is immediately followed by an almost symmetric pulse splitting and SC generation. The energy balance is as follows: 18% of the input energy is lost due to five photon absorption and absorption by the free electron plasma, and the central core contains 14% of the remaining energy, so assuming that both sub-pulses possess similar energies, the trailing sub-pulse carries just 6% of the input pulse energy. Since the total energy conversion to the self-phase-matched SH is estimated at 2.8% at $\theta = 32^\circ$ (as shown in the inset of Fig. 1.3),

we conclude that almost half of the trailing sub-pulse energy is converted into the self-phase-matched SH.

Such an efficient conversion is due to the fact that generation of self-phase-matched SH is group velocity matched with the pump as well, as the SH radiation takes the spatiotemporal shape of an X-wave, as demonstrated in [98]. As a result, the trailing sub-pulse undergoes considerable energy loss and distortion, which counteracts the effect of both, quadratic and cubic self-steepenings, preventing the blue-shifted spectral broadening of the SC. As the energy conversion to self-phase-matched SH gradually drops with increasing $\theta$, the role of self-steepening increases, resulting in larger blue-shift. Eventually, at very large $\Delta k$ ($\theta > 42.5°$), the generation of self-phase-matched SH ceases completely, as well as the effect of quadratic self-steepening. Here the blue-shifted spectral broadening is entirely controlled by cubic self-steepening, yielding a constant blue-shifted extension of the SC. The above considerations are also supported by the fact that the red-shifted leading sub-pulse has no self-phase matching, so the red-shifted extent of the SC is not affected and remains fairly constant over the entire $\Delta k$ range.

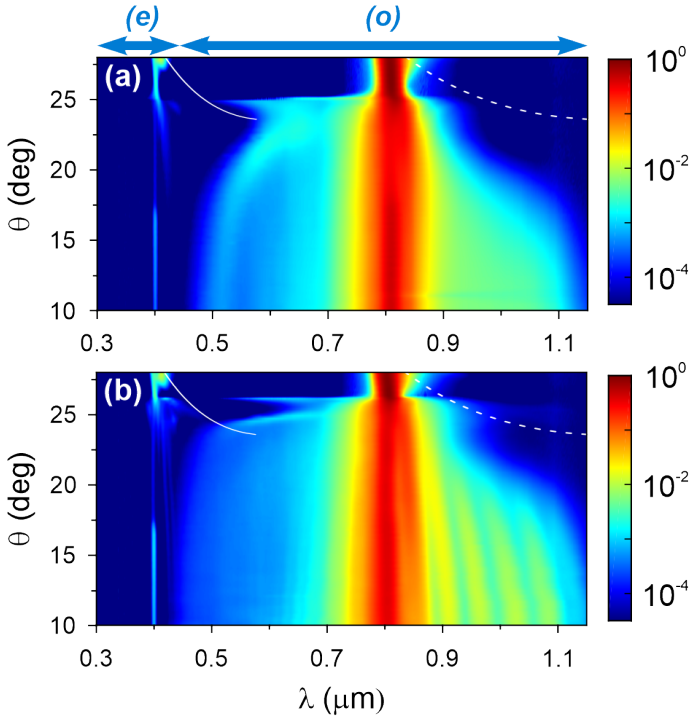


Figure 1.6: Spectral measurements in the range of positive phase mismatch with input pulse energies of (a) 0.6 $\mu$J and (b) 1 $\mu$J. Logarithmic intensity scale is used to highlight fine spectral features. The solid and dashed curves depict the self-phase matching curve for an axial SH component and the corresponding wavelengths in the spectrally broadened input pulse, respectively.

A different situation is then expected at positive phase mismatch, where self-phase matching is still possible [104], but within a reduced $\theta$ range, wherein the spectral components of the fundamental pulse satisfying the self-phase matching condition are absent and so no self-phase matched SH is generated. Figure 1.6 illustrates the spectral measurements in the $\theta$ range of 10-28°, which demonstrate markedly different dynamics of spectral broadening, which were measured with elevated input pulse energies of 0.6 $\mu$J and 1 $\mu$J as due to reduced values of $n_2^{\text{eff}}$, resulting from a negative contribution of $n_2^{\text{casc}}$ [see Fig. 1.1(b)]. More specifically, we observe the control of both, blue-shifted and red-shifted spectral broadenings in the $\theta$ angle range of 17-25°. This result may be explained by the competition between quadratic and cubic self-steepenings, which in the present case are of opposite signs [100], resulting in reduction of the overall self-steepening, acting on both, leading and trailing fronts of the sub-pulses. As the phase mismatch increases ($\theta$ decreases), the contribution of quadratic self-steepening gradually becomes negligible leading to increased blue and red shifts of the SC spectrum. Eventually, for $\theta < 17°$, the overall spectral extent of the SC becomes fairly constant, defined by the cubic self-steepening only.

As a final note, no SC generation was observed in the region between the zero-focusing angle $\theta_{zf}$ and the perfect phase matching angle for SH generation $\theta_{SHG}$ due to the absence of filamentation in the self-defocusing regime, as seen both in Fig. 1.2 and Fig. 1.6.

## 1.2. Supercontinuum generation in the anomalous group velocity dispersion region

The second section is dedicated to the investigation of SC generation and its spatiotemporal properties as obtained in a $\beta$-BBO crystal using 90 fs, 1.8 $\mu$m pulses with the input wavelength chosen so as to fall into the anomalous GVD region of the material. As in the previous case the sample was placed on a rotational stage in order to vary the phase mismatch parameter. Once again, for a summary of the experimental methods and input parameters used in the following experiments please refer to the *Experimental Methods* chapter. Similarly, the same procedure as in the previous section was used to calculate the nonlinear refractive index curves depicted in Fig. 1.7. Suffice it to say, the self-focusing regions I and IV possess rather different values of $n_2^{\text{eff}}$, thereby the experiments were performed using two different input pulse energies: 1) 1.35 $\mu$J and 2) 0.36 $\mu$J, respectively, so as to achieve stable and reproducible SC generation. Since a detailed analysis of Fig. 1.7 would be very similar to Fig. 1.1, we refrain from further discussion of this subject and refer the reader to Section 1.1 or the reprinted article [**A1**] for a more detailed view.

The results presented in Fig. 1.8 show the spectra at ordinary and extraordinary polarizations versus the angle $\theta$. The output spectra were analyzed in

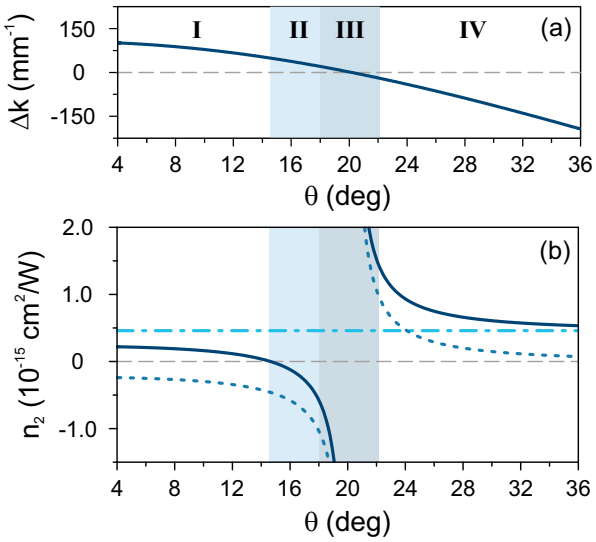


Figure 1.7: (a) Calculated phase mismatch parameter $\Delta k$ in $\beta$-BBO crystal for $\lambda_p = 1.8$ $\mu$m and $\lambda_{SH} = 0.9$ $\mu$m. (b) Nonlinear refractive indices: $n_2^{\text{Kerr}}$ (dash-dotted line), $n_2^{\text{casc}}$ (dotted curve) and $n_2^{\text{eff}}$ (solid curve) versus the angle $\theta$. Roman numerals and shading mark four distinct regions, which refer to focusing (I, IV) and defocusing (II) effective nonlinearities, and efficient SHG (III), where the cascading approximation breaks down.

polarization using a broadband dielectric polarizer, allowing to capture evolution of ordinarily- and extraordinarily-polarized spectral components. The ordinarily-polarized SC spectra [Figs. 1.8(a) and 1.8(c)] exhibit very similar features as to those reported in isotropic dielectric media with anomalous GVD: a very broad spectrum spanning from 0.52 $\mu$m to 2.5 $\mu$m with the mid-IR wavelength being limited by the detection range of the spectrometer and featuring a distinct intense blue-shifted peak. However, unlike in isotropic dielectric media, here, we demonstrate the ability to readily control the SC generation process by simply varying the angle $\theta$, i.e. by adjusting the sign and magnitude of the effective nonlinear refractive index.

At first glance, the observed spectral features bear resemblance to the ones discussed in the previous section. For one, in the negative phase mismatch region, SC generation is observed only for a certain range of angles ($21.5° < \theta < 27°$) as seen in Fig. 1.8(a). The lower limit is set by the decrease of the input pulse peak power due to efficient energy transfer from the pump wave to the second harmonic wave nearing the perfect phase matching angle. Whereas, the upper limit is set by the phase mismatch dependent critical power for self-focusing, which increases above the input pulse peak power with decreasing effective nonlinear refractive index. This is clearly seen in Fig. 1.1 region IV bearing in mind that $P_{cr} \propto \frac{1}{n_2}$. Of note, however, is the

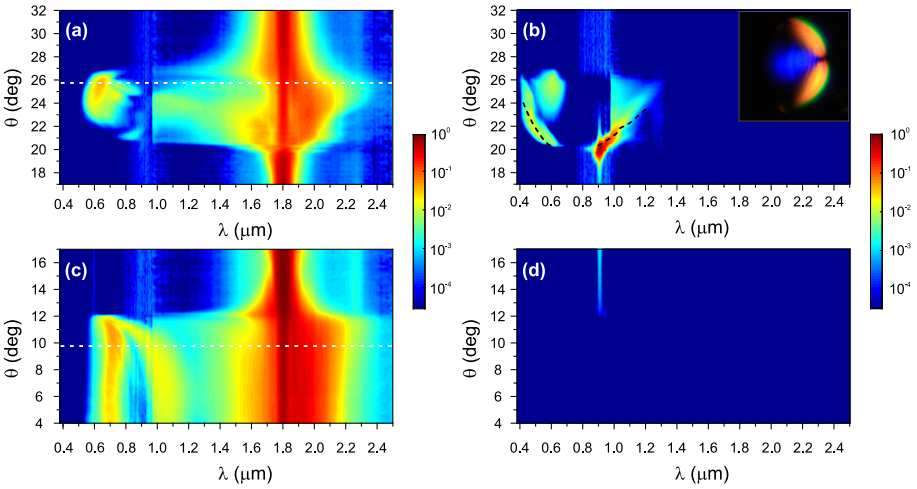


Figure 1.8: Experimentally measured spectra as functions of angle $\theta$ at ordinary (a), (c) and extraordinary (b), (d) polarizations. The input pulse energy: (a), (b) $E = 0.36$ $\mu$J, (c), (d) $E = 1.35$ $\mu$J. The self-phase matching curve for SHG is depicted by the black dashed curves in panel (b). Note that (a), (c) and (b), (d) share the same normalized logarithmic intensity scales, respectively. Inset: photo of the SH radiation at $\theta = 24.3°$. White dashed lines mark the angles at which the spatiotemporal intensity profiles were measured.

fact that due to the overall increase of the effective nonlinear refractive index in the negative phase mismatch region, SC generation is achieved with very low input pulse energies (0.36 $\mu$J), which are almost twice below the critical power for self-focusing ($0.62P_{\mathrm{cr}}$, where $P_{\mathrm{cr}} = 6.46$ MW). Therefore, the use of cascaded-quadratic nonlinearity offers a straightforward way of reducing the SC generation threshold down to sub-critical power values for self-focusing. The absence of this effect in the normal GVD regime is feasibly explained by the spatiotemporal features, namely the diminished role of the trailing sub-pulse due to efficient SH generation, discussed in the previous section. Conversely, in the region of positive phase mismatch ($\theta < \theta_{\mathrm{pm}}$) more than three times higher input pulse energy (1.35 $\mu$J) is required for efficient SC generation due to opposite signs of competing cascaded-quadratic and cubic nonlinearities that lead to a decrease of the effective nonlinear refractive index. Two distinct regions may be identified in Fig. 1.8(c). For $\theta > 12°$ SC generation is not observed due to either defocusing ($\theta_{\mathrm{zf}} < \theta < \theta_{\mathrm{pm}}$) or even higher input pulse energies ($12° < \theta < \theta_{\mathrm{zf}}$) required to achieve SC generation. While, for $\theta < 12°$ the beam undergoes self-focusing and a stable and controllable SC is generated.

The spectral dynamics of the extraordinary-polarized spectral components presented in Figs. 1.8(b) and 1.8(d) are almost identical to the ones seen and discussed in the previous section. Since the same considerations apply we refer the reader to Section 1.1 or the reprinted article [**A1**] for more details.

The SC spatiotemporal features were investigated by the use of three-dimensional imaging briefly described in the *Experimental Methods* chapter. The measurements were performed at two different angles as marked by white dashed lines in Figs. 1.8(a) and 1.8(c), where SC is generated at negative and positive phase mismatch, respectively. The results, as shown in Fig. 1.9, indicate a remarkable transformation and space-time compression of the input Gaussian-shaped wave packet. In both cases the measured spatiotemporal intensity distributions, despite large difference in the input pulse energy, are almost identical and consist of an intense self-compressed central core surrounded by a delocalized low intensity periphery, which is a characteristic feature of spatiotemporal light bullets in bulk dielectric media with anomalous GVD [20]. The apparent absence of a definite ring-shaped periphery could be attributed to the short length of the nonlinear medium used in the experiment, thus measuring the spatiotemporal profile of the emerging light bullet at its early formation stage.

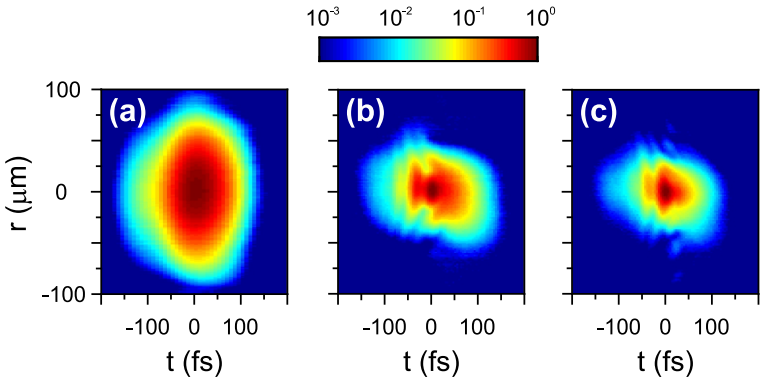


Figure 1.9: Experimentally measured spatiotemporal intensity profiles of the (a) input Gaussian wave packet and the emerging light bullets with two different sets of parameters: (b) $\theta = 9.6°$, $E = 1.35$ $\mu$J, (c) $\theta = 25.7°$, $E = 0.36$ $\mu$J. The logarithmic intensity scale is used to highlight fine spatiotemporal features.

Figure 1.10 shows the axial cross-correlation functions and corresponding spectra of the light bullets, which indicate three- to four-fold pulse compression due to opposite contributions of self-phase modulation and anomalous GVD. More specifically, pulse compression from 90 fs down to 31 fs and 21 fs is measured, as shown in Figs. 1.10(a) and 1.10(c), respectively, which are close to the zero phase Fourier transform limit as obtained from the corresponding spectra.

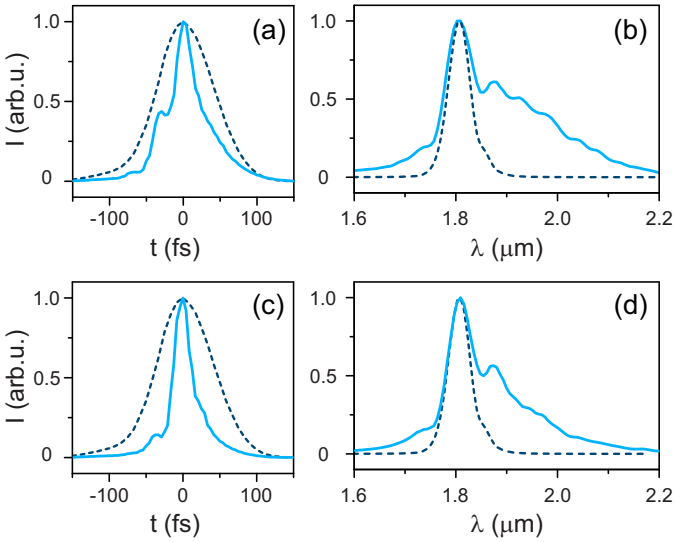


Figure 1.10: The axial cross-correlation functions of the light bullets and their corresponding spectra (solid curves) with two different sets of parameters: as in Figs. 1.9(b) and 1.9(c). The input pulse and its spectrum is represented by dashed curves.

## 1.3. Controllable filamentation-free self-compression of mid-infrared femtosecond pulses

In the last section we further exploit the interplay between the cubic and quadratic-cascaded nonlinearities along with anomalous GVD in order to demonstrate controllable self-compression. The pulse undergoes self-frequency modulation of varying degree due to different contributions of phase mismatch dependent quadratic-cascaded and constant Kerr nonlinear refractive indices. For positive effective nonlinear refractive index values, anomalous GVD counteracts the effect of SPM, therefore the pulse experiences self-compression. In the following experiments, we demonstrate the most favorable conditions for self-compression in such media, and provide evidence of excellent energy scalability. In order to avoid nonlinear losses, the experiments were performed in the absence of self-focusing and filamentation of the input beam. This was achieved by placing the nonlinear crystal on a combined stage allowing not only independent rotation but also translation of the crystal. The crystal position $z$ with respect to the geometric focus ($z = 0$ cm) was translated along the beam propagation path, providing control over the input beam diameter and intensity. Simultaneously, the rotation of the crystal permitted fine adjustment of the angle $\theta$, allowing us to control the effective nonlinear index of refraction. The same procedure as in the previous sections was used for the estimation of the effective nonlinear refractive index curve depicted in Fig. 1.11(a).

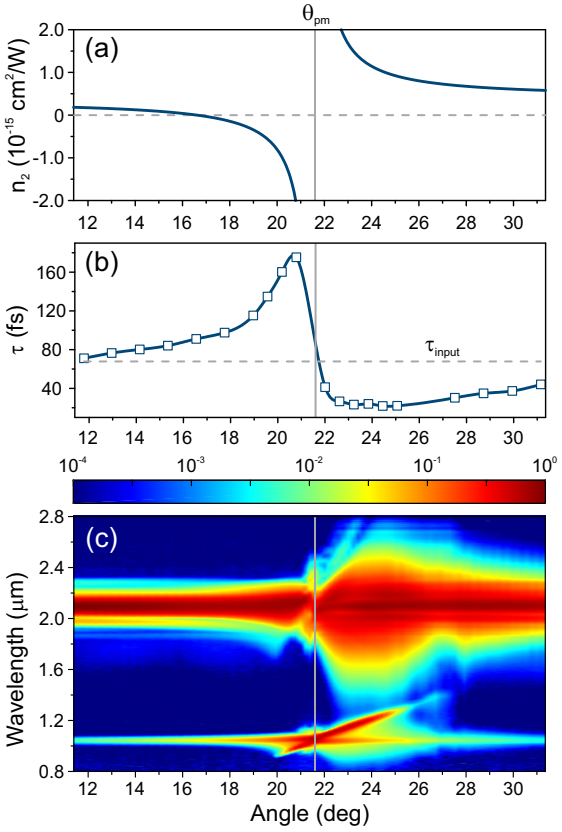


Figure 1.11: (a) The effective nonlinear refractive index $n_2^{\text{eff}}$ of $\beta$-BBO crystal as estimated using the cascaded approximation for $\lambda_p = 2.1$ $\mu$m and $\lambda_{SH} = 1.05$ $\mu$m, (b) temporal and (c) spectral dynamics versus the angle $\theta$ in a 5.5 mm thick $\beta$-BBO crystal located at $z = -7.7$ cm. The input pulse duration is 68 fs, energy 73 $\mu$J. Vertical lines indicate the perfect phase matching angle $\theta_{\text{pm}} = 21.6°$ for SH generation.

Figs. 1.11(b) and 1.11(c) show the output pulse temporal and spectral dynamics versus the angle $\theta$ as obtained using 68 fs, 73 $\mu$J, 2.1 $\mu$m input pulses in a $\beta$-BBO crystal located 7.7 cm before the geometric focal point ($I = 84$ GW/cm$^2$ at $z = -7.7$ cm). The pulse durations in Fig. 1.11(b) were retrieved using a SFG-FROG setup, which is briefly described in the *Experimental Methods* chapter. The spectral features, namely the large spectral broadening and the generation of phase mismatched and self-phase matched SH, are identical to those observed in section 1.2. Therefore, we turn our attention to the discussion of the controllable temporal self-compression and broadening as evidenced by the measurement results in Fig. 1.11(b).

For crystal angles $\theta > \theta_{\text{pm}}$, significant pulse self-compression, accompanied by a considerable SPM-induced spectral broadening, is observed. The duration

of the self-compressed pulse is determined by the balance between the large positive SPM and anomalous GVD. The most favorable conditions for self-compression, with the largest spectral broadening and retrieved pulse durations of less than 30 fs are found in the angle range of $22.5° < \theta < 25°$. However, a further increase of the angle $\theta$ leads to a gradual reduction of the spectral bandwidth due to diminishing effect of SPM, therefore resulting in a steady increase of the retrieved pulse width. Figure 1.12 shows the SFG-FROG traces and spectra of the input and self-compressed pulses and compares the retrieved intensity profiles and phases of both pulses at the maximum self-compression angle $\theta_{\rm opt} = 24.5°$ ($n_2^{\rm eff} = 10 \times 10^{-16}$ cm$^2$/W). The pulse exhibits more than three-fold self-compression from 68 fs to 22 fs, which is equivalent to 3.1 optical cycles, and was retrieved within grid size of 256 $\times$ 256 pixels and a FROG trace reconstruction error of 0.5%.

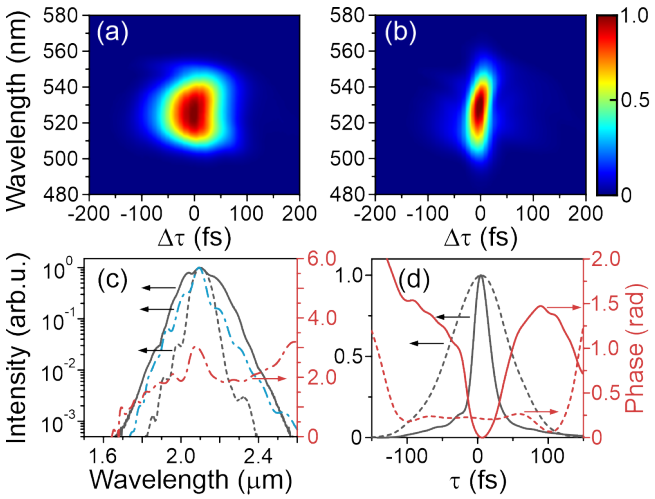


Figure 1.12: Self-compression of 68 fs, 73 $\mu$J pulses at 2.1 $\mu$m down to 22 fs in a $\beta$-BBO crystal located at $z = -7.7$ cm: the measured SFG-FROG traces of (a) input and (b) self-compressed ($\theta_{\rm opt} = 24.5°$) pulses, (c) measured (solid curve) and retrieved spectra and spectral phase (dash-dotted curves), (d) retrieved intensity profile and phase of the self-compressed pulse. Dashed curves in (c) and (d) show the spectrum, intensity profile and phase of the input pulse.

In contrast, for $\theta < \theta_{\rm pm}$, only temporal broadening of the pulse is observed and is attributed to two distinct modes of propagation. In the self-defocusing regime, in the angle range of $16.6° < \theta < 21°$, where $n_2^{\rm eff} < 0$, the pulse experiences negative SPM, which in combination with anomalous GVD leads to a considerable increase of the pulse duration. Approaching the angle of zero focusing ($\theta_{\rm zf} = 16.6°$), the SPM-induced spectral broadening diminishes, as well as leading to a decrease of the dispersive broadening of the pulse. For the crystal angles $\theta < \theta_{\rm zf}$, in the regime of reduced self-focusing, the dispersive

broadening of the pulse remains dominant due to insufficient positive SPM.

Figure 1.13(a) shows the transmission of total and fundamental harmonic energies as well as the SH generation efficiency as functions of the angle $\theta$. It is important to note that the total energy transmission measurements clearly indicate the absence of nonlinear losses due to multiphoton absorption, which is inherent to the filamentation regime. Figs. 1.13(b) and 1.13(c) show the near-field profiles of the input beam, as measured before the focusing lens and the output beam carrying the self-compressed pulse, respectively. Smooth, slightly super-Gaussian spatial intensity distribution attests the absence of beam filamentation. We identify SH generation and Fresnel reflections as the main sources of energy loss. At the vicinity of perfect phase matching for SH generation, a considerable depletion of the pulse at fundamental frequency is observed, with the SH conversion efficiency reaching up to 49%. In contrast, as the crystal is rotated out of phase matching, a quick decline of the SH efficiency results in a virtually lossless self-compression with the maximum energy throughput of 86.3% at the angle of maximum self-compression $\theta_{\mathrm{opt}} = 24.5°$. In this case, the energy throughput is simply limited by the Fresnel reflections from the input and output faces of the $\beta$-BBO crystal and the self-phase matched SH generation, which consumes just a small fraction (0.7%) of the input pulse energy.

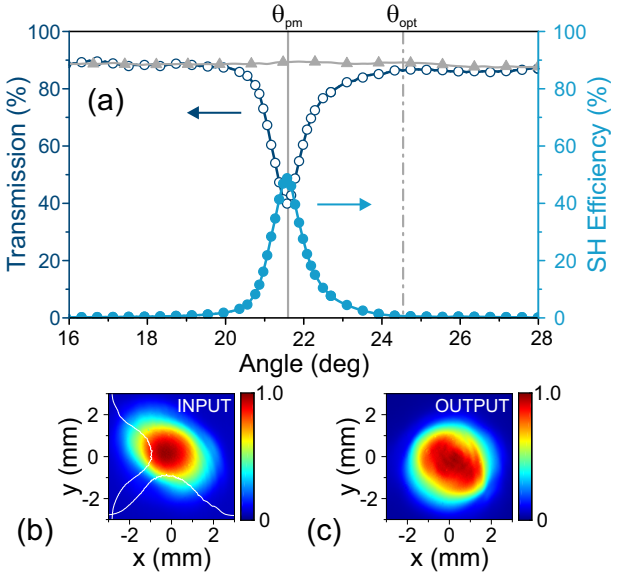


Figure 1.13: The transmission of total (triangles) and fundamental harmonic (open circles) energies, and the SH efficiency (filled circles) as functions of angle $\theta$. The parameters of the input pulse are the same as in Fig. 1.11. Vertical lines mark the angles of perfect phase matching for SH generation ($\theta_{\mathrm{pm}}$) and maximum self-compression ($\theta_{\mathrm{opt}}$). Near-field profiles of (b) input and (c) output at $\theta$=$\theta_{\mathrm{opt}}$ beams.

Owing to the possibility to vary the effective nonlinear index of refraction via crystal angle, filamentation-free self-compression could be efficiently performed for a relatively wide range of the input pulse energies and intensities, allowing to scale the energy and peak power of the self-compressed pulses. To demonstrate so, the input pulses were further amplified in a complementary optical parametric amplification stage consisting of a 2-mm $\beta$-BBO crystal cut for type-II phase matching ($\theta = 28°$, $\phi = 0°$) that delivers up to 215 $\mu$J energy pulses at 2.1 $\mu$m with a duration of 95 fs. Subsequently, to avoid filamentation due to significantly increased intensities and to preserve the balance between the SPM and anomalous GVD, the sample was moved further away from the geometric focus and placed at $z = -12.2$ cm ($I = 94$ GW/cm$^2$). More than three-fold self-compression (see Fig. 1.14) down to 27 fs (equivalent to 3.9 optical cycles) with the energy throughput of 85% was achieved yielding the self-compressed pulse with 4.5 GW peak power. Even further energy scaling might be achieved by placing the crystal after the geometrical focus, where self-focusing effect is in part compensated by the input beam divergence.

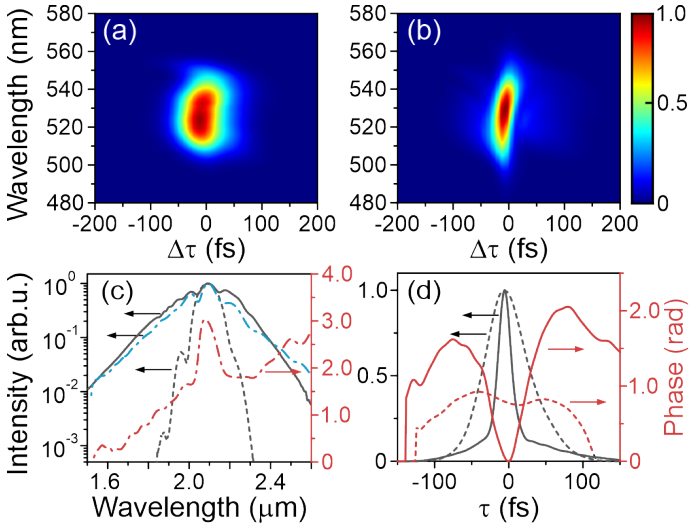


Figure 1.14: Self-compression of amplified 95 fs, 215 $\mu$J pulses at 2.1 $\mu$m down to 27 fs in a $\beta$-BBO crystal located at $z = -12.2$ cm: the measured SFG-FROG traces of (a) input and (b) self-compressed ($\theta_{\text{opt}} = 24.5°$) pulses, (c) measured (solid curve) and retrieved spectra and spectral phase (dash-dotted curves), (d) retrieved intensity profile and phase of the self-compressed pulse. Dashed curves in (c) and (d) show the spectrum, intensity profile and phase of the input pulse.

## Summary of the results

In this chapter we have demonstrated that competing cascaded-quadratic and intrinsic cubic nonlinear responses may be used to control filamentation and SC generation dynamics in birefringent nonlinear media. The experiments were performed in $\beta$-BBO crystal within a broad range of positive and negative phase mismatch parameters, which lead to either reduction or enhancement of the effective nonlinear refractive index, respectively, and in both, the normal and anomalous GVD regions. We uncovered that control of the SC spectral extent stems from the complex interplay between the self-phase-matched SH generation and self-steepening processes which arise from cubic and cascaded-quadratic nonlinearities, and which bring remarkably different contributions to the spectral broadening in the range of negative and positive phase mismatch.

In the normal GVD region, we have shown that in the range of negative phase mismatch, the blue-shifted spectral broadening and the short wavelength cut-off of the SC spectrum is fully controllable in the 410 – 700 nm range by varying the phase mismatch parameter. The achieved spectral control is very robust in terms of the input pulse energy and is attributed to efficient generation of the self-phase-matched SH, which introduces a considerable energy loss and distortion of the trailing sub-pulse shape, counteracting the joint effect of cascaded-quadratic and cubic self-steepenings. In contrast, in the range of positive phase mismatch, where self-phase matched SH is absent and the effective self-focusing nonlinearity is still prevailing, the control of both the short-wavelength and the long-wavelength side of the SC spectrum is demonstrated and is explained by the competition between the cubic and phase-mismatch-dependent cascaded-quadratic self-steepenings.

A number of other interesting findings regarding SH generation under these conditions are uncovered. In particular, we observe filamentation of the SH pulses at perfect phase matching, which leads to extraordinarily polarized SC, which spans from 300 nm to 610 nm and induces a considerable spectral broadening around the fundamental wavelength, ranging from 650 nm to 1 $\mu$m. In the range of negative phase mismatch, self-phase-matched SH generation yielding tunable ultraviolet radiation in the $300 - 400$ nm range is captured.

In the anomalous GVD region, we find that in the case of large negative phase mismatch the filamentation threshold is markedly reduced, leading to SC generation at sub-critical powers for self-focusing. In contrast, positive phase mismatch yields strong negative cascaded nonlinearity which competes with the intrinsic one, resulting in SC generation at elevated intensities. By use of spatiotemporal imaging, we have verified that in both cases SC generation is facilitated by three-dimensional self-focusing of the input pulses, which transform into the self-compressed spatiotemporal light bullets with three- to four-fold compression factors.

Finally, we have demonstrated virtually lossless, filamentation-free, more than three-fold self-compression of mid-infrared laser pulses at 2.1 $\mu$m. In contrast to soliton compression mechanism that utilizes the second-order cascading to achieve the self-defocusing propagation regime in the range of normal GVD, we have shown that second-order cascading may be exploited to produce large effective self-focusing nonlinearity that facilitates self-compression in the range of anomalous GVD. To this end, beam filamentation effects are avoided by choosing an appropriate input beam diameter, which guarantees essentially one dimensional (temporal) dynamics leading to soliton compression without the onset of beam filamentation and associated nonlinear losses. More specifically, we have demonstrated self-compression of 68 fs, 73 $\mu$J pulses at 2.1 $\mu$m down to 22 fs with an energy throughput of 86.3%, with the energy losses originating just from Fresnel reflections and SH generation. In addition, the ability for energy and peak power scaling was demonstrated by increasing the input pulse energy up to 215 $\mu$J, which yielded self-compressed pulses with 4.5 GW peak power. The demonstrated method provides freedom in the choice of the input conditions, as both, the input pulse intensity and the effective nonlinearity could be tuned independently.

# 2. SUPERCONTINUUM GENERATION IN DISORDERED MEDIA

## Motivation

Development of high-peak power near- and mid-IR femtosecond OPA systems spurred a rapid interest in SC generation in the mid-IR spectral range [1] benefiting a wide array of applications ranging from detection of various pollutants via vibrational spectroscopy in the so called molecular fingerprint region [51] to the development of state-of-the art ultrabroadband few-optical cycle laser sources [105]. Suffice it to say the accessibility of mid-IR laser sources significantly increased the number of available nonlinear materials suitable for achieving a considerable SC spectral broadening [106]. Alongside broadly used wide bandgap dielectric crystals and glasses [24–27, 107–110], other nonlinear media possessing narrower bandgaps, and thus larger cubic nonlinearities, such as soft glasses, narrow bandgap dielectrics and semiconductors proved to be efficient nonlinear materials for ultrabroadband SC generation in the mid-IR spectral range [33, 51, 111–117].

Among those, of particular interest, are disordered materials, which represent a certain class of nonlinear photonic crystals [118], often termed as random, or short-range order nonlinear photonic crystals [119]. Baudrier et al. demonstrated that due to the disordered nature of such media the phase-matching conditions are greatly relaxed and allow phase matching for any three-wave interaction to be fulfilled [52]. Therefore, broadband frequency conversion within a wide spectral range is made possible with the limitations of the bandwidth being imposed just by the transparency window of the material. This phenomenon stemming from the random nature of the nonlinear domains was appropriately called "random quasi-phase matching" (RQPM). However, in contrast with quasi-phase matching, the intensity of the waves generated during the RQPM process scales linearly instead of quadratically with the number of domains, regardless of the domain size and its dispersion [120, 121]. Extremely broadband frequency conversion was demonstrated in various disordered media [122–127], including periodically poled crystals featuring non-ideal domain structure due to various defects [128, 129].

Polycrystals are one of the simplest disordered materials composed of a large number of single-crystal domains with random orientations, shapes and sizes [130]. In particular, zinc-blende semiconductors - a class of naturally grown polycrystalline wide-bandgap semiconductors are distinguishable due to the exceptional optical properties suitable for a wide array of applications ranging from laser physics to ultrafast nonlinear optics. As a direct consequence of its cubic crystal structure and $\bar{4}$3m symmetry point group such media are

optically isotropic and possess a non-zero second-order nonlinearity [64] in addition to exhibiting considerably extended long-wave transmittance, relatively wide bandgap [60], large cubic nonlinearities [131] and high optical damage thresholds [132]. It is important to note that monocrystalline versions of these materials, even though less common, are also readily available.

A large body of studies using both, the mono- and poly-crystalline zinc-blende materials, has already been performed. Transition metal-doped zinc sulphide (ZnS) and zinc selenide (ZnSe) were shown to serve as rather unique laser host materials, exhibiting superb ultrafast lasing capabilities [133], on which rely a whole new generation of femtosecond mid-IR laser oscillators and amplifiers [134, 135]. In the field of nonlinear optics, a variety of nonlinear interactions were demonstrated, namely, harmonic [136–139], sum [140] and difference-frequency [52, 141–143] generation and more recently, optical parametric oscillation [144]. Femtosecond filamentation and spectral broadening with wavelength-tunable near-IR laser pulses was experimentally studied in ZnSe [145] with multioctave SC spectra reported in both ZnS [27] and ZnSe [146]. Accompanying SC generation, surprisingly efficient second-order interactions were observed in polycrystalline ZnSe [53], opening new avenues for studies of extreme light-matter interactions and harmonics generation in solid state media [54–56]. Finally, recent numerical simulations predicted efficient self-compression and sub-cycle light bullet generation via filamentation in ZnSe using femtosecond mid and long wavelength IR pulses whose wavelengths fall into the range of anomalous GVD of the material [147].

Disordered polydomain media, such as strontium barium niobate (SBN), may also be used for various nonlinear optical processes at multiple wavelengths, including second and third harmonic generation without the need of angle or temperature tuning [148]. In contrast to polycrystalline zinc-blende semiconductors, polydomain SBN consists of birefringent needle-like randomly distributed ferroelectric domains whose widths vary between a few nanometers and a few micrometers and whose lengths are of a few hundreds of micrometers [149]. Broadband second and third harmonic generation in SBN was widely studied regarding harmonic spatial patterns, speckle structure, statistics and polarization properties [122–125, 150–156]. Eventually, these studies resulted in practical applications, demonstrating adjustment-insensitive techniques for characterization of ultrashort light pulses [157–159]. However, the nonlinear effects related to the third-order nonlinearity in SBN have not been explicitly addressed so far.

This chapter is based on the research published in papers **[A3, A5, A6]** and presents a detailed study of SC generation process in various disordered materials such as polycrystalline ZnS, ZnSe and polydomain SBN. A comparative study of SC generation in polycrystalline samples of ZnS and ZnSe and monocrystalline zinc telluride (ZnTe) is also provided.

## 2.1. Even and odd harmonics enhanced supercontinuum generation in polycrystalline ZnSe: the role of random quasi-phase matching

The first section is dedicated to the investigation of SC generation and filamentation in polycrystalline ZnSe. In what follows, we demonstrate that the role of RQPM is vital in order to explain the broadband spectral features observable during such nonlinear interactions, therefore a large part of the section is reserved for the discussion of this topic.

The following experiments were performed using 2.4 $\mu$m, 100 fs pulses focused into a 5 mm-long polycrystalline ZnSe sample. The input pulse energy was varied in the range of 0.1 - 5 $\mu$J, which, taking into account the $\approx$17% losses due to Fresnel reflection from the input surface of the crystal, corresponded to a peak power range of $1.1 - 52.5\ P_{\mathrm{cr}}$, where $P_{\mathrm{cr}} = 0.59$ MW. The spectral measurements were acquired using a scanning prism spectrometer equipped with Ge and PbSe photodetectors covering the effective $0.55 - 4.3$ $\mu$m range and described in further detail in the *Experimental Methods* chapter. The measured spectral dynamics versus the input pulse energy are shown in Fig. 2.1.

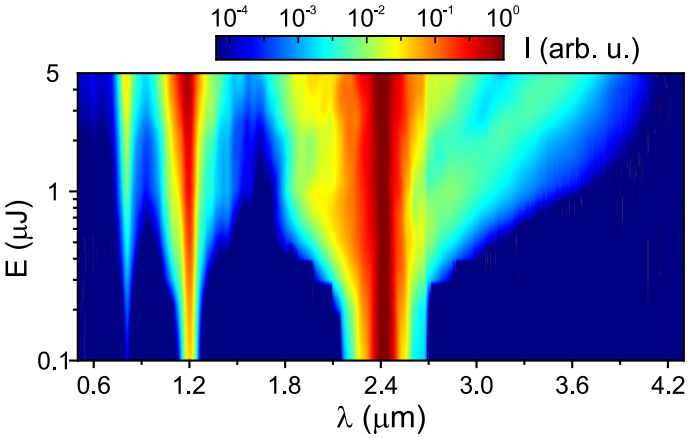


Figure 2.1: Output pulse spectral dynamics versus the input pulse energy as acquired using incident pulses of 2.4 $\mu$m. Logarithmic intensity scale is used to highlight fine spectral features.

First of all, we observe no spectral broadening around the fundamental wavelength for input pulse energies below 300 nJ. This indicates the absence of beam filamentation despite that the input peak power markedly exceeds $P_{\mathrm{cr}}$. Even though surprising, it could be explained in part due to imprecise knowledge of the ZnSe nonlinear refractive index $n_2$ as its value in literature is given for a more than twice shorter wavelength [131]. In addition, we clearly see the intense spectral peaks of second and third harmonics at 1.2 $\mu$m and 800 nm, respectively, which may also contribute to some energy loss and depletion of the incident radiation.

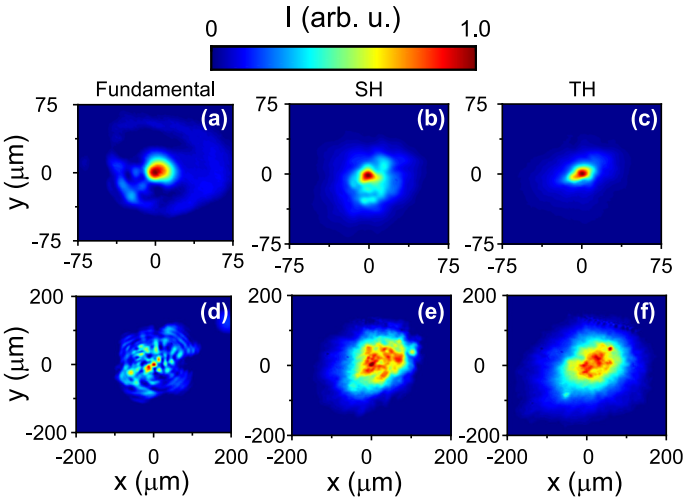


Figure 2.2: Near field intensity distributions at the output of the crystal, as measured in the single (top row) and multiple (bottom row) filamentation regimes using input pulse energies of 0.5 $\mu$J and 3 $\mu$J, respectively: (a),(d) fundamental beam at 2.4 $\mu$m, (b),(e) SH at 1.2 $\mu$m, and (c),(f) TH at 0.8 $\mu$m.

Secondly, for input pulses above 300 nJ, the incident beam undergoes filamentation as evidenced by broadband SC generation in the mid-IR part of the spectra. Measurements of the near field intensity profile of the output beam confirm the existence of a single filament with central core FWHM diameter of 16 $\mu$m, surrounded by a characteristic ring-shaped periphery, as shown in Fig. 2.2(a). Incidentally, the light filament of that size perfectly fits into the area of a single crystallite with the same considerations applying to the SH and TH beams [Figs. 2.2(b) and 2.2(c)]. The dimensions of SH and TH beams are bound to the filament size, demonstrating that efficient SH and TH generation and their spectral broadenings are tightly linked to filamentation of the fundamental beam.

Finally, for input pulses above 1 $\mu$J, we access the regime of multiple filamentation as confirmed by the near field intensity distributions of fundamental, SH and TH beams at the crystal output shown in Figs. 2.2(d)-2.2(f). Here, we see the beam break-up into multiple hot spots, which act as nuclei for the formation of several or more filaments [2]. The SC spectrum still exhibits a progressive red-shifted broadening that extends up to 4.2 $\mu$m, as well as further predominantly red-shifted broadening of the SH and TH spectra. Eventually, including the weak fourth harmonic peak at 600 nm, the overall spectral width of the output radiation spans the wavelength range from 600 nm to 4.2 $\mu$m limited only by the short wave detection edge of our spectrometer.

At a first glance, the observed spectral dynamics and characteristic spectral features are somewhat reminiscent of the process of odd harmonics-enhanced

SC generation in isotropic solid state medium [109]. However, in what follows we demonstrate that in the present case the underlying mechanism of harmonics generation is substantially different and relies on RQPM three wave mixing. Such generation due to the polycrystalline structure of ZnSe poses a number of specific signatures, which we have verified by measurements of harmonics spectral content, polarization and conversion efficiency.

Figure 2.3 compares the output spectra as recorded in the single (dashed curve) and multiple (solid curve) filamentation regimes shown in Fig. 2.2 and presented in the energy scale. The spectral shapes of SH and TH appear as almost exact replicas of the spectrally broadened fundamental pulse, as due to largely relaxed random quasi-phase matching conditions stemming from the disorder in orientations of the individual crystallites, that support frequency conversion over very large bandwidths, see e.g. [122–125]. Similar considerations may be readily applied also to the spectral shapes of fourth, fifth and sixth harmonics, which were reported elsewhere with incident pulses of longer wavelengths [138, 139].

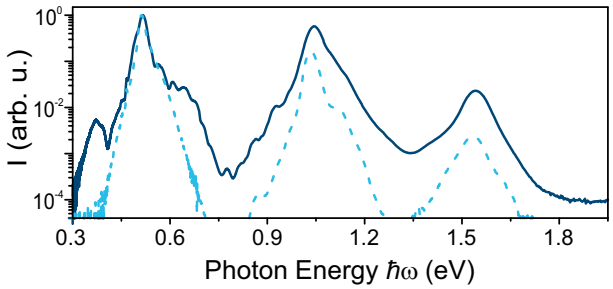


Figure 2.3: Supercontinuum and harmonics spectra recorded with incident wavelength of 2.4 $\mu$m in single (dashed curve) and multiple (solid curve) filamentation regimes using input pulse energies of 0.5 $\mu$J and 3 $\mu$J, respectively.

Random orientations of the individual crystallites also result in generation of unpolarized harmonics. The unpolarized (or randomly polarized) SH was already noticed in the very first application of polycrystalline ZnSe for frequency doubling of $CO_2$ laser [160]. In fact, it comes as no surprise as a result of $\bar{4}3m$ crystal symmetry, which sets equal non-vanishing second-order nonlinear-optical coefficients $d_{xyz} = d_{zxy} = d_{yzx} = d_{36}$ thereby providing equal contributions to the harmonic generation process. Figure 2.4 presents the polarization analysis of the output spectra, as performed using a broadband polarizer (Glan-Taylor prism, $YVO_4$), that was aligned to transmit either parallel (solid curve) or perpendicular (dashed curve) polarization with respect to the incident polarization. Our measurement confirms that both, SH and TH, are randomly polarized, whereas the infrared SC retains the linear polarization that coincides with that of the incident beam.

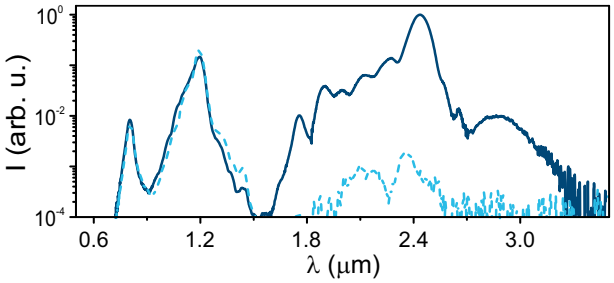


Figure 2.4: Transmitted spectra after Glan-Taylor prism polarizer at parallel (solid curve) and perpendicular (dashed curve) polarization with respect to the incident polarization of 2.4 $\mu$m input pulses.

Finally, the intensities of fields generated by the RQPM process are expected to be linear functions of the sample thickness, as demonstrated in the cases of difference frequency [52] and second harmonic [121] generation. Therefore we measured the output energy fractions contained in SH and TH as functions of the propagation distance $z$ and number of crystallites $N$ in the beam (filament) path by using three ZnSe samples of different length (3 mm, 5 mm and 10 mm). The conversion to SH and TH was retrieved by the integration of spectra shown in Fig. 2.1, in the energy range of $0.3 - 1$ $\mu$J, which mostly refers to a single filament regime, where the spectral broadening intervals around the incident wavelength and the individual harmonics do not overlap and could be easily distinguished. The results shown in Fig. 2.5 confirm the linear trends of energy conversion into SH and TH. The surprisingly high fraction of the output energy contained in the SH (up to 19%) is feasibly explained as occurring due to the accompanying filamentary propagation regime, which ensures high peak intensity within a filament and serves as a narrow and intense pump beam.

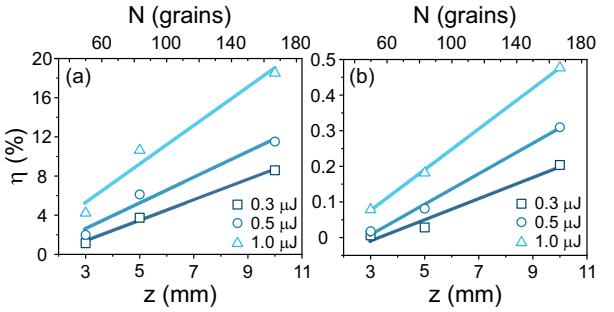


Figure 2.5: Output energy fractions contained in (a) SH and (b) TH as functions of ZnSe sample thickness $z$ and average number of crystallites $N$ as measured with the incident wavelength of 2.4 $\mu$m. The linear-fit lines serve as a guide to the eye.

## 2.2. Even and odd harmonics enhanced supercontinuum generation in various zincblende semiconductors: ZnS, ZnSe and ZnTe

In the previous section we have shown that SC generation in polycrystalline ZnSe is accompanied by broadband emissions at second and higher harmonics via simultaneous randomly quasi-phase matched three-wave mixing processes. Here, in order to further expand on this idea, we demonstrate that such characteristic spectral features are made even more distinct by using longer pump wavelengths deeper in the mid-IR spectral region. The universal nature of this phenomenon is demonstrated for two different polycrystalline zinc-blende materials (ZnS and ZnSe) of various thickness. We compare the results against using a monocrystalline zincblende material (ZnTe) so as to show the importance of polycrystallinity.

The following experiments were performed using 60 fs, 3.6 $\mu$m and 100 fs, 4.6 $\mu$m input pulses produced by difference frequency generation between the signal and idler outputs of a commercial OPA system. The spectral measurements were acquired using a scanning prism spectrometer equipped with Si and InAsSb photodetectors covering the effective $0.3-5.8$ $\mu$m range. For more details on the experimental setup please refer to the *Experimental Methods* chapter. In order to better distinguish the higher-order harmonics, the spectra in this section are shown in logarithmic wavelength and intensity scales.

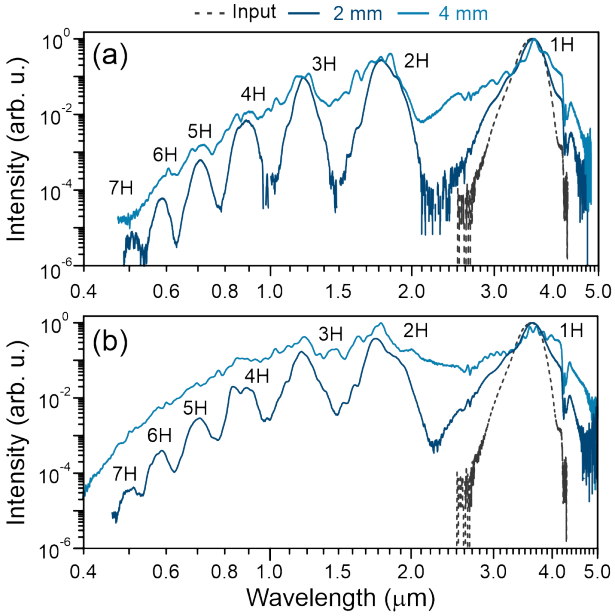


Figure 2.6: The output spectra measured in 2 mm and 4 mm-thick polycrystalline ZnS samples with the input pulse energies of (a) 0.5 $\mu$J and (b) 0.73 $\mu$J. The dashed dark gray curves show the input pulse spectra. The labels 1H, 2H, etc., stand for the harmonics order.

Figure 2.6 presents the experimentally measured output spectra in polycrystalline ZnS samples of 2 mm and 4 mm thickness using 60 fs, 3.6 $\mu$m input pulses with energies of 0.5 $\mu$J and 0.73 $\mu$J. With the input pulse energy of 0.5 $\mu$J, the spectrum measured at the output of a 2 mm-thick ZnS sample exhibits a slight broadening around the carrier wavelength, which is accompanied by the occurrence of distinct multiple peaks, which correspond to the individual harmonics, as shown in Fig. 2.6(a). Even and odd harmonics up to 7th order are clearly visible. We suppose a simple harmonics generation mechanism, which relies on RQPM sum-frequency generation involving the fundamental harmonic as one of the pump waves. In that way, the third harmonic is produced via sum-frequency generation between the fundamental and second harmonic waves, the fourth harmonic – via sum-frequency generation between the fundamental and third harmonic, and so on. By increasing the input pulse energy up to 0.73 $\mu$J, in the sample of the same thickness (2 mm) we observe further spectral broadening around the carrier wavelength and generated individual harmonics, whose spectra start to overlap, as shown in Fig. 2.6(b). Notice that the individual harmonics spectra are almost exact replicas of the broadened input pulse spectrum, attesting to the broadband character of the RQPM process as previously shown in chapter 2.1. In a 4 mm-thick ZnS sample, the harmonics spectra become broadened so much that the individual harmonic peaks are barely distinguishable even with the lowest input pulse energy of 0.5 $\mu$J [see Fig. 2.6(a)]. A further increase of the input pulse energy up to 0.73 $\mu$J leads to all the harmonics spectra merging into a broadband, almost uniform SC radiation spanning the $0.4 - 5$ $\mu$m wavelength range, which corresponds to 3.6 optical octaves [see Fig. 2.6(b)]. Notably, the blue-shifted portion of the SC radiation extends right down to the short-wave transparency edge of the crystal. A distinct double dip around 4.25 $\mu$m clearly distinguishable in all broadened spectra is attributed to the absorption of atmospheric $CO_2$.

Almost identical spectral features were recorded in ZnSe samples as presented in Fig. 2.7. However, in ZnSe fewer harmonics (up to 6th order) were generated due to its smaller bandgap and reduced transmittance in the visible spectral range. The broadest SC spectrum covering the $0.5 - 5$ $\mu$m wavelength range, that corresponds to 3.3 optical octaves, was recorded with the input pulse energy of 1.88 $\mu$J in 3 mm-thick sample, as shown in Fig. 2.7(b). Also notice a remarkably high spectral intensity of the second harmonic, that exceeds the spectral intensity of the fundamental wavelength. A considerable depletion of the fundamental harmonic attests to a very high efficiency RQPM frequency conversion process as we have previously shown in chapter 2.1.

In contrast to the above results, spectral broadening in ZnTe single crystal shows marked differences. The measured spectra in ZnTe monocrystalline samples of 0.6 mm and 1.2 mm thickness are presented in Fig. 2.8. First of all, only the second and third harmonics were observed, whose intensities, de-

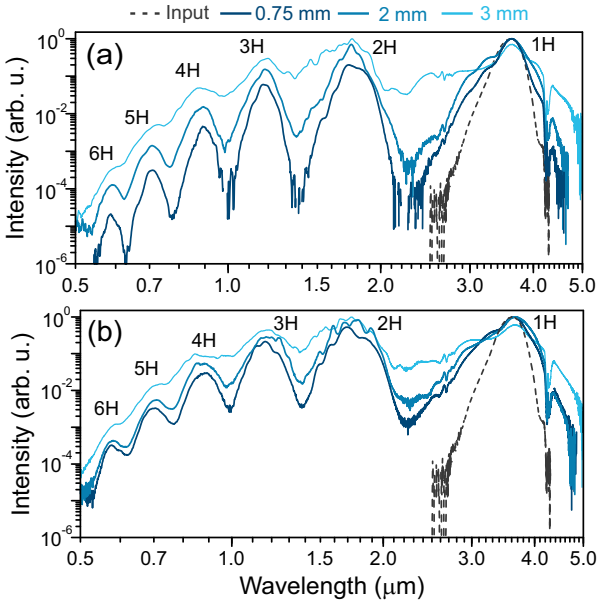


Figure 2.7: The output spectra measured in 0.75 mm, 2 mm and 3 mm thick polycrystalline ZnSe samples with the input pulse energies of (a) 0.73 $\mu$J and (b) 1.88 $\mu$J. The labelling is the same as in Fig. 2.6.

spite larger second-order coefficient of ZnTe (see Table 2 in the *Experimental Methods* chapter), are considerably lower than the intensities of corresponding harmonics generated in polycrystalline ZnS and ZnSe. This fact even further confirms the pivotal role of RQPM in the harmonics generation process. Secondly, the second harmonic spectrum shows a persisting spectral modulation, which could be attributed to the interference of free and driven second harmonic waves that are generated at the boundary of the nonlinear medium in the conditions of large phase and group velocity mismatch [98, 161]. At its maximum extent, the measured spectrum in a single ZnTe crystal covers the wavelength range from 1.08 $\mu$m to 4.8 $\mu$m with the short-wave cut-off being notably far from the short-wave transparency edge of the crystal.

Finally, we demonstrate how the number of generated harmonics in polycrystalline ZnS and ZnSe samples increases when excited by incident pulses with a longer wavelength. Figure 2.9 presents the output spectra measured in 2 mm-thick ZnS and 3 mm-thick ZnSe polycrystalline samples by using 100 fs, 1.5 $\mu$J input pulses with a carrier wavelength of 4.6 $\mu$m. The input pulse energy of 1.5 $\mu$J was set so as to produce a single filament, which in turn produces only a slight spectral broadening around the fundamental wavelength. On the other hand, a full set of even and odd harmonics up to 10th order was measured in ZnS [see Fig. 2.9(a)] and up to 8th order in ZnSe [see Fig. 2.9(b)], being limited by the short-wave transmission cut-offs of the crystals. As in the

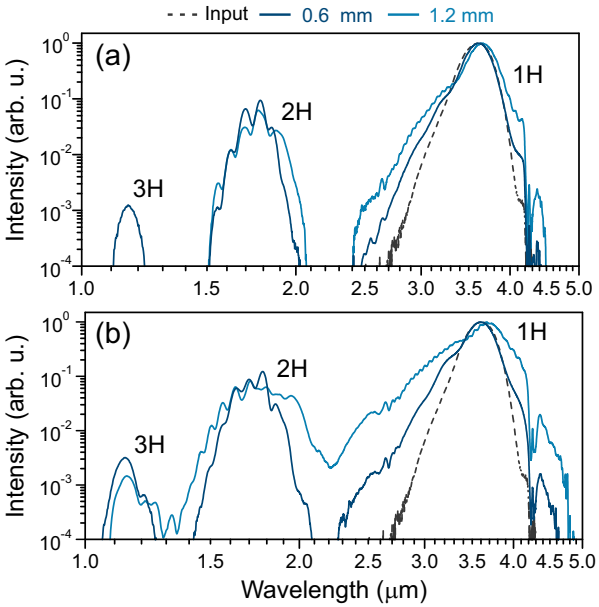


Figure 2.8: The output spectra measured in 0.6 mm and 1.2 mm thick ZnTe single crystal samples with the input pulse energies of (a) 0.73 $\mu$J and (b) 1.88 $\mu$J. The labelling is the same as in Fig. 2.6.

previous case, the lowest-order harmonics possess relatively high spectral intensities, resulting from efficient RQPM three-wave interactions available due to polycrystalline structure of the samples. Conversely, the extension of SC spectrum by harmonics generation in polycrystalline media is far more efficient as compared to the materials with sole cubic nonlinearity, where extension of the SC spectrum by overlap of spectrally broadened odd harmonics is produced by a different mechanism, which involves cascaded four-wave interactions and cross-phase modulation [109].

To end with, please see Fig. 2.10 for a quick summary of the SC generation results obtained in Section 2.1 and Section 2.2 . It is evident that the number of generated harmonics increases with incident wavelength, whereas the total spectral extent remains fairly similar.

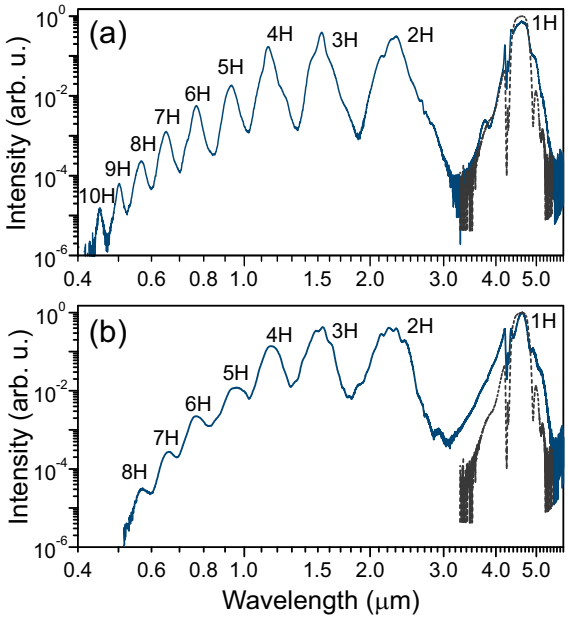


Figure 2.9: The output spectra of (a) 2 mm-thick ZnS and (b) 3 mm-thick ZnSe polycrystalline samples, as generated with 100 fs, 1.5 $\mu$J input pulses at 4.6 $\mu$m. The input pulse spectra are shown by dark gray dashed curves. The labelling is the same as in Fig. 2.6.

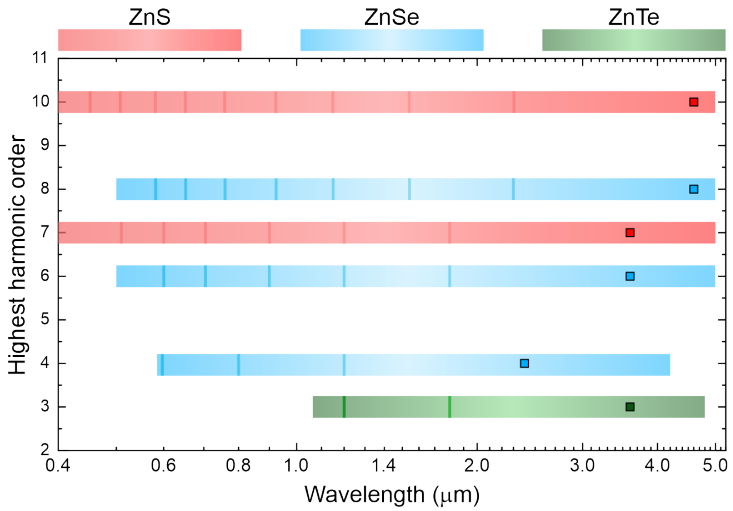


Figure 2.10: Harmonics-enhanced SC generation results in monocrystalline and polycrystalline zinc-blende media. The squares mark the incident pulse wavelength used in the experiment. The horizontal bars, placed at the highest observed harmonic order, depict the SC spectral extent. The vertical lines indicate second and higher generated harmonics. Note the logarithmic wavelength scale used. Please refer to the legend for the corresponding material.

In this last section we demonstrate that even though other disordered materials such as polydomain SBN possess some similar characteristic features to the ones discussed in previous sections, namely RQPM harmonic generation, the unique structure of the SBN crystal gives rise to some important differences as well. In order to study these features we have measured the SC spectra in polydomain SBN as generated in the ranges of its normal, zero and anomalous GVD. The pump pulse energies were set slightly above the threshold energies for filamentation, where blue-shifted broadenings of the spectra saturate and no refocusing of the filament is observed. The spectra were measured using a SPS equipped with Ge and InAsSb photodetectors covering the effective $0.6-5.8$ $\mu$m range described in the *Experimental Methods* chapter. The results, shown in Fig. 2.11, demonstrate that a smooth, more than an octave-spanning SC spectra in the wavelength ranges of $0.8-1.81$ $\mu$m, $1.04-2.5$ $\mu$m and $1.0-3.32$ $\mu$m (defined at the $10^{-4}$ intensity level) are obtained using pump pulses with carrier wavelengths of 1.2 $\mu$m, 2.0 $\mu$m and 2.4 $\mu$m, respectively. These affirm that disordered materials might serve as excellent nonlinear media for generation of infrared SC.

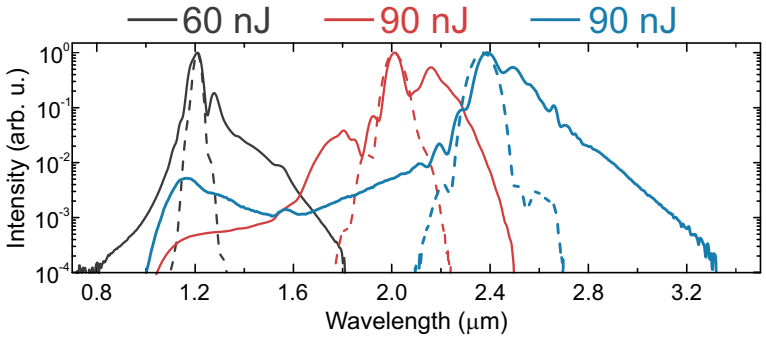


Figure 2.11: Supercontinuum spectra generated in SBN using pump pulses with carrier wavelengths of 1.2 $\mu$m (black curve), 2.0 $\mu$m (red curve) and 2.4 $\mu$m (blue curve). The energies of the pump pulses are indicated on the top. The input spectra are depicted by dashed curves.

Figure 2.12 shows filamentation and SC generation dynamics in more detail by collation of the images of SH traces and related spectral evolutions as functions of the input pulse energy in the cases of normal, zero and anomalous GVD. The energy ranges for each input wavelength were chosen to preserve a single filament propagation regime and to avoid the occurrence of multiple filamentation. Planar SH generation in pollycrystaline SBN is a well known phenomenon occurring due to the random distribution of the needle-like domains, which provides a continuous set of reciprocal grating vectors that satisfy the phase

matching conditions for a wide range of spectral components [122,148]. The series of SH images depicted in Figs. 2.12(a), 2.12(c) and 2.12(e) reveal that such broadband SH emission closely follows the intensity distribution along the light filament and can be readily used to monitor filamentation dynamics similarly to a more common method of filament visualization based on filament-induced luminescence observed in various single crystals, see e.g. [162–164].

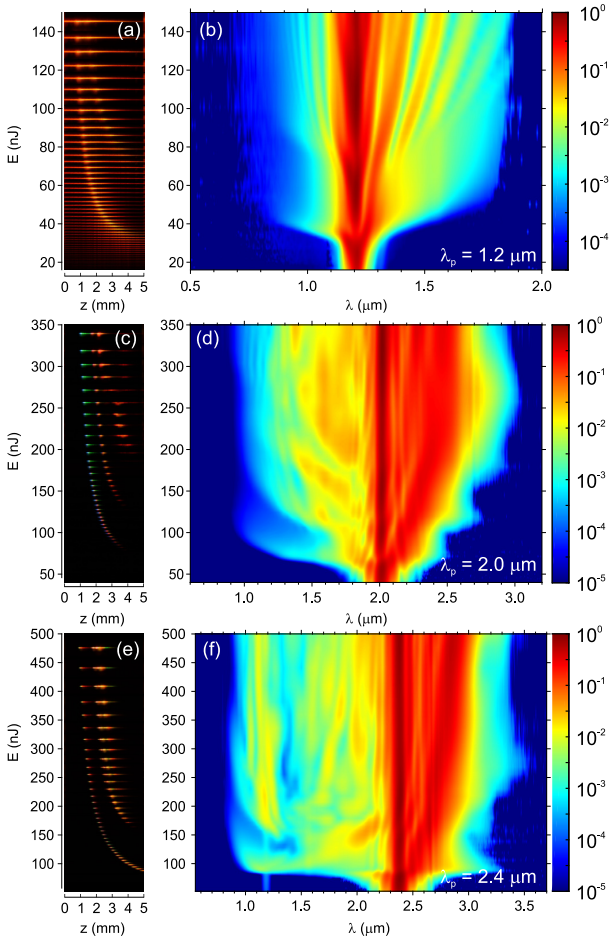


Figure 2.12: (a,c,e) Composite images of SH traces and (b,d,f) related dynamics of spectral broadening as functions of the pump pulse energy in the cases of normal (1.2 $\mu$m), zero (2.0 $\mu$m) and anomalous (2.4 $\mu$m) GVD.

It is very clear that the occurrence of intense planar SH emission manifests the onset of filamentation, which was experimentally detected with pump pulse energies of less than 100 nJ and sub-MW peak powers: 32 nJ (0.35 MW) at 1.2 $\mu$m, 54 nJ (0.53 MW) at 2.0 $\mu$m and 74 nJ (0.56 MW) at 2.4 $\mu$m, as justified by an explosive broadening of the spectrum. The most intense part of the SH trace maps the position of the nonlinear focus, which first appears at the end of

the sample and thereafter shifts toward its input face as the energy of the pump pulse increases. The intensity variation along the SH trace also nicely captures filament refocusing at elevated pump pulse energy, which is indicated by the emergence of a secondary intensity peak in the SH trace which correlates with a secondary boost of spectral broadening and the occurrence of interference pattern in the SC spectrum, very clearly visible with 1.2 $\mu$m and somewhat less pronounced with 2.0 $\mu$m and 2.4 $\mu$m pump pulses.

To summarize the observed spectral dynamics presented in Fig. 2.12, the spectral broadening versus the input pulse energy shows several interesting features, which are quite general from the point of view of underlying physics. First, an apparent shrinking of the SC spectra (especially well-pronounced on the short wavelength side) is observed before the filament refocusing takes place in all investigated cases. This spectral shrinking is attributed to the defocusing and absorption of free electron plasma that push a large portion of the pulse energy out of the propagation axis after the first nonlinear focus, see [164] for details. Second, each refocusing cycle in the cases of zero (2.0 $\mu$m) and anomalous (2.4 $\mu$m) GVD precedes the constant red shift. Such spectral behavior was also observed in various nonlinear media ($CaF_2$ and LiF single crystals and fused silica, see [32]), and was attributed to the periodic cycle of dissipation and reconstruction of the light bullet [21]. The same consideration applies also to the case of zero GVD, where pulse splitting takes place, and the spectrum of the trailing sub-pulse that is responsible for the red shift, falls into the range of anomalous GVD of the crystal.

Figure 2.13 compares the spectra of planar SH emissions produced by filamentation of 1.2 $\mu$m and 2.4 $\mu$m pulses and measured with a fiber spectrometer (Ocean Optics QE65000). Figure 2.13(a) shows the recorded SH spectrum produced with the pump wavelength of 1.2 $\mu$m. The SH spectrum spans the wavelength range from 480 to 800 nm and represents an almost exact replica of the entire SC spectrum with the peak spectral intensity at 600 nm, which is the second harmonic of the pump. With the pump wavelength of 2.4 $\mu$m, the SH spectrum covers the wavelength range from 460 nm to 970 nm, which is the long-wave detection limit of the spectrometer, see Fig. 2.13(b), attesting that such broadband SH emission is produced by frequency doubling of the blue-shifted part of the SC spectrum. An interesting variation of color along the SH trace indicates the propagation distances at which the particular spectral components of the SC have the highest intensities. This feature is particularly well pronounced in the case of 2.0 $\mu$m pumping, see Fig. 2.11(c). These spectral measurements demonstrate an extremely wide SH conversion bandwidth provided by RQPM.

Series of SH emission traces shown in Figs. 2.12(a), 2.12(c) and 2.12(e) were further exploited in order to determine the nonlinear refractive index of the material. In doing so, each SH trace was converted into greyscale and

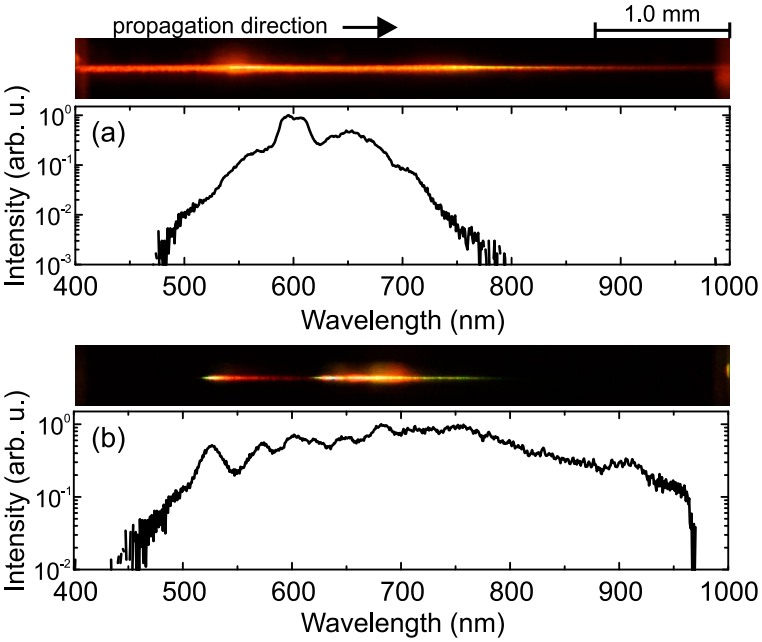


Figure 2.13: Photographs of representative SH traces and SH spectra recorded with a fiber spectrometer using (a) 1.2 $\mu$m, 85 nJ and (b) 2.4 $\mu$m, 408 nJ incident pulses.

integrated along the height of the image. The position of the first intensity maximum (that appears closest to the input face of the crystal) was considered to be the nonlinear focal point. Thereafter the retrieved datasets of positions of the nonlinear foci versus the pump energy (power) for each pump wavelength were fitted using Marburger's empirical formula for the position of nonlinear focus [3]:

$$z_{\mathrm{sf}} = \frac{0.367\ z_R}{\sqrt{[(P/P_{\mathrm{cr}})^{1/2} - 0.852]^2 - 0.0219}}, \tag{2.1}$$

The results for the pump wavelengths of 1.2 $\mu$m, 2.0 $\mu$m and 2.4 $\mu$m are summarized in Fig. 2.14, which shows the retrieved positions of experimental nonlinear foci versus the pump pulse energy and power and the respective best fits using Eq.(2.1). The fitting procedure was performed taking the radii of input beams and pulse durations from Table 1 in the *Experimental Methods* chapter. However, the best fits were obtained using the radii of the input beams as additional free parameters, yielding $1/e^2$ beam radii of 26 $\mu$m, 43 $\mu$m and 44 $\mu$m for the input beams with carrier wavelengths of 1.2 $\mu$m, 2.0 $\mu$m and 2.4 $\mu$m, respectively. These systematically smaller beam sizes may be attributed to a slightly elliptical shapes of the input beams and unknown amounts of input pulse chirp, which both could slightly alter the position of the nonlin-

ear focus [103]. The best fits yielded the following values of nonlinear refractive indices: $(44 \pm 7) \times 10^{-16}$ cm$^2$/W at 1.2 $\mu$m, $(81 \pm 23) \times 10^{-16}$ cm$^2$/W at 2.0 $\mu$m and $(100 \pm 15) \times 10^{-16}$ cm$^2$/W at 2.4 $\mu$m.

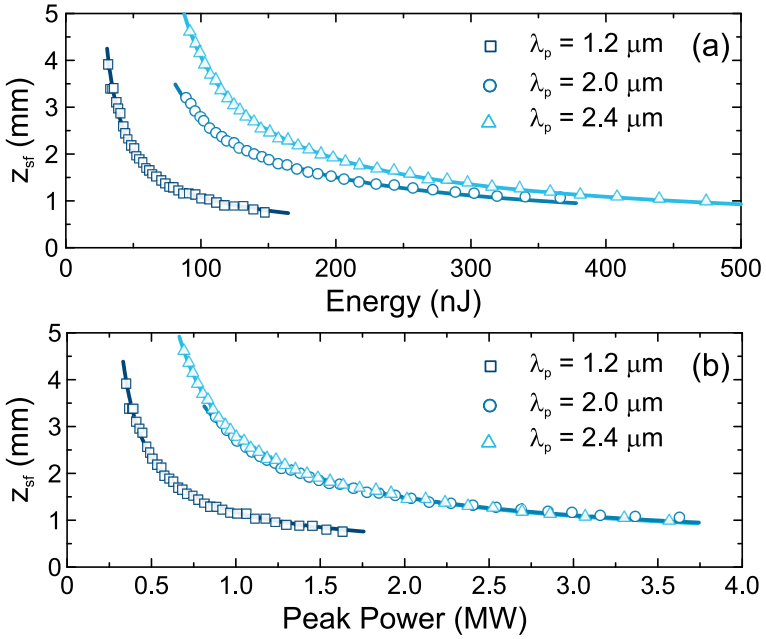


Figure 2.14: (a) The positions of the nonlinear foci versus the pump pulse energy (dots) and the best fits using Marburger's formula (curves) for pump wavelengths of 1.2 $\mu$m (squares), 2.0 $\mu$m (circles) and 2.4 $\mu$m (triangles). (b) same data represented in terms of peak power and used for estimation of $n_2$.

The obtained $n_2$ value at 1.2 $\mu$m compares favorably with the previously reported value of $52.4 \times 10^{-16}$ cm$^2$/W at 1064 nm [61], however, much larger $n_2$ values obtained at 2.0 $\mu$m and 2.4 $\mu$m look quite surprising. Indeed, these large values appear in stark contrast with what can be expected from a general dispersion law of $n_2$, suggesting the maximum $n_2$ value around the edge of two photon absorption ($\sim$ 730 nm for SBN) and gradual decrease of $n_2$ toward longer wavelengths [61]. This result cannot be explained by the contribution of the cascaded nonlinearity due to phase-mismatched SH generation, as the wavevector mismatch for any type of possible three-wave interaction, see [125], for the wavelengths of interest is always positive, so suggesting that the contribution of the cascaded nonlinearity to effective $n_2$ is negative. On the other hand, these large $n_2$ values are confirmed by very low beam powers for filamentation and SC generation thresholds determined experimentally for pump wavelengths of 2.0 $\mu$m and 2.4 $\mu$m.

We have demonstrated that SC generation in polycrystalline media is accompanied by the generation of multiple even and odd harmonics. Using 2.4 $\mu$m incident pulses, we have achieved 2.8 octave-wide harmonics-enhanced SC generation spanning the $0.6 - 4.2$ $\mu$m wavelength range in polycrystalline ZnSe with the maximum blue-shift of the spectra limited by the 4th harmonic spectrum. In addition, using sub-$\mu$J, 60 fs, 3.6 $\mu$m input pulses, 3.6 octave-wide harmonics-enhanced SC spanning the $0.4 - 5$ $\mu$m wavelength range in ZnS, and 3.3 octave-wide SC spanning the $0.5 - 5$ $\mu$m wavelength range in ZnSe, was generated, whose maximum blue shifts were limited by the short-wave absorption of the crystals. In the latter case, up to 7th, and 6th harmonic was generated in ZnS and ZnSe, respectively. A full set of even and odd harmonics up to 10th order in ZnS and up to 8th order in ZnSe were recorded with 100 fs input pulses at 4.6 $\mu$m. In contrast, only moderate spectral broadening, fewer number of harmonics (only second and third) and considerably lower harmonics conversion efficiency due to large phase mismatch, was observed in ZnTe single crystal.

More importantly, our results have shown the central role of RQPM in the harmonics generation process. The provided spectral features, polarization and linear energy trend measurements prove that efficient generation of even and odd harmonics stems from polycrystalline structure of these materials, which provides broadband RQPM for multiple simultaneous three-wave mixing processes considerably extending the spectral range of the output radiation.

Finally, we have demonstrated that polydomain SBN also serves as an efficient nonlinear medium for SC generation in the infrared spectral range. More than an octave-spanning infrared SC spectra were produced with reasonably low input peak powers in the ranges of normal, zero and anomalous GVD of the crystal. We have shown that RQPM in disordered SBN provides an extremely broad, octave-spanning bandwidth for planar SH generation, which precisely maps the intensity distribution along the filament of light, and so could be used to visualize the self-focusing and filamentation dynamics. This feature was exploited so as to determine the nonlinear index of refraction of SBN at 1.2 $\mu$m, 2.0 $\mu$m and 2.4 $\mu$m.

The recorded SC spectra reveal a great potential of disordered semiconductors for the generation of ultrabroadband radiation that covers a remarkably broad spectral range from the visible to the mid-infrared.

# CONCLUSIONS

1. Using incident wavelengths, which fall into either the normal or anomalous group velocity dispersion range of the material, filamentation along with phase-mismatched type-I second harmonic generation in a quadratic anisotropic $\beta$-BBO crystal results in generation of radiation, controllable by varying the phase mismatch parameter $\Delta$k, and polarized along the ordinary and the extraordinary axis of the nonlinear crystal. The extraordinarily polarized radiation is attributed to phase mismatched second harmonic generation whose intensity decreases further from the perfect phase matching angle, and self-phase matched second harmonic generation, accessed by a certain range of supercontinuum spectral components. The ordinarily polarized radiation is a result of the complex interplay between the quadratic cascaded and cubic nonlinearities with the tunable blue cut-off of the spectra being limited by the efficient transfer of energy from the trailing sub-pulse to the self-phase matched second harmonic. The latter effect is diminished in the anomalous group velocity dispersion region due to the temporal pulse self-compression instead of pulse splitting.

2. In the normal group velocity dispersion region, supercontinuum generation in a quadratic nonlinear $\beta$-BBO crystal results in the incident pulse splitting into two sub-pulses. Cross-correlation measurements confirm that pulse-splitting dynamics are phase mismatch parameter dependent with axial pulse reconstruction and subsequent secondary pulse-splitting events occurring at higher effective nonlinear refractive index values. On the other hand, in the anomalous group velocity dispersion region, spatially and more than four-fold temporally self-compressed light bullets are observed as confirmed by spatiotemporal imaging of the output pulse.

3. Pulse self-compression, which is a result of self-phase modulation counteracting the effect of anomalous group velocity dispersion, may be controlled by varying the phase mismatch dependent effective nonlinear refractive index. This way, filamentation-free pulse self compression from 68 fs, 73 $\mu$J at 2.1 $\mu$m down to 22 fs, and in order to demonstrate energy scalability, from 95 fs, 215 $\mu$J at 2.1 $\mu$m down to 27 fs, was demonstrated in a quadratic nonlinear $\beta$-BBO crystal.

4. Supercontinuum generation in polycrystalline zinc-blende media is accompanied by multiple broadband even and odd harmonics resulting in spectra spanning several optical octaves. The accompanying harmonic generation is facilitated by random quasi-phase matched three-wave interactions inherent to disordered media. This is confirmed by a number

of specific signatures linked to harmonic generation via random quasi-phase matching, namely the broadband nature of the generated harmonics, which replicate the fundamental harmonic spectrum in the frequency scale, random polarization and a linear conversion efficiency dependence on the number of crystallites.

5. The blue-shifted portion of the SC spectra in polycrystalline zinc-blende materials is limited by the number and spectral broadening of even and odd harmonics generated in the media. The highest order of the generated harmonics increases with incident wavelength and is only limited by the short-wave transparency edge of the crystal. This way, using 60 fs, 3.6 $\mu$m and 100 fs, 4.6 $\mu$m incident pulses, we have demonstrated almost uniform harmonics enhanced SC radiation in polycrystalline ZnS and ZnSe in the spectral ranges of 0.4–5 $\mu$m and 0.5–5 $\mu$m, respectively. In the first case, up to 7th and 6th, and in the second case, up to 10th and 8th order harmonic radiation was observed.

6. In the normal (1.2 $\mu$m), zero (2.0 $\mu$m) and anomalous (2.4 $\mu$m) group velocity dispersion regimes supercontinuum generation in disordered polydomain SBN crystal yields more than an octave spanning spectra in the ranges of 0.8 - 1.81 $\mu$m, 1.04 - 2.5 $\mu$m and 1.0 - 3.32 $\mu$m, respectively. Supercontinuum generation is accompanied by random quasi-phase matching induced broadband planar second harmonic generation, which closely follows the intensity distribution along the light filament allowing to determine the positions of the nonlinear foci and therefore the nonlinear refractive index values of the material at three measured incident wavelengths: $(44 \pm 7) \times 10^{-16}$ cm$^2$/W at 1.2 $\mu$m, $(81 \pm 23) \times 10^{-16}$ cm$^2$/W at 2.0 $\mu$m and $(100 \pm 15) \times 10^{-16}$ cm$^2$/W at 2.4 $\mu$m.

# SANTRAUKA LIETUVIŲ KALBA

## Įvadas

Superkontinuumo generacija yra vienas įspūdingiausių netiesinės optikos reiškinių, kurio metu, intensyviam ultratrumpajam lazerio impulsui sąveikaujant su skaidria terpe, stebimas erdviškai ir laikiškai koherentinės labai plataus dažnių spektro spinduliuotės atsiradimas. Šio reiškinio kilmė glaudžiai susijusi su šviesos gijų formavimosi procesu [1].

Šviesos gijomis vadinamos dinaminės pluošto struktūros, turinčios intensyvią centrinę dalį bei pasižyminčios subdifrakciniu sklidimu terpėje [2]. Šių šviesos darinių formavimasis paprastai yra siejamas su dviejų tipų spinduliuotės atsiradimu: 1) mažos skėsties, erdvėje bei laike koherentinės, itin plataus spektro spinduliuotės, vadinamosios superkontinuumo generacijos; 2) didelės skėsties, kūginės spinduliuotės, kurios skirtingi dažnio komponentai sklinda skirtingais kampais. Nors abu šie procesai yra neatsiejami vienas nuo kito, ilgą laiką nebuvo vieningos teorijos, kuri galėtų juos paaiškinti. Dabar žinoma, jog superkontinuumo generacijos bei kūginės spinduliuotės atsiradimas yra sudėtingos laikinių bei erdvinių reiškinių tokių kaip fokusavimasis, fazės moduliavimasis, daugiafotonė sugertis bei grupinių greičių dispersija tarpusavio sąveikos rezultatas. Toliau bus trumpai aptariami šie reiškiniai bei jų įtaka šviesos gijų formavimosi procesui, o tuo pačiu ir superkontinuumo generacijai.

Fokusavimasis yra reiškinys, kurio metu intensyviam lazeriniam pluoštui sklindant netiesine terpe, stebimas savaiminis jo matmenų mažėjimas. Šio reiškinio atsiradimas yra lemiamas terpės kubinio netiesiškumo, dėl kurio netiesinis medžiagos lūžio rodiklis yra laikinai modifikuojamas: $n = n_0 + n_2 I$, čia $n_0$ - tiesinis lūžio rodiklis, $n_2$ - Kero netiesinis lūžio rodiklis, I - intensyvumas. Netiesinio lūžio rodiklio priklausomybė nuo intensyvumo lemia, jog cilindriškai simetriško Gauso pluošto sklidimo atveju, kai $n_2 > 0$, centrinės pluošto dalys sklinda lėčiau nei periferinės, tad fazinis frontas tampa įgaubtas ir pluoštas ima fokusuotis. Svarbu pažymėti, jog pluošto fokusavimasis galimas tik tuomet, kai pluošto smailinė galia viršija tam tikrą kritinę $P_{cr}$, kurią pasiekus kompensuojama difrakcinė skėstis:

$$P_{cr} = \frac{3.77\lambda^2}{8\pi n_o n_2}, \tag{1}$$

čia $\lambda$ yra žadinančiosios spinduliuotės bangos ilgis.

Spinduliuotės galiai viršijus $P_{cr}$ pluoštas fokusuosis atstumu $z_{sf}$, kuris gali būti įvertintas pasinaudojant empirine Marburgerio formule [3]:

$$z_{\mathrm{sf}} = \frac{0.367\ z_R}{\sqrt{[(P/P_{\mathrm{cr}})^{1/2} - 0.852]^2 - 0.0219}}, \tag{2}$$

čia $z_R = \pi n_0 \omega_0^2/\lambda$ yra Gauso pluošto Reilėjaus ilgis, $\omega_o$ pluošto spindulys $1/e^2$ intensyvumo aukštyje.

Akivaizdu, jog pluošto matmenys negali tapti nykstamai maži, tad turi egzistuoti pluošto fokusavimąsi stabdantys fizikiniai reiškiniai. Fokusavimasis yra apribojamas netiesinių nuostolių, atsirandančių dėl daugiafotonės sugerties bei laisvųjų elektronų plazmos formavimosi, kuri ne tik sugeria spinduliuotę, tačiau ir dėl neigiamo netiesinio lūžio rodiklio lemia pluošto defokusavimąsi. Be to, pasiekiamas maksimalus intensyvumas yra apribojamas daugiafotonės sugerties efektyvumo, kuris pasižymi stipria priklausomybe nuo intensyvumo $\propto I^K$, čia K - daugiafotonės sugerties eilė, kuri gali būti įvertinta kaip $(E_g/\hbar\omega_p) + 1$ sveikoji dalis, o čia $E_g$ - medžiagos draustinės juostos tarpas, $\omega_p$ - žadinančiosios spinduliuotės dažnis [4, 5].

Pažymėtina, jog esant itin didelėms pluošto galioms gali būti stebimi du ar daugiau fokusavimosi/defokusavimosi ciklai. Šis reiškinys gali būti intuityviai paaiškinamas remiantis vadinamuoju dinaminio erdvinio atstatymo modeliu [6], kuriame teigiama: 1) pluoštas, kurio galia $P > P_{cr}$ fokusuojasi; 2) centrinė intensyvi besiformuojančios šviesos gijos dalis netenka dalies energijos dėl daugiafotonės sugerties poveikio; 3) netiesinio židinio aplinkoje dėl daugiafotonės sugerties poveikio susiformavusi laisvųjų elektronų plazma sugeria dalį energijos bei lemia centrinės intensyviausios pluošto dalies defokusavimąsi; 4) jei po šių procesų pluošto galia vis dar viršija $P_{cr}$, pluoštas vėl ima fokusuotis. Taigi, žinoma, jog šviesos gijų formavimasis yra inicijuojamas fokusavimosi. Tai patvirtina ir eksperimentiniai rezultatai, kuriuose pademonstruota, jog superkontinuumo generacijos, o kartu ir šviesos gijų formavimosi, slenkstis įvairiose terpėse yra labai artimas (10% ribose) kritinei fokusavimosi galiai $P_{cr}$ [5].

Laikinėje plotmėje netiesinio lūžio rodiklio priklausomybė nuo intensyvumo lemia šviesos impulsų fazės moduliavimąsi, kuris savo ruožtu įgalina naujų dažnių komponentų atsiradimą bei žadinančiojo impulso spektro išplitimą [2]:

$$\omega(t) = -\frac{\partial \phi}{\partial t} \propto \omega_p - \frac{n_2 \omega_p}{c} z \frac{\partial I(r,t)}{\partial t}, \tag{3}$$

čia $z$ - sklidimo nuotolis, $c$ - šviesos greitis.

Impulso, kuriame stebimas spektro plitimas dėl fazės moduliavimosi, spektro plotis gali būti įvertinamas atsižvelgiant į impulso intensyvumo priekinio ar galinio fronto statumą bei krypties koeficientą $\frac{\partial I(r,t)}{\partial t}$, netiesinį lūžio rodiklį $n_2$ bei sklidimo atstumą $z$. Didžioji dauguma netiesinių terpių pasižymi teigiamu netiesiniu lūžio rodikliu $n_2 > 0$, tad tokiose terpėse priekinis impulso frontas lemia išplitimą į mažesniųjų dažnių pusę (raudonųjų bangos ilgių), o galinis - į didesniųjų dažnių pusę (mėlynųjų bangos ilgių). Spektrinis išplitimas dėl fazės moduliavimosi tampa itin didelis fokusavimosi metu dėl netiesiniame židinyje pasiekiamo milžiniško intensyvumo. Šią sąsają patvirtina eksperimentiniai rezultatai, kurių metu buvo pademonstruota, jog superkontinuumo

generacija yra negalima, kai daugiafotonės sugerties eilė $K < 3$, dėl nedidelio intensyvumo, o tuo pačiu ir silpno fazės moduliavimosi, pasiekiamo esant mažos eilės daugiafotonei sugerčiai.

Be visų jau aptartų reiškinių superkontinuumo generacijai nemažą įtaką daro grupinių greičių dispersija [7,8], lemianti skirtingo dažnio bangų sklidimą skirtingais grupiniais greičiais $k^{''} = \partial^2 k/\partial\omega^2|_{\omega_p}$, čia $k = \omega_p n_0/c$ yra bangos skaičius. Normaliosios grupinių greičių dispersijos atveju ($k^{''} > 0$), mažesniųjų dažnių komponentai sklinda greičiau nei didesniųjų. Anomaliosios grupinių greičių dispersijos atveju ($k^{''} < 0$) stebimas priešingas procesas. Skirtingi grupinių greičių dispersijos režimai lemia labai skirtingas superkontinuumo generacijos bei šviesos gijų formavimosi savybes.

Eksperimentinių matavimų [12, 13] bei skaitmeninio modeliavimo [9–11] metu buvo pademonstruota, jog, normaliojoje grupinių greičių dispersijos srityje, impulsas pluošto fokusavimosi metu skyla į du subimpulsus. Vėliau, parodyta, jog impulso skilimas yra neatsiejama šviesos gijų formavimosi bei superkontinuumo generacijos normaliojoje grupinių greičių dispersijos srityje dalis [14, 15], lemianti asimetrinį superkontinuumo spektro, pasižyminčio pjedestalu mėlynojoje spektro srityje, plitimą [5, 16, 17].

Kita vertus, anomaliosios grupinių greičių dispersijos srityje, dėl priešingo fazės moduliavimosi bei grupinių greičių dispersijos poveikio, stebima žadinančiosios spinduliuotės bangų paketo spūda ne tik erdvėje, tačiau ir laike. Tai lemia šviesos kulkų - erdvėje bei laike lokalizuotų bangų paketų, pasižyminčių subdifrakciniu bei subdispersiniu sklidimu netiesinėje terpėje [18–21], savaimine centrinės smailės rekonstrukcija [22] bei gaubtinės nešlio fazės stabilumu [23], formavimąsi bei itin plataus, simetriškai plintančio, net kelias optines oktavas siekiančio superkontinuumo generaciją [24–27].

Nulinės grupinių greičių dispersijos srityje galima superkontinuumo generacija su normaliosios bei anomaliosios grupinių greičių dispersijos savybėmis, t.y. impulsų skilimu į du subimpulsus bei žymiu, simetrišku spektriniu plitimu [28].

Aukščiau paminėtų efektų įtaka yra įskaitoma vadinamajame efektiniame tribangio maišymosi modelyje, kuriame superkontinuumo bei kūginės spinduliuotės atsiradimas yra aprašomas kaip nuo netiesinio poliarizuotumo bangos išsklaidytos žadinančiosios bangos rezultatas [7, 8]. Dėl efektinio tribangio maišymosi modelio, šviesos gijų formavimasis bei superkontinuumo generacija šiuo metu yra suprantama kaip savaiminė žadinančiosios spinduliuotės bangų paketo transformacija į netiesines X [30] ar O-bangas [20].

Iki šiol superkontinuumo generacija buvo stebėta daugybėje plačios draustinės juostos kietakūnių dielektrinių terpių žadinimui naudojant impulsus, kurių bangos ilgiai yra nuo ultravioletinės iki viduriniosios infraraudonosios srities [17, 24–27, 31–34]. Dėl itin gerų savybių, tokių kaip laikinio bei erdvinio koherentiškumo, plataus spektro įvairiose dažnių srityse, impulsų savispūdos, superkontinuumo spinduliuotė yra plačiai naudojama metrologi-

joje [35], žadinimo-zondavimo spektroskopijoje [36] ar kaip užkrato signalas optiniuose parametriniuose stiprintuvuose [37] arba faziškai moduliuotų impulsų parametriniuose stiprintuvuose [38, 39]. Vis labiau plečiantis įvairioms taikymų sritims, didėja itin plačiu spektru vidurinėje infraraudonojoje srityje ar kontroliuojamomis spektrinėmis bei laikinėmis savybėmis pasižyminčios superkontinuumo spinduliuotės poreikis.

Visgi, iki šiol didžioji dalis tyrimų atlikti tik izotropinėse centrosimetrinėse terpėse, pasižyminčiose kubiniu netiesiškumu, kuriose superkontinuumo spektrinių bei laikinių savybių valdymas yra ribotas arba pagrįstas gan sudėtingais metodais tokiais kaip žadinančiojo impulso formos [40, 41], poliarizacijos [42], fazės [43–45] ar fokusavimosi sąlygų [46] keitimas. Kita vertus, anizotropinės terpės, pasižyminčios ne tik kubiniu, tačiau ir kvadratiniu netiesiškumu, dėl galimo pakopinių reiškinių valdymo, suteikia unikalią galimybę kontroliuoti superkontinuumo generacijos procesą. Šiose terpėse, esant faziniam nederinimui, galima pakopinė antrosios harmonikos generacija, kurios metu vyksta nuolatiniai energijos mainai tarp pagrindinio dažnio bei antrosios harmonikos spinduliuotės. Šio proceso metu regeneruojama pagrindinio dažnio spinduliuotė sklinda mažesniu arba didesniu efektiniu faziniu greičiu, t.y. atsiranda tam tikras pagrindinio dažnio bangos fazės poslinkis, kurio įtaka, analogiškai optiniam Kero efektui, gali būti įvertinta pasitelkiant pakopinį netiesinį lūžio rodiklį [47, 48]. Kadangi pakopinės antrosios harmonikos generacijos sąlygos gali būti lengvai kontroliuojamos nesudėtingais metodais, t.y. keičiant fazinio nederinimo parametrą $\Delta$k tarp žadinančiosios bei antrosios harmonikos bangų, pvz., keičiant netiesinio kristalo posūkio kampą ar temperatūrą, tai suteikia unikalią galimybę valdyti terpės efektinį (dėl suminio Kero bei pakopinių netiesiškumų poveikio) netiesinį lūžio rodiklį bei tuo pačiu superkontinuumo spektrinę bei laikinę dinamiką.

Kita vertus, vis daugiau mokslinių tyrimų atliekama vidurinėje infraraudonoje srityje, ypatingai svarbioje virpesinei spektroskopijai [51], siekiant atrasti superkontinuumo generacijai šioje srityje optimaliai tinkamas naudoti medžiagas [1]. Netvarkios polikristalinės ar polidomeninės terpės yra itin patrauklios superkontinuumo generacijai šioje srityje dėl atsitiktinio fazinio kvazisinchronizmo, atsirandančio dėl netvarkios šių kristalų struktūros ir leidžiančio efektyviai vykti įvairioms tribangėms sąveikoms plačiame dažnių diapazone [52]. Taigi, superkontinuumo generacijos metu tokiose terpėse stebimas ne tik spektrinis išplitimas aplink pagrindinį žadinančiosios spinduliuotės dažnį, tačiau ir plačiajuostė antrosios bei aukštesniųjų harmonikų generacija, kuri žymiai padidina superkontinuumo generacijos metu pasiekiamą spektrinį išplitimą [53].

### Darbo tikslas

Šios disertacijos darbo tikslas yra ištirti šviesos gijų formavimosi bei superkontinuumo generacijos ypatumus tvarkiose monokristalinėse bei netvarkiose polikristalinėse ir polidomeninėse terpėse, pasižyminčiose konkuruojančiais kubiniu bei kvadratiniu netiesiškumais, naudojant femtosekundinius infraraudonuosius impulsus, kurių bangos ilgis patenka į šių terpių normaliosios, nulinės bei anomaliosios grupinių greičių dispersijos sritis.

### Sprendžiami uždaviniai

- Šviesos gijų formavimosi, superkontinuumo generacijos bei erdvėlaikinių savybių tyrimas terpėse su konkuruojančiais kvadratiniu ir kubiniu netiesiškumais, t.y. $\beta$-BBO kristale, normaliosios ir anomaliosios grupinių greičių dispersijos srityse.

- Įvairios energijos viduriniosios infraraudonosios srities impulsų savispūda be netiesinių nuostolių pasitelkiant konkuruojančius kubinį bei kvadratinį pakopinį netiesiškumus.

- Atsitiktinio fazinio kvazisinchronizmo įtakos superkontinuumo generacijai bei šviesos gijų formavimuisi tyrimas polikristalinėse zinc-blende terpėse (ZnSe, ZnS) ir polidomeninėje SBN terpėje normaliosios, nulinės bei anomaliosios grupinių greičių dispersijos srityse.

- Netiesinio lūžio rodiklio įvertinimas SBN kristalinėje terpėje pasinaudojant šviesos gijų pėdsakais, kurie yra išryškinti antrosios harmonikos, generuojamos plokštumoje, lygiagrečioje šoniniam kristalo paviršiui ir sutampančioje su žadinančiojo pluošto sklidimo kryptimi.

### Mokslinis darbo naujumas

- Pademonstruota, jog $\beta$-BBO kristale su konkuruojančiais kvadratiniu-pakopiniu ir kubiniu netiesiškumais, galimas šviesos gijų formavimosi ir superkontinuumo generacijos valdymas normaliosios bei anomaliosios grupinių greičių dispersijos srityse. Šiomis sąlygomis stebima dviejų ortogonalių poliarizacijų spinduliuotė, kurių prigimtis priskiriama atitinkamai superkontinuumo generacijai bei savaiminio fazinio sinchronizmo metu generuojamai antrajai harmonikai. Parodyta, jog superkontinuumo mėlynojo spektro krašto valdymas yra lemiamas efektyvios antrosios harmonikos generacijos bei konkuruojančių kvadratinio-pakopinio ir kubinio netiesiškumų šioje srityje, o antrosios harmonikos valdymas - tikslaus savaiminio fazinio sinchronizmo tam tikriems generuojamo superkontinuumo mėlynojo krašto komponentams.

- Nustatyta, kad $\beta$-BBO kristale su konkuruojančiais kvadratiniu-pakopiniu ir kubiniu netiesiškumais, šviesos gijų formavimosi bei superkontinuumo generacijos savybės yra panašios į įprastinėse izotropinėse dielektrinėse terpėse stebimo superkontinuumo savybes normaliosios bei anomaliosios grupinių greičių dispersijos srityse. Normaliosios grupinių greičių dispersijos srityje stebimas impulso skilimas į du subimpulsus, o didėjant efektiniam netiesiniam lūžio rodikliui, centrinės smailės rekonstrukcija bei pakartotinis skilimas. Kita vertus, anomaliosios grupinių greičių dispersijos srityje matomas erdvėje bei laike lokalizuotų bangų paketų - šviesos kulkų formavimasis.

- Parodyta, jog efektinio netiesinio lūžio rodiklio kitimas, keičiant fazinio nederinimo parametrą, įgalina impulsų savispūdos, atsirandančios dėl priešingo anomaliosios grupinių greičių dispersijos bei fazės moduliavimosi poveikio, valdymą. Tokiu būdu pademonstruota be netiesinių nuostolių vykstanti impulsų savispūda iki daugiau nei trijų kartų ($< 30$ fs).

- Atliktų tyrimų metu nustatyta, jog žadinant vidurinės infraraudonosios srities femtosekundiniais impulsais, zinc-blende polikristalinėse terpėse (ZnS, ZnSe) stebima superkontinuumo generacija, kurios spektras praturtinamas antrosios bei aukštesniųjų eilių harmonikomis. Esant 3,6 $\mu$m bangos ilgio žadinančiajai spinduliuotei ZnS and ZnSe polikristaluose buvo pademonstruotas superkontinuumas, kurio spektras atitinkamai išplinta 0,4-5 $\mu$m bei 0,5-5 $\mu$m bangos ilgių diapazone. To paties pločio, tačiau iki 10-osios harmonikos ZnS ir iki 8-osios ZnSe, spektrai buvo gauti, kai žadinančiosios spinduliuotės bangos ilgis siekė 4,6 $\mu$m.

- Pademonstruota, jog antrosios bei aukštesniųjų eilių harmonikų generacija polikristalinėse zinc-blende terpėse galima dėl atsitiktinio fazinio kvazisinchronizmo sąlygojamų tribangių sąveikų. Dėl šios priežasties generuojamos harmonikos pasižymi: 1) itin plačiu spektriniu diapazonu, kuris dažninėje erdvėje atkartoja pagrindinio dažnio spinduliuotės spektrą; 2) atsitiktine poliarizacija; 3) tiesine generacijos efektyvumo priklausomybe nuo kristalitų polikristalinėje terpėje skaičiaus.

- Netvarkioje polidomeninėje SBN terpėje pademonstruotas efektyvus superkontinuumo spektro plitimas 0,8 - 1,81 $\mu$m, 1,04 - 2,5 $\mu$m bei 1,0 - 3,32 $\mu$m spektriniuose diapazonuose, kai žadinančiojo impulso bangos ilgis patenka į terpės normaliosios (1,2 $\mu$m), nulinės (2,0 $\mu$m) bei anomaliosios (2,4 $\mu$m) grupinių greičių dispersijos sritis. Kartu su superkontinuumo generacija buvo stebima dėl atsitiktinio fazinio kvazisinchronizmo atsirandanti antrosios harmonikos generacija plokštumoje, lygiagrečioje šoniniam kristalo paviršiui, ir sutampančioje su žadinančiojo pluošto sklidimo kryptimi. Dėl šio reiškinio išryškinami šviesos gijų pėdsakai buvo

panaudoti netiesiniam SBN terpės lūžio rodikliui nustatyti prie kiekvieno iš trijų naudotų bangos ilgių.

Ginamieji teiginiai

- Netiesinėse terpėse, I tipo antrosios harmonikos generacijos, esant faziniam nederinimui, metu, kai žadinančiosios spinduliuotės bangos ilgis patenka į normaliosios arba anomaliosios grupinių greičių dispersijos sritį, sąlygomis kuomet galimas šviesos gijų formavimasis, stebima dviejų ortogonalių poliarizacijų spinduliuotė: paprastosios poliarizacijos superkontinuumo spinduliuotė, bei nepaprastosios poliarizacijos pastovaus bei kintamo bangos ilgio antrosios harmonikos spinduliuotė.

- Superkontinuumo generacijos metu, netiesinėse terpėse, pasižyminčiose konkuruojančiais kvadratiniu ir kubiniu netiesiškumais, normaliosios grupinių greičių dispersijos srityje stebimas žadinančiosios spinduliuotės impulsų skilimas į du subimpulsus, o anomaliosios grupinių greičių dispersijos srityje - erdvėje bei laike lokalizuotų bangų paketų - šviesos kulkų, formavimasis.

- Efektinio netiesinio lūžio rodiklio varijavimas, keičiant fazinio nederinimo parametrą, gali būti panaudotas be netiesinių nuostolių vykstančiai valdomai infraraudonųjų impulsų savispūdai anomaliosios grupinių greičių dispersijos srityje pasiekti.

- Polikristalinėse zinc-blende terpėse stebima superkontinuumo generacija yra praturtinta atsitiktinio fazinio kvazisinchronizmo sąlygojamos plačiajuostės antrosios bei aukštesniųjų harmonikų generacijos, kurią riboja tik kristalo trumpabangės sugerties juostos kraštas.

- Netvarkioje polidomeninėje SBN terpėje, kai žadinančiosios spinduliuotės bangos ilgis patenka į normaliosios, nulinės arba anomaliosios grupinių greičių dispersijos sritis, galima plataus daugiau nei vienos optinės oktavos superkontinuumo spektro generacija. Kartu su superkontinuumo generacija yra stebima dėl atsitiktinio fazinio kvazisinchronizmo atsirandanti antrosios harmonikos generacija plokštumoje, lygiagrečioje šoniniam kristalo paviršiui, ir sutampančioje su žadinančiojo pluošto sklidimo kryptimi. Šios spinduliuotės pėdsakas, stebimas kristalo paviršiuje, atkartoja susiformavusios šviesos gijos sklidimą, tad gali būti panaudojamas terpės netiesinio lūžio rodiklio nustatymui.

Atlikti šviesos gijų formavimosi bei superkontinuumo generacijos tyrimai anizotropiniame necentrosimetriniame $\beta$-BBO kristale, esant 120 fs, 0,8 $\mu$m bei 90 fs, 1,8 $\mu$m bangos ilgio žadinančiosios spinduliuotės impulsams, kurių bangos ilgis patenka į atitinkamai normaliosios bei anomaliosios grupinių greičių dispersijos sritis [**A1, A2**]. Tyrimų metu išmatavus spektrinę dinamiką pastebėta, jog šiomis sąlygomis galima dviejų ortogonalių, kristalo optinės ašies atžvilgiu, poliarizacijų spinduliuotės generacija: paprastosios, atsirandančios dėl superkontinuumo generacijos, bei nepaprastosios, lemiamos antrosios harmonikos generacijos dėl savaiminio fazinio sinchronizmo. Pademonstruota, jog superkontinuumo spektrinės bei erdvėlaikinės savybės gali būti kontroliuojamos priklausomai nuo fazinio nederinimo parametro antrosios harmonikos generacijai, kuris buvo keičiamas keičiant kampą $\theta$ tarp kristalo optinės ašies ir žadinančiosios spinduliuotės sklidimo krypties. Pastarasis reiškinys buvo sąlygojamas efektinio netiesinio lūžio rodiklio valdymo galimo dėl konkurencijos tarp pakopinio-kvadratinio bei kubinio netiesiškumų. Taip pat parodyta, jog efektinio netiesinio lūžio rodiklio dydis turi žymią įtaką superkontinuumo generacijos slenkstinei energijai, t.y. esant dideliam neigiamam faziniam nederinimui, superkontinuumo generacijos slenkstis yra gerokai mažesnis ir pluoštų fokusavimasis gali vykti esant subkritinėms galioms, lyginant su įprastiniu Kero netiesiniu lūžio rodikliu. Kita vertus, esant teigiamam faziniam nederinimui, superkontinuumo generacija dėl neigiamo pakopinio netiesinio lūžio rodiklio įtakos yra negalima, arba vyksta esant didesnėms žadinančiojo impulso energijoms. Galiausiai, pademonstruota, jog dėl savaiminio fazinio sinchronizmo generuojama nepaprastosios poliarizacijos antroji harmonika, taip pat gali būti valdoma, keičiant fazinio nederinimo parametrą. Šio valdymo prigimtis buvo paaiškinta kaip atsirandanti dėl savaiminio fazinio sinchronizmo tenkinamo tam tikriems superkontinuumo mėlynojo krašto spektriniam komponentams.

Normaliosios grupinių greičių dispersijos srityje, analogiškai kaip ir izotropinėse centrosimetrinėse terpėse, buvo stebimas žadinančiojo impulso skilimas į du subimpulsus, o esant didelėms smailinėms galioms ir impulso centrinės smailės rekonstrukcija bei pakartotinis skilimas į du subimpulsus. Nustatyta, jog eksperimento sąlygomis maždaug pusė galinio subimpulso energijos atitenka antrosios harmonikos generacijai, o tai, kartu su konkurencija tarp pakopinio-kvadratinio bei kubinio netiesiškumų, lemia efektyvų mėlynojo superkontinuumo spektro krašto valdymą. Kita vertus, anomaliosios grupinių greičių dispersijos srityje pasinaudojant trimate lazerine tomografija buvo išmatuoti erdvėlaikiniai intensyvumo skirstiniai, kurie patvirtino, jog šioje srityje formuojasi erdvėje bei laike lokalizuoti bangų paketai - šviesos kulkos. Įvertinus kryžminių koreliacijų duomenis gautus trimatės tomografijos metu, pasiekta impulsų spūda nuo trijų iki keturių kartų.

Pademonstruota femtosekundinių 2,1 $\mu$m bangos ilgio impulsų savispūda bei jos valdymas anomaliosios grupinių greičių dispersijos srityje [**A4**] $\beta$-BBO kristale. Savispūda vyksta dėl priešingo fazės moduliavimosi bei grupinių greičių dispersijos poveikio, o impulso trukmė gali būti valdoma keičiant fazinio nederinimo parametrą, o tuo pačiu ir efektinį netiesinį lūžio rodiklį. Šviesos gijų formavimosi, o kartu ir netiesinių nuostolių, atsirandančių dėl daugiafotonės sugerties bei plazmos formavimosi, buvo išvengta parenkant tinkamą žadinančiojo pluošto spindulį ant priekinio kristalo paviršiaus. Tokiu būdu buvo pademonstruota 68 fs, 73 $\mu$J impulsų spūda iki 22 fs, bei siekiant parodyti, jog metodas tinkamas taikyti aukštesnėms energijoms, 95 fs, 215 $\mu$J impulsų spūda iki 27 fs. Impulsų savispūdos metu patiriami nuostoliai buvo artimi atsirandantiems dėl dviejų Frenelio atspindžių nuo priekinio bei galinio kristalo paviršiaus ir neviršijo 15%.

Atlikti superkontinuumo generacijos bei šviesos gijų formavimosi tyrimai įvairaus storio zinc-blende netvarkiose polikristalinėse terpėse (ZnS, ZnSe) žadinant femtosekundiniais impulsais, kurių bangos ilgis buvo keičiamas 2,4 - 4,6 $\mu$m srityje [**A3, A5**]. Nustatyta, jog tokiose terpėse stebima superkontinuumo generacija praturtinta intensyviomis antrosios bei aukštesniųjų eilių harmonikomis. Parodyta, jog generuojamo spektro plotis didėja, didėjant žadinančiosios bangos ilgiui, o mėlynasis spektro kraštas tokiose terpėse yra apribojamas kristalo trumpabangės sugerties juostos krašto. Tokiu būdu, polikristalinėje ZnSe terpėje, žadinant 2,4 $\mu$m femtosekundiniais impulsais, buvo gautas spektrinis išplitimas 0,6 - 4,2 $\mu$m bangos ilgių diapazone. Taip pat žadinant 3,6 $\mu$m bangos ilgio spinduliuote buvo gauti 0,4-5 $\mu$m bei 0,5-5 $\mu$m pločio spektrai atitinkamai ZnS bei ZnSe polikristalinėse terpėse, kurių mėlynasis kraštas apribotas atitinkamai 7-osios bei 6-osios harmonikų. Padidinus žadinančiosios spinduliuotės bangos ilgį iki 4,6 $\mu$m, buvo gautas spektrinis išplitimas iki 10-os bei iki 8-os harmonikos atitinkamai ZnS bei ZnSe polikristaluose. Lyginamosios analizės metu, monokristaliniame ZnTe, buvo stebima tik palyginti nedidelio efektyvumo antrosios bei trečiosios harmonikų generacija ir mažesnis spektrinis išplitimas.

Atliktų tyrimų metu pademonstruota, jog tokio tipo spektrinis išplitimas polikristalinėse zinc-blende terpėse yra nulemtas įvairių tribangių sąveikų, kurios galimos dėl atsitiktinio fazinio kvazisinchronizmo [**A3**]. Tai buvo įrodyta eksperimentiškai patvirtinus, jog tokiu būdu generuojamos harmonikos pasižymi: itin plačiu spektru dažninėje erdvėje atkartojančiu žadinančiosios spinduliuotės spektrą; atsitiktine poliarizacija; bei tiesine harmonikų generacijos efektyvumo priklausomybe nuo kristalitų polikristalinėje terpėje skaičiaus.

Galiausiai buvo ištirti superkontinuumo generacijos bei šviesos gijų formavimosi ypatumai netvarkioje polidomeninėje SBN terpėje žadinant 85-125 fs trukmės infraraudonaisiais impulsais [**A6**]. Žadinančiajam bangos ilgiui esant 1,2 $\mu$m, 2,0 $\mu$m bei 2,4 $\mu$m buvo pademonstruota superkontinuumo generacija

normaliojoje, nulinėje bei anomaliojoje grupinių greičių dispersijos srityje bei gauti superkontinuumo spektrai besitęsiantys 0,8 - 1,81 $\mu$m, 1,04 - 2,5 $\mu$m, 1,0 - 3,32 $\mu$m spektriniame diapazone. Skirtingai nei polikristalinėse terpėse, dėl atsitiktinio fazinio kvazisinchronizmo bei bei unikalios SBN feroelektrinių domenų išsidėstymo struktūros atsirandanti antrosios harmonikos generacija, buvo stebima statmena pluošto sklidimui kryptimi. Nustatyta, jog tokio tipo terpėse antrosios harmonikos generacija išryškina žadinančiosios spinduliuotės šviesos gijų pėdsakus matomus stebint viršutinį kristalo paviršių. Šie pėdsakai buvo užregistruoti skaitmeniniu veidrodiniu fotoaparatu atliekant seriją matavimų keičiant žadinančiojo impulso energiją. Kiekvienoje nuotraukoje nustačius netiesinio židinio padėtį ir pasinaudojant Marburgerio formule buvo nustatytas netiesinis SBN terpės lūžio rodiklis prie kiekvieno iš naudotų bangos ilgių.

1. Anizotropiniame kvadratiniu netiesiškumu pasižyminčiame $\beta$-BBO kristale I tipo antrosios harmonikos generacijos, esant faziniam nederinimui, metu, žadinant impulsais, kurių centrinis bangos ilgis vienu atveju patenka į normaliosios, o kitu į anomaliosios grupinių greičių dispersijos sritį, sąlygomis kuomet galimas šviesos gijų formavimasis, stebima dviejų skirtingos prigimties ortogonalių poliarizacijų (paprastosios bei nepaprastosios) spinduliuotė, kurios spektrinių savybių valdymas realizuojamas keičiant fazinio nederinimo parametrą $\Delta$k. Nepaprastosios poliarizacijos spinduliuotės atsiradimas lemiamas antrosios harmonikos generacijos: esant faziniam išderinimui, bei dėl savaiminio fazinio sinchronizmo, kuris yra tenkinamas tam tikriems superkontinuumo dažniniams komponentams. Tuo tarpu, paprastosios poliarizacijos spinduliuotė stebima dėl superkontinuumo generacijos, kurios spektro mėlynasis kraštas, normaliosios grupinių greičių dispersijos atveju, gali būti nesunkiai valdomas, keičiant fazinio nederinimo parametrą. Toks valdymas įmanomas dėl efektyvios energijos pernašos iš galinio subimpulso į antrąją harmoniką. Šio efekto poveikis anomaliosios grupinių greičių dispersijos atveju yra nežymus dėl erdvėlaikinės impulso spūdos vietoje impulsų skilimo.

2. Atlikus laikinius matavimus, nustatyta, jog anizotropiniame kvadratiniu netiesiškumu pasižyminčiame $\beta$-BBO kristale, superkontinuumo generacijos metu, normaliosios grupinių greičių dispersijos atveju, stebimas žadinančiojo impulso skilimas į du subimpulsus, o energija, reikalinga impulso skilimui stebėti, priklauso nuo žadinančiojo pluošto sklidimo krypties kristalo optinės ašies atžvilgiu, t.y. nuo fazinio nederinimo parametro $\Delta$k. Tuo tarpu, anomaliosios grupinių greičių dispersijos atveju, stebimas šviesos kulkų - erdvėje bei laike lokalizuotų bangų paketų formavimasis.

3. Terpės efektinio netiesinio lūžio rodiklio kitimas, keičiant fazinio nederinimo parametrą, gali būti panaudotas kontroliuojamai impulsų savispūdai dėl priešingo anomaliosios grupinių greičių dispersijos ir fazės moduliavimosi poveikio pasiekti. Tokiu būdu buvo pademonstruota be netiesinių nuostolių vykstanti 2.1 $\mu$m centrinio bangos ilgio 68 fs, 73 $\mu$J impulsų savispūda iki 22 fs, bei 95 fs, 215 $\mu$J impulsų savispūda iki 27 fs.

4. Polikristalinėse zinc-blende terpėse, žadinant femtosekundiniais infraraudonaisiais impulsais, stebima superkontinuumo, pasižyminčio itin plačiu spektru, generacija, praturtinta atsitiktinio fazinio kvazisinchronizmo sąlygojamų plačiajuosčių antrosios bei aukštesniųjų harmonikų. Pastarojo reiškinio kilmė patvirtinta nustačius, jog tenkinama eilė savybių atsirandančių generacijos dėl atsitiktinio fazinio kvazisinchronizmo metu: 1) plati generacijos juosta, kuri atkartoja pagrindinio dažnio spin-

duliuotės spektrą; 2) atsitiktinė poliarizacija; 3) tiesinė keitimo efektyvumo priklausomybė nuo kristalitų skaičiaus polikristaliniuose bandiniuose.

5. Polikristalinėse zinc-blende terpėse, žadinant femtosekundiniais infraraudonaisiais impulsais, mėlynasis superkontinuumo spektro kraštas yra ribojamas generuojamų lyginių bei nelyginių harmonikų skaičiaus bei jų spektrinio išplitimo. Šis savo ruožtu auga didėjant žadinančiosios spinduliuotės bangos ilgiui, ir yra ribojamas tik terpės trumpabangės sugerties juostos krašto. Tokiu būdu pademonstruota superkontinuumo generacija 0,4–5 $\mu$m bei 0,5–5 $\mu$m spektriniuose diapazonuose ZnS bei ZnSe, žadinant 60 fs, 3,6 $\mu$m bei 100 fs, 4,6 $\mu$m spinduliuote. Pirmuoju atveju buvo stebima iki 7-osios ir iki 6-osios, o antruoju, iki 10-osios ir iki 8-osios harmonikų generacija.

6. Polidomeninėje SBN terpėje, žadinant spinduliuote, kurios bangos ilgis patenka į normaliosios (1,2 $\mu$m), nulinės (2,0 $\mu$m) bei anomaliosios (2,4 $\mu$m) grupinių greičių dispersijos sritis, stebimas superkontinuumo spektro plitimas 0,8 - 1,81 $\mu$m, 1,04 - 2,5 $\mu$m bei 1,0 - 3,32 $\mu$m spektrinėse srityse. Kartu su superkontinuumo generacija stebima antrosios harmonikos, generuojamos plokštumoje, lygiagrečioje šoniniam kristalo paviršiui, ir sutampančioje su žadinančiojo pluošto sklidimo kryptimi, generacija. Parodyta, jog antrosios harmonikos spinduliuotės intensyvumo pasiskirstymas gerai atkartoja šviesos gijų sklidimo dinamiką, tad gali būti panaudotas terpės netiesinio lūžio rodiklio nustatymui pasinaudojant Marbugerio formule. Tokiu būdu gauta, jog netiesinis lūžio rodiklis SBN terpėje lygus: $(44 \pm 7) \times 10^{-16}$ cm$^2$/W, esant 1.2 $\mu$m, $(81 \pm 23) \times 10^{-16}$ cm$^2$/W, esant 2.0 $\mu$m bei $(100 \pm 15) \times 10^{-16}$ cm$^2$/W, esant 2.4 $\mu$m bangos ilgio spinduliuotei.

# BIBLIOGRAPHY


[1] A. Dubietis, G. Tamošauskas, R. Šuminas, V. Jukna, A. Couairon, Ultrafast supercontinuum generation in bulk condensed media, Lith. J. Phys. **57**(3), 113–157 (2017).

[2] A. Couairon, A. Mysyrowicz, Femtosecond filamentation in transparent media, Phys. Rep. **441**(2), 47–189 (2007).

[3] J. Marburger, Self-focusing: theory, Prog. Quantum Electron. **4**, 35–110 (1975).

[4] A. Brodeur, S. Chin, Band-gap dependence of the ultrafast white-light continuum, Phys. Rev. Lett. **80**(20), 4406 (1998).

[5] A. Brodeur, S. Chin, Ultrafast white-light continuum generation and self-focusing in transparent condensed media, J. Opt. Soc. Am. B **16**(4), 637–650 (1999).

[6] M. Mlejnek, E. M. Wright, J. V. Moloney, Dynamic spatial replenishment of femtosecond pulses propagating in air, Opt. Lett. **23**(5), 382–384 (1998).

[7] M. Kolesik, G. Katona, J. V. Moloney, E. M. Wright, Physical factors limiting the spectral extent and band gap dependence of supercontinuum generation, Phys. Rev. Lett. **91**(4), 043905 (2003).

[8] M. Kolesik, G. Katona, J. V. Moloney, E. M. Wright, Theory and simulation of supercontinuum generation in transparent bulk media, Appl. Phys. B **77**(2-3), 185–195 (2003).

[9] J. E. Rothenberg, Pulse splitting during self-focusing in normally dispersive media, Opt. Lett. **17**(8), 583–585 (1992).

[10] J. E. Rothenberg, Space–time focusing: breakdown of the slowly varying envelope approximation in the self-focusing of femtosecond pulses, Opt. Lett. **17**(19), 1340–1342 (1992).

[11] P. Chernev, V. Petrov, Self-focusing of light pulses in the presence of normal group-velocity dispersion, Opt. Lett. **17**(3), 172–174 (1992).

[12] J. K. Ranka, R. W. Schirmer, A. L. Gaeta, Observation of pulse splitting in nonlinear dispersive media, Phys. Rev. Lett. **77**(18), 3783 (1996).

[13] J. K. Ranka, A. L. Gaeta, Breakdown of the slowly varying envelope approximation in the self-focusing of ultrashort pulses, Opt. Lett. **23**(7), 534–536 (1998).

[14] A. A. Zozulya, S. A. Diddams, Dynamics of self-focused femtosecond laser pulses in the near and far fields, Opt. Express **4**(9), 336–343 (1999).

[15] A. L. Gaeta, Catastrophic collapse of ultrashort pulses, Phys. Rev. Lett. **84**(16), 3582 (2000).

[16] W. Liu, S. Petit, A. Becker, N. Aközbek, C. Bowden, S. Chin, Intensity clamping of a femtosecond laser pulse in condensed matter, Opt. Commun. **202**(1-3), 189–197 (2002).

[17] M. Bradler, P. Baum, E. Riedle, Femtosecond continuum generation in bulk laser host materials with sub-$\mu$J pump pulses, Appl. Phys. B **97**(3), 561 (2009).

[18] M. Durand, A. Jarnac, A. Houard, Y. Liu, S. Grabielle, N. Forget, A. Durécu, A. Couairon, A. Mysyrowicz, Self-guided propagation of ultrashort laser pulses in the anomalous dispersion region of transparent solids: a new regime of filamentation, Phys. Rev. Lett. **110**(11), 115003 (2013).

[19] E. O. Smetanina, V. O. Kompanets, A. E. Dormidonov, S. V. Chekalin, V. P. Kandidov, Light bullets from near-IR filament in fused silica, Laser Phys. Lett. **10**(10), 105401 (2013).

[20] D. Majus, G. Tamošauskas, I. Gražulevičiūtė, N. Garejev, A. Lotti, A. Couairon, D. Faccio, A. Dubietis, Nature of spatiotemporal light bullets in bulk Kerr media, Phys. Rev. Lett. **112**(19), 193901 (2014).

[21] S. V. Chekalin, A. E. Dokukina, A. E. Dormidonov, V. O. Kompanets, E. O. Smetanina, V. P. Kandidov, Light bullets from a femtosecond filament, J. Phys. B **48**(9), 094008 (2015).

[22] I. Gražulevičiūtė, G. Tamošauskas, V. Jukna, A. Couairon, D. Faccio, A. Dubietis, Self-reconstructing spatiotemporal light bullets, Opt. Express **22**(25), 30613–30622 (2014).

[23] I. Gražulevičiūtė, R. Šuminas, G. Tamošauskas, A. Couairon, A. Dubietis, Carrier-envelope phase-stable spatiotemporal light bullets, Opt. Lett. **40**(16), 3719–3722 (2015).

[24] F. Silva, D. R. Austin, A. Thai, M. Baudisch, M. Hemmer, D. Faccio, A. Couairon, J. Biegert, Multi-octave supercontinuum generation from mid-infrared filamentation in a bulk crystal, Nature Commun. **3**, 807 (2012).

[25] J. Darginavičius, D. Majus, V. Jukna, N. Garejev, G. Valiulis, A. Couairon, A. Dubietis, Ultrabroadband supercontinuum and third-harmonic generation in bulk solids with two optical-cycle carrier-envelope phase-stable pulses at 2 $\mu$m, Opt. Express **21**(21), 25210–25220 (2013).

[26] J. A. Dharmadhikari, R. A. Deshpande, A. Nath, K. Dota, D. Mathur, A. K. Dharmadhikari, Effect of group velocity dispersion on supercontinuum generation and filamentation in transparent solids, Appl. Phys. B **117**(1), 471–479 (2014).

[27] H. Liang, P. Krogen, R. Grynko, O. Novak, C.-L. Chang, G. J. Stein, D. Weerawarne, B. Shim, F. X. Kärtner, K.-H. Hong, Three-octave-spanning supercontinuum generation and sub-two-cycle self-compression

of mid-infrared filaments in dielectrics, Opt. Lett. **40**(6), 1069–1072 (2015).

[28] S. Skupin, L. Bergé, Self-guiding of femtosecond light pulses in condensed media: Plasma generation versus chromatic dispersion, Physica D **220**(1), 14–30 (2006).

[29] M. Kolesik, E. M. Wright, J. V. Moloney, Interpretation of the spectrally resolved far field of femtosecond pulses propagating in bulk nonlinear dispersive media, Opt. Express **13**(26), 10729–10741 (2005).

[30] D. Faccio, M. A. Porras, A. Dubietis, F. Bragheri, A. Couairon, P. Di Trapani, Conical emission, pulse splitting, and x-wave parametric amplification in nonlinear dynamics of ultrashort light pulses, Phys. Rev. Lett. **96**(19), 193901 (2006).

[31] C. Nagura, A. Suda, H. Kawano, M. Obara, K. Midorikawa, Generation and characterization of ultrafast white-light continuum in condensed media, Appl. Opt. **41**(18), 3735–3742 (2002).

[32] N. Garejev, G. Tamošauskas, A. Dubietis, Comparative study of multioctave supercontinuum generation in fused silica, YAG, and LiF in the range of anomalous group velocity dispersion, J. Opt. Soc. Am. B **34**(1), 88–94 (2017).

[33] A. Marcinkevičiūtė, V. Jukna, R. Šuminas, N. Garejev, G. Tamošauskas, A. Dubietis, Femtosecond filamentation and supercontinuum generation in bulk silicon, Opt. Lett. **44**(6), 1343–1346 (2019).

[34] A. Marcinkevičiūtė, G. Tamošauskas, A. Dubietis, Supercontinuum generation in mixed thallous halides KRS-5 and KRS-6, Opt. Mater. **78**, 339–344 (2018).

[35] R. S. S. Kumar, K. Deepak, D. N. Rao, Depolarization properties of the femtosecond supercontinuum generated in condensed media, Phys. Rev. A **78**(4), 043818 (2008).

[36] C. Calabrese, A. M. Stingel, L. Shen, P. B. Petersen, Ultrafast continuum mid-infrared spectroscopy: probing the entire vibrational spectrum in a single laser shot with femtosecond time resolution, Opt. Lett. **37**(12), 2265–2267 (2012).

[37] G. Cerullo, S. De Silvestri, Ultrafast optical parametric amplifiers, Rev. Sci. Instrum. **74**(1), 1–18 (2003).

[38] A. Dubietis, R. Butkus, A. P. Piskarskas, Trends in chirped pulse optical parametric amplification, IEEE J. Sel. Top. Quantum Electron. **12**(2), 163–172 (2006).

[39] A. Harth, M. Schultze, T. Lang, T. Binhammer, S. Rausch, U. Morgner, Two-color pumped opcpa system emitting spectra spanning 1.5 octaves from vis to nir, Opt. Express **20**(3), 3076–3081 (2012).

[40] D. Schumacher, Controlling continuum generation, Opt. Lett. **27**(6), 451–453 (2002).

[41] J. Dharmadhikari, A. Dharmadhikari, K. Dota, D. Mathur, Influencing supercontinuum generation by phase distorting an ultrashort laser pulse, Opt. Lett. **40**(2), 241–244 (2015).

[42] A. Srivastava, D. Goswami, Control of supercontinuum generation with polarization of incident laser pulses, Appl. Phys. B **77**(2-3), 325–328 (2003).

[43] V. Kartazaev, R. Alfano, Supercontinuum generated in calcite with chirped femtosecond pulses, Opt. Lett. **32**(22), 3293–3295 (2007).

[44] C. Romero, R. Borrego-Varillas, A. Camino, G. Mínguez-Vega, O. Mendoza-Yero, J. Hernández-Toro, J. R. V. de Aldana, Diffractive optics for spectral control of the supercontinuum generated in sapphire with femtosecond pulses, Opt. Express **19**(6), 4977–4984 (2011).

[45] N. Kaya, J. Strohaber, A. Kolomenskii, G. Kaya, H. Schröder, H. Schuessler, White-light generation using spatially-structured beams of femtosecond radiation, Opt. Express **20**(12), 13337–13346 (2012).

[46] V. Jukna, J. Galinis, G. Tamosauskas, D. Majus, A. Dubietis, Infrared extension of femtosecond supercontinuum generated by filamentation in solid-state media, Appl. Phys. B **116**(2), 477–483 (2014).

[47] R. DeSalvo, H. Vanherzeele, D. J. Hagan, M. Sheik-Bahae, G. Stegeman, E. W. Van Stryland, Self-focusing and self-defocusing by cascaded second-order effects in KTP, Opt. Lett. **17**(1), 28–30 (1992).

[48] G. I. Stegeman, D. J. Hagan, L. Torner, $\chi$ (2) cascading phenomena and their applications to all-optical signal processing, mode-locking, pulse compression and solitons, Opt. Quantum Electron. **28**(12), 1691–1740 (1996).

[49] F. W. Wise, J. Moses, Self-focusing and self-defocusing of femtosecond pulses with cascaded quadratic nonlinearities, Top. Appl. Phys. **114**, 481–506 (2009).

[50] B. B. Zhou, A. Chong, F. W. Wise, M. Bache, Ultrafast and octave-spanning optical nonlinearities from strongly phase-mismatched quadratic interactions, Phys. Rev. Lett. **109**(4), 043902 (2012).

[51] Y. Yu, X. Gai, T. Wang, P. Ma, R. Wang, Z. Yang, D.-Y. Choi, S. Madden, B. Luther-Davies, Mid-infrared supercontinuum generation in chalcogenides, Opt. Mater. Express **3**(8), 1075–1086 (2013).

[52] M. Baudrier-Raybaut, R. Haidar, P. Kupecek, P. Lemasson, E. Rosencher, Random quasi-phase-matching in bulk polycrystalline isotropic nonlinear materials, Nature **432**(7015), 374–376 (2004).

[53] E. Migal, F. Potemkin, V. Gordienko, Highly efficient optical parametric amplifier tunable from near-to mid-IR for driving extreme nonlinear optics in solids, Opt. Lett. **42**(24), 5218–5221 (2017).

[54] T. Kanai, P. Malevich, S. S. Kangaparambil, K. Ishida, M. Mizui, K. Yamanouchi, H. Hoogland, R. Holzwarth, A. Pugzlys, A. Baltuska, Parametric amplification of 100 fs mid-infrared pulses in $ZnGeP_2$ driven by a Ho:YAG chirped-pulse amplifier, Opt. Lett. **42**(4), 683–686 (2017).

[55] A. Lanin, E. Stepanov, A. Fedotov, A. Zheltikov, Mapping the electron band structure by intraband high-harmonic generation in solids, Optica **4**(5), 516–519 (2017).

[56] C. B. Marble, S. P. O'Connor, D. T. Nodurft, V. V. Yakovlev, A. W. Wharmby, Zinc selenide: an extraordinarily nonlinear material, Proc. SPIE **10528**, 105281X (2018).

[57] J. B. Ashcom, R. R. Gattass, C. B. Schaffer, E. Mazur, Numerical aperture dependence of damage and supercontinuum generation from femtosecond laser pulses in bulk fused silica, J. Opt. Soc. Am. B **23**(11), 2317–2322 (2006).

[58] M. A. Potenza, S. Minardi, J. Trull, G. Blasi, D. Salerno, A. Varanavičius, A. Piskarskas, P. Di Trapani, Three dimensional imaging of short pulses, Opt. Commun. **229**(1-6), 381–390 (2004).

[59] R. Trebino, K. W. DeLong, D. N. Fittinghoff, J. N. Sweetser, M. A. Krumbügel, B. A. Richman, D. J. Kane, Measuring ultrashort laser pulses in the time-frequency domain using frequency-resolved optical gating, Rev. Sci. Instrum. **68**(9), 3277–3295 (1997).

[60] M. J. Weber, *Handbook of optical materials* (London: CRC press, 2003).

[61] M. Sheik-Bahae, D. C. Hutchings, D. J. Hagan, E. W. Van Stryland, Dispersion of bound electron nonlinear refraction in solids, IEEE J. Quantum Electron. **27**(6), 1296–1309 (1991).

[62] R. DeSalvo, A. A. Said, D. J. Hagan, E. W. Van Stryland, M. Sheik-Bahae, Infrared to ultraviolet measurements of two-photon absorption and $n_2$ in wide bandgap solids, IEEE J. Quantum Electron. **32**(8), 1324–1333 (1996).

[63] M. Bache, H. Guo, B. Zhou, X. Zeng, The anisotropic Kerr nonlinear refractive index of the beta-barium borate ($\beta$-$BaB_2O_4$) nonlinear crystal, Opt. Mater. Express **3**(3), 357–382 (2013).

[64] H. P. Wagner, M. Kühnelt, W. Langbein, J. M. Hvam, Dispersion of the second-order nonlinear susceptibility in ZnTe, ZnSe, and ZnS, Phys. Rev. B **58**(16), 10494 (1998).

[65] I. Shoji, H. Nakamura, K. Ohdaira, T. Kondo, R. Ito, T. Okamoto, K. Tatsuki, S. Kubota, Absolute measurement of second-order nonlinear-optical coefficients of $\beta$-$BaB_2O_4$ for visible to ultraviolet second-harmonic wavelengths, J. Opt. Soc. Am. B **16**(4), 620–624 (1999).

[66] M. Debenham, Refractive indices of zinc sulfide in the 0.405–13-$\mu$m wavelength range, Appl. Opt. **23**(14), 2238–2239 (1984).

[67] T. Woike, T. Granzow, U. Dörfler, C. Poetsch, M. Wöhlecke, R. Pankrath, Refractive indices of congruently melting $Sr_{0.61}Ba_{0.39}Nb_2O_6$, Phys. Status Solidi A **186**(1), R13–R15 (2001).

[68] D. Zhang, Y. Kong, J.-y. Zhang, Optical parametric properties of 532-nm-pumped beta-barium-borate near the infrared absorption edge, Opt. Commun. **184**(5), 485–491 (2000).

[69] F. Träger, *Springer handbook of lasers and optics* (Springer Science & Business Media, 2012).

[70] D. N. Nikogosyan, *Nonlinear optical crystals: a complete survey* (Springer Science & Business Media, 2006).

[71] R. L. Sutherland, *Handbook of nonlinear optics* (CRC press, 2003).

[72] R. C. Miller, Optical second harmonic generation in piezoelectric crystals, Appl. Phys. Lett. **5**(1), 17–19 (1964).

[73] K. Wang, L. Qian, H. Luo, P. Yuan, H. Zhu, Ultrabroad supercontinuum generation by femtosecond dual-wavelength pumping in sapphire, Opt. Express **14**(13), 6366–6371 (2006).

[74] A. Kolomenskii, J. Strohaber, N. Kaya, G. Kaya, A. Sokolov, H. Schuessler, White-light generation control with crossing beams of femtosecond laser pulses, Opt. Express **24**(1), 282–293 (2016).

[75] S. Ashihara, J. Nishina, T. Shimura, K. Kuroda, Soliton compression of femtosecond pulses in quadratic media, J. Opt. Soc. Am. B **19**(10), 2505–2510 (2002).

[76] J. Moses, F. W. Wise, Soliton compression in quadratic media: high-energy few-cycle pulses with a frequency-doubling crystal, Opt. Lett. **31**(12), 1881–1883 (2006).

[77] F. Hache, A. Zéboulon, G. Gallot, G. Gale, Cascaded second-order effects in the femtosecond regime in $\beta$-barium borate: self-compression in a visible femtosecond optical parametric oscillator, Opt. Lett. **20**(14), 1556–1558 (1995).

[78] M. Bache, H. Guo, B. Zhou, Generating mid-IR octave-spanning supercontinua and few-cycle pulses with solitons in phase-mismatched quadratic nonlinear crystals, Opt. Mater. Express **3**(10), 1647–1657 (2013).

[79] M. Bache, B. Zhou, Multiple-octave spanning mid-IR supercontinuum generation in bulk quadratic nonlinear crystals, APL Photon. **1**, 050802 (2016).

[80] B. Zhou, H. Guo, M. Bache, Energetic mid-IR femtosecond pulse generation by self-defocusing soliton-induced dispersive waves in a bulk quadratic nonlinear crystal, Opt. Express **23**(5), 6924–6936 (2015).

[81] M. Seidel, J. Brons, G. Arisholm, K. Fritsch, V. Pervak, O. Pronin, Efficient high-power ultrashort pulse compression in self-defocusing bulk media, Sci. Rep. **7**(1), 1–8 (2017).

[82] R. S. S. Kumar, S. S. Harsha, D. N. Rao, Broadband supercontinuum generation in a single potassium di-hydrogen phosphate (KDP) crystal achieved in tandem with sum frequency generation, Appl. Phys. B **86**(4), 615–621 (2007).

[83] N. K. M. N. Srinivas, S. S. Harsha, D. N. Rao, Femtosecond supercontinuum generation in a quadratic nonlinear medium (KDP), Opt. Express **13**(9), 3224–3229 (2005).

[84] S. A. Ali, P. Bisht, A. Nautiyal, V. Shukla, K. Bindra, S. Oak, Conical emission in $\beta$-barium borate under femtosecond pumping with phase matching angles away from second harmonic generation, J. Opt. Soc. Am. B **27**(9), 1751–1756 (2010).

[85] C. Vicario, B. Monoszlai, G. Arisholm, C. P. Hauri, Generation of 1.5-octave intense infrared pulses by nonlinear interactions in DAST crystal, J. Opt. **17**(9), 094005 (2015).

[86] K. Krupa, A. Labruyère, A. Tonello, B. M. Shalaby, V. Couderc, F. Baronio, A. B. Aceves, Polychromatic filament in quadratic media: spatial and spectral shaping of light in crystals, Optica **2**(12), 1058–1064 (2015).

[87] R. Šuminas, G. Tamošauskas, V. Jukna, A. Couairon, A. Dubietis, Second-order cascading-assisted filamentation and controllable supercontinuum generation in birefringent crystals, Opt. Express **25**(6), 6746–6756 (2017).

[88] H. Wang, A. Alismail, G. Barbiero, M. Wendl, H. Fattahi, Cross-polarized, multi-octave supercontinuum generation, Opt. Lett. **42**(13), 2595–2598 (2017).

[89] R. Šuminas, G. Tamošauskas, G. Valiulis, A. Dubietis, Spatiotemporal light bullets and supercontinuum generation in $\beta$-BBO crystal with competing quadratic and cubic nonlinearities, Opt. Lett. **41**(9), 2097–2100 (2016).

[90] B. Bravy, V. Gordienko, V. Platonenko, Self-compression of terawatt level picosecond 10 $\mu$m laser pulses in nacl, Laser Phys. Lett. **11**(6), 065401 (2014).

[91] B. Bravy, V. Gordienko, V. Platonenko, Kerr effect-assisted self-compression in dielectric to single-cycle pulse width and to terawatt power level in mid-IR, Opt. Commun. **344**, 7–11 (2015).

[92] A. Voronin, A. Zheltikov, Asymptotically one-dimensional dynamics of high-peak-power ultrashort laser pulses, J. Opt. **18**(11), 115501 (2016).

[93] A. Voronin, A. Zheltikov, Pulse self-compression to single-cycle pulse widths a few decades above the self-focusing threshold, Phys. Rev. A **94**(2), 023824 (2016).

[94] W. Li, Y. Li, Y. Xu, X. Guo, J. Lu, P. Wang, Y. Leng, Design and simulation of a single-cycle source tunable from 2 to 10 micrometers, Opt. Express **25**(6), 7101–7111 (2017).

[95] A. Balakin, A. Kim, A. Litvak, V. Mironov, S. Skobelev, Extreme self-compression of laser pulses in the self-focusing mode resistant to transverse instability, Phys. Rev. A **94**(4), 043812 (2016).

[96] A. Marcinkevičiūtė, N. Garejev, R. Šuminas, G. Tamošauskas, A. Dubietis, A compact, self-compression-based sub-3 optical cycle source in the 3–4 $\mu$m spectral range, J. Opt. **19**(10), 105505 (2017).

[97] V. Shumakova, P. Malevich, S. Ališauskas, A. Voronin, A. Zheltikov, D. Faccio, D. Kartashov, A. Baltuška, A. Pugžlys, Multi-millijoule few-cycle mid-infrared pulses through nonlinear self-compression in bulk, Nat. Commun. **7**(1), 1–6 (2016).

[98] G. Valiulis, V. Jukna, O. Jedrkiewicz, M. Clerici, E. Rubino, P. Di Trapani, Propagation dynamics and X-pulse formation in phase-mismatched second-harmonic generation, Phys. Rev. A **83**(4), 043834 (2011).

[99] A. Jarnac, G. Tamosauskas, D. Majus, A. Houard, A. Mysyrowicz, A. Couairon, A. Dubietis, Whole life cycle of femtosecond ultraviolet filaments in water, Phys. Rev. A **89**(3), 033809 (2014).

[100] J. Moses, F. W. Wise, Controllable self-steepening of ultrashort pulses in quadratic nonlinear media, Phys. Rev. Lett. **97**(7), 073903 (2006).

[101] J. Moses, B. A. Malomed, F. W. Wise, Self-steepening of ultrashort optical pulses without self-phase-modulation, Phys. Rev. A **76**(2), 021802 (2007).

[102] A. L. Gaeta, Spatial and temporal dynamics of collapsing ultrashort laser pulses, Top. Appl. Phys. **114**, 399–411 (2009).

[103] A. Couairon, E. Brambilla, T. Corti, D. Majus, O. d. J. Ramírez-Góngora, M. Kolesik, Practitioner's guide to laser pulse propagation models and simulation, Eur. Phys. J. Special Topics **199**(1), 5–76 (2011).

[104] B. Zhou, H. Guo, M. Bache, Soliton-induced nonlocal resonances observed through high-intensity tunable spectrally compressed second-harmonic peaks, Phys. Rev. A **90**(1), 013823 (2014).

[105] H. Pires, M. Baudisch, D. Sanchez, M. Hemmer, J. Biegert, Ultrashort pulse generation in the mid-IR, Prog. Quantum. Electron. **43**, 1 – 30 (2015).

[106] S. Frolov, V. Trunov, V. Leshchenko, E. Pestryakov, Multi-octave supercontinuum generation with IR radiation filamentation in transparent solid-state media, Appl. Phys. B **122**(5), 124 (2016).

[107] M. Liao, W. Gao, T. Cheng, X. Xue, Z. Duan, D. Deng, H. Kawashima, T. Suzuki, Y. Ohishi, Five-octave-spanning supercontinuum generation in fluoride glass, Appl. Phys. Express **6**(3), 032503 (2013).

[108] A. Dormidonov, V. Kompanets, S. Chekalin, V. Kandidov, Giantically blue-shifted visible light in femtosecond mid-IR filament in fluorides, Opt. Express **23**(22), 29202–29210 (2015).

[109] N. Garejev, V. Jukna, G. Tamošauskas, M. Veličkė, R. Šuminas, A. Couairon, A. Dubietis, Odd harmonics-enhanced supercontinuum in bulk solid-state dielectric medium, Opt. Express **24**(15), 17060–17068 (2016).

[110] H. Fattahi, H. Wang, A. Alismail, G. Arisholm, V. Pervak, A. M. Azzeer, F. Krausz, Near-PHz-bandwidth, phase-stable continua generated from a Yb:YAG thin-disk amplifier, Opt. Express **24**(21), 24337–24346 (2016).

[111] S. Ashihara, Y. Kawahara, Spectral broadening of mid-infrared femtosecond pulses in gaas, Opt. Lett. **34**(24), 3839–3841 (2009).

[112] M. Liao, W. Gao, T. Cheng, Z. Duan, X. Xue, H. Kawashima, T. Suzuki, Y. Ohishi, Ultrabroad supercontinuum generation through filamentation in tellurite glass, Laser Phys. Lett. **10**(3), 036002 (2013).

[113] A. Lanin, A. Voronin, E. Stepanov, A. Fedotov, A. Zheltikov, Multioctave, 3–18 $\mu$m sub-two-cycle supercontinua from self-compressing, self-focusing soliton transients in a solid, Opt. Lett. **40**(6), 974–977 (2015).

[114] O. Mouawad, P. Béjot, F. Billard, P. Mathey, B. Kibler, F. Désévédavy, G. Gadret, J.-C. Jules, O. Faucher, F. Smektala, Mid-infrared filamentation-induced supercontinuum in As–S and an As-free Ge–S counterpart chalcogenide glasses, Appl. Phys. B **121**(4), 433–438 (2015).

[115] P. Béjot, F. Billard, C. Peureux, T. Diard, J. Picot-Clémente, C. Strutynski, P. Mathey, O. Mouawad, O. Faucher, K. Nagasaka, et al., Filamentation-induced spectral broadening and pulse shortening of infrared pulses in tellurite glass, Opt. Commun. **380**, 245–249 (2016).

[116] Y. Yang, M. Liao, X. Li, W. Bi, Y. Ohishi, T. Cheng, Y. Fang, G. Zhao, W. Gao, Filamentation and supercontinuum generation in lanthanum glass, J. Appl. Phys. **121**(2), 023107 (2017).

[117] A. M. Stingel, H. Vanselous, P. B. Petersen, Covering the vibrational spectrum with microjoule mid-infrared supercontinuum pulses in nonlinear optical applications, J. Opt. Soc. Am. B **34**(6), 1163–1169 (2017).

[118] V. Berger, Nonlinear photonic crystals, Phys. Rev. Lett. **81**, 4136–4139 (1998).

[119] A. Arie, N. Voloch, Periodic, quasi-periodic, and random quadratic nonlinear photonic crystals, Laser Photonics Rev. **4**(3), 355–373 (2010).

[120] E. Y. Morozov, A. A. Kaminskii, A. S. Chirkin, D. B. Yusupov, Second optical harmonic generation in nonlinear crystals with a disordered domain structure, JETP Lett. **73**(12), 647–650 (2001).

[121] X. Vidal, J. Martorell, Generation of light in media with a random distribution of nonlinear domains, Phys. Rev. Lett. **97**(1), 013902 (2006).

[122] R. Fischer, S. Saltiel, D. Neshev, W. Krolikowski, Y. S. Kivshar, Broadband femtosecond frequency doubling in random media, Appl. Phys. Lett. **89**(19), 191105 (2006).

[123] W. Wang, V. Roppo, K. Kalinowski, Y. Kong, D. Neshev, C. Cojocaru, J. Trull, R. Vilaseca, K. Staliunas, W. Krolikowski, S. M. Saltiel, Y. Kivshar, Third-harmonic generation via broadband cascading in disordered quadratic nonlinear media, Opt. Express **17**(22), 20117–20123 (2009).

[124] A. Aleksandrovsky, A. Vyunishev, A. Zaitsev, V. Slabko, Random quasi-phase-matched conversion of broadband radiation in a nonlinear photonic crystal, Phys. Rev. A **82**(5), 055806 (2010).

[125] L. Mateos, P. Molina, J. F. Galisteo-López, C. López, L. E. Bausá, M. O. Ramírez, Ultrabroadband generation of multiple concurrent nonlinear coherent interactions in random quadratic media, Appl. Phys. Lett. **103**(10), 101101 (2013).

[126] A. Aleksandrovsky, A. Vyunishev, A. Zaitsev, V. Slabko, Random quasi-phase-matched nonlinear optical conversion of supercontinuum to the ultraviolet, Appl. Phys. Lett. **103**(25), 251104 (2013).

[127] P. Trabs, F. Noack, A. S. Aleksandrovsky, A. I. Zaitsev, V. Petrov, Generation of coherent radiation in the vacuum ultraviolet using randomly quasi-phase-matched strontium tetraborate, Opt. Lett. **41**(3), 618–621 (2016).

[128] S. Stivala, A. C. Busacca, A. Pasquazi, R. L. Oliveri, R. Morandotti, G. Assanto, Random quasi-phase-matched second-harmonic generation in periodically poled lithium tantalate, Opt. Lett. **35**(3), 363–365 (2010).

[129] C.-Y. Yang, C. Lin, C. Liljestrand, W.-M. Su, C. Canalias, C.-S. Chuu, Parametric down-conversion with nonideal and random quasi-phase-matching, Sci. Rep. **6**, 26079 (2016).

[130] S. E. Skipetrov, Disorder is the new order, Nature **432**(7015), 285–286 (2004).

[131] T. D. Krauss, F. W. Wise, Femtosecond measurement of nonlinear absorption and refraction in CdS, ZnSe, and ZnS, Appl. Phys. Lett. **65**(14), 1739–1741 (1994).

[132] L. Gallais, M. Commandré, Laser-induced damage thresholds of bulk and coating optical materials at 1030 nm, 500 fs, Appl. Opt. **53**(4), A186–A196 (2014).

[133] S. Vasilyev, I. Moskalev, M. Mirov, V. Smolski, S. Mirov, V. Gapontsev, Ultrafast middle-IR lasers and amplifiers based on polycrystalline Cr:ZnS and Cr:ZnSe, Opt. Mater. Express **7**(7), 2636–2650 (2017).

[134] S. B. Mirov, I. S. Moskalev, S. Vasilyev, V. Smolski, V. V. Fedorov, D. Martyshkin, J. Peppers, M. Mirov, A. Dergachev, V. Gapontsev, Frontiers of mid-IR lasers based on transition metal doped chalcogenides, IEEE J. Quantum Electron. **24**(5), 1–29 (2018).

[135] X. Ren, L. H. Mach, Y. Yin, Y. Wang, Z. Chang, Generation of 1 kHz, 2.3 mJ, 88 fs, 2.5 $\mu$m pulses from a $Cr^{2+}$:ZnSe chirped pulse amplifier, Opt. Lett. **43**(14), 3381–3384 (2018).

[136] L. O. Hocker, C. F. Dewey Jr, Enhancement of second-harmonic generation in zinc selenide by crystal defects, Appl. Phys. Lett. **28**(5), 267–270 (1976).

[137] R. Alfano, Q. Wang, T. Jimbo, P. Ho, R. Bhargava, B. Fitzpatrick, Induced spectral broadening about a second harmonic generated by an intense primary ultrashort laser pulse in ZnSe crystals, Phys. Rev. A **35**(1), 459 (1987).

[138] G. M. Archipovaite, S. Petit, J.-C. Delagnes, E. Cormier, 100 kHz Yb-fiber laser pumped 3 $\mu$m optical parametric amplifier for probing solid-state systems in the strong field regime, Opt. Lett. **42**(5), 891–894 (2017).

[139] A. H. Chin, O. G. Calderón, J. Kono, Extreme midinfrared nonlinear optics in semiconductors, Phys. Rev. Lett. **86**(15), 3292 (2001).

[140] T. D. Chinh, W. Seibt, K. Siegbahn, Dot patterns from second-harmonic and sum-frequency generation in polycrystalline ZnSe, J. Appl. Phys. **90**(5), 2612–2614 (2001).

[141] C. Dewey Jr, L. Hocker, Enhanced nonlinear optical effects in rotationally twinned crystals, Appl. Phys. Lett. **26**(8), 442–444 (1975).

[142] R. Haıdar, A. Mustelier, P. Kupecek, E. Rosencher, R. Triboulet, P. Lemasson, G. Mennerat, Largely tunable midinfrared (8–12 $\mu$m) difference frequency generation in isotropic semiconductors, J. Appl. Phys. **91**(4), 2550–2552 (2002).

[143] A. Mustelier, E. Rosencher, P. Kupecek, A. Godard, M. Baudrier, M. Lefebvre, M. Poulat, G. Mennerat, C. Pasquer, P. Lemasson, Mid-infrared difference frequency generation in quasi-phase matched diffusion bonded ZnSe plates, Appl. Phys. Lett. **84**(22), 4424–4426 (2004).

[144] Q. Ru, N. Lee, X. Chen, K. Zhong, G. Tsoy, M. Mirov, S. Vasilyev, S. B. Mirov, K. L. Vodopyanov, Optical parametric oscillation in a random polycrystalline medium, Optica **4**(6), 617–618 (2017).

[145] M. Durand, A. Houard, K. Lim, A. Durécu, O. Vasseur, M. Richardson, Study of filamentation threshold in zinc selenide, Opt. Express **22**(5), 5852–5858 (2014).

[146] O. Mouawad, P. Béjot, F. Billard, P. Mathey, B. Kibler, F. Désévédavy, G. Gadret, J.-C. Jules, O. Faucher, F. Smektala, Filament-induced visible-to-mid-IR supercontinuum in a ZnSe crystal: Towards multi-octave supercontinuum absorption spectroscopy, Opt. Mater. **60**, 355–358 (2016).

[147] R. I. Grynko, G. C. Nagar, B. Shim, Wavelength-scaled laser filamentation in solids and plasma-assisted subcycle light-bullet generation in the long-wavelength infrared, Phys. Rev. A **98**(2), 023844 (2018).

[148] P. Molina, M. de la O. Ramirez, and L. E. Bausa, Strontium barium niobate as a multifunctional two-dimensional nonlinear "photonic glass", Adv. Funct. Mater. **18**(5), 709–715 (2008).

[149] K. Terabe, S. Takekawa, M. Nakamura, K. Kitamura, S. Higuchi, Y. Gotoh, A. Gruverman, Imaging and engineering the nanoscale-domain structure of a $Sr_{0.61}Ba_{0.39}Nb_2O_6$ crystal using a scanning force microscope, Appl. Phys. Lett. **81**(11), 2044–2046 (2002).

[150] A. R. Tunyagi, M. Ulex, K. Betzler, Noncollinear optical frequency doubling in strontium barium niobate, Phys. Rev. Let. **90**(24), 243901 (2003).

[151] V. Roppo, W. Wang, K. Kalinowski, Y. Kong, C. Cojocaru, J. Trull, R. Vilaseca, M. Scalora, W. Krolikowski, Y. Kivshar, The role of ferroelectric domain structure in second harmonic generation in random quadratic media, Opt. Express **18**(5), 4012–4022 (2010).

[152] W. Wang, K. Kalinowski, V. Roppo, Y. Sheng, K. Koynov, Y. Kong, C. Cojocaru, J. Trull, R. Vilaseca, W. Krolikowski, Second-and third-harmonic parametric scattering in disordered quadratic media, J. Phys. B **43**(21), 215404 (2010).

[153] F. J. Rodríguez, C. Yao, J. L. Domínguez-Juárez, J. Bravo-Abad, J. Martorell, Observation of speckle pattern formation in transparent nonlinear random media, Opt. Lett. **36**(8), 1347–1349 (2011).

[154] C. Yao, F. J. Rodriguez, J. Martorell, Controlling the diffused nonlinear light generated in random materials, Opt. Lett. **37**(10), 1676–1678 (2012).

[155] C. Hermann-Avigliano, I. Salinas, D. Rivas, B. Real, A. Mančić, C. Mejía-Cortés, A. Maluckov, R. A. Vicencio, Spatial rogue waves in photorefractive SBN crystals, Opt. Lett. **44**(11), 2807–2810 (2019).

[156] M. Ayoub, M. Paßlick, J. Imbrock, C. Denz, Controlling the effective second-order susceptibility in random quadratic media, Opt. Express **23**(26), 33980–33991 (2015).

[157] J. Trull, S. Saltiel, V. Roppo, C. Cojocaru, D. Dumay, W. Krolikowski, D. Neshev, R. Vilaseca, K. Staliunas, Y. S. Kivshar, Characterization of femtosecond pulses via transverse second-harmonic generation in random nonlinear media, Appl. Phys. B **95**(3), 609–615 (2009).

[158] J. Trull, I. Sola, B. Wang, A. Parra, W. Krolikowski, Y. Sheng, R. Vilaseca, C. Cojocaru, Ultrashort pulse chirp measurement via transverse second-harmonic generation in strontium barium niobate crystal, Appl. Phys. Lett. **106**(22), 221108 (2015).

[159] B. Wang, C. Cojocaru, W. Krolikowski, Y. Sheng, J. Trull, Transverse single-shot cross-correlation scheme for laser pulse temporal measurement via planar second harmonic generation, Opt. Express **24**(19), 22210–22218 (2016).

[160] C. Patel, Optical harmonic generation in the infrared using a $CO_2$ laser, Phys. Rev. Lett. **16**(14), 613 (1966).

[161] M. Mlejnek, E. M. Wright, J. V. Moloney, N. Bloembergen, Second harmonic generation of femtosecond pulses at the boundary of a nonlinear dielectric, Phys. Rev. Lett. **83**(15), 2934 (1999).

[162] A. Dharmadhikari, J. Dharmadhikari, D. Mathur, Visualization of focusing–refocusing cycles during filamentation in $BaF_2$, Appl. Phys. B **94**(2), 259–263 (2009).

[163] D. Kudarauskas, G. Tamošauskas, M. Vengris, A. Dubietis, Filament-induced luminescence and supercontinuum generation in undoped, Yb-doped, and Nd-doped YAG crystals, Appl. Phys. Lett. **112**(4), 041103 (2018).

[164] V. Jukna, N. Garejev, G. Tamošauskas, A. Dubietis, Role of external focusing geometry in supercontinuum generation in bulk solid-state media, J. Opt. Soc. Am. B **36**(2), A54–A60 (2019).

# CURRICULUM VITAE


**Name:** Rosvaldas

**Surname:** Šuminas

Date of birth: 1991-07-07

Place of birth: Vilnius, Lithuania

E-mail: Rosvaldas.Suminas@gmail.com


**Education:**

| | |
|---|---|
| 1998–2010 | "Vilniaus Gabijos Gimnazijos" secondary school, Vilnius. |
| 2010–2014 | Vilnius University, Faculty of Physics |
| | *Bachelor degree.* |
| 2014–2016 | Vilnius University, Faculty of Physics |
| | *Master degree.* |
| 2016–2020 | Vilnius University, Faculty of Physics, |
| | *Ph.D. studies.* |

**Work experience:**

| | |
|---|---|
| 2016–2020 | Junior researcher at Vilnius University. |
| | Laser Research Center. |
| 2012–2018 | Lab assistant at Vilnius University. |
| | Laser Research Center. |

# TRUMPOS ŽINIOS APIE AUTORIŲ


**Vardas:** Rosvaldas

**Pavardė:** Šuminas

Gimimo data: 1991-07-07

Gimimo vieta: Vilnius, Lietuva

El. paštas: Rosvaldas.Suminas@gmail.com


**Išsilavinimas:**

| | |
|---|---|
| 1998–2010 | Vilniaus Gabijos gimnazija. |
| 2010–2014 | Vilniaus universitetas, Fizikos fakultetas, *Bakalauro kvalifikacinis laipsnis.* |
| 2014–2016 | Vilniaus universitetas, Fizikos fakultetas, *Magistro kvalifikacinis laipsnis.* |
| 2016–2020 | Vilniaus universitetas, Fizikos fakultetas, *Doktorantūra.* |

**Profesinė veikla:**

| | |
|---|---|
| 2016–2020 | Jaunesnysis mokslo darbuotojas, Vilniaus universitetas, Lazerinių tyrimų centras. |
| 2012–2018 | Laborantas, Vilniaus universitetas, Lazerinių tyrimų centras. |

# ACKNOWLEDGEMENTS

First of all, I would like to express my most sincere gratitude to my academic supervisor prof. habil. dr. Audrius Dubietis who has given me the opportunity to be a part of his research team for the last 7 years. He was always ready to extend a helping hand if needed and to provide his invaluable guidance, which throughout these years has proven to have been the main driving force pushing our research efforts further and beyond.

Second of all, I would like to thank assoc. prof. dr. Gintaras Tamošauskas who has always been the technical guru of our team. He provided valuable technological insight and kept most of the laser and diagnostic equipment up and running. He was also responsible for the creation and development of our home-built scanning prism spectrometer and other diagnostic equipment, which were used in most of the experiments. Suffice it to say that without his expertise most of the experiments would not have been possible.

I also wish to thank dr. Nail Garejev whose programming knowledge made the data acquisition and analysis workflow less tedious, whose photography skills brought the visual appeal of our research into the limelight and whose LaTeX dissertation template helped me and will surely help many other PhD students in the future.

I am also grateful to assoc. prof. dr. Vytautas Jukna, prof. dr. Gintaras Valiulis and prof. Arnaud Couairon all of whom had contributed in providing numerical simulations or other insight in order to make sense of the experimental data.

Last but certainly not the least, I want to thank my wife Agnė Šuminienė for the aid provided in some of the experiments and most importantly for the support without which this work would have never seen the light of day.

This research was partly funded by the Research Council of Lithuania (APP-8/2016) and the European Development Fund (project No 1.2.2-LMT-K-718-02-0017).

# COPIES OF PUBLICATIONS

[A1] **R. Šuminas**, G. Tamošauskas, G. Valiulis, A. Dubietis, Spatiotemporal light bullets and supercontinuum generation in $\beta$-BBO crystal with competing quadratic and cubic nonlinearities, Opt. Lett. **41**, 2097–2100 (2016).

[A2] **R. Šuminas**, G. Tamošauskas, G. Valiulis, V. Jukna, A. Couairon, A. Dubietis, Second-order cascading-assisted filamentation and controllable supercontinuum generation in birefringent crystals, Opt. Express **25**, 6746–6756 (2017).

[A3] **R. Šuminas**, G. Tamošauskas, G. Valiulis, V. Jukna, A. Couairon, A. Dubietis, Multi-octave spanning nonlinear interactions induced by femtosecond filamentation in polycrystalline ZnSe, Appl. Phys. Lett. **110**, 241106 (2017).

[A4] **R. Šuminas**, G. Tamošauskas, A. Dubietis, Filamentation-free self-compression of mid-infrared pulses in birefringent crystal with second-order cascading-enhanced self-focusing nonlinearity, Opt. Lett. **43**, 235–238 (2018).

[A5] **R. Šuminas**, A. Marcinkevičiūtė, G. Tamošauskas, A. Dubietis, Even and odd harmonics-enhanced supercontinuum generation in zinc-blende semiconductors, J. Opt. Soc. Am. B **36**, A22–A27 (2019).

[A6] **R. Šuminas**, N. Garejev, A. Šuminienė, V. Jukna, G. Tamošauskas, A. Dubietis, Femtosecond filamentation, supercontinuum generation and determination of $n_2$ in polycrystalline SBN, J. Opt. Soc. Am. B **37**, 1530–1534 (2020).

# A1

# SPATIOTEMPORAL LIGHT BULLETS AND SUPERCONTINUUM GENERATION IN $\beta$-BBO CRYSTAL WITH COMPETING QUADRATIC AND CUBIC NONLINEARITIES

**R. Šuminas**, G. Tamošauskas, G. Valiulis, A. Dubietis

Opt. Lett. **41**, 2097–2100 (2016)

# Spatiotemporal light bullets and supercontinuum generation in $\beta$-BBO crystal with competing quadratic and cubic nonlinearities

R. ŠUMINAS , G. TAMOŠAUSKAS , G. VALIULIS , AND A. DUBIETIS*

*Department of Quantum Electronics, Vilnius University, Saulėtekio Avenue 10, LT-10223 Vilnius, Lithuania*
**Corresponding author: audrius.dubietis@ff.vu.lt*

*Compiled March 25, 2016*

**We experimentally study filamentation and supercontinuum generation in a birefringent medium ($\beta$-BBO crystal) pumped by intense 90 fs, 1.8 $\mu$m laser pulses whose carrier wavelength falls in the range of anomalous group velocity dispersion of the crystal. We demonstrate that the competition between the intrinsic cubic and cascaded-quadratic nonlinearities may serve as a useful tool for controlling the self-action effects via phase matching condition. In particular, we found that spectral superbroadening of the ordinary polarization is linked to three-dimensional self-focusing and formation of self-compressed spatiotemporal light bullets that could be accessed within a certain range of either positive or negative phase mismatch. In the extraordinary polarization, we detect giant spectral shifts of the second harmonic radiation, which are attributed to a light bullet-induced self-phase matching.** 

***OCIS codes:*** *(320.5520) Pulse compression; (320.6629) Supercontinuum generation; (320.7120) Ultrafast phenomena.*

http://dx.doi.org/10.1364/ao.XX.XXXXXX

Femtosecond filamentation is a universal phenomenon arising from the nonlinear interaction between the intense ultrashort laser pulse and transparent dielectric medium, which modifies the spatial, temporal, and spectral properties of the incident radiation, and induces temporary or permanent modification of the optical properties of the medium itself [1]. Therefore femtosecond filaments are increasingly gaining scientific and technological interest, offering diverse applications in laser material processing, time-resolved spectroscopy, photonics and ultrafast nonlinear optics. A particularly interesting regime of filamentation refers to self-focusing of intense near- and mid-infrared ultrashort laser pulses in solid-state dielectric media with anomalous group velocity dispersion (GVD), where the input wave packet undergoes simultaneous self-compression in spatial and temporal domains. This leads to a qualitatively new filamentation regime, producing self-compressed spatiotemporal light bullets, which exhibit quasistationary, sub-dispersive and sub-diffractive propagation over extended distances in the nonlinear medium [2–5], exceptional robustness against perturbations [6], maintain stable carrier envelope phase [7] and give rise to generation of ultrabroadband, several octave-spanning supercontinuum (SC) [8–11].

So far, these experiments were performed in isotropic materials, where the nonlinear effects arise from the intrinsic cubic (Kerr) nonlinearity, and whose linear and nonlinear properties are fixed for a given input wavelength. On the other hand, self-action in birefringent media, which possess both, quadratic and cubic nonlinearities opens new perspectives in the field, in particular, regarding the possibility to manipulate the nonlinear index of refraction. It is well known that phase mismatched second-harmonic generation (SHG) in birefringent crystals with second-order nonlinearity leads to recurrent energy exchange (cascading) that imprints large nonlinear phase shifts on the interacting waves. The cascading effect mimics the Kerr-like behavior arising from intrinsic cubic nonlinearity and hence produces large effective nonlinear index of refraction [12, 13], whose sign and magnitude could be suitably tuned by varying the phase mismatch between the interacting waves. Indeed, the cascaded nonlinearities were employed to induce either focusing or defocusing of the interacting laser beams [14–16], while the attained large phase shifts were exploited for pulse compression [17, 18] and spatiotemporal soliton generation [19]. Strong defocusing effect due to cascaded nonlinearity was exploited for compensation of Kerr effect-induced self-focusing [20], and eventually, for pulse compression, spectral broadening, temporal soliton and broadband dispersive wave generation [21–26].

Several studies reported on the SC generation in basic nonlinear crystals, such as KDP and $\beta$-BBO, with or without simultaneous SHG, however, generally neglecting the role of second-order cascading [27–30]. More recent numerical study suggested that the cascaded-quadratic nonlinearity may be favorably exploited in the self-focusing regime [31]. In that regard, the interplay between the cascaded-quadratic and cubic nonlinearities has led to experimental demonstration of filamentation and SC generation with nearly monochromatic, picosecond laser pulse in MgO:$LiNbO_3$ crystal [32]. In this Letter, we investigate a filamentation regime in $\beta$-BBO crystal, which makes

use of either enhancement or reduction of the effective nonlinear refractive index via second-order cascading, whose interplay with anomalous GVD facilitates three-dimensional self-focusing that in turn leads to formation of spatiotemporal light bullets and SC generation.

The experiment was performed using 90 fs idler pulses from an optical parametric amplifier (Topas Prime, Light Conversion Ltd.), which was pumped by the amplified Ti:sapphire laser system (Spitfire-PRO, Newport-Spectra Physics). The output beam was spatially filtered and focused by $f = +100$ mm lens into a 70 $\mu$m FWHM focal spot located on the input face of 5.5-mm-long $\beta$-BBO crystal cut for type I phase matching. The input pulse wavelength of 1.8 $\mu$m was chosen so as to fall into the anomalous GVD range of $\beta$-BBO crystal whose zero GVD point is at 1.49 $\mu$m. The crystal orientation was set so that the input pulse had an ordinary polarization. The crystal was placed on a mechanical rotation stage, which allowed varying the angle $\theta$ between the incident wave and the optical axis of the crystal in the range of $\pm 15^\circ$ around the perfect phase matching angle for the SHG ($\theta_{\rm pm} = 20.2^\circ$).

Figure 1 shows the calculated phase mismatch parameter $\Delta k = k_{2\omega} - 2k_\omega$ and nonlinear refractive indices as functions of the angle $\theta$. The calculations of the nonlinear cascaded refractive index $n_2^{\rm casc}$ were performed using the standard cascading model [13]. The quadratic effective nonlinear coefficient $d_{\rm eff}$ was estimated using the quadratic nonlinear coefficients $|d_{22}| = 2.2$ pm/V and $|d_{31}| = 0.04$ pm/V [33], which were scaled to 1.8 $\mu$m by applying Miller's rule [34] and the Sellmeier equations [35]. The cubic nonlinear coefficient $c_{11}$ was estimated using the wavelength-independent Miller's delta $\Delta_{1111} = 52.8 \times 10^{-24}$ m$^2$/V$^2$ [36] which was used to obtain the Kerr nonlinear refractive index $n_2^{\rm Kerr} = 4.6 \times 10^{-16}$ cm$^2$/W. Finally, the effective nonlinear refractive index was estimated as $n_2^{\rm eff} = n_2^{\rm Kerr} + n_2^{\rm casc}$ providing four distinct regions of crystal orientation which determine the character of the nonlinear interaction. In the case of large positive phase mismatch (region I), the contribution of the negative cascaded-quadratic nonlinearity is small, thus leading to a positive effective nonlinear index of refraction (self-focusing region). In contrast, in region II, the negative cascaded-quadratic nonlinearity exceeds the intrinsic (Kerr) one, resulting in a negative effective refractive index (self-defocusing region). Note that a zero focusing angle can be identified ($\theta_{zf} = 14.6^\circ$), where the contributions of cascaded-quadratic and cubic nonlinearities compensate each other, marking the boundary between the two distinct regions. For small either positive or negative phase mismatch values the cascading approximation breaks down due to increased efficiency of SHG (region III, $|\Delta kL| \ll 2\pi$). Finally, for negative phase mismatch (region IV), cubic and cascaded-quadratic nonlinearities are of the same sign, thus leading to a large positive effective nonlinear index of refraction, where enhanced self-focusing is expected.

Experimentally, the spectra were recorded using two calibrated fiber spectrometers (AvaSpec-2048 and AvaSpec-NIR256-2.5), altogether covering 0.3-2.5 $\mu$m effective spectral range. The output spectra were analyzed in polarization using a broadband dielectric polarizer, allowing to capture evolution of ordinary- and extraordinary-polarized spectral components versus the angle $\theta$. Since the self-focusing regions I and IV possess rather different values of $n_2^{\rm eff}$, the corresponding measurements were performed with different input pulse energies of 1.35 $\mu$J (in region I) and 0.36 $\mu$J (in region IV) so as to achieve stable and reproducible SC generation. The results are presented

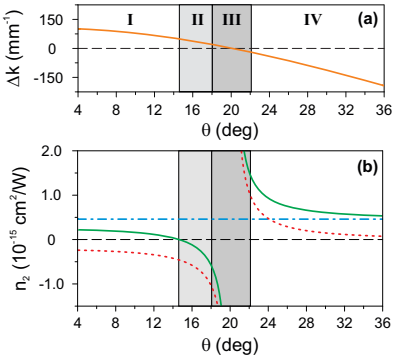


**Fig. 1.** (a) Calculated phase mismatch parameter $\Delta k$. (b) Nonlinear refractive indices: $n_2^{\rm Kerr}$ (blue dash-dotted line), $n_2^{\rm casc}$ (red dotted curve) and $n_2^{\rm eff}$ (green solid curve) versus the angle $\theta$. Roman numerals and shading mark four distinct regions, which refer to focusing (I, IV) and defocusing (II) effective nonlinearities, and efficient SHG (III), where the cascading approximation breaks down.

in Fig. 2, which shows the spectra at ordinary and extraordinary polarizations versus angle $\theta$. The ordinary-polarized SC spectra (Figs. 2(a) and 2(c)) exhibit very similar features as to those reported in isotropic dielectric media with anomalous GVD: a very broad spectrum spanning from 0.52 $\mu$m to 2.5 $\mu$m with the longest wavelength being limited by the detection range of the spectrometer and featuring a distinct intense blue-shifted peak. However, SC generation dynamics uncover unique and fascinating features that, to the best of our knowledge, have not been reported yet. Our results demonstrate that the SC generation process is readily controlled by varying the angle $\theta$, i.e. by adjusting the sign and magnitude of the effective nonlinear index of refraction, as follows from Fig. 1.

In particular, in the negative phase mismatch region ($\theta > \theta_{\rm pm}$), due to an increase of the effective nonlinear refractive index, SC generation occurs at a very low input pulse energy (0.36 $\mu$J), which is almost twice below the critical power for self-focusing ($0.62P_{\rm cr}$, where $P_{\rm cr} = 0.15\lambda_0^2/n_0 n_2^{\rm Kerr} = 6.46$ MW is the critical power for self-focusing in $\beta$-BBO). Therefore, the use of cascaded-quadratic nonlinearity offers a straightforward way of reducing the SC generation threshold down to sub-critical power values for self-focusing. Also, as can be seen in Fig. 2(a), SC generation can only be achieved for a certain range of angles ($21.5^\circ < \theta < 27^\circ$). The lower limit is set by the pump depletion due to increased efficiency of SHG, while the upper limit is set by the decrease of the effective nonlinear refractive index which in turn leads to an increase of the SC generation threshold. Conversely, in the region of positive phase mismatch ($\theta < \theta_{\rm pm}$) more than three times higher input pulse energy (1.35 $\mu$J) is required for efficient SC generation due to opposite signs of competing cascaded-quadratic and cubic nonlinearities that lead to a decrease of the effective nonlinear refractive index. Furthermore, as predicted by the calculations, two distinct regions may be identified in Fig. 2(c). For $\theta > 12^\circ$ SC generation

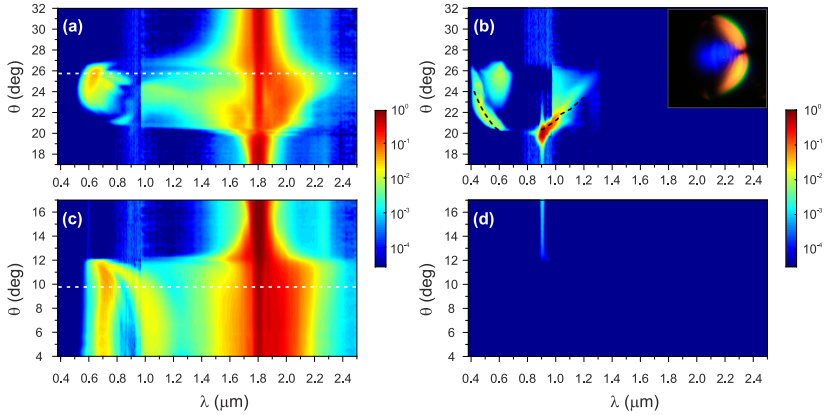


**Fig. 2.** Experimentally measured spectra as functions of angle $\theta$ at ordinary (a), (c) and extraordinary (b), (d) polarizations. The input pulse energy: (a), (b) $E = 0.36$ $\mu$J, (c), (d) $E = 1.35$ $\mu$J. The self-phase matching curve for SHG is depicted by the black dashed curves in panel (b). Note that (a), (c) and (b), (d) share the same normalized logarithmic intensity scales, respectively. Inset: photo of the SH radiation at $\theta = 24.3^\circ$. White dashed lines mark the angles at which the spatiotemporal intensity profiles were measured.

is not observed due to either defocusing ($\theta_{zf} < \theta < \theta_{pm}$) or even higher input pulse energies ($12^\circ < \theta < \theta_{zf}$) required to achieve SC generation. While, for $\theta < 12^\circ$ the beam undergoes self-focusing and a stable and controllable SC is generated.

Spectral dynamics of the extraordinary-polarized spectral components are presented in Figs. 2(b) and 2(d) and show a remarkably different character of spectral features around the SH wavelength (900 nm). In the region of negative phase mismatch (Fig. 2(b)) we observe giant red and blue spectral shifts of the SH radiation that increase with the increase of angle $\theta$. The spectral shifts are associated with SC generation at the ordinary polarization and occur due to phase matched SHG by certain spectral components of the SC which satisfy the collinear phase matching condition (so called self-phase matching [37], which is equivalent to the soliton-induced SH sideband formation [38]). Notice how the measured spectral shifts coincide with the self-phase matching curve, which is calculated using Eq. (28) from [37] and depicted by the black dashed curves in Fig. 2(b). Also see how the occurrence of the SH spectral shifts correlates with SC generation at the ordinary polarization, as shown in Fig. 2(a), which in turn attests formation of spatially and temporally compressed light bullet (see below). The additional broadening of the SH spectrum around 600 nm occurs as a result of non-collinear phase matching. Here the green-red spectral components are generated off the propagation axis, as shown in the inset of Fig. 2(b), which presents the screen shot of the SH radiation at $\theta = 24.3^\circ$. In contrast, for positive $\Delta k$ (Fig. 2(d)), no specific spectral features occur due to the absence of any scalar or vectorial phase matchings, and SH intensity quickly ceases with decreasing $\theta$.

The formation of spatially and temporally compressed light bullets is verified by the measurements of spatiotemporal intensity distributions of the wave packet at the output face of the crystal, performed using a three-dimensional imaging technique. More specifically, the spatially resolved cross-correlation function was recorded by the sum-frequency generation in a thin (20 $\mu$m) $\beta$-BBO crystal using a short (20 fs) gating pulse at 685 nm, which was produced by the noncollinear optical parametric amplifier (Topas-White, Light Conversion Ltd), see e.g. [4, 6] for more details. The measurements were performed at two different angles (as marked by white dashed lines in Figs. 2(a) and 2(c), where SC is generated at negative and positive phase mismatch, respectively. The results, as shown in Fig. 3, indicate a remarkable transformation and space-time compression of the input Gaussian-shaped wave packet. In both cases the measured spatiotemporal intensity distributions, despite large difference in the input pulse energy, are almost identical and consist of an intense self-compressed central core surrounded by a delocalized low intensity periphery, which is a characteristic feature of spatiotemporal light bullets in bulk dielectric media with anomalous GVD [4]. The apparent absence of a definite ring-shaped periphery could be attributed to

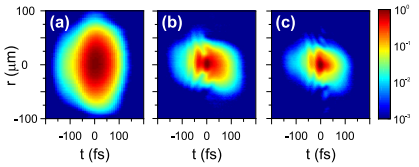


**Fig. 3.** Experimentally measured spatiotemporal intensity profiles of the (a) input Gaussian wave packet and the emerging light bullets with two different sets of parameters: (b) $\theta = 9.6^\circ$, $E = 1.35$ $\mu$J, (c) $\theta = 25.7^\circ$, $E = 0.36$ $\mu$J. The logarithmic intensity scale is used to highlight fine spatiotemporal features.

a short length of the nonlinear medium used in the experiment, where we measure the spatiotemporal profile of the emerging light bullet at its early formation stage.

Figure 4 shows the axial cross-correlation functions and corresponding spectra of the light bullets, which indicate three- to four-fold pulse compression due to opposite contributions of self-phase modulation and anomalous GVD. More specifically, pulse compression from 90 fs down to 31 fs and 21 fs is measured, as shown in Figs. 4(a) and 4(c), respectively, which are close to the zero phase Fourier transform limit as obtained from the corresponding spectra.

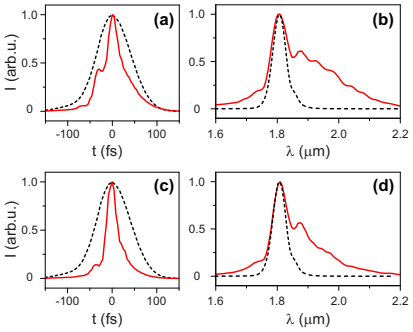


**Fig. 4.** The axial cross-correlation functions of the light bullets and their corresponding spectra (red solid lines) with two different sets of parameters: as in Figs. 3(b) and 3(c). The input pulse and its spectrum is represented by black dashed curves.

In conclusion, we demonstrated that competing cascaded-quadratic and intrinsic cubic nonlinear responses may be used for control of filamentation and supercontinuum generation dynamics in birefringent nonlinear medium. The experiments were performed in $\beta$-BBO crystal within a broad range of positive and negative phase mismatch parameters, which lead to either reduction or enhancement of the effective nonlinear refractive index, respectively. In particular, we found that in the case of large negative phase mismatch the filamentation threshold is markedly reduced, leading to SC generation at sub-critical powers for self-focusing. In contrast, positive phase mismatch yields strong negative cascaded nonlinearity which competes with the intrinsic one, resulting in SC generation at elevated intensities. By the use of three-dimensional imaging, we verified that in both cases the SC generation is facilitated by three-dimensional self-focusing of the input pulses, which transform into the self-compressed spatiotemporal light bullets with three- to four-fold compression factors. Giant spectral shifts of the orthogonally polarized second harmonic radiation were observed in the region of negative phase mismatch and attributed to a light bullet-induced self-phase matching.

This research was funded by a grant No. APP-16-012 from the Research Council of Lithuania.

## REFERENCES

1. A. Couairon and A. Mysyrowicz, Phys. Rep. **441**, 47 (2007).
2. M. Durand, A. Jarnac, A. Houard, Y. Liu, S. Grabielle, N. Forget, A. Durécu, A. Couairon, and A. Mysyrowicz, Phys. Rev. Lett. **110**, 115003 (2013).
3. E. O. Smetanina, V. O. Kompanets, A. E. Dormidonov, S. V. Chekalin, and V. P. Kandidov, Laser Phys. Lett. **10**, 105401 (2013).
4. D. Majus, G. Tamošauskas, I. Gražulevičiūtė, N. Garejev, A. Lotti, A. Couairon, D. Faccio, and A. Dubietis, Phys. Rev. Lett. **112**, 193901 (2014).
5. S. V. Chekalin, A. E. Dokukina, A. E. Dormidonov, V. O. Kompanets, E. O. Smetanina, and V. P. Kandidov, J. Phys. B **48**, 094008 (2015).
6. I. Gražulevičiūtė, G. Tamošauskas, V. Jukna, A. Couairon, D. Faccio, and A. Dubietis, Opt. Express **22**, 30613 (2014).
7. I. Gražulevičiūtė, R. Šuminas, G. Tamošauskas, A. Couairon, and A. Dubietis, Opt. Lett. **40**, 3719 (2015).
8. F. Silva, D. R. Austin, A. Thai, M. Baudisch, M. Hemmer, D. Faccio, A. Couairon, and J. Biegert, Nature Commun. **3**, 807 (2012).
9. J. Darginavičius, D. Majus, V. Jukna, N. Garejev, G. Valiulis, A. Couairon, and A. Dubietis, Opt. Express **21**, 25210 (2013).
10. J. A. Dharmadhikari, R. A. Deshpande, A. Nath, K. Dota, D. Mathur, and A. K. Dharmadhikari, Appl. Phys. B **117**, 471 (2014).
11. H. Liang, P. Krogen, R. Grynko, O. Novak, C.-L. Chang, G. J. Stein, D. Weerawarne, B. Shim, F. X. Kärtner, and K.-H. Hong, Opt. Lett. **40**, 1069 (2015).
12. R. DeSalvo, H. Vanherzeele, D. J. Hagan, M. Sheik-Bahae, G. Stegeman, and E. W. Van Stryland, Opt. Lett. **17**, 28 (1992).
13. G. I. Stegeman, D. J. Hagan, and L. Torner, Opt. Quantum Electron. **28**, 1691 (1996).
14. K. Beckwitt, F. W. Wise, L. Qian, L. A. Walker, and E. Canto-Said, Opt. Lett. **26**, 1696 (2001).
15. P. Di Trapani, A. Bramati, S. Minardi, W. Chinaglia, C. Conti, S. Trillo, J. Kilius, and G. Valiulis, Phys. Rev. Lett. **87**, 183902 (2001).
16. C. Conti, S. Trillo P. Di Trapani, J. Kilius, A. Bramati, S. Minardi, W. Chinaglia, and G. Valiulis, J. Opt. Soc. Am. B **19**, 852 (2002).
17. X. Liu, L. Qian, and F. Wise, Opt. Lett. **24**, 1777 (1999).
18. S. Ashihara, J. Nishina, T. Shimura, and K. Kuroda, J. Opt. Soc. Am. B **19**, 2505 (2002).
19. X. Liu, L. J. Qian, and F. W. Wise, Phys. Rev. Lett. **82**, 4631 (1999).
20. K. Krupa, F. Baronio, M. Conforti, S. Trillo, A. Tonello, and V. Couderc, Opt. Lett. **39**, 925 (2014).
21. M. Conforti, F. Baronio, and C. De Angelis, J. Opt. Soc. Am. B **28**, 1231 (2011).
22. C. R. Phillips, C. Langrock, J. S. Pelc, M. M. Fejer, I. Hartl, and M. E. Fermann, Opt. Express **19**, 18754 (2011).
23. B. B. Zhou, A. Chong, F. W. Wise, and M. Bache, Phys. Rev. Lett. **109**, 043902 (2012).
24. M. Bache, H. Guo, and B. Zhou, Opt. Mater. Express **3**, 1647 (2013).
25. B. Zhou, H. Guo, and M. Bache, Opt. Express. **23**, 6924 (2015).
26. B. Zhou and M. Bache, Opt. Lett. **40**, 4257 (2015).
27. N. K. M. N. Srinivas, S. S. Harsha, and D. N. Rao, Opt. Express **13**, 3224 (2005).
28. R. S. S. Kumar, S. S. Harsha, and D. N. Rao, Appl. Phys. B **86**, 615 (2007).
29. L. Wang, Y. X. Fan, H. Zhu, Z. D. Yan, H. Zeng, H.-T. Wang, S. N. Zhu, and Z. L. Wang, Phys. Rev. A **84**, 063831 (2011).
30. J. Rolle, L. Bergé, G. Duchateau, and S. Skupin, Phys. Rev. A **90**, 023834 (2014).
31. M. Conforti and F. Baronio, J. Opt. Soc. Am. B **30**, 1041 (2013).
32. K. Krupa, A. Labruyère, A. Tonello, B. M. Shalaby, V. Couderc, F. Baronio, and A. B. Aceves, Optica **2**, 1058 (2015).
33. I. Shoji, H. Nakamura, K. Ohdaira, T. Kondo, R. Ito, T. Okamoto, K. Tatsuki, and S. Kubota, J. Opt. Soc. Am. B **16**, 620 (1999).
34. R. C. Miller, Appl. Phys. Lett. **5**, 17 (1964).
35. D. Zhang, Y. Kong, and J.-Y. Zhang, Opt. Commun. **184**, 485 (2000).
36. M. Bache, H. Guo, B. Zhou, and X. Zeng, Opt. Mater. Express **3**, 357 (2013).
37. G. Valiulis, V. Jukna, O. Jedrkiewicz, M. Clerici, E. Rubino, and P. Di Trapani, Phys. Rev. A **83**, 043834 (2011).
38. B. Zhou, H. Guo, and M. Bache, Phys. Rev. A **90**, 013823 (2014).

## REFERENCES


1. A. Couairon and A. Mysyrowicz, "Femtosecond filamentation in transparent media," Phys. Rep. **441**, 47–189 (2007).
2. M. Durand, A. Jarnac, A. Houard, Y. Liu, S. Grabielle, N. Forget, A. Durécu, A. Couairon, and A. Mysyrowicz, "Self-guided propagation of ultrashort laser pulses in the anomalous dispersion region of transparent solids: a new regime of filamentation," Phys. Rev. Lett. **110**, 115003 (2013).
3. E. O. Smetanina, V. O. Kompanets, A. E. Dormidonov, S. V. Chekalin, and V. P. Kandidov, "Light bullets from near-IR filament in fused silica," Laser Phys. Lett. **10**, 105401 (2013).
4. D. Majus, G. Tamošauskas, I. Gražulevičiūtė, N. Garejev, A. Lotti, A. Couairon, D. Faccio, and A. Dubietis, "Nature of spatiotemporal light bullets in bulk Kerr media," Phys. Rev. Lett. **112**, 193901 (2014).
5. S. V. Chekalin, A. E. Dokukina, A. E. Dormidonov, V. O. Kompanets, E. O. Smetanina, and V. P. Kandidov, "Light bullets from a femtosecond filament," J. Phys. B **48**, 094008 (2015).
6. I. Gražulevičiūtė, G. Tamošauskas, V. Jukna, A. Couairon, D. Faccio, and A. Dubietis, "Self-reconstructing spatiotemporal light bullets," Opt. Express **22**, 30613–30622 (2014).
7. I. Gražulevičiūtė, R. Šuminas, G. Tamošauskas, A. Couairon, and A. Dubietis, "Carrier-envelope phase-stable spatiotemporal light bullets," Opt. Lett. **40**, 3719–3722 (2015).
8. F. Silva, D. R. Austin, A. Thai, M. Baudisch, M. Hemmer, D. Faccio, A. Couairon, and J. Biegert, "Multi-octave supercontinuum generation from mid-infrared filamentation in a bulk crystal," Nature Commun. **3**, 807 (2012).
9. J. Darginavičius, D. Majus, V. Jukna, N. Garejev, G. Valiulis, A. Couairon, and A. Dubietis, "Ultrabroadband supercontinuum and third-harmonic generation in bulk solids with two optical-cycle carrier-envelope phase-stable pulses at 2 $\mu$m," Opt. Express **21**, 25210–25220 (2013).
10. J. A. Dharmadhikari, R. A. Deshpande, A. Nath, K. Dota, D. Mathur, and A. K. Dharmadhikari, "Effect of group velocity dispersion on supercontinuum generation and filamentation in transparent solids," Appl. Phys. B **117**, 471–479 (2014).
11. H. Liang, P. Krogen, R. Grynko, O. Novak, C.-L. Chang, G. J. Stein, D. Weerawarne, B. Shim, F. X. Kärtner, and K.-H. Hong, "Three-octave-spanning supercontinuum generation and sub-two-cycle self-compression of mid-infrared filaments in dielectrics," Opt. Lett. **40**, 1069–1072 (2015).
12. R. DeSalvo, H. Vanherzeele, D. J. Hagan, M. Sheik-Bahae, G. Stegeman, and E. W. Van Stryland, "Self-focusing and self-defocusing by cascaded second-order effects in KTP," Opt. Lett. **17**, 28–30 (1992).
13. G. I. Stegeman, D. J. Hagan, and L. Torner, "$\chi^{(2)}$ cascading phenomena and their applications to all-optical signal processing, mode-locking, pulse compression and solitons," Opt. Quantum Electron. **28**, 1691–1740 (1996).
14. K. Beckwitt, F. W. Wise, L. Qian, L. A. Walker, and E. Canto-Said, "Compensation for self-focusing by use of cascade quadratic nonlinearity," Opt. Lett. **26**, 1696–1698 (2001).
15. P. Di Trapani, A. Bramati, S. Minardi, W. Chinaglia, C. Conti, S. Trillo, J. Kilius, and G. Valiulis, "Focusing versus defocusing nonlinearities due to parametric wave mixing," Phys. Rev. Lett. **87**, 183902 (2001).
16. C. Conti, S. Trillo P. Di Trapani, J. Kilius, A. Bramati, S. Minardi, W. Chinaglia, and G. Valiulis, "Effective lensing effects in parametric frequency conversion," J. Opt. Soc. Am. B **19**, 852–859 (2002).
17. X. Liu, L. Qian, and F. Wise, "High-energy pulse compression by use of negative phase shifts produced by the cascade $\chi^{(2)}:\chi^{(2)}$ nonlinearity," Opt. Lett. **24**, 1777–1779 (1999).
18. S. Ashihara, J. Nishina, T. Shimura, and K. Kuroda, "Soliton compression of femtosecond pulses in quadratic media," J. Opt. Soc. Am. B **19**, 2505–2510 (2002).
19. X. Liu, L. J. Qian, and F. W. Wise, "Generation of optical spatiotemporal solitons," Phys. Rev. Lett. **82**, 4631–4634 (1999).
20. K. Krupa, F. Baronio, M. Conforti, S. Trillo, A. Tonello, and V. Couderc, "Zero focusing via competing nonlinearities in beta-barium-borate crystals," Opt. Lett. **39**, 925–928 (2014).
21. M. Conforti, F. Baronio, and C. De Angelis, "Modeling of ultrabroadband and single-cycle phenomena in anisotropic quadratic crystals," J. Opt. Soc. Am. B **28**, 1231–1237 (2011).
22. C. R. Phillips, C. Langrock, J. S. Pelc, M. M. Fejer, I. Hartl, and M. E. Fermann, "Supercontinuum generation in quasi-phasematched waveguides," Opt. Express **19**, 18754–18773 (2011).
23. B. B. Zhou, A. Chong, F. W. Wise, and M. Bache, "Ultrafast and octave-spanning optical nonlinearities from strongly phase-mismatched quadratic interactions," Phys. Rev. Lett. **109**, 043902 (2012).
24. M. Bache, H. Guo, and B. Zhou, "Generating mid-IR octave-spanning supercontinua and few-cycle pulses with solitons in phase-mismatched quadratic nonlinear crystals," Opt. Mater. Express **3**, 1647–1657 (2013).
25. B. Zhou, H. Guo, and M. Bache, "Energetic mid-IR femtosecond pulse generation by self-defocusing soliton-induced dispersive waves in a bulk quadratic nonlinear crystal," Opt. Express. **23**, 6924–6936 (2015).
26. B. Zhou and M. Bache, "Dispersive waves induced by self-defocusing temporal solitons in a beta-barium-borate crystal," Opt. Lett. **40**, 4257–4260 (2015).
27. N. K. M. N. Srinivas, S. S. Harsha, and D. N. Rao, "Femtosecond supercontinuum generation in a quadratic nonlinear medium (KDP)," Opt. Express **13**, 3224–3229 (2005).
28. R. S. S. Kumar, S. S. Harsha, and D. N. Rao, "Broadband supercontinuum generation in a single potassium di-hydrogen phosphate (KDP) crystal achieved in tandem with sum frequency generation," Appl. Phys. B **86**, 615–621 (2007).
29. L. Wang, Y. X. Fan, H. Zhu, Z. D. Yan, H. Zeng, H.-T. Wang, S. N. Zhu, and Z. L. Wang, "Broadband colored-crescent generation in a single $\beta$-barium-borate crystal by intense femtosecond pulses," Phys. Rev. A **84**, 063831 (2011).
30. J. Rolle, L. Bergé, G. Duchateau, and S. Skupin, "Filamentation of ultrashort laser pulses in silica glass and KDP crystals: A comparative study," Phys. Rev. A **90**, 023834 (2014).
31. M. Conforti and F. Baronio, "Extreme high-intensity and ultrabroadband interactions in anisotropic $\beta$-$BaB_2O_4$ crystals," J. Opt. Soc. Am. B **30**, 1041–1047 (2013).
32. K. Krupa, A. Labruyère, A. Tonello, B. M. Shalaby, V. Couderc, F. Baronio, and A. B. Aceves, "Polychromatic filament in quadratic media: spatial and spectral shaping of light in crystals," Optica **2**, 1058–1064 (2015).
33. I. Shoji, H. Nakamura, K. Ohdaira, T. Kondo, R. Ito, T. Okamoto, K. Tatsuki, and S. Kubota, "Absolute measurement of second-order nonlinear-optical coefficients of $\beta$-$BaB_2O_4$ for visible to ultraviolet second-harmonic wavelengths," J. Opt. Soc. Am. B **16**, 620–624 (1999).
34. R. C. Miller, "Optical second harmonic generation in piezoelectric crystals," Appl. Phys. Lett. **5**, 17–19 (1964).
35. D. Zhang, Y. Kong, and J.-Y. Zhang, "Optical parametric properties of 532-nm-pumped beta-barium-borate near the infrared absorption edge," Opt. Commun. **184**, 485–491 (2000)
36. M. Bache, H. Guo, B. Zhou, and X. Zeng, "The anisotropic Kerr nonlinear refractive index of the beta-barium borate ($\beta$-$BaB_2O_4$) nonlinear crystal," Opt. Mater. Express **3**, 357–382 (2013).
37. G. Valiulis, V. Jukna, O. Jedrkiewicz, M. Clerici, E. Rubino, and P. Di Trapani, "Propagation dynamics and X-pulse formation in phase-mismatched second-harmonic generation," Phys. Rev. A **83**, 043834 (2011).
38. B. Zhou, H. Guo, and M. Bache, "Soliton-induced nonlocal resonances observed through high-intensity tunable spectrally compressed second-harmonic peaks," Phys. Rev. A **90**, 013823 (2014).

# A2

# SECOND-ORDER CASCADING-ASSISTED FILAMENTATION AND CONTROLLABLE SUPERCONTINUUM GENERATION IN BIREFRINGENT CRYSTALS

**R. Šuminas**, G. Tamošauskas, G. Valiulis, V. Jukna,
A. Couairon, A. Dubietis

Opt. Express **25**, 6746–6756 (2017)

# Second-order cascading-assisted filamentation and controllable supercontinuum generation in birefringent crystals

ROSVALDAS ŠUMINAS,[1] GINTARAS TAMOŠAUSKAS,[1] VYTAUTAS JUKNA,[2] ARNAUD COUAIRON,[3] AND AUDRIUS DUBIETIS[1]

[1]*Department of Quantum Electronics, Vilnius University, Saulėtekio Avenue 10, LT-10223 Vilnius, Lithuania*
[2]*Laboratoire d'Optique Appliquée, ENSTA ParisTech, Ecole Polytechnique, Université Paris-Saclay, F-91762 Palaiseau, France*
[3]*Centre de Physique Théorique, CNRS, Ecole Polytechnique, Université Paris-Saclay, F-91128 Palaiseau, France*
*audrius.dubietis@ff.vu.lt

**Abstract:** We experimentally investigate filamentation and supercontinuum generation in a birefringent medium (BBO crystal), in the self-focusing regime where intrinsic cubic nonlinearity is either enhanced or reduced by the second-order cascading due to phase-mismatched second harmonic generation. We demonstrate that the supercontinuum spectral extent is efficiently controlled by varying the phase mismatch parameter. In the range of negative phase mismatch, we achieve full control of the blue-shifted spectral broadening, which is very robust and independent on the input pulse energy. In the range of positive phase mismatch, both the blue-shifted and the red-shifted spectral broadenings are controlled simultaneously, however showing a certain dependence on the input pulse energy. The results are interpreted in terms of complex interplay between the self-phase-matched second harmonic generation, which is a process inherent to narrow ultrashort pulsed laser beams and concurrent self-steepening processes which arise from cubic and cascaded-quadratic nonlinearities.



**OCIS codes:** (320.6629) Supercontinuum generation; (190.2620) Harmonic generation and mixing; (190.5940) Self-action effects; (190.7110) Ultrafast nonlinear optics.

## References and links

1. A. Couairon and A. Mysyrowicz, "Femtosecond filamentation in transparent media," Phys. Rep. **441**, 47–189 (2007).
2. A. Brodeur and S. L. Chin, "Ultrafast white-light continuum generation and self-focusing in transparent condensed media," J. Opt. Soc. Am. B **16**, 637–650 (1999).
3. C. Nagura, A. Suda, H. Kawano, M. Obara, and K. Midorikawa, "Generation and characterization of ultrafast white-light continuum in condensed media," Appl. Opt. **41**, 3735–3742 (2002).
4. M. Bradler, P. Baum, and E. Riedle, "Femtosecond continuum generation in bulk laser host materials with sub-$\mu$J pump pulses," Appl. Phys. B **97**, 561–574 (2009).
5. F. Silva, D. R. Austin, A. Thai, M. Baudisch, M. Hemmer, D. Faccio, A. Couairon, and J. Biegert, "Multi-octave supercontinuum generation from mid-infrared filamentation in a bulk crystal," Nature Commun. **3**, 807 (2012).
6. J. Darginavičius, D. Majus, V. Jukna, N. Garejev, G. Valiulis, A. Couairon, and A. Dubietis, "Ultrabroadband supercontinuum and third-harmonic generation in bulk solids with two optical-cycle carrier-envelope phase-stable pulses at 2 $\mu$m," Opt. Express **21**, 25210–25220 (2013).
7. H. Liang, P. Krogen, R. Grynko, O. Novak, C.-L. Chang, G. J. Stein, D. Weerawarne, B. Shim, F. X. KÃd'rtner, and K.-H. Hong, "Three octave-spanning supercontinuum generation and sub-two-cycle selfcompression of mid-infrared filaments in dielectrics," Opt. Lett. **40**, 1069–1072 (2015).
8. N. Garejev, G. Tamošauskas, and A. Dubietis, "Comparative study of multioctave supercontinuum generation in fused silica, YAG and LiF in the range of anomalous group velocity dispersion," J. Opt. Soc. Am. B **34**, 88–94 (2017).
9. A. Brodeur and S. L. Chin, "Band-gap dependence of the ultrafast white-light continuum," Phys. Rev. Lett. **80**, 4406–4409 (1998).
10. M. Kolesik, G. Katona, J. V. Moloney, and E. M. Wright, "Physical factors limiting the spectral extent and band gap dependence of supercontinuum generation," Phys. Rev. Lett. **91**, 043905 (2003).

11. N. L. Boling, A. J. Glass, and A. Owyoung, "Empirical relations for predicting nonlinear refractive index changes in optical solids," IEEE J. Quantum Electron. **14**, 601–608 (1978).
12. M. Sheik-Bahae, D. J. Hagan, and E. W. Van Stryland, "Dispersion and band-gap scaling of the electronic Kerr effect in solids associated with two-photon absorption," Phys. Rev. Lett. **65**, 96–99 (1990).
13. D. Schumacher, "Controlling continuum generation," Opt. Lett. **27**, 451–453 (2002).
14. J. A. Dharmadhikari, A. K. Dharmadhikari, K. Dota, and D. Mathur, "Influencing supercontinuum generation by phase distorting an ultrashort laser pulse," Opt. Lett. **40**, 241–244 (2015).
15. V. Kartazaev and R. R. Alfano, "Supercontinuum generated in calcite with chirped femtosecond pulses," Opt. Lett. **32**, 3293–3295 (2007).
16. A. Srivastava and A. Goswami, "Control of supercontinuum generation with polarization of incident laser pulses," Appl. Phys. B **77**, 325–328 (2003).
17. C. Romero, R. Borrego-Varillas, A. Camino, G. Mínguez-Vega, O. Mendoza-Yero, Juan Hernández-Toro, and J. R. Vázquez de Aldana, "Diffractive optics for spectral control of the supercontinuum generated in sapphire with femtosecond pulses," Opt. Express **19**, 4977–4984 (2011).
18. N. Kaya, J. Strohaber, A. A. Kolomenskii, G. Kaya, H. Schroeder, and H. A. Schuessler, "White-light generation using spatially-structured beams of femtosecond radiation," Opt. Express **20**, 13337–13346 (2012).
19. V. Jukna, J. Galinis, G. Tamošauskas, D. Majus, and A. Dubietis, "Infrared extension of femtosecond supercontinuum generated by filamentation in solid-state media," Appl. Phys. B **116**, 477–483 (2014).
20. K. Wang, L. Qian, H. Luo, P. Yuan, and H. Zhu, "Ultrabroad supercontinuum generation by femtosecond dual-wavelength pumping in sapphire," Opt. Express **14**, 6366–6371 (2006).
21. A. A. Kolomenskii, J. Strohaber, N. Kaya, G. Kaya, A. V. Sokolov, and H. A. Schuessler, "White-light generation control with crossing beams of femtosecond laser pulses," Opt. Express **24**, 282–293 (2016).
22. G. I. Stegeman, D. J. Hagan, and L. Torner, "$\chi^{(2)}$ cascading phenomena and their applications to all-optical signal processing, mode-locking, pulse compression and solitons," Opt. Quantum Electron. **28**, 1691–1740 (1996).
23. F. W. Wise and J. Moses, "Self-focusing and self-defocusing of femtosecond pulses with cascaded quadratic nonlinearities," Top. Appl. Phys. **114**, 481–506 (2009).
24. B. B. Zhou, A. Chong, F. W. Wise, and M. Bache, "Ultrafast and octave-spanning optical nonlinearities from strongly phase-mismatched quadratic interactions," Phys. Rev. Lett. **109**, 043902 (2012).
25. S. Ashihara, J. Nishina, T. Shimura, and K. Kuroda, "Soliton compression of femtosecond pulses in quadratic media," J. Opt. Soc. Am. B **19**, 2505-2510 (1999).
26. J. Moses and F. W. Wise, "Soliton compression in quadratic media: high-energy few-cycle pulses with a frequency-doubling crystal," Opt. Lett. **31**, 1881-1883 (2006).
27. M. Bache, H. Guo, and B. Zhou, "Generating mid-IR octave-spanning supercontinua and few-cycle pulses with solitons in phase-mismatched quadratic nonlinear crystals," Opt. Mater. Express **3**, 1647–1657 (2013).
28. B. Zhou and M. Bache, "Dispersive waves induced by self-defocusing temporal solitons in a beta-barium-borate crystal," Opt. Lett. **40**, 4257-4260 (2015).
29. B. Zhou and M. Bache, "Multiple-octave spanning mid-IR supercontinuum generation in bulk quadratic nonlinear crystals," APL Photon. **1**, 050802 (2016).
30. N. K. M. N. Srinivas, S. S. Harsha, and D. N. Rao, "Femtosecond supercontinuum generation in a quadratic nonlinear medium (KDP)," Opt. Express **13**, 3224–3229 (2005).
31. R. S. S. Kumar, S. S. Harsha, and D. N. Rao, "Broadband supercontinuum generation in a single potassium di-hydrogen phosphate (KDP) crystal achieved in tandem with sum frequency generation," Appl. Phys. B **86**, 615–621 (2007).
32. S. Akbar Ali, P. B. Bisht, A. Nautiyal, V. Shukla, K. S. Bindra, and S. M. Oak, "Conical emission in $\beta$-barium borate under femtosecond pumping with phase matching angles away from second harmonic generation," J. Opt. Soc. Am. B **27**, 1751–1756 (2010).
33. K. Krupa, A. Labruyère, A. Tonello, B. M. Shalaby, V. Couderc, F. Baronio, and A. B. Aceves, "Polychromatic filament in quadratic media: spatial and spectral shaping of light in crystals," Optica **2**, 1058–1064 (2015).
34. R. Šuminas, G. Tamošauskas, G. Valiulis, and A. Dubietis, "Spatiotemporal light bullets and supercontinuum generation in $\beta$-BBO crystal with competing quadratic and cubic nonlinearities," Opt. Lett. **41**, 2097–2100 (2016).
35. M. Bache, H. Guo, B. Zhou, and X. Zeng, "The anisotropic Kerr nonlinear refractive index of the beta-barium borate ($\beta$-$BaB_2O_4$) nonlinear crystal," Opt. Mater. Express **3**, 357–382 (2013).
36. G. Valiulis, V. Jukna, O. Jedrkiewicz, M. Clerici, E. Rubino, and P. Di Trapani, "Propagation dynamics and X-pulse formation in phase-mismatched second-harmonic generation," Phys. Rev. A **83**, 043834 (2011).
37. A. L. Gaeta, "Catastrophic collapse of ultrashort pulses," Phys. Rev. Lett. **84**, 3582–3585 (2000).
38. J. K. Ranka, R. W. Schirmer, and A. L. Gaeta, "Observation of pulse splitting in nonlinear dispersive media," Phys. Rev. Lett. **77**, 3783–3786 (1996).
39. A. Jarnac, G. Tamošauskas, D. Majus, A. Houard, A. Mysyrowicz, A. Couairon, and A. Dubietis, "Whole life cycle of femtosecond ultraviolet filaments in water," Phys. Rev. A **89**, 033809 (2014).
40. J. Moses and F. W. Wise, "Controllable self-steepening of ultrashort pulses in quadratic nonlinear media," Phys. Rev. Lett. **97**, 073903 (2006).
41. J. Moses, B. A. Malomed, and F. W. Wise, "Self-steepening of ultrashort optical pulses without self-phase-modulation," Phys. Rev. A **76**, 021802 (2007).

42. A. L. Gaeta, "Spatial and temporal dynamics of collapsing ultrashort laser pulses," Top. Appl. Phys. **114**, 399–411 (2009).
43. A. Couairon, E. Brambilla, T. Corti, D. Majus, O. de J. Ramírez-Góngora, and M. Kolesik, "Practitioner's guide to laser pulse propagation models and simulation," Eur. Phys. J. Special Topics **199**, 5–76 (2011).
44. B. Zhou, H. Guo, and M. Bache, "Soliton-induced nonlocal resonances observed through high-intensity tunable spectrally compressed second-harmonic peaks," Phys. Rev. A **90**, 013823 (2014).

## 1. Introduction

Supercontinuum (SC) generation is one of the most spectacular nonlinear optical phenomena arising from nonlinear propagation of intense ultrashort light pulses in transparent dielectric media. The physical picture of SC generation is fairly well understood in the framework of femtosecond filamentation, which is a complex process involving an intricate coupling between spatial and temporal effects [1]. In the time domain, the complex interplay between self-focusing, multiphoton absorption, self-phase modulation and group velocity dispersion leads to self-steepening of the pulse, which ends up with either pulse splitting in normally dispersive medium or pulse compression in the range of anomalous group velocity dispersion. These dramatic transformations take place at the vicinity of the nonlinear focus, beyond which they produce an explosive spectral broadening, termed SC generation, as observed in a variety of wide bandgap solid state media and with input pulse wavelengths ranging from the ultraviolet to the mid-infrared, see e.g. [2–8]. The spectral extent of the SC is defined essentially by the laser wavelength and by linear or nonlinear properties of the medium, such as the medium dispersion, the bandgap and the nonlinear index of refraction [9, 10], which possess fundamental mutual relationships [11, 12].

The rapidly expanding field of applications calls for achieving broadband radiation with desired temporal and spectral properties, which in turn require setting an efficient control of the filamentation process. Since the relevant parameters of an isotropic medium are generally fixed for a given input wavelength, a certain control of SC generation was demonstrated by tailoring the shape [13, 14] and the chirp [15] of the input pulse, by varying the polarization state [16], phase [17, 18] and the numerical aperture [19] of the input beam. More sophisticated methods are based on performing two color filamentation in collinear [20] and noncollinear [21] geometries.

However, the achieved degree of control of the SC spectrum is rather limited, and most of these methods require more or less complex technical implementation. In that regard, the use of birefringent nonlinear media, which possesses both, quadratic and cubic nonlinearities, may provide a desired degree of freedom to perform the nonlinear interactions in a fully controlled fashion. The second-order cascading, which results from the phase-mismatched second harmonic (SH) generation [22], produces a cascaded-quadratic Kerr-like nonlinearity, which contributes to the nonlinear index of refraction. Thus the light wave sees a material with an effective nonlinear index of refraction, $n_2^{\text{eff}} = n_2^{\text{Kerr}} + n_2^{\text{casc}}$, whose cascaded counterpart, $n_2^{\text{casc}} \propto -d_{\text{eff}}^2/\Delta k$, may be varied in sign and magnitude by setting an appropriate phase mismatch, $\Delta k = k_{2\omega} - 2k_{\omega}$. Therefore the interplay between the cascaded-quadratic and intrinsic cubic (Kerr) nonlinearities may be readily exploited to either enhance or suppress the nonlinear effects [23, 24] and to access qualitatively different regimes of nonlinear propagation.

The self-defocusing regime ($n_2^{\text{eff}} < 0$) is achieved within a certain range of positive phase mismatch, leading to spectral broadening and SC generation via formation of temporal soliton in the range of normal group velocity dispersion [25, 27–29, 40]. In contrast, the self-focusing regime ($n_2^{\text{eff}} > 0$) is achieved within a wide range of either positive or negative phase mismatch, leading to SC generation via filametation [30–32]. More recent experiments demonstrate the feasibility of the self-focusing regime for spatial, spectral and temporal shaping of light within a wide input parameter space, ranging from picosecond [33] to few optical cycle pulses [34].

In this paper we demonstrate that the second-order cascading assisted filamentation of 120 fs, 800 nm laser pulses in beta barium borate (BBO) crystal in the operating conditions of prevailing self-focusing nonlinearity, leads to SC generation with fully controllable spectral extent, which is achieved by varying the phase mismatch parameter for SH generation. We propose a physical interpretation based on the competition between the self-steepening due to Kerr nonlinearity and the phase mismatch-dependent nonlinear effects which arise from the second-order cascading: self-phase-matched SH generation and quadratic self-steepening.

## 2. Results and discussion

The experiments were performed using a commercial Ti:sapphire laser system (Spitfire-PRO, Newport-Spectra Physics) providing 120 fs, 800 nm laser pulses at a 500 Hz repetition rate. The input pulse energy was varied in the range of 50 nJ - 1 $\mu$J, which corresponds to a peak power range of $0.37-7.4$ $P_{cr}$, where $P_{cr} = 0.15\lambda_0^2/n_0 n_2^{Kerr} = 1.12$ MW is the critical power for self-focusing in BBO, with $n_0 = 1.66$ being the linear and $n_2^{Kerr} = 5.15 \times 10^{-16}$ cm$^2$/W the Kerr nonlinear refractive index [35]. The ordinarily polarized laser beam was focused by a $f = +125$ mm lens into a 25 $\mu$m FWHM focal spot located at the front face of a 4.85-mm-long BBO crystal cut for type I phase matching. The crystal was placed on a mechanical rotation stage, which allowed varying the angle $\theta$ between the incident beam and the optical axis of the crystal in the phase matching plane for SH generation. Rotation of the crystal permitted the control of the phase mismatch parameter $\Delta k$ in the positive and negative regions as shown in Fig. 1(a) as well as the effective nonlinear index of refraction, as illustrated in Fig. 1(b).

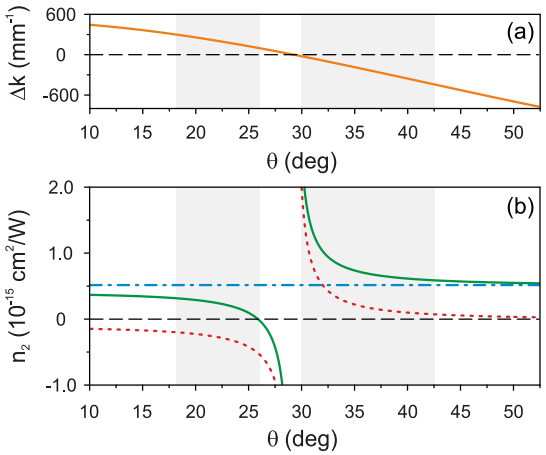


Fig. 1. (a) Calculated phase mismatch parameter $\Delta k$. (b) Nonlinear refractive indices: $n_2^{Kerr}$ (blue dash-dotted line), $n_2^{casc}$ (red dotted curve) and $n_2^{eff}$ (green solid curve) versus the angle $\theta$. Note the two available propagation regimes: self-defocusing, where $n_2^{eff} < 0$ and self-focusing, where $n_2^{eff} > 0$. The shaded areas mark the angle range where control of SC spectral extent was experimentally observed.

Figure 2 presents the experimental data of spectral broadening versus the angle $\theta$ in the range of negative phase mismatch for several input pulse energies. The spectral ranges of ordinarily (around the fundamental wavelength) and extraordinarily (around the SH wavelength) polarized spectral components are labelled as *o* and *e*, respectively. The measured dynamics immediately reveal a number of interesting features, associated with spectral broadenings at ordinary and

extraordinary polarizations.

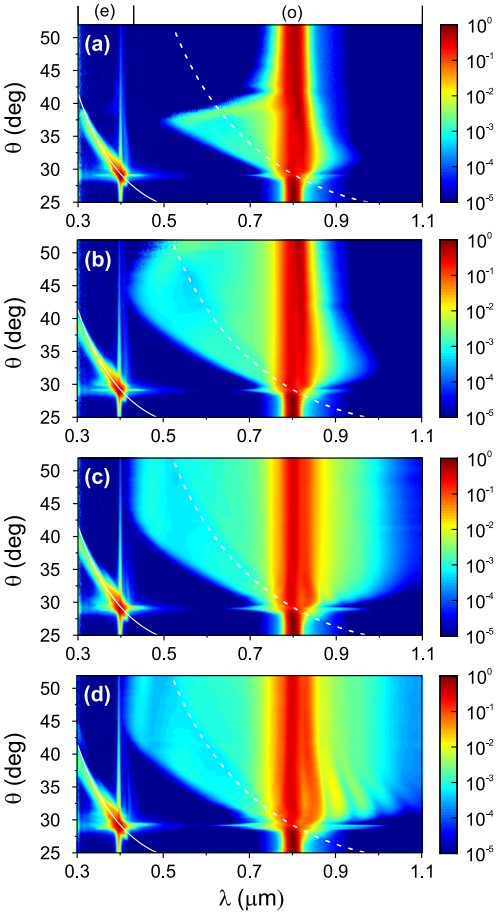


Fig. 2. Experimentally measured spectra as functions of angle $\theta$ with various input pulse energies: (a) 160 nJ, (b) 190 nJ, (c) 280 nJ, (d) 410 nJ. Each plot is composed of 110 individual spectra. The logarithmic intensity scale is used to highlight fine spectral features. The solid and dashed curves depict the self-phase matching curve for an axial SH component and the corresponding wavelengths in the spectrally broadened fundamental pulse, respectively.

First of all, at perfect phase matching for SH generation ($\theta = 29.2^\circ$), we capture a considerable spectral broadening around the SH (400 nm) and fundamental (800 nm) wavelengths. The nature of this phenomenon may be explained by filamentation of the SH beam itself. In fact, it is of no surprise considering efficient SH generation and bearing in mind the $\lambda_0^2$ dependence of the critical power for self-focusing. More precisely, with 45% energy conversion (see Fig. 3), the power of the SH pulse even with the input pulse energy of 160 nJ, well exceeds the critical power for self focusing, where $P_{\rm cr} = 0.23$ MW for $\lambda_0 = 400$ nm, with an account of an increased nonlinear index of refraction, $n_2^{\rm Kerr} = 6.3 \times 10^{-16}$ cm$^2$/W [35]. Hence filamentation of the SH

pulse leads to generation of the extraordinarily polarized SC, which spans from 300 to 610 nm and induces a considerable spectral broadening (from 650 nm to 1 $\mu$m) around the fundamental wavelength due to cross-phase modulation.

Secondly, we measure a complex spectrum of the extraordinarily polarized SH, which consists of two distinct peaks. The narrow spectral peak centered at exactly 400 nm is attributed to the phase mismatched SH, whose intensity rapidly drops as the crystal is rotated out of phase matching. The second peak is broader and much more intense and is tunable in the $300-400$ nm range. Its occurrence is attributed to the so-called self-phase matching (solid curves in Fig. 2), which is inherent to SH generation by narrow light beams carrying broadband pulses [36], and which is accessed by a certain range of spectral components (dashed curves in Fig. 2) present in a spectrally broadened fundamental pulse. Figure 3 shows the energy conversion efficiency to SH as a function of the angle $\theta$ for the input pulse energies of 160 nJ and 280 nJ. Here the total energy was estimated by the integration of the spectra presented in Figs. 2(a) and 2(c) over the entire $300-1100$ nm range, while the energy contained in the SH was estimated by the integration in the $300-450$ nm range. At the vicinity of phase matching, the SH energy was estimated by the integration over wider, $300-610$ nm spectral range, due to SC generation by the SH pulse. For $\theta > 32^\circ$, we may readily distinguish between the energy conversions to self-phase-matched SH (tunable in wavelength) and phase-mismatched SH (at 400 nm), as shown in the inset.

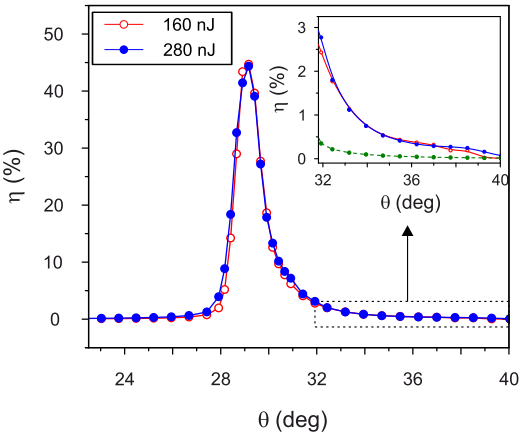


Fig. 3. The total second harmonic energy conversion efficiency as a function of the angle $\theta$ with the input pulse energies of 160 nJ (red solid curve) and 280 nJ (blue solid curve). The inset shows a magnified fraction of the graph, which distinguishes between the self-phase-matched and phase mismatched (green dashed curve) SH generation.

Thirdly, and most importantly, at the ordinary polarization, the spectral broadening around the carrier wavelength shows a qualitatively different behavior in the $\theta$ range above and below $42.5^\circ$. In the range of very large negative phase mismatch ($\theta > 42.5^\circ$) and for relatively low input pulse energies the spectral broadening is almost absent [Fig. 2(a)] or unstable, as seen from ragged blue-shifted edge of the SC spectrum in Fig. 2(b). At higher input pulse energies, a stable SC, which spans from 410 nm to 1.1 $\mu$m is generated, whose spectral extent is independent on the phase mismatch [Figs. 2(c) and 2(d)]. These results are rather obvious, since in this angle range the contribution of the cascaded second-order nonlinearity to the effective nonlinear index of refraction quickly vanishes, as seen from Fig. 1(b). Therefore for the input pulse energy of

160 nJ, its power just very slightly exceeds $P_{cr}$ and the beam is not able to self-focus within the crystal. For the input pulse energy of 190 nJ, the nonlinear focus is located very close to the output face of the crystal, resulting in unstable spectral broadening due to small fluctuations of laser pulse energy. Only with the input energies of 280 and 410 nJ a stable filamention regime is achieved.

However, the most striking behavior of the spectral broadening is observed in the $\theta$ range of $30^\circ - 42.5^\circ$. Here the extension of the blue-shifted part of the SC spectrum shows a very strong dependence on the angle $\theta$, while the extent of the red-shifted part is almost constant over the entire angle range, especially with higher input pulse energies, as seen in Figs. 2(c) and 2(d). The most fascinating feature of the SC spectrum is that its blue-shifted cut-off gradually extends to shorter wavelengths while varying angle $\theta$ from $30^\circ$ to $42.5^\circ$. Moreover, the cut-off wavelength is remarkably stable for a given crystal orientation and does not change with the input pulse energy, suggesting a complete control of the blue-shifted spectral extent of the SC via phase mismatch. This is illustrated in more detail in Fig. 4, which shows the cut-off wavelength (defined at the $10^{-4}$ intensity level) as a function of the input pulse energy for several values of angle $\theta$.

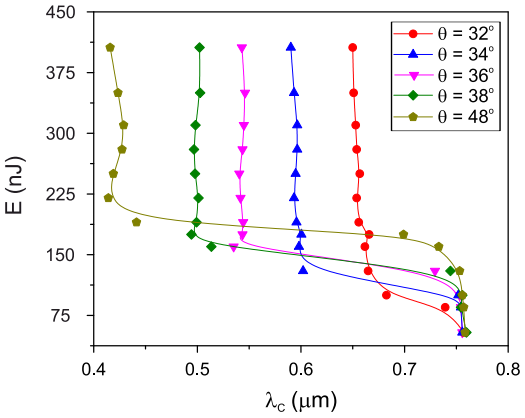


Fig. 4. The blue-shifted cut-off of the SC spectrum as a function of the input pulse energy and angle $\theta$.

In order to get more insight into the underlying phenomena, we consider the effects of pulse splitting and self-steepening, which play the key role in producing the spectral broadening in the filamentation regime [37, 38]. For that purpose we measured the axial cross-correlation functions of the SC pulses generated at several crystal orientations, which yield the SC spectra with different blue-shifted broadenings. The cross-correlation measurements were performed by sampling the output pulse with a short, 25-fs gating pulse at 700 nm from a noncollinear optical amplifier (Topas-White, Light Conversion Ltd) via sum-frequency generation in a thin (20 $\mu$m) BBO crystal.

The results presented in Fig. 5 confirm, that the pulse splitting is clearly detected over the entire range of angle $\theta$, where the spectral broadening takes place. For a fixed input pulse energy and different values of $\theta$, we capture the split sub-pulses at various stages of their evolution, in line with the whole evolution cycle of femtosecond filaments in the range of normal group velocity dispersion [39]. More precisely, as the pulse splitting event takes place at the nonlinear focus, a large part of the energy is expelled out of propagation axis, and thereafter with further propagation rebuilds the axial pulse at the center (at the zero delay). If its power exceeds the

critical power for self-focusing, the reconstructed pulse undergoes another self-focusing cycle with subsequent secondary splitting event.

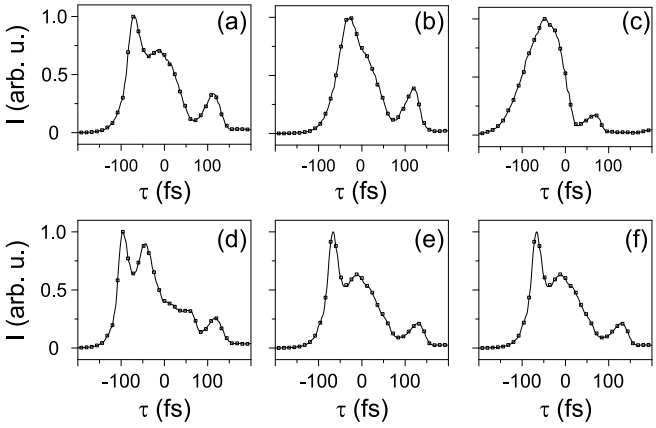


Fig. 5. The axial cross-correlation functions measured with two input pulse energies: 190 nJ (top row) and 280 nJ (bottom row) and at various angles $\theta$: (a),(d) 32.4°, (b),(e) 37.5°, (c),(f) 42.6°.

Indeed, the measured cross correlation functions confirm the above scenario in great detail, taking into account the inverse relationship between $n_2^{\text{eff}}$ and $\theta$ as shown in Fig. 1(b). As for the high values of $n_2^{\text{eff}}$, the nonlinear focus is located closer to the input face of the crystal, there remains a sufficient propagation distance to rebuild the axial pulse after the pulse splitting event, as shown in Fig. 5(a). In contrast, for the lower values of $n_2^{\text{eff}}$, only the split subpulses are measured, as the pulse splitting takes place closer to the output face of the crystal [Figs. 5(b) and 5(c)].

Similar considerations apply to the results shown in Figs. 5(d)-5(e), here however, due to higher input pulse energy, the nonlinear focus and so the pulse splitting event is shifted even closer to the input face of the nonlinear crystal, therefore the reconstructed pulse is present in all measurements. For the highest value of $n_2^{\text{eff}}$, we capture the splitting of the reconstructed pulse after the secondary nonlinear focus, as shown in Fig. 5(d). The secondary splitting produces periodic modulation in the SC spectrum due to temporally separated pairs of the sub-pulses at the leading and trailing edges. This is barely seen in Fig. 2(c) but clearly emerges in Fig. 2(d).

Therefore the cross-correlation measurements confirm the fundamental relationship between pulse splitting and SC generation. On the other hand, the spectral superbroadening is a direct consequence of self-steepening, and the spectral blue shift is associated with the self-steepening of the trailing front of the trailing sub-pulse [37]. The earlier studies of spectral broadening in the absence of filamentation demonstrated that quadratic self-steepening due to second-order cascading has a nearly identical effect as cubic self-steepening, with the additional property of being inversely proportional to the phase mismatch parameter $\Delta k$, and hence controllable in sign and magnitude [40, 41]. More precisely, in the range of relatively small negative phase mismatch (note the opposite sign in the definition of $\Delta k$ in [40]), the quadratic self-steepening is expected to amplify the effect of cubic self-steepening, giving rise to a considerable blue-shifted spectral broadening. However, our measurements presented in Fig. 2 show directly the opposite. Therefore, at this point we refer to the results of Fig. 3 and its inset in particular, which demonstrate that even at large phase mismatch, a still reasonable amount of the input pulse energy is converted into the self-phase-matched SH. More importantly, the blue-shift of

the self-phase-matched SH wavelength suggests that it is generated only by the trailing sub-pulse, whose carrier frequency is blue-shifted [42].

In order to estimate the energy fraction carried by the trailing sub-pulse, we performed the numerical simulation using a standard filamentation model in media with cubic nonlinearity, which is based on solving the paraxial unidirectional propagation equation with cylindrical symmetry for the nonlinear pulse envelope coupled with an evolution equation for the electron density generated by the high-intensity pulse [43]. The model simulated filamention as if the second-order nonlinear effects were absent, corresponding to the experimental situation far away from the phase matching. The numerical data show that a light filament with a 5 $\mu$m FWHM diameter emerges after 1.5 mm of propagation, and is immediately followed by an almost symmetric pulse splitting and SC generation. The energy balance is as follows: 18% of the input energy is lost due to five photon absorption and absorption by the free electron plasma, and the central core contains 14% of the remaining energy, so the trailing sub-pulse carries just 6% of the input pulse energy. Assuming the total energy conversion to the self-phase-matched SH of, e.g. 2.8% at $\theta = 32^\circ$ (as shown in the inset of Fig. 3), almost a half of the trailing sub-pulse energy is converted into the self-phase-matched SH.

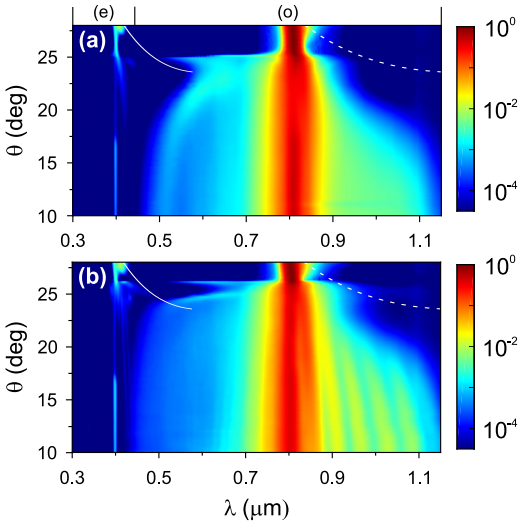


Fig. 6. Experimentally measured spectra in the range of positive phase mismatch with the input pulse energies of (a) 0.6 $\mu$J and (b) 1 $\mu$J. The curve designations are the same as in Fig. 2. A weak signal centered at 400 nm is the phase-mismatched SH.

Such an efficient conversion is due to the fact, that generation of self-phase-matched SH is group velocity matched with the pump as well, as the SH radiation takes the spatiotemporal shape of an X-wave, as demonstrated in [36]. As a result, the trailing sub-pulse undergoes a considerable energy loss and distortion, which counteracts the effect of both, quadratic and cubic self-steepenings, preventing the blue-shifted spectral broadening of the SC. As the energy conversion to self-phase-matched SH gradually drops with increasing $\theta$, the role of self-steepenings increases, resulting in larger blue-shift. Eventually, at very large $\Delta k$ ($\theta > 42.5^\circ$), the generation of self-phase-matched SH ceases completely, as well as the effect of quadratic self-steepening. Here the blue-shifted spectral broadening is entirely controlled by cubic self-steepening, yielding a constant blue-shifted extension of the SC. The above considerations are also supported

by the fact that the red-shifted leading sub-pulse has no self-phase matching, so the red-shifted extent of the SC is not affected and remains fairly constant over the entire $\Delta k$ range.

A different situation is then expected at positive phase mismatch, where self-phase matching is still possible [44], but within a reduced $\theta$ range, wherein the spectral components of the fundamental pulse satisfying the self-phase matching condition are absent and so no self-phase matched SH is generated. Figure 6 illustrates the spectral measurements in the $\theta$ range of $10-28^{\circ}$, which demonstrate markedly different dynamics of spectral broadening, which were measured with elevated input pulse energies of 0.6 $\mu$J and 1 $\mu$J as due to reduced values of $n_2^{\text{eff}}$, resulting from a negative contribution of $n_2^{\text{casc}}$ [see Fig. 1(b)]. More specifically, we observe the control of both, blue-shifted and red-shifted spectral broadenings in the $\theta$ angle range of $17-25^{\circ}$. This result may be explained by the competition between quadratic and cubic self-steepenings, which in the present case are of opposite signs [40], resulting in reduction of the overall self-steepening, acting on both, leading and trailing fronts of the sub-pulses. As the phase mismatch increases ($\theta$ decreases), the contribution of quadratic self-steepening gradually ceases leading to increased blue and red shifts of the SC spectrum. Eventually, for $\theta < 17^{\circ}$, the overall spectral extent of the SC becomes fairly constant, defined by the cubic self-steepening only. Finally, an interesting, yet unexplained spectral behavior accompanied by a considerable spectral broadening of a weak phase-mismatched SH is captured within a narrow $\theta$ range of around $\theta = 25^{\circ}$, which is close to the region of self-defocusing.

## 3. Conclusion

In conclusion, we demonstrated fully controllable SC generation with 120 fs, 800 nm laser pulses in BBO crystal in the regime of second-order cascading-assisted filamentation. We uncover that the control of the SC spectral extent stems from the complex interplay between the self-phase-matched second harmonic generation and self-steepening processes which arise from cubic and cascaded-quadratic nonlinearities, and which bring remarkably different contributions to the spectral broadening in the range of negative and positive phase mismatch. In particular, we show that in the range of negative phase mismatch, the blue-shifted spectral broadening and the short wavelength cut-off of the SC spectrum is fully controlled in the $410-700$ nm range by varying the phase mismatch parameter. The achieved spectral control is very robust in terms of the input pulse energy and is attributed to efficient generation of the self-phase-matched SH, which introduces a considerable energy loss and distortion of the trailing sub-pulse shape, counteracting the joint effect of cascaded-quadratic and cubic self-steepenings. In contrast, in the range of positive phase mismatch, where self-phase matched SH is absent and where the effective self-focusing nonlinearity is still prevailing, the control of the entire SC spectrum is demonstrated and is explained by the competition between the cubic and phase-mismatch-dependent cascaded-quadratic self-steepenings.

We also uncover a number of other interesting findings regarding the SH generation. In particular, we observe filamentation of the SH pulses at perfect phase matching, which leads to extraordinarily polarized SC, which spans from 300 nm to 610 nm and induces a considerable spectral broadening around the fundamental wavelength, ranging from 650 nm to 1 $\mu$m. In the range of negative phase mismatch, we also capture the self-phase-matched SH generation, which yields tunable ultraviolet radiation in the $300-400$ nm range.

We expect that the discovered mechanism of the spectral control is universal and could be applied to any nonlinear crystal possessing both quadratic and cubic nonlinearities, opening the route to perform ultrafast nonlinear interactions over a wide spectral range in a simple and fully controlled fashion.

## Funding

This research was funded by a grant No. APP-8/2016 from the Research Council of Lithuania.

# A3

# MULTI-OCTAVE SPANNING NONLINEAR INTERACTIONS INDUCED BY FEMTOSECOND FILAMENTATION IN POLYCRYSTALLINE ZNSE

**R. Šuminas**, G. Tamošauskas, G. Valiulis, V. Jukna,
A. Couairon, A. Dubietis

Appl. Phys. Lett. **110**, 241106 (2017)

# Multi-octave spanning nonlinear interactions induced by femtosecond filamentation in polycrystalline ZnSe

R. Šuminas,[1] G. Tamošauskas,[1] G. Valiulis,[1] V. Jukna,[2,3] A. Couairon,[3] and A. Dubietis[1,a)]
[1)] *Department of Quantum Electronics, Vilnius University, Saulėtekio Avenue 10, LT-10223 Vilnius, Lithuania*
[2)] *Laboratoire d'Optique Appliquée, ENSTA ParisTech, Ecole Polytechnique, Université Paris-Saclay, F-91762 Palaiseau, France*
[3)] *Centre de Physique Théorique, CNRS, Ecole Polytechnique, Université Paris-Saclay, F-91128 Palaiseau, France*

(Dated: 29 May 2017)

We report on filamentation and supercontinuum generation in polycrystalline ZnSe by intense femtosecond laser pulses whose center wavelength is tunable in the $1.5-2.4$ $\mu$m range. By varying the input pulse energy, single and multiple filamentation regimes were accessed, as verified by the measurements of near field intensity distributions. Along with supercontinuum generation, efficient simultaneous generation of broadband second, third and fourth harmonics is observed. We uncover that extremely efficient harmonics generation stems from randomly quasi phase matched three wave mixing processes, which are facilitated by filamentation of the input beam, as verified by the spectral and energy conversion dynamics, and by polarization measurements.

Nonlinear photonic crystals are the structures with spatially modulated quadratic nonlinearity[1] offering new possibilities to manipulate the nonlinear three wave interactions in a desired way. Varying the periodicity and dimensionality of the nonlinear photonic crystals enables all-optical control and shaping of the spatial, spectral, temporal and polarization properties of the light, finding numerous applications in photonics, contemporary nonlinear and quantum optics[2].

Naturally grown disordered polycrystalline materials consisting of a large number of single-crystal domains with random orientations, random shapes and random sizes, represent a particular class of nonlinear photonic crystals, often termed as random, or short-range order nonlinear photonic crystals. The so called "random quasi phase matching", which stems from the disorder of the nonlinear domains[3], greatly extends the fundamental limits of frequency conversion that are imposed by the phase mismatch between the interacting waves, without any additional adjustments[4]. In the random quasi phase matching process, the intensity of frequency up- or down-converted light grows linearly with the number of domains, regardless of the domain size and its dispersion[3,5,6]. Due to greatly relaxed phase matching conditions, random quasi phase matching allows phase matching conditions for any second-order (three wave interaction) process to be fulfilled, therefore enabling a broadband frequency conversion within a wide spectral range, with the limitations of the bandwidth being imposed just by the transparency window of the material, as demonstrated in dielectric polycrystalline materials with random distributions of ferroelectric domains, such as strontium barium niobate (SBN) and strontium tetraborate (SBO)[7–12], as well as in periodically poled crystals featuring non-ideal domain structure due to various defects[13,14].

Polycrystalline materials, such as zinc-blende semiconductors, appear as attractive nonlinear media in the mid-infrared spectral range. These materials are optically isotropic, but do not have a center of inversion as they belong to the point group $\bar{4}3$m, thereby possessing a nonzero second-order nonlinearity. In particular, polycrystalline zinc selenide (ZnSe) is a long-known nonlinear crystal for frequency conversion in the mid-infrared spectral range[15]. With the energy bandgap $E_g = 2.71$ eV, the transparency range of $0.5-20$ $\mu$m[16], reasonably high values of the second-order nonlinear coefficient $d_{36} = 25$ pm/V [17] and the nonlinear index of refraction $n_2 = 6\times10^{-15}$ cm$^2$/W [18], and relatively high optical damage threshold of 0.53 J/cm$^2$ (measured for 500 fs pulses at 1030 nm[19]), ZnSe owes an attractive set of optical properties for hosting the nonlinear interactions in the near- and mid-infrared spectral range.

To this end, a substantial enhancement of the second-order nonlinear effects due to the polycrystalline structure of ZnSe was reported in the second-harmonic[20,21], sum[22] and difference frequency[3,23–25] generation experiments. Simultaneous generation of odd and even harmonics up to sixth[26] and seventh[27] orders was observed with 3 $\mu$m and 3.5 $\mu$m pump wavelengths, respectively. Filamentation threshold in ZnSe was studied in the near-infrared spectral range[28], and broadband supercontinuum generation was observed in the multifilamentation regime with femtosecond mid-infrared laser pulses[29], although the authors of the latter works did not specify which, mono or poly crystalline version of ZnSe was used.

In this paper we investigate self-focusing of intense wavelength-tunable (in the $1.5-2.4$ $\mu$m range) femtosecond pulses in polycrystalline ZnSe, in the regimes of single and multiple filamentation. We observe a broadband supercontinuum emission in the infrared, which is accompanied by very efficient simultaneous generation of the second, third and fourth harmonics via randomly quasi-

[a)] Corresponding author: audrius.dubietis@ff.vu.lt

phase matched three wave mixing.

The experiment was performed using wavelength tunable (in the $1.5-2.4$ $\mu$m range) pulses with a duration of 100 fs from an optical parametric amplifier (Topas-Prime, Light Conversion Ltd.), which was pumped by an amplified Ti:sapphire laser system (Spitfire-PRO, Newport-Spectra Physics). The linearly polarized beam was focused using an achromatic f = +100 mm lens into 50 $\mu$m FWHM focal spot located at the front face of polycrystalline ZnSe sample with crystallite size of $50-70$ $\mu$m (the average crystallite size 60 $\mu$m).

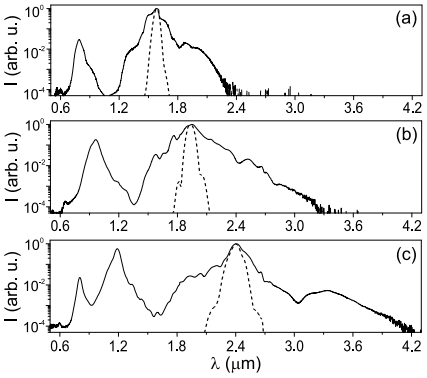


FIG. 1. The output spectra of 5 mm-long polycrystalline ZnSe sample, as generated with incident wavelengths: (a) $\lambda_i = 1.55$ $\mu$m, (b) $\lambda_i = 1.9$ $\mu$m, (c) $\lambda_i = 2.4$ $\mu$m. The input pulse energies are 1.25 $\mu$J, 1.9 $\mu$J and 3 $\mu$J, respectively. The input spectra are shown by dashed curves.

Figure 1 presents the measured spectra after a 5 mm-long ZnSe sample with three different input wavelengths of 1.55 $\mu$m, 1.9 $\mu$m and 2.4 $\mu$m, which were recorded with a homemade scanning prism spectrometer with calibrated Ge and PbSe photodetectors covering the effective $0.55-4.3$ $\mu$m range. The input pulse energy (1.25 $\mu$J, 1.9 $\mu$J and 3 $\mu$J) at each incident wavelength was chosen so as to keep a fairly constant ratio of the input power to the critical power for self-focusing ($\approx 50$). The chosen input wavelengths correspond to the incident photon energies of 0.8, 0.65 and 0.52 eV, so as to access the regimes of four, five and six photon absorption, respectively.

The measurements presented in Fig. 1 show how the spectral broadening around the carrier wavelength increases with increasing the incident wavelength, leading to an increase of spectral bandwidth of the infrared supercontinuum (SC), as might be expected from an increase of the multiphoton absorption order. Moreover, generation of the infrared SC is accompanied by broadband emissions at wavelengths, corresponding to laser harmonics. More specifically, broadband second harmonic (SH) emission centered at 775 nm is observed with $\lambda_i = 1.55$ $\mu$m [Fig. 1(a)]. With $\lambda_i = 1.9$ $\mu$m, along with generation of broadband second harmonic at 850 nm, a weak third harmonic (TH) peak at 633 nm becomes detectable [Fig. 1(b)]. With $\lambda_i = 2.4$ $\mu$m, broadband second and third harmonics at 1.2 $\mu$m and 800 nm, respectively, are accompanied by a small peak at 600 nm, which corresponds to fourth harmonic [Fig. 1(c)].

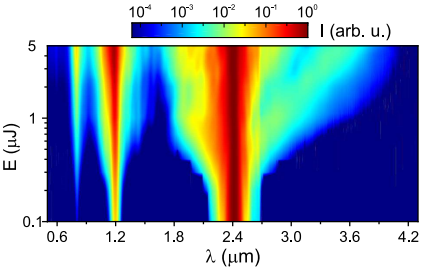


FIG. 2. Dynamics of spectral broadening of incident pulses at 2.4 $\mu$m in 5-mm-long ZnSe crystal versus energy. The logarithmic intensity scale is used to highlight fine spectral features.

To study the processes of SC and harmonics generation in more detail, we recorded the spectral dynamics versus the input pulse energy with a fixed input wavelength of 2.4 $\mu$m. The input pulse energy was varied in the range of 100 nJ - 5 $\mu$J, which corresponded to a peak power range of $1.7-84.7$ $P_{\rm cr}$, where $P_{\rm cr} = 0.59$ MW is the estimated critical power for self-focusing in ZnSe at 2.4 $\mu$m. The results are shown in Fig. 2 and capture three distinct propagation regimes.

No filamentation is detected for a range of the input pulse energies below 300 nJ, despite the fact that the input power slightly exceeds $P_{\rm cr}$. The absence of filamentation could be explained by the energy loss due to intrinsic absorption of ZnSe (70% transmission for 5 mm crystal over the entire transparency range) and in part due to imprecise knowledge of $n_2$, as its value in the literature is given for a more than twice shorter wavelength[18]. However, in this propagation regime we clearly detect intense spectral peaks of second and third harmonics at 1.2 $\mu$m and 800 nm, respectively, which also contribute to the energy loss and depletion of the incident radiation.

The emergence of the filament is manifested by the spectral broadening around the carrier wavelength, which gives rise to generation of the infrared SC, whose blue shift saturates at $\sim 1.7$ $\mu$m for the input pulse energies higher than 0.6 $\mu$J, as due to the combined actions of the dispersion landscape and intensity clamping[30]. Measurements of the near field intensity profile of the output beam indicated a single filament with central core FWHM diameter of 16 $\mu$m, surrounded by a character-

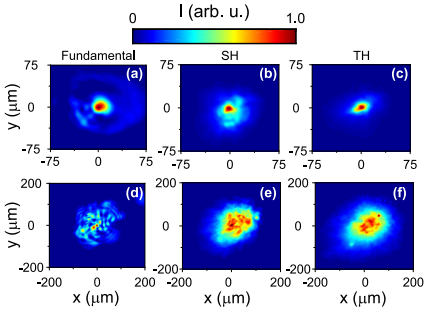


FIG. 3. Near field intensity distributions at the output of 5-mm-long ZnSe crystal, as measured in the single (top row) and multiple (bottom row) filamentation regimes with the input pulse energies of 500 nJ and 3 $\mu$J, respectively: (a),(d) fundamental beam at 2.4 $\mu$m, (b),(e) SH at 1.2 $\mu$m, and (c),(f) TH at 0.8 $\mu$m.

istic ring-shaped periphery, as shown in Fig. 3(a). The central core carries approximately 25% of the beam energy, while the rest of the energy is distributed in the beam periphery, as obtained by integration of the near and far field intensity distributions presented in Figs. 3(a) and 4(a), respectively. The light filament of that size perfectly fits into the area of a single crystallite and so the SH and TH beams [Figs. 3(b) and 3(c)]. The dimensions of SH and TH beams are bounded to the filament size, demonstrating that efficient SH and TH generation and their spectral broadenings are tightly linked to filamentation of the input beam. As a result, SH and TH beams exhibit high spatial coherence, in contrast to diffuse light and speckle patterns of harmonics emission as generated by extended laser beams[22,31,32].

With an increase of the input pulse energy above 1 $\mu$J, we access the regime of multiple filamentation; examples of the near field intensity distributions of fundamental, SH and TH beams at the crystal output are shown in Figs. 3(d)-3(f). In the multiple filamentation regime, the SC spectrum still exhibits a progressive red-shifted broadening that extends up to 4.2 $\mu$m, as well as further (predominantly, red-shifted) broadening of the SH and TH spectra. Eventually, with the occurrence of a weak fourth harmonic peak at 600 nm, whose wavelength falls to the short wave detection edge of our spectrometer, the overall spectral width of the output radiation spans the wavelength range from 600 nm to 4.2 $\mu$m.

Figure 4 shows the infrared conical emission patterns in the far field around the incident wavelength (2.4 $\mu$m), in the regimes of single and multiple filamentation, as captured with bolometric DataRay camera at the focal plane of f = +40 mm achromatic lens. In the multiple filamentation regime, the output beam is composed of multiple

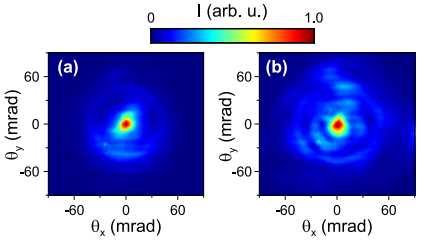


FIG. 4. Far-field images of the conical emission as recorded around the incident wavelength (2.4 $\mu$m) in the regimes of (a) single and (b) multiple filamentation.

irregular spots, representing the individual filaments, as seen in Fig. 3(d). As multiple filaments represent a dynamic structure in terms of intensity distribution in the transverse plane, integration of the far field profile shown in Fig. 4(b) yielded almost twice less fraction of the energy localized along the beam axis, as compared to the case of a single filament.

At a first glance, the observed spectral dynamics and characteristic spectral features are somewhat reminiscent to the process of odd harmonics-enhanced SC generation in isotropic solid state medium[33], however, in what follows we demonstrate that in the present case the underlying mechanism of harmonics generation is substantially different and relies on randomly quasi phase matched three wave mixing. Harmonic generation via random quasi phase matching due to the polycrystalline structure of ZnSe poses a number of specific signatures, which were verified by the measurements of harmonics spectral content, polarization and conversion efficiency.

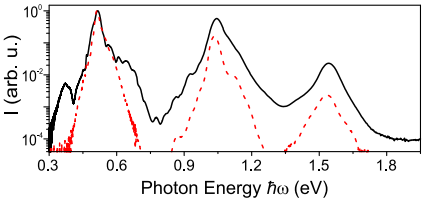


FIG. 5. Supercontinuum and harmonics spectra recorded with incident wavelength of 2.4 $\mu$m in single (dashed curve) and multiple (solid curve) filamentation regimes, with the input pulse energies of 500 nJ and 3 $\mu$J, respectively.

Figure 5 compares the output spectra as recorded in the single (red curve) and multiple (black curve) filamentation regimes shown in Fig. 3 and presented in the energy scale. The spectral shapes of SH and TH appear as almost exact replicas of the spectrally broadened fun-

damental pulse, as due to largely relaxed random quasi phase matching conditions stemming from the disorder in orientations of the individual crystallites, that support frequency conversion over very large bandwidths, see e.g.[7–10]. Similar considerations may be readily applied also to the spectral shapes of fourth, fifth and sixth harmonics, which were reported elsewhere with incident pulses of longer wavelengths[26,27].

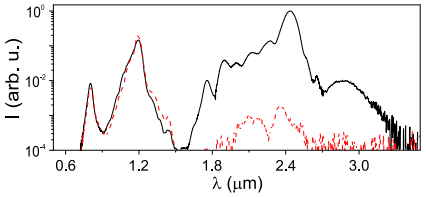


FIG. 6. Transmitted spectra after Glan-Taylor prism polarizer at parallel (solid curve) and perpendicular (dashed curve) polarization with respect to the incident polarization of 2.4 $\mu$m input pulses.

Random orientations of the individual crystallites also result in generation of unpolarized harmonics. The unpolarized (or randomly polarized) SH was already noticed in the very first application of polycrystalline ZnSe for frequency doubling of $CO_2$ laser[15]. In fact, it comes as no surprise as a result of $\bar{4}3$m crystal symmetry, which sets equal non-vanishing second-order nonlinear-optical coefficients $d_{xyz} = d_{zxy} = d_{yzx} = d_{36}$ thereby providing equal contributions to harmonics generation process. Figure 6 presents the polarization analysis of the output spectra, as performed using broadband polarizer (Glan-Taylor prism made of $YVO_4$), that was aligned to transmit either parallel (black curve) or perpendicular (red curve) polarization with respect to the incident polarization. Our measurement confirms that both, second and third harmonics are randomly polarized, whereas the infrared SC retains the linear polarization that coincides with that of the incident beam.

Finally, the intensities of fields generated by random quasi phase matching process are expected to be linear functions of the sample thickness, as demonstrated in the cases of difference frequency[3] and second harmonics[6] generation. Therefore we measured the output energy fractions contained in SH and TH as functions of the propagation distance $z$ and number of crystallites $N$ in the beam (filament) path by using three ZnSe samples of different length (3 mm, 5 mm and 10 mm). The conversion to SH and TH was retrieved by the integration of spectra shown in Fig. 2, in the energy range of $0.3-1$ $\mu$J, which mostly refers to a single filament regime, where the spectral broadenings around the incident wavelength (the infrared SC) and the individual harmonics do not overlap and spectral intervals corresponding to fundamental, SH and TH could be easily distinguished. The

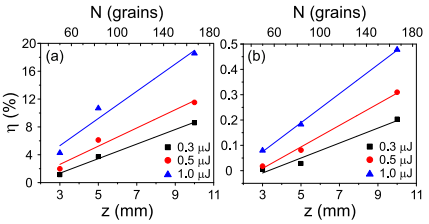


FIG. 7. Output energy fractions contained in (a) second and (b) third harmonics as functions of ZnSe sample thickness $z$ and average number of crystallites $N$ as measured with the incident wavelength of 2.4 $\mu$m.

results shown in Fig. 7 confirm the linear trends of energy conversion into SH and TH, which are very much in line with the nature of random quasi phase matching process. Moreover, extremely high conversion to the harmonics, and to SH in particular (19%), are achieved due to filamentary propagation which ensures high peak intensity within a filament, which serves as a narrow and intense pump beam.

In conclusion, we studied self-focusing and filamentation of $1.5-2.4$ $\mu$m tunable femtosecond pulses in polycrystalline ZnSe. In particular, with 2.4 $\mu$m incident wavelength, we generated infrared SC accompanied by broadband emissions at second, third and fourth harmonics, providing the total spectral coverage from 600 nm to 4.2 $\mu$m, that corresponds to 2.8 optical octaves. Spectral features, polarization properties and linear energy trends prove that harmonics are generated via simultaneous randomly quasi phase matched three-wave mixing processes due to nonvanishing quadratic nonlinearity of the crystal. Extremely high conversion to broadband SH and TH (19% and 0.5%, respectively) is achieved due to filamentary propagation. Summarizing the above, polycrystalline ZnSe shares the properties of both, isotropic nonlinear material and random nonlinear photonic crystal, opening intriguing perspectives in the rapidly developing field of ultrafast mid-infrared nonlinear optics.

This research was funded by a grant No. APP-8/2016 from the Research Council of Lithuania.

[1]V. Berger, Phys. Rev. Lett. **81**, 4136 (1998).
[2]A. Arie and N. Voloch, Laser Photon. Rev. **4**, 355 (2010).
[3]M. Baudrier-Raybaut, R. Haïdar, Ph. Kupecek, Ph. Lemasson, and E. Rosencher, Nature **432**, 374 (2004).
[4]S. E. Skipetrov, Nature **432**, 285 (2004).
[5]E. Yu. Morozov, A. A. Kaminskii, A. S. Chirkin, and D. B. Yusupov, JETP Lett. **73**, 647 (2001).
[6]X. Vidal and J. Martorell, Phys. Rev. Lett. **97**, 013902 (2006).
[7]R. Fischer, S. M. Saltiel, D. N. Neshev, W. Krolikowski, and Yu. S. Kivshar, Appl. Phys. Lett. **89**, 191105 (2006).
[8]W. Wang, V. Roppo, K. Kalinowski, Y. Kong, D. N. Neshev, C. Cojocaru, J. Trull, R. Vilaseca, K. Staliunas, W. Krolikowski, S. M. Saltiel, and Yu. Kivshar, Opt. Express **17**, 20117 (2009).
[9]L. Mateos, P. Molina, J. F. Galisteo-Lopez, C. Lopez, L. E. Bausa, and M. O. Ramirez, Appl. Phys. Lett. **103**, 101101 (2013).

[10]A. S. Aleksandrovsky, A. M. Vyunishev, A. I. Zaitsev, and V. V. Slabko, Phys. Rev. A **82**, 055806 (2010).
[11]A. S. Aleksandrovsky, A. M. Vyunishev, A. I. Zaitsev, and V. V. Slabko, Appl. Phys. Lett. **103**, 251104 (2013).
[12]P. Trabs, F. Noack, A. S. Aleksandrovsky, A. I. Zaitsev, and V. Petrov, Opt. Lett. **41**, 618 (2016).
[13]S. Stivala, A. C. Busacca, A. Pasquazi, R. L. Oliveri, R. Morandotti, and G. Assanto, Opt. Lett. **35**, 363 (2010).
[14]C.-Y. Yang, C. Lin, C. Liljestrand, W.-M. Su, C. Canalias, and C.-S. Chuu, Sci. Rep. **6**, 26079 (2016).
[15]C. K. N. Patel, Phys. Rev. Lett. **16**, 613 (1966).
[16]M. J. Weber, *Handbook of optical materials* (CRC, 2003).
[17]H. P. Wagner, M. Kühnelt, W. Langbein, and J. M. Hvam, Phys. Rev. B **58**, 10494 (1998).
[18]T. D. Krauss and F. W. Wise, Appl. Phys. Lett. **65**, 1739 (1994).
[19]L. Gallais and M. Commandré, Appl. Opt. **53**, A186 (2014).
[20]L. O. Hocker and C. F. Dewey Jr., Appl. Phys. Lett. **28**, 267 (1976).
[21]R. R. Alfano, Q. Z. Wang, T. Jimbo, P. P. Ho, R. N. Bhargava, and B. J. Fitzpatrick, Phys. Rev. A **35**, 459 (1987).
[22]T. D. Chinh, W. Seibt, and K. Siegbahn, J. Appl. Phys. **90**, 2612 (2001).
[23]C. F. Dewey Jr. and L. O. Hocker, Appl. Phys. Lett. **26**, 442 (1975).
[24]R. Haïdar, A. Mustelier, Ph. Kupecek, E. Rosencher, R. Triboulet, Ph. Lemasson, and G. Mennerat, J. Appl. Phys. **91**, 2550 (2002).
[25]A. Mustelier, E. Rosencher, Ph. Kupecek, A. Godard, M. Baudrier, M. M. Poulat, G. Mennerat, C. Pasquer, and Ph. Lemasson, Appl. Phys. Lett. **84**, 4424 (2004).
[26]G. M. Archipovaite, S. Petit, J.-C. Delagnes, and E. Cormier, Opt. Lett. **42**, 891 (2017).
[27]A. H. Chin, O. G. Calderón, and J. Kono, Phys. Rev. Lett. **86**, 3292 (2001).
[28]M. Durand, A. Houard, K. Lim, A. Durécu, O. Vasseur, and M. Richardson, Opt. Express **22**, 5852 (2014).
[29]O. Mouawad, P. Béjot, F. Billard, P. Mathey, B. Kibler, F. Désévédavy, G. Gadret, J.-C. Jules, O. Faucher, and F. Smektala, Opt. Mater. **60**, 355 (2016).
[30]M. Kolesik, G. Katona, J. V. Moloney, and E. M. Wright, Phys. Rev. Lett. **91**, 043905 (2003).
[31]F. J. Rodríguez, C. Yao, J. L. Domínguez-Juárez, J. Bravo-Abad, and J. Martorell, Opt. Lett. **36**, 1347 (2011).
[32]C. Yao, F. J. Rodríguez, and J. Martorell, Opt. Lett. **37**, 1676 (2012).
[33]N. Garejev, V. Jukna, G. Tamošauskas, M. Veličkė, R. Šuminas, A. Couairon, and A. Dubietis, Opt. Express **24**, 17060 (2016).

# A4

# FILAMENTATION-FREE SELF-COMPRESSION OF MID-INFRARED PULSES IN BIREFRINGENT CRYSTAL WITH SECOND-ORDER CASCADING-ENHANCED SELF-FOCUSING NONLINEARITY

**R. Šuminas**, G. Tamošauskas, A. Dubietis

Opt. Lett. **43**, 235–238 (2018)

# Filamentation-free self-compression of mid-infrared pulses in birefringent crystals with second-order cascading-enhanced self-focusing nonlinearity

ROSVALDAS ŠUMINAS*, GINTARAS TAMOŠAUSKAS , AND AUDRIUS DUBIETIS

*Laser Research Center, Vilnius University, Saulėtekio Avenue 10, LT-10223 Vilnius, Lithuania*
**Corresponding author: rosvaldas.suminas@ff.stud.vu.lt*

*Compiled December 7, 2017*

**We experimentally demonstrate virtually lossless, filamentation-free and energy-scalable more than three-fold self-compression of mid-infrared laser pulses at 2.1 $\mu$m in a birefringent medium ($\beta$-BBO crystal), which stems from favorable interplay between the second-order cascading-enhanced self-phase modulation and anomalous group velocity dispersion. By choosing an appropriate input beam diameter and intensity, the self-compression down to sub-30 fs pulse widths with GW peak power is achieved without the onset of beam filamentation and associated nonlinear losses due to the multiphoton absorption, yielding the energy throughput greater than 86%.**



***OCIS codes:*** (190.2620) Harmonic generation and mixing; (320.5520) Pulse compression; (320.7110) Ultrafast nonlinear optics.

http://dx.doi.org/10.1364/ao.XX.XXXXXX

Pulse compression based on increasing the spectral bandwidth via self-phase modulation (SPM) in a bulk solid-state medium beyond the bandwidth supported by laser or optical parametric amplifiers and subsequent removal of the frequency modulation by using an appropriate dispersive delay line, represents a simple and robust method for obtaining few optical cycle pulses [1, 2]. This pulse compression technique works well with femtosecond and sub-picosecond pulses [3, 4], and provides a possibility to scale the energy [5–7] and wavelength [8, 9] of the compressed pulses.

Even more simple and thus very attractive approach for extracavity pulse compression makes use of the spectral broadening in bulk solid-state media featuring anomalous group velocity dispersion (GVD). Here in contrast, no additional dispersive elements to compensate frequency modulation are required: the job is done by the anomalous GVD of the medium itself. To this end, self-compression is demonstrated at various stages of filamentation in transparent dielectric [10–15] and semiconductor [16] media, however, at the cost of the energy losses due to multiphoton and plasma absorption and reshaping of the beam, so the self-compressed pulse carries just a relatively small fraction of the incident energy [17].

A more practical realization of the anomalous GVD-induced self-compression regime, referred as soliton compression, relies upon using a shorter nonlinear medium and a larger input beam, extracting the self-compressed pulse before the catastrophic self-focusing and filamentation regime sets in. Numerical simulations suggest that filamentation-free self-compression could yield pulse widths approaching a single optical cycle and could be scaled in wavelength and energy, as long as one dimensional dynamics of the input pulse are maintained [18–23]. To date, soliton compression was experimentally demonstrated with microjoule [24] and milijoule [25] input pulse energies in the $3-4$ $\mu$m wavelength range, yielding self-compressed pulses with homogenous spatial profiles and durations of sub-three optical cycles.

Ultrafast Kerr-like nonlinearity in birefringent crystals that arises from the second-order cascading due to phase-mismatched second harmonic (SH) generation, is exploited to either enhance or suppress the nonlinear effects and so to access qualitatively different regimes of nonlinear propagation (self-focusing, self-defocusing or zero focusing) by varying the phase mismatch parameter [26]. To this end, soliton compression was demonstrated in the self-defocusing regime, where negative effective nonlinearity imprints a frequency modulation that is compressible by the normal GVD of the medium [27–29]. Such soliton compression regime could be attained in a variety of nonlinear crystals [30] producing ultrabroadband supercontinuum [31] and allowing scaling of energy [32] and average power [33] of the self-compressed pulses. In contrast, in the self-focusing regime in the range of normal GVD, second-order cascading was exploited to achieve large scale spectral broadening [34] and to control the filamentation dynamics [35] and spectral extent of supercontinuum [36], while in the range of anomalous GVD, generation of self-compressed spatiotemporal light bullets [37] and cross-polarized supercontinuum [38] was reported.

In this paper we experimentally demonstrate controllable self-compression of mid-infrared laser pulses in $\beta$-BBO crystal, that stems from the interplay between the SPM, which is enhanced by the second-order cascading-induced self-focusing nonlinearity,

and anomalous GVD. Favorable conditions for self-compression and energy scaling of the self-compressed pulses are demonstrated in the absence of self-focusing and filamentation of the input beam.

The experiment was performed using linearly polarized idler pulses with a central wavelength of 2.1 $\mu$m, duration of 68 fs and an energy of 73 $\mu$J from a commercial optical parametric amplifier (Topas-C, Light Conversion Ltd.), which was pumped by a regeneratively amplified Ti:sapphire laser system (Spitfire PRO, Newport-Spectra Physics). The incident wavelength was chosen so as to fall into the anomalous GVD range of $\beta$-BBO crystal, whose zero GVD point is at 1.49 $\mu$m and where the crystal absorption is still reasonably small. The input beam of 2.7 mm FWHM diameter was focused using a $f = 250$ mm fused silica lens onto a 5.5 mm thick $\beta$-BBO crystal cut for type-I phase matching ($\theta = 24.3^\circ$, $\phi = 90^\circ$), which was mounted on a combined stage allowing independent rotation and translation of the crystal. The crystal position $z$ with respect to the geometric focus ($z = 0$ cm) was translated along the beam propagation path, providing control over the input beam diameter and intensity. Simultaneously, the rotation of the crystal permitted fine adjustment of the angle $\theta$ between the input beam and the optical axis of the crystal, allowing us to control the effective nonlinear index of refraction. Figure 1(a) shows the calculated effective nonlinear refractive index $n_2^{\text{eff}} = n_2^{\text{casc}} + n_2^{\text{Kerr}}$ as a function of the angle $\theta$. An estimate of the Kerr nonlinear refractive index $n_2^{\text{Kerr}} = 4.44 \times 10^{-16}$ cm$^2$/W was obtained using the wavelength independent Miller's delta $\Delta_{1111} = 52.8 \times 10^{-24}$ m$^2$/V$^2$ [39], whereas the cascaded counterpart was evaluated using the standard cascaded approximation $n_2^{\text{casc}} \propto -\frac{d_{\text{eff}}^2}{\Delta k}$ [39], where $\Delta k = k_{2\omega} - 2k_\omega$ is the phase mismatch parameter and $d_{\text{eff}} = d_{31}\sin\theta - d_{22}\cos\theta\sin(3\phi)$ is the quadratic effective nonlinear coefficient. The quadratic nonlinear coefficients $|d_{22}| = 2.2$ pm/V and $|d_{31}| = 0.04$ pm/V [40] were scaled to 2.1 $\mu$m by applying Miller's rule [41] and the Sellmeier equations [42].

The output beam was collimated using a concave Al-coated mirror with a curvature radius of $R = -450$ mm and directed for further characterization. The temporal intensity profiles were retrieved from the sum-frequency generation-based frequency-resolved optical gating (SFG-FROG) measurements using 19 fs, 707 nm reference pulses from a SH-pumped noncollinear optical parametric amplifier (Topas-White, Light Conversion Ltd.). The output pulse spectra were measured using a home-built scanning prism spectrometer with a PbSe detector. The energy transmission and SH generation efficiency measurements were performed using an energy meter (Ophir) with a pyroelectric detector (PE9-SH).

Temporal and spectral dynamics of 68 fs, 73 $\mu$J pulses in $\beta$-BBO crystal located at 7.7 cm before the geometric focus ($z = -7.7$ cm, FWHM beam diameter at the input face 1.03 mm, intensity 84 GW/cm$^2$) versus the angle $\theta$ are presented in Figs. 1(b) and 1(c), respectively. These measurements reveal complex spectral dynamics, which emerge along with the effects of either self-compression or temporal broadening of the pulse.

For the crystal angles $\theta > \theta_{\text{pm}}$, significant pulse self-compression, accompanied by a considerable SPM-induced spectral broadening, is observed. The pulse self-compression occurs due to favorable interplay between the large positive SPM and the anomalous GVD of the nonlinear medium, the balance between which determines the duration of the self-compressed pulse. The most favorable conditions for self-compression, with

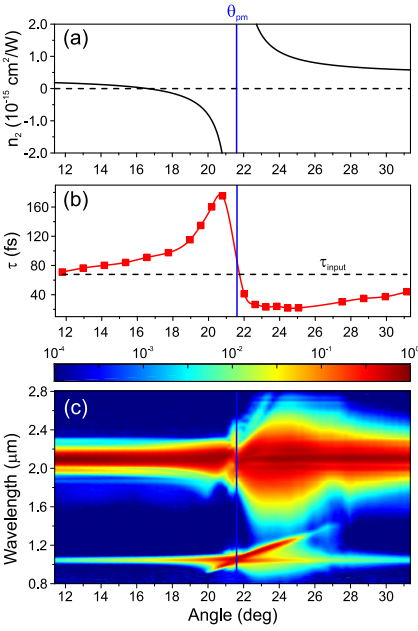


**Fig. 1.** (a) The effective nonlinear refractive index $n_2^{\text{eff}}$ as estimated using the cascaded approximation, (b) temporal and (c) spectral dynamics versus the angle $\theta$ in a 5.5 mm thick $\beta$-BBO crystal located at $z = -7.7$ cm. The input pulse duration is 68 fs, energy 73 $\mu$J. Vertical lines indicate the perfect phase matching angle $\theta_{\text{pm}} = 21.6^\circ$ for SH generation.

the largest spectral broadening and retrieved pulse durations of less than 30 fs are found in the angle range of $22.5^\circ < \theta < 25^\circ$. However, a further increase of the angle $\theta$ leads to a gradual reduction of the spectral bandwidth due to diminishing effect of the SPM, therefore resulting in a steady increase of the retrieved pulse width. Figure 2 shows the SFG-FROG traces and spectra of the input and self-compressed pulses and compares the retrieved intensity profiles and phases of both pulses at the maximum self-compression angle $\theta_{\text{opt}} = 24.5^\circ$ ($n_2^{\text{eff}} = 10 \times 10^{-16}$ cm$^2$/W). The pulse exhibits more than three-fold self-compression from 68 fs to 22 fs, which is equivalent to 3.1 optical cycles, and was retrieved within grid size of $256 \times 256$ pixels and a FROG trace reconstruction error of 0.5%.

In contrast, for the crystal angles $\theta < \theta_{\text{pm}}$, only temporal broadening of the pulse is observed and is attributed to two distinct modes of propagation. In the self-defocusing regime, in the angle range of $16.6^\circ < \theta < 21^\circ$, where $n_2^{\text{eff}} < 0$, the pulse experiences negative SPM, which in combination with anomalous GVD leads to a considerable increase of the pulse duration. Approaching the angle of zero focusing ($\theta_{zf} = 16.6^\circ$),

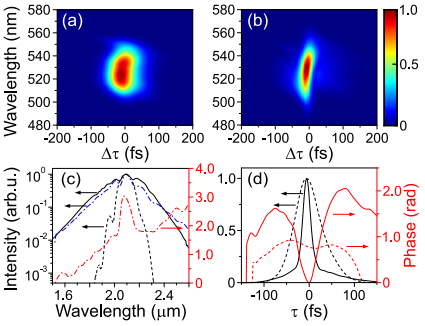


**Fig. 2.** Self-compression of 68 fs, 73 $\mu$J pulses at 2.1 $\mu$m down to 22 fs in a $\beta$-BBO crystal located at $z = -7.7$ cm: the measured SFG-FROG traces of (a) input and (b) self-compressed ($\theta_{opt} = 24.5°$) pulses, (c) measured (solid curve) and retrieved spectra and spectral phase (dash-dotted curves), (d) retrieved intensity profile and phase of the self-compressed pulse. Dashed curves in (c) and (d) show the spectrum, intensity profile and phase of the input pulse.

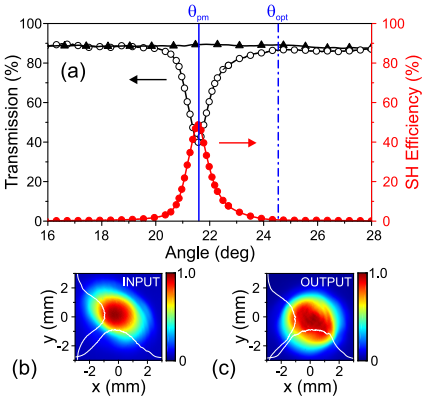


**Fig. 3.** The transmission of total (triangles) and fundamental harmonic (open circles) energies, and the SH efficiency (red filled circles) as functions of angle $\theta$. The parameters of the input pulse are the same as in Fig. 1. Vertical lines mark the angles of perfect phase matching for SH generation ($\theta_{pm}$) and maximum self-compression ($\theta_{opt}$). Near-field profiles of (b) input and (c) output at $\theta$=$\theta_{opt}$ beams.

the SPM-induced spectral broadening diminishes, and so the dispersive broadening of the pulse. For the crystal angles $\theta < \theta_{zf}$, in the regime of reduced self-focusing, the dispersive broadening of the pulse remains dominant due to insufficient positive SPM.

Spectral measurements also reveal the generation of extraordinarily polarized SH wave possessing a distinct double peaked spectral structure. The narrow central peak centered at 1050 nm and visible throughout the entire $\theta$ range is attributed to the phase mismatched SH, whose intensity rapidly drops as the crystal is rotated out of phase matching. The second peak is tunable in wavelength and emerges due to the so-called self-phase matching [43], which is equivalent to the soliton-induced SH sideband formation [44].

Figure 3(a) shows the transmission of total and fundamental harmonic energies as well as the SH generation efficiency as functions of the angle $\theta$. It is important to note that the total energy transmission measurements clearly indicate the absence of nonlinear losses due to multiphoton absorption, which is inherent to the filamentation regime. Figs. 3(b) and 3(c) show the near-field profiles of the input beam, as measured before the focusing lens and the output beam carrying the self-compressed pulse, as measured after the collimating mirror, respectively. Smooth, slightly super-Gaussian spatial intensity distribution attests the absence of beam filamentation.

We identify SH generation and Fresnel reflections as the main sources of energy loss. At the vicinity of perfect phase matching for SH generation, a considerable depletion of the pulse at fundamental frequency is observed, with the SH conversion efficiency reaching up to 49%. In contrast, as the crystal is rotated out of phase matching, a quick decline of the SH efficiency results in a virtually lossless self-compression with the maximum energy throughput of 86.3% at the angle of maximum self-compression $\theta_{opt} = 24.5°$. In this case, the energy throughput is simply limited by the Fresnel reflections from the input and output faces of the $\beta$-BBO crystal and the self-phase matched SH generation, which consumes just a small fraction (0.7%) of the input pulse energy.

Owing to the possibility to vary the effective nonlinear index of refraction via crystal angle, filamentation-free self-compression could be efficiently performed for a relatively wide range of the input pulse energies and intensities, allowing to scale the energy and peak power of the self-compressed pulses. To demonstrate so, the input pulses were further amplified in a complimentary optical parametric amplification stage consisting of a 2-mm $\beta$-BBO crystal cut for type-II phase matching ($\theta = 28°$, $\phi = 0°$) that delivers up to 215 $\mu$J energy pulses at 2.1 $\mu$m with a duration of 95 fs. Subsequently, to avoid filamentation due to significantly increased intensities and to preserve the balance between the SPM and anomalous GVD, the sample was moved further away from the geometric focus and placed at $z = -12.2$ cm (FWHM beam diameter at the input face 1.41 mm, intensity 94 GW/cm$^2$). More than three-fold self-compression (Fig. 4) down to 27 fs (equivalent to 3.9 optical cycles) with the energy throughput of 85% was achieved yielding the self-compressed pulse with 4.5 GW peak power. Even further energy scaling might be achieved by placing the crystal after the geometrical focus, where self-focusing effect is in part compensated by the input beam divergence.

In conclusion, we have experimentally demonstrated virtually lossless, filamentation-free, more than three-fold self-compression of mid-infrared laser pulses at 2.1 $\mu$m in $\beta$-BBO crystal. In contrast to soliton compression mechanism that utilizes the second-order cascading to achieve the self-defocusing propagation regime in the range of normal GVD, in the present case we exploit the second-order cascading to produce large effective self-focusing nonlinearity that facilitates self-compression in the range of anomalous GVD. Beam filamentation effects are

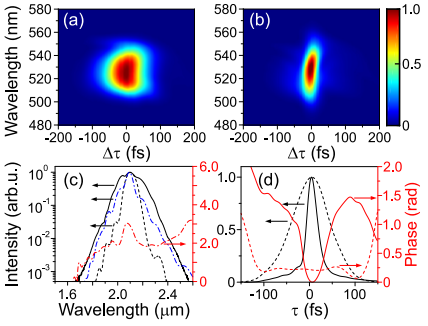


**Fig. 4.** Self-compression of amplified 95 fs, 215 $\mu$J pulses at 2.1 $\mu$m down to 27 fs in a $\beta$-BBO crystal located at $z = -12.2$ cm: the measured SFG-FROG traces of (a) input and (b) self-compressed ($\theta_{\text{opt}} = 24.5^{\circ}$) pulses, (c) measured (solid curve) and retrieved spectra and spectral phase (dash-dotted curves), (d) retrieved intensity profile and phase of the self-compressed pulse. Dashed curves in (c) and (d) show the spectrum, intensity profile and phase of the input pulse.

avoided by choosing an appropriate input beam diameter, which guarantees essentially one dimensional (temporal) dynamics leading to soliton compression without the onset of beam filamentation and associated nonlinear losses. More specifically, we demonstrate self-compression of 68 fs, 73 $\mu$J pulses at 2.1 $\mu$m down to 22 fs with an energy throughput of 86.3%, with the energy losses originating just from Fresnel reflections and SH generation. We also demonstrate the energy and peak power scaling by increasing the input pulse energy up to 215 $\mu$J, that yields the self-compressed pulse with 4.5 GW peak power. The demonstrated method provides freedom in the choice of the input conditions, as both, the input pulse intensity and the effective nonlinearity could be tuned independently. For what concerns self-compression at longer wavelengths, nonlinear crystals with better infrared transparency, e.g. $LiNbO_3$, could be readily employed.

This research was funded by a grant No. APP-8/2016 from the Research Council of Lithuania.

## REFERENCES


1. C. Rolland and P. B. Corkum, J. Opt. Soc. Am. B **5**, 641 (1988).
2. E. Mével, O. Tcherbakoff, F. Salin, and E. Constant, J. Opt. Soc. Am. B **20**, 105 (2003).
3. M. Seidel, G. Arisholm, J. Brons, V. Pervak, and O. Pronin, Opt. Express **24**, 9412 (2016).
4. J. Schulte, T. Sartorius, J. Weitenberg, A. Vernaleken, and P. Russbueldt, Opt. Lett. **41**, 4511 (2016).
5. C.-H. Lu, Y.-J. Tsou, H.-Y. Chen, B.-H. Chen, Y.-C. Cheng, S.-D. Yang, M.-C. Chen, C.-C. Hsu, and A. H. Kung, Optica **1**, 400 (2014).
6. P. He, Y. Liu, K. Zhao, H. Teng, X. He, P. Huang, H. Huang, S. Zhong, Y. Jiang, S. Fang, X. Hou, and Z. Wei, Opt. Lett. **42**, 474 (2017).
7. A. A. Voronin, A. M. Zheltikov, T. Ditmire, B. Rus, and G. Korn, Opt. Commun. **291**, 299 (2013).
8. A. A. Lanin, A. A. Voronin, E. A. Stepanov, A. B. Fedotov, and A. M. Zheltikov, Opt. Lett. **39**, 6430 (2014).
9. E. A. Stepanov, A. A. Lanin, A. A. Voronin, A. B. Fedotov, and A. M. Zheltikov, Phys. Rev. Lett. **117**, 043901 (2016).
10. M. Durand, A. Jarnac, A. Houard, Y. Liu, S. Grabielle, N. Forget, A. Durécu, A. Couairon, and A. Mysyrowicz, Phys. Rev. Lett. **110**, 115003 (2013).
11. S. V. Chekalin, A. E. Dokukina, A. E. Dormidonov, V. O. Kompanets, E. O. Smetanina, and V. P. Kandidov, J. Phys. B **48**, 094008 (2015).
12. H. Liang, P. Krogen, R. Grynko, O. Novak, C.-L. Chang, G. J. Stein, D. Weerawarne, B. Shim, F. X. Kärtner, and K.-H. Hong, Opt. Lett. **40**, 1069 (2015).
13. I. Gražulevičiūtė, R. Šuminas, G. Tamošauskas, A. Couairon, and A. Dubietis, Opt. Lett. **40**, 3719–3722 (2015).
14. M. Hemmer, M. Baudisch, A. Thai, A. Couairon, and J. Biegert, Opt. Express **21**, 28095 (2013).
15. M. Baudisch, H. Pires, H. Ishizuki, T. Taira, M. Hemmer, and J. Biegert, J. Opt. **17**, 094002 (2015).
16. A. A. Lanin, A. A. Voronin, E. A. Stepanov, A. B. Fedotov, and A. M. Zheltikov, Opt. Lett. **40**, 974 (2015).
17. D. Majus, G. Tamošauskas, I. Gražulevičiūtė, N. Garejev, A. Lotti, A. Couairon, D. Faccio, and A. Dubietis, Phys. Rev. Lett. **112**, 193901 (2014).
18. B. G. Bravy, V. M. Gordienko, and V. T. Platonenko, Laser Phys. Lett. **11**, 065401 (2014).
19. B. G. Bravy, V. M. Gordienko, and V. T. Platonenko, Opt. Commun. **344**, 7 (2015).
20. A. A. Voronin and A. M. Zheltikov, J. Opt. **18**, 115501 (2016).
21. A. A. Voronin and A. M. Zheltikov, Phys. Rev. A **94**, 023824 (2016).
22. W. Li, Y. Li, Y. Xu, X. Guo, J. Lu, P. Wang, and Y. Leng, Opt. Express **25**, 7101 (2017).
23. A. A. Balakin, A. V. Kim, A. G. Litvak, V. A. Mironov, and S. A. Skobelev, Phys. Rev. A **94**, 043812 (2016).
24. A. Marcinkevičiūtė, N. Garejev, R. Šuminas, G. Tamošauskas, and A. Dubietis, J. Opt. **19**, 105505 (2017).
25. V. Shumakova, P. Malevich, S. Ališauskas, A. Voronin, A. M. Zheltikov, D. Faccio, D. Kartashov, A. Baltuška, and A. Pugžlys, Nat. Commun. **7**, 12877 (2016).
26. B. B. Zhou, A. Chong, F. W. Wise, and M. Bache, Phys. Rev. Lett. **109**, 043902 (2012).
27. S. Ashihara, J. Nishina, T. Shimura, and K. Kuroda, J. Opt. Soc. Am. B **19**, 2505 (1999).
28. J. Moses and F. W. Wise, Opt. Lett. **31**, 1881 (2006).
29. F. Hache, A. Zéboulon, G. Gallot, and G. M. Gale, Opt. Lett. **20**, 1556 (1995).
30. M. Bache, H. Guo, and B. Zhou, Opt. Mater. Express **3**, 1647 (2013).
31. B. Zhou and M. Bache, APL Photon. **1**, 050802 (2016).
32. B. Zhou, H. Guo, and M. Bache, Opt. Express. **23**, 6924 (2015).
33. M. Seidel, J. Brons, G. Arisholm, K. Fritsch, V. Pervak, and O. Pronin, Sci. Rep. **7**, 1410 (2017).
34. C. Vicario, B. Monoszlai, G. Arisholm, and C. P. Hauri, J. Opt. **17**, 094005 (2015).
35. K. Krupa, A. Labruyère, A. Tonello, B. M. Shalaby, V. Couderc, F. Baronio, and A. B. Aceves, Optica **2**, 1058 (2015).
36. R. Šuminas, G. Tamošauskas, V. Jukna, A. Couairon, and A. Dubietis, Opt. Express **25**, 6746 (2017).
37. R. Šuminas, G. Tamošauskas, G. Valiulis, and A. Dubietis, Opt. Lett. **41**, 2097 (2016).
38. H. Wang, A. Alismail, G. Barbiero, M. Wendl, and H. Fattahi, Opt. Lett. **42**, 2595 (2017).
39. M. Bache, H. Guo, B. Zhou and X. Zeng, Opt. Mater. Express **3**, 357 (2013).
40. I. Shoji, H. Nakamura, K. Ohdaira, T. Kondo, R. Ito, T. Okamoto, K. Tatsuki, and S. Kubota, J. Opt. Soc. Am. B **16**, 620 (1999).
41. R. C. Miller, Appl. Phys. Lett. **5**, 17 (1964).
42. D. Zhang, Y. Kong, and J.-Y. Zhang, Opt. Commun. **184**, 485 (2000).
43. G. Valiulis, V. Jukna, O. Jedrkiewicz, M. Clerici, E. Rubino, and P. Di Trapani, Phys. Rev. A **83**, 043834 (2011).
44. B. Zhou, H. Guo, and M. Bache, Phys. Rev. A **90**, 013823 (2014).

## REFERENCES


1. C. Rolland and P. B. Corkum, Compression of high-power optical pulses, J. Opt. Soc. Am. B **5**, 641–647 (1988).
2. E. Mével, O. Tcherbakoff, F. Salin, and E. Constant, Extracavity compression technique for high-energy femtosecond pulses, J. Opt. Soc. Am. B **20**, 105–108 (2003).
3. M. Seidel, G. Arisholm, J. Brons, V. Pervak, and O. Pronin, All solid-state spectral broadening: an average and peak power scalable method for compression of ultrashort pulses, Opt. Express **24**, 9412–9428 (2016).
4. J. Schulte, T. Sartorius, J. Weitenberg, A. Vernaleken, and P. Russbueldt, Nonlinear pulse compression in a multi-pass cell, Opt. Lett. **41**, 4511–4514 (2016).
5. C.-H. Lu, Y.-J. Tsou, H.-Y. Chen, B.-H. Chen, Y.-C. Cheng, S.-D. Yang, M.-C. Chen, C.-C. Hsu, and A. H. Kung, Generation of intense supercontinuum in condensed media, Optica **1**, 400–406 (2014).
6. P. He, Y. Liu, K. Zhao, H. Teng, X. He, P. Huang, H. Huang, S. Zhong, Y. Jiang, S. Fang, X. Hou, and Z. Wei, High-efficiency supercontinuum generation in solid thin plates at 0.1 TW level, Opt. Lett. **42**, 474–477 (2017).
7. A. A. Voronin, A. M. Zheltikov, T. Ditmire, B. Rus, and G. Korn, Subexawatt few-cycle light wave generation via multipetawatt pulse compression, Opt. Commun. **291**, 299–303 (2013).
8. A. A. Lanin, A. A. Voronin, E. A. Stepanov, A. B. Fedotov, and A. M. Zheltikov, Frequency-tunable sub-two-cycle 60-MW-peak-power free-space waveforms in the mid-infrared, Opt. Lett. **39**, 6430–6433 (2014).
9. E. A. Stepanov, A. A. Lanin, A. A. Voronin, A. B. Fedotov, and A. M. Zheltikov, Solid-state source of subcycle pulses in the midinfrared, Phys. Rev. Lett. **117**, 043901 (2016).
10. M. Durand, A. Jarnac, A. Houard, Y. Liu, S. Grabielle, N. Forget, A. Durécu, A. Couairon, and A. Mysyrowicz, Self-guided propagation of ultrashort laser pulses in the anomalous dispersion region of transparent solids: a new regime of filamentation, Phys. Rev. Lett. **110**, 115003 (2013).
11. S. V. Chekalin, A. E. Dokukina, A. E. Dormidonov, V. O. Kompanets, E. O. Smetanina, and V. P. Kandidov, Light bullets from a femtosecond filament, J. Phys. B **48**, 094008 (2015).
12. H. Liang, P. Krogen, R. Grynko, O. Novak, C.-L. Chang, G. J. Stein, D. Weerawarne, B. Shim, F. X. Kärtner, and K.-H. Hong, Three-octave-spanning supercontinuum generation and sub-two-cycle self-compression of mid-infrared filaments in dielectrics, Opt. Lett. **40**, 1069–1072 (2015).
13. I. Gražulevičiūtė, R. Šuminas, G. Tamošauskas, A. Couairon, and A. Dubietis, Carrier-envelope phase-stable spatiotemporal light bullets, Opt. Lett. **40**, 3719–3722 (2015).
14. M. Hemmer, M. Baudisch, A. Thai, A. Couairon, and J. Biegert, Self-compression to sub-3-cycle duration of mid-infrared optical pulses in dielectrics, Opt. Express **21**, 28095–28102 (2013).
15. M. Baudisch, H. Pires, H. Ishizuki, T. Taira, M. Hemmer, and J. Biegert, Sub-4-optical-cycle, 340 MW peak power, high stability mid-IR source at 160 kHz, J. Opt. **17**, 094002 (2015).
16. A. A. Lanin, A. A. Voronin, E. A. Stepanov, A. B. Fedotov, and A. M. Zheltikov, Multioctave, $3-18$ $\mu$m sub-two-cycle supercontinua from self-compressing, self-focusing soliton transients in a solid, Opt. Lett. **40**, 974–977 (2015).
17. D. Majus, G. Tamošauskas, I. Gražulevičiūtė, N. Garejev, A. Lotti, A. Couairon, D. Faccio, and A. Dubietis, Nature of spatiotemporal light bullets in bulk Kerr media, Phys. Rev. Lett. **112**, 193901 (2014).
18. B. G. Bravy, V. M. Gordienko, and V. T. Platonenko, Self-compression of terawatt level picosecond 10 $\mu$m laser pulses in NaCl, Laser Phys. Lett. **11**, 065401 (2014).
19. B. G. Bravy, V. M. Gordienko, and V. T. Platonenko, Kerr effect-assisted self-compression in dielectric to single-cycle pulse width and to terawatt power level in mid-IR, Opt. Commun. **344**, 7–11 (2015).
20. A. A. Voronin and A. M. Zheltikov, Asymptotically one-dimensional dynamics of high-peak-power ultrashort laser pulses, J. Opt. **18**, 115501 (2016).
21. A. A. Voronin and A. M. Zheltikov, Pulse self-compression to single-cycle pulse widths a few decades above the self-focusing threshold, Phys. Rev. A **94**, 023824 (2016).
22. W. Li, Y. Li, Y. Xu, X. Guo, J. Lu, P. Wang, and Y. Leng, Design and simulation of a single-cycle source tunable from 2 to 10 micrometers, Opt. Express **25**, 7101–7111 (2017).
23. A. A. Balakin, A. V. Kim, A. G. Litvak, V. A. Mironov, and S. A. Skobelev, Extreme self-compression of laser pulses in the self-focusing mode resistant to transverse instability, Phys. Rev. A **94**, 043812 (2016).
24. A. Marcinkevičiūtė, N. Garejev, R. Šuminas, G. Tamošauskas, and A. Dubietis, A compact, self-compression-based sub-3 optical cycle source in the $3-4$ $\mu$m spectral range, J. Opt. **19**, 105505 (2017).
25. V. Shumakova, P. Malevich, S. Ališauskas, A. Voronin, A. M. Zheltikov, D. Faccio, D. Kartashov, A. Baltuška, and A. Pugžlys, Multi-millijoule few-cycle mid-infrared pulses through nonlinear self-compression in bulk, Nat. Commun. **7**, 12877 (2016).
26. B. B. Zhou, A. Chong, F. W. Wise, and M. Bache, Ultrafast and octave-spanning optical nonlinearities from strongly phase-mismatched quadratic interactions, Phys. Rev. Lett. **109**, 043902 (2012).
27. S. Ashihara, J. Nishina, T. Shimura, and K. Kuroda, Soliton compression of femtosecond pulses in quadratic media, J. Opt. Soc. Am. B **19**, 2505–2510 (1999).
28. J. Moses and F. W. Wise, Soliton compression in quadratic media: high-energy few-cycle pulses with a frequency-doubling crystal, Opt. Lett. **31**, 1881–1883 (2006).
29. F. Hache, A. Zéboulon, G. Gallot, and G. M. Gale, Cascaded second-order effects in the femtosecond regime in $beta$-barium borate: self-compression in a visible femtosecond optical parametric oscillator, Opt. Lett. **20**, 1556–1558 (1995).
30. M. Bache, H. Guo, and B. Zhou, Generating mid-IR octave-spanning supercontinua and few-cycle pulses with solitons in phase-mismatched quadratic nonlinear crystals, Opt. Mater. Express **3**, 1647–1657 (2013).
31. B. Zhou and M. Bache, Multiple-octave spanning mid-IR supercontinuum generation in bulk quadratic nonlinear crystals, APL Photon. **1**, 050802 (2016).
32. B. Zhou, H. Guo, and M. Bache, Energetic mid-IR femtosecond pulse generation by self-defocusing soliton-induced dispersive waves in a bulk quadratic nonlinear crystal, Opt. Express. **23**, 6924–6936 (2015).
33. M. Seidel, J. Brons, G. Arisholm, K. Fritsch, V. Pervak, and O. Pronin, Efficient high-power ultrashort pulse compression in self-defocusing bulk media, Sci. Rep. **7**, 1410 (2017).
34. C. Vicario, B. Monoszlai, G. Arisholm, and C. P. Hauri, Generation of 1.5-octave intense infrared pulses by nonlinear interactions in DAST crystal, J. Opt. **17**, 094005 (2015).
35. K. Krupa, A. Labruyère, A. Tonello, B. M. Shalaby, V. Couderc, F. Baronio, and A. B. Aceves, Polychromatic filament in quadratic media: spatial and spectral shaping of light in crystals, Optica **2**, 1058–1064 (2015).
36. R. Šuminas, G. Tamošauskas, V. Jukna, A. Couairon, and A. Dubietis, Second-order cascading-assisted filamentation and controllable supercontinuum generation in birefringent crystals, Opt. Express **25**, 6746–6756 (2017).
37. R. Šuminas, G. Tamošauskas, G. Valiulis, and A. Dubietis, Spatiotemporal light bullets and supercontinuum generation in $\beta$-BBO crystal with competing quadratic and cubic nonlinearities, Opt. Lett. **41**, 2097–2100 (2016).
38. H. Wang, A. Alismail, G. Barbiero, M. Wendl, and H. Fattahi, Cross-polarized, multi-octave supercontinuum generation, Opt. Lett. **42**, 2595–2598 (2017).
39. M. Bache, H. Guo, B. Zhou and X. Zeng, The anisotropic Kerr nonlinear refractive index of the beta-barium borate ($\beta$-$BaB_2O_4$) nonlinear crystal, Opt. Mater. Express **3**, 357–382 (2013).
40. I. Shoji, H. Nakamura, K. Ohdaira, T. Kondo, R. Ito, T. Okamoto, K. Tatsuki, and S. Kubota, Absolute measurement of second-order nonlinear-optical coefficients of $\beta$-$BaB_2O_4$ for visible to ultraviolet second-harmonic wavelengths, J. Opt. Soc. Am. B **16**, 620–624 (1999).
41. R. C. Miller, Optical second harmonic generation in piezoelectric crystals, Appl. Phys. Lett. **5**, 17–19 (1964).
42. D. Zhang, Y. Kong, and J.-Y. Zhang, Optical parametric properties of

532-nm-pumped beta-barium-borate near the infrared absorption edge, Opt. Commun. **184**, 485–491 (2000).
43. G. Valiulis, V. Jukna, O. Jedrkiewicz, M. Clerici, E. Rubino, and P. Di Trapani, Propagation dynamics and X-pulse formation in phase-mismatched second-harmonic generation, Phys. Rev. A **83**, 043834 (2011).
44. B. Zhou, H. Guo, and M. Bache, Soliton-induced nonlocal resonances observed through high-intensity tunable spectrally compressed second-harmonic peaks, Phys. Rev. A **90**, 013823 (2014).

# A5

# EVEN AND ODD HARMONICS-ENHANCED SUPERCONTINUUM GENERATION IN ZINC-BLENDE SEMICONDUCTORS

**R. Šuminas**, A. Marcinkevičiūtė, G. Tamošauskas, A. Dubietis

J. Opt. Soc. Am. B **36**, A22–A27 (2019)

# Even and odd harmonics-enhanced supercontinuum generation in zinc-blende semiconductors

ROSVALDAS ŠUMINAS,* AGNĖ MARCINKEVIČIŪTĖ, GINTARAS TAMOŠAUSKAS, AND AUDRIUS DUBIETIS,

*Laser Research Center, Vilnius University, Saulėtekio Avenue 10, LT-10223 Vilnius, Lithuania*
*rosvaldas.suminas@ff.stud.vu.lt*

**Abstract:** We report on even and odd harmonics-enhanced supercontinuum generation in polycrystalline ZnS and ZnSe samples, as pumped by femtosecond mid-infrared pulses. We demonstrate that efficient generation of multiple harmonics takes place due to random quasi phase matching, which is an intrinsic property of polycrystalline structure and which supports multiple simultaneous three-wave mixing processes over a broad wavelength range. More specifically, using sub-$\mu$J, 60 fs, 3.6 $\mu$m input pulses we measured multioctave supercontinuum spectra spanning the $0.4 - 5$ $\mu$m and $0.5 - 5$ $\mu$m wavelength ranges in ZnS and ZnSe samples of few mm thickness, respectively. Even and odd harmonics up to 10th order in ZnS and up to 8th order in ZnSe were recorded with the input pulses at 4.6 $\mu$m. In contrast, filamentation in ZnTe single crystal is shown to produce only a moderate spectral broadening, which is accompanied by the generation of just second and third harmonics, highlighting the advantages of polycrystalline structure of zinc-blende semiconductors for the generation of ultrabroadband radiation.



## 1. Introduction

Filamentation of intense femtosecond laser pulses in bulk solid-state nonlinear media leads to unprecedented spectral broadening termed supercontinuum (SC) generation, opening exciting perspectives for many applications in contemporary time-resolved spectroscopy, ultrafast nonlinear optics and photonics [1]. Currently there is a growing interest in SC generation in the mid-infrared spectral range. Mid-infrared pumping markedly extends the nomenclature of nonlinear materials that are suitable to achieve a considerable spectral broadening [2]. Therefore alongside broadly used wide bandgap dielectric crystals and glasses [3–12], other nonlinear media possessing narrower bandgaps, and thus larger cubic nonlinearities, such as soft glasses, narrow bandgap dielectrics and semiconductors proved to be efficient nonlinear materials for ultrabroadband SC generation in the mid-infrared spectral range [13–22].

Owing to unique set of optical properties, zinc-blende semiconductors find many applications in diverse areas of laser physics and ultrafast nonlinear optics. Transition metal-doped zinc sulphide (ZnS) and zinc selenide (ZnSe) serve as rather unique laser host materials, exhibiting superb ultrafast lasing capabilities [23], on which rely the whole new generation of femtosecond mid-infrared laser oscillators and amplifiers [24]. Recently, sub-100 fs pulses with several mJ energy at 1 kHz repetition rate were produced by $Cr^{2+}$:ZnSe chirped pulse amplifier [25].

Zinc-blende semiconductor crystals are optically isotropic, but owing to $\bar{4}3m$ symmetry, posses large second-order nonlinearity [26]. Polycrystalline versions of these materials may be regarded as short range order nonlinear photonic crystals [27], suggesting intriguing opportunities for ultrabroadband frequency conversion via second-order nonlinear interactions, which rely on random quasi phase matching that stems from random orientation of tens-of-microns sized crystallites [28]. These features are readily exploited for broadband sum- and difference-frequency generation and more recently, for optical parametric oscillation [29].

As compared to dielectric crystals, zinc-blende semiconductor materials exhibit considerably extended long-wave transmittances, large cubic nonlinearities [30] and relatively high optical damage thresholds [31], so emerging as very attractive nonlinear media in the mid-infrared spectral range. Femtosecond filamentation and spectral broadening with wavelength-tunable near-infrared laser pulses was experimentally studied in ZnSe [32]. Multioctave SC spectra have been reported in ZnS [7] and ZnSe [33] crystals, in the regimes of either single or multiple filamentation, however without discussing the relevant effects that may lead to such large scale spectral broadening. More recent studies demonstrated that along with SC generation, filamentation in polycrystalline ZnSe facilitates surprisingly efficient simultaneous broadband second-order interactions (sum-frequency and harmonics generation) [34, 35], opening new avenues for studies of extreme light matter interactions and harmonics generation in solid state media [36–40]. Finally, recent numerical simulations predicted efficient self-compression and sub-cycle light bullet generation via filamentation in ZnSe using femtosecond mid and long wavelength infrared pulses whose wavelengths fall into the range of anomalous group velocity dispersion (GVD) of the material [41].

In this paper we report on SC generation in zinc-blende semiconductor crystals: polycrystalline ZnS and ZnSe, and zinc telluride (ZnTe) single crystal, as pumped by femtosecond pulses with carrier wavelengths of 3.6 $\mu$m and 4.6 $\mu$m. Multioctave supercontinua spanning the $0.4 - 5$ $\mu$m and $0.5 - 5$ $\mu$m wavelength ranges, were generated in polycrystalline ZnS and ZnSe samples, respectively. We demonstrate that the maximum spectral blue shifts extend right to the short-wave absorption edge of the crystals and are contributed by efficient generation of multiple even and odd harmonics via random quasi phase matching that is achieved due to non-vanishing second-order nonlinearity and polycrystalline structure of these materials. In contrast, in ZnTe single crystal, in the absence of random phase matching, only a moderate spectral broadening accompanied just by second and third harmonics with considerably lower conversion efficiency was observed.

## 2. Experimental setup and materials

The nonlinear media used were polycrystalline samples of ZnS (the average crystallite size 30 $\mu$m), ZnSe (the average crystallite size 60 $\mu$m) and ZnTe single crystal of different lengths so as to capture the characteristic features of spectral evolutions imposed by filamentation process. The relevant linear and nonlinear optical parameters: energy bandgap, transparency range, linear and nonlinear refraction indexes, nonlinear second-order optical coefficients and zero GVD wavelengths of these materials are listed in Table 1.

Figure 1 shows the dispersion curves for ZnS, ZnSe and ZnTe, as calculated from the dispersion equations provided in [42, 43]. In the experiment, the carrier wavelengths of the input pulses (3.6 $\mu$m and 4.6 $\mu$m) were chosen to nearly match the zero GVD wavelengths of ZnS and ZnSe, respectively, as illustrated in Fig. 1.

The experimental scheme is depicted in Fig. 2. The 60 fs pulses at 3.6 $\mu$m and 100 fs pulses at 4.6 $\mu$m were produced by the difference frequency generation (DFG) in a 1-mm long KTA crystal cut for type-II phase matching ($\theta = 43°$, $\phi = 0°$) between suitably predelayed signal and idler outputs of a commercial optical parametric amplifier (TOPAS-Prime, Light Conversion Ltd.). The residual signal and idler waves were filtered out using a dichroic mirror, and the DFG beam of $\sim 1.9$ mm FWHM diameter was focused using a $BaF_2$ lens (focal length of $f = +100$ mm) onto the front face of the nonlinear medium. The input pulse energy was varied by using a variable density neutral filter placed in the optical path of the signal wave. The output beam was imaged using a $4f$ imaging system consisting of two Al-coated parabolic mirrors onto the slit of a home-built scanning prism spectrometer, which was equipped with Si and InAsSb photodetectors, allowing us to perform spectral measurements in the $0.3 - 5.8$ $\mu$m wavelength range. The spectra were measured by scanning through each spectral data point with an average of 4 laser shots. We

Table 1. Linear and nonlinear parameters of zinc-blende semiconductor materials. $E_g$ is the energy bandgap, the transparency range is defined at 10% transmission level of 1 mm thick sample, $n_0$ is the refractive index at 3.6 $\mu$m (all data from [42, 43]), $n_2$ is the nonlinear index of refraction as evaluated at 3.6 $\mu$m using the formalism described in [44], with an updated dimensionless parameter $K = 7.33 \times 10^{-9}$ [45], $d = d_{14} = d_{25} = d_{36}$ is the nonlinear optical coefficient for second harmonic generation at 1.321 $\mu$m [26], $\lambda_0$ is the zero GVD wavelength, LIDT is the laser-induced damage threshold as measured using 1.03 $\mu$m, 500 fs laser pulses [31].

| Material | ZnS | ZnSe | ZnTe |
|---|---|---|---|
| $E_g$, eV | 3.68 | 2.71 | 2.30 |
| Transparency range, $\mu$m | 0.4–12.5 | 0.5–20 | 0.55–25 |
| $n_0$ | 2.25 | 2.43 | 2.70 |
| $n_2$, $\times 10^{-16}$ cm$^2$/W | 22 | 66 | 106 |
| $d$, pm/V | 8 | 30 | 52 |
| $\lambda_0$, $\mu$m | 3.6 | 4.8 | 6.2 |
| LIDT, J/cm$^2$ | 1.1 | 0.53 | |

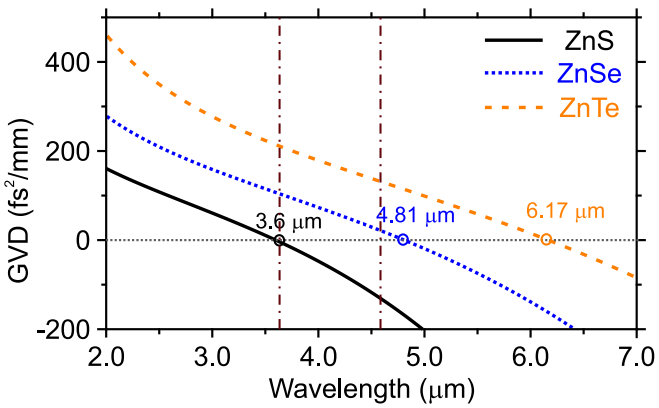


Fig. 1. Group velocity dispersion curves for ZnS (solid curve), ZnSe (dotted curve) and ZnTe (dashed curve) crystals. Dashed-dotted lines mark the input wavelengths. Arrows denote zero GVD wavelengths.

also recorded characteristic filament-induced luminescence spectra of the investigated nonlinear materials, which were captured by coupling the luminescence signal from the side of the sample into a commercial fiber spectrometer (Ocean Optics, QE65000).

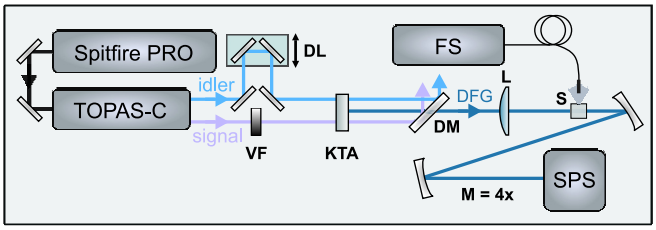


Fig. 2. Layout of the experimental setup. Variable density filter (VF); delay line (DL); difference frequency generator (KTA); dichroic mirror (DM); $BaF_2$ focusing lens (L); ZnSe, ZnS or ZnTe sample (S); 4 $f$ imaging system with 4× magnification (M); home-built scanning prism spectrometer (SPS); commercial fiber spectrometer (FS).

## 3. Results and discussion

In what follows, we present the results of spectral measurements versus sample length and for different input pulse energies. We demonstrate that the build-up of supercontinuum spectra, and particularly the blue-shifted spectral broadening in these materials, is unambiguously attributed to the process of randomly quasi-phase matched harmonic generation. Figure 3 presents the experimentally measured output spectra in ZnS samples of 2 mm and 4 mm thickness, using 60 fs, 3.6 $\mu$m input pulses with energies of 0.5 $\mu$J and 0.73 $\mu$J.

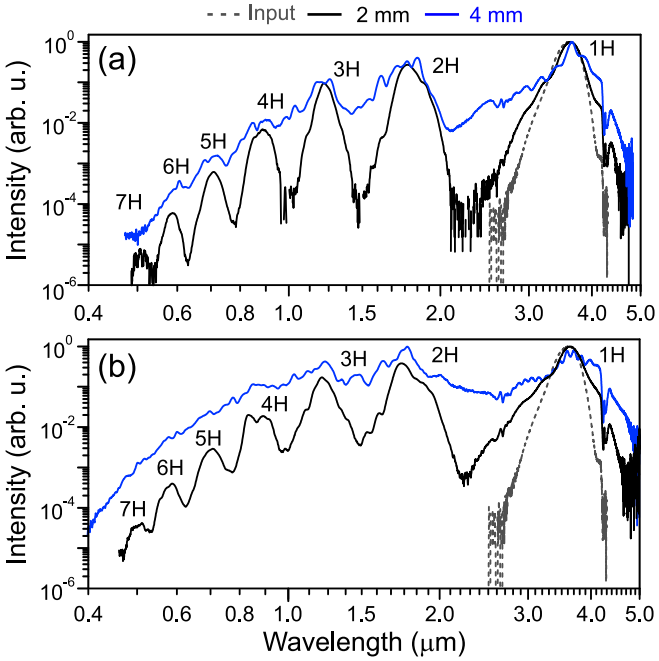


Fig. 3. The output spectra measured in 2 mm and 4 mm-thick polycrystalline ZnS samples with the input pulse energies of (a) 0.5 $\mu$J and (b) 0.73 $\mu$J. The dashed gray curves show the input pulse spectra. The labels 1H, 2H, etc., stand for the harmonics order.

With the input pulse energy of 0.5 $\mu$J, the spectrum measured at the output of a 2 mm-thick ZnS sample exhibits a slight broadening around the carrier wavelength, which is accompanied by the occurrence of distinct multiple peaks, which correspond to the individual harmonics, as shown in Fig. 3(a). Even and odd harmonics up to 7th order are clearly visible. We suppose a simple harmonics generation mechanism, which relies on randomly quasi phase-matched sum-frequency generation involving the fundamental harmonic as one of the pump waves. In that way, the third harmonic is produced via sum-frequency generation between the fundamental and second harmonic waves, the fourth harmonic – via sum-frequency generation between the fundamental and third harmonic, and so on. Our assumption is based on the fact that phase mismatch for that kind of three wave interactions is the smallest compared to phase mismatch for other possible combinations of frequencies. For instance, fourth harmonic could be generated via either $\omega + 3\omega$ or $2\omega + 2\omega$ interactions. The estimated phase mismatch parameters for these processes are $\Delta k_{431} = k(4\omega) - k(3\omega) - k(\omega) = 182 mm^{-1}$ and $\Delta k_{422} = k(4\omega) - 2k(2\omega) = 233 mm^{-1}$, respectively, so clearly in favour of the $\omega + 3\omega$ process. The same is true for the generation of fifth and all subsequent harmonics, and the same considerations apply to ZnSe as well. By increasing the input pulse energy up to 0.73 $\mu$J, in the sample of the same thickness (2 mm) we observe further spectral broadening of the fundamental (around the carrier wavelength) and generated individual harmonics, whose spectra start to overlap, as shown in Fig. 3(b). Notice that the individual harmonics spectra are almost exact replicas of the broadened input pulse spectrum, confirming the broadband character of random quasi phase matching process, which provides greatly relaxed phase matching conditions for multiple simultaneous three-wave interactions within a wide spectral range.

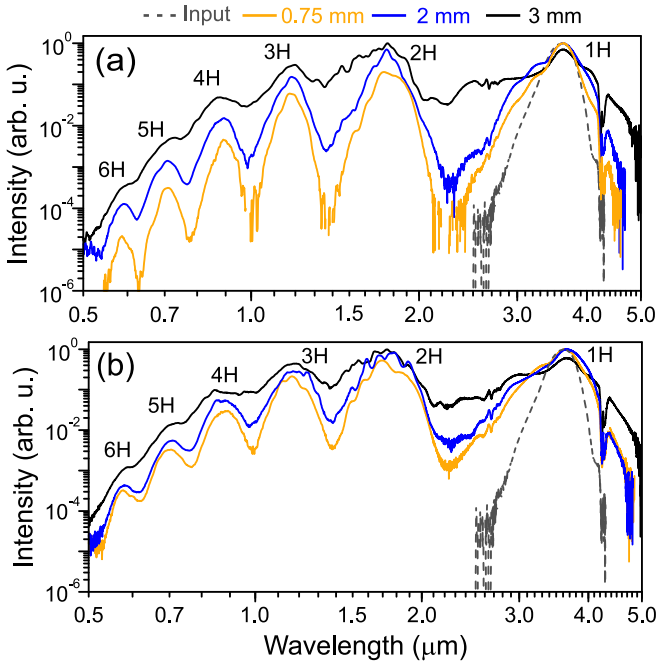


Fig. 4. The output spectra measured in 0.75 mm, 2 mm and 3 mm-thick polycrystalline ZnSe samples with the input pulse energies of (a) 0.73 $\mu$J and (b) 1.88 $\mu$J. The labelling is the same as in Fig. 3.

In ZnS sample of 4 mm thickness, the harmonics spectra become broadened so much that the individual harmonic peaks are barely distinguishable even with the lowest input pulse energy of 0.5 $\mu$J [Fig. 3(a)]. Eventually, increasing the input pulse energy up to 0.73 $\mu$J, all the harmonics spectra merge into a broadband and almost uniform SC radiation spanning the 0.4 – 5 $\mu$m wavelength range, that corresponds to 3.6 optical octaves [Fig. 3(b)]. Notably, the blue-shifted portion of the SC radiation extends right down to the short-wave transparency edge of the crystal. A distinct double dip around 4.25 $\mu$m clearly distinguishable in all broadened spectra is attributed to the absorption of atmospheric $CO_2$.

Almost identical spectral features and spectral evolutions as functions of the sample length and the input pulse energy were recorded in ZnSe samples, as presented in Fig. 4. However, in ZnSe fewer harmonics (up to 6th order) were generated due to its smaller bandgap and reduced transmittance in the visible spectral range. The broadest SC spectrum covering the 0.5 – 5 $\mu$m wavelength range, that corresponds to 3.3 optical octaves, was recorded with the input pulse energy of 1.88 $\mu$J in 3 mm-thick sample, as shown in Fig. 4(b). Also, notice that each spectrum is normalized to the highest spectral intensity in order to highlight the remarkably high spectral intensity of the second harmonic exceeding that of the fundamental wavelength. This indicates a considerable depletion of the fundamental harmonic, as the spectral bandwidths (in the frequency scale) of fundamental and second harmonics are nearly the same and attests to a very high efficiency of randomly quasi phase matched frequency conversion process, during which the intensities of the generated fields are expected to grow linearly as functions of the sample thickness, see e.g. [35].

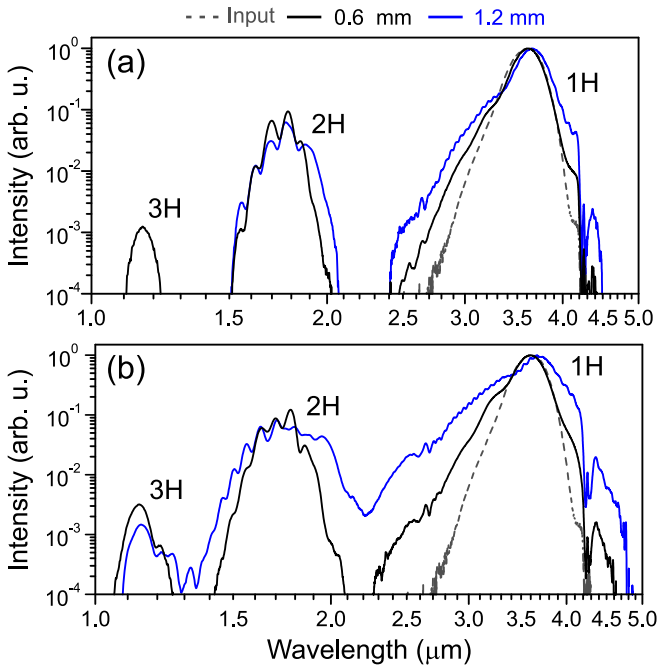


Fig. 5. The output spectra measured in ZnTe single crystal samples of 0.6 mm and 1.2 mm thickness with the input pulse energies of (a) 0.73 $\mu$J and (b) 1.88 $\mu$J. The labelling is the same as in Fig. 3.

In contrast to the above results, spectral broadening in ZnTe single crystal shows marked differences. The measured spectra in ZnTe single crystal samples of 0.6 mm and 1.2 mm thickness are presented in Fig. 5. First of all, only the second and third harmonics were observed, whose intensities, despite larger second-order coefficient of ZnTe (see Table 1), are considerably lower than the intensities of corresponding harmonics generated in polycrystalline ZnS and ZnSe. This fact actually confirms the pivotal role of random quasi phase matching in the harmonics generation process. Secondly, the second harmonic spectrum shows a persisting spectral modulation, which could be attributed to the interference of free and driven second harmonic waves that are generated at the boundary of the nonlinear medium in the conditions of large phase and group velocity mismatch [46,47]. At its maximum extent, the measured spectrum in a single ZnTe crystal covers the wavelength range from 1.08 $\mu$m to 4.8 $\mu$m with the short-wave cut-off being notably far from the short-wave transparency edge of the crystal.

In addition to the measurements of the SC spectra, we also performed the spectral measurements of the filament-induced luminescence traces in these materials. Photoluminescence originates from the relaxation of electron excitations by the multiphoton absorption and readily serves as a simple tool to monitor filament formation and its intensity dynamics inside the nonlinear medium, see e.g. [48]. Luminescence spectra in direct bandgap semiconductors (to which belong the investigated materials) are expected to correspond to the bandgap edge emission. Indeed, the previous study of filament-induced luminescence in ZnSe demonstrated that the luminescence spectrum is relatively narrow and has a characteristic peak at 460 nm, whose wavelength is independent on the excitation wavelength [32].

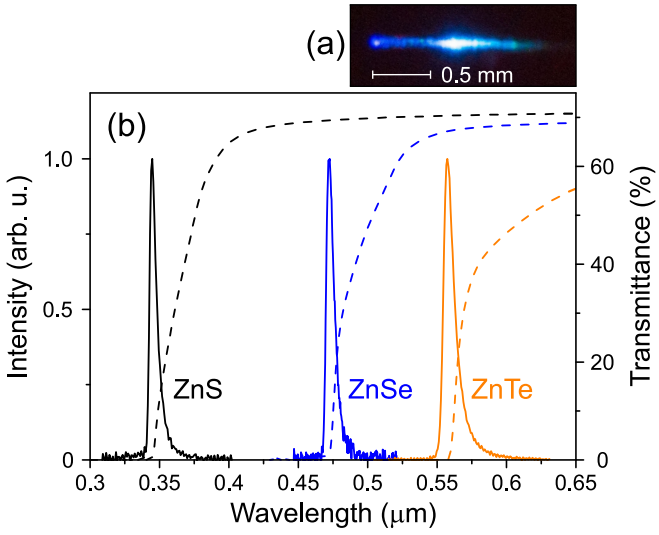


Fig. 6. (a) Filament-induced luminescence trace captured from a side view of ZnSe crystal. The beam propagates from left to right. (b) Normalized luminescence spectra of ZnS (black solid curve), ZnSe (blue solid curve) and ZnTe (orange solid curve) crystals. The dashed curves depict the evaluated transmittances of 1 mm-thick crystal samples.

In the present experiment, the luminescence in ZnS, ZnSe and ZnTe crystals was induced by 11, 8 and 7 photon absorption, respectively, assuming the incident photon energy of 0.34 eV that corresponds to the carrier wavelength (3.6 $\mu$m) of the input pulse. Figure 6(a) shows an example of the filament-induced luminescence trace in ZnSe crystal, where its maximum is

associated with the nonlinear focus of the beam. The measured filament-induced luminescence spectra in ZnS, ZnSe and ZnTe are plotted in Fig. 6(b), demonstrating characteristic emissions at wavelengths of 345, 472 and 557 nm, respectively. Interestingly, the peak position (472 nm) of the measured luminescence spectrum in ZnSe slightly differs from the reported in the literature (460 nm) [32]. We attribute the 12 nm red shift of the luminescence peak to the crystal absorption, as the filament was located approximately 1 mm from the side surface of the crystal, so the luminescence signal was captured from the crystal volume. In such acquisition geometry, the luminescence signal experiences a particularly strong absorption of its short-wave components, resulting in an asymmetric luminescence spectrum with a very steep slope at its short-wave side, and therefore its peak wavelength is a function of propagation distance in the crystal. The same consideration could be applied also to the luminescence spectra of ZnS and ZnTe, which are also expected to show slight red shifts of their observed luminescence peaks. To verify this, in Fig. 6(b) we plotted the actual transmittances of 1 mm-thick crystal samples, as evaluated from the measurements using a spectrophotometer, demonstrating that the luminescence maxima perfectly coincide with the short-wave transmission cut-offs of the materials.

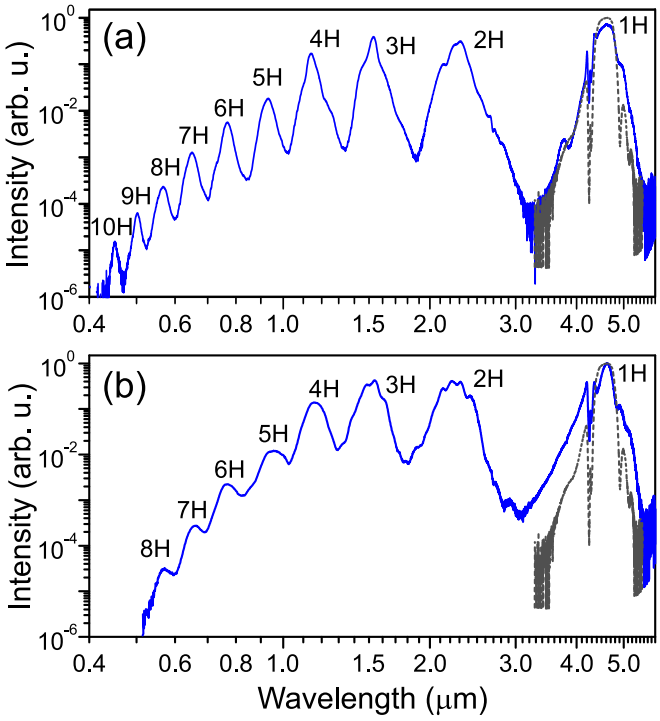


Fig. 7. The output spectra of (a) 2 mm-thick ZnS and (b) 3 mm-thick ZnSe polycrystalline samples, as generated with 100 fs, 1.5 $\mu$J input pulses at 4.6 $\mu$m. The input pulse spectra are shown by gray dashed curves. The labelling is the same as in Fig. 3.

Finally, we demonstrate how the number of generated harmonics in polycrystalline ZnS and ZnSe samples increases, as being excited by femtosecond pulses with a longer carrier wavelength. Figure 7 presents the output spectra measured in 2 mm-thick ZnS and 3 mm-thick ZnSe polycrystalline samples, by launching 100 fs, 1.5 $\mu$J input pulses with a carrier wavelength

of 4.6 $\mu$m. The input pulse energy of 1.5 $\mu$J was set so as to produce a single filament, which in turn produces only a slight spectral broadening around the carrier wavelength. On the other hand, a full set of even and odd harmonics up to 10th order was measured in ZnS [Fig. 7(a)] and up to 8th order in ZnSe [Fig. 7(b)], being limited by the short-wave transmission cut-offs of the crystals. Notice also high spectral intensities of the lowest-order harmonics, resulting from random quasi phase matching due to polycrystalline structure of the samples. Moreover, it is worth noticing that that the extension of the SC spectrum by the harmonics generation in polycrystalline materials is far more efficient as compared to the materials with sole cubic nonlinearity. In the latter case, the SC spectrum which manifests itself as an overlap of spectrally broadened odd harmonics is produced by a different mechanism, which involves cascaded four-wave interactions and cross-phase modulation [9].

## 4. Conclusions

In conclusion, we demonstrated multioctave harmonics-enhanced SC generation in polycrystalline ZnS and ZnSe. We show that efficient generation of even and odd harmonics stems from polycrystalline structure of these materials, which provides broadband random quasi phase matching for multiple simultaneous three-wave mixing processes considerably extending the spectral range of the output radiation. More specifically, using sub-$\mu$J, 60 fs, 3.6 $\mu$m input pulses, 3.6 octave-wide harmonics-enhanced SC spanning the $0.4-5$ $\mu$m wavelength range was generated in ZnS, and 3.3 octave-wide SC spanning the $0.5-5$ $\mu$m wavelength range was generated in ZnSe, whose maximum blue shifts were limited by the short-wave absorption of the crystals. A full set of even and odd harmonics up to 10th order in ZnS and up to 8th order in ZnSe were recorded with 100 fs input pulses at 4.6 $\mu$m. In contrast, only a moderate spectral broadening, fewer number of harmonics (only second and third) and considerably lower harmonics conversion efficiency due to large phase mismatch, was observed in ZnTe single crystal. We also captured filament-induced characteristic luminescence spectra, which correspond to the edge emissions of these materials. Our results demonstrate the central role of random quasi phase matching in the harmonics generation process, which is an intrinsic property of polycrystalline media. The recorded SC spectra reveal a great potential of polycrystalline semiconductors for the generation of ultrabroadband radiation that covers a remarkably broad spectral range from the visible to the mid-infrared.

## References


1. A. Dubietis, G. Tamošauskas, R. Šuminas, V. Jukna, and A. Couairon, "Ultrafast supercontinuum generation in bulk condensed media," Lith. J. Phys. **57**, 113–157 (2017).
2. S. A. Frolov, V. I. Trunov, V. E. Leshchenko, E. V. Pestryakov, "Multi-octave supercontinuum generation with IR radiation filamentation in transparent solid-state media," Appl. Phys. B **122**, 124 (2016).
3. F. Silva, D. R. Austin, A. Thai, M. Baudisch, M. Hemmer, D. Faccio, A. Couairon, and J. Biegert, "Multi-octave supercontinuum generation from mid-infrared filamentation in a bulk crystal," Nature Commun. **3**, 807 (2012).
4. J. Darginavičius, D. Majus, V. Jukna, N. Garejev, G. Valiulis, A. Couairon, and A. Dubietis, "Ultrabroadband supercontinuum and third-harmonic generation in bulk solids with two optical-cycle carrier-envelope phase-stable pulses at 2 $\mu$m," Opt. Express **21**, 25210–25220 (2013).
5. M. Liao, W. Gao, T. Cheng, X. Xue, Z. Duan, D. Deng, H. Kawashima, T. Suzuki, and Y. Ohishi, "Five-octave-spanning supercontinuum generation in fluoride glass," Appl. Phys. Express **6**, 032503 (2013).
6. J. A. Dharmadhikari, R. A. Deshpande, A. Nath, K. Dota, D. Mathur, and A. K. Dharmadhikari, "Effect of group velocity dispersion on supercontinuum generation and filamentation in transparent solids," Appl. Phys. B **117**, 471–479 (2014).
7. H. Liang, P. Krogen, R. Grynko, O. Novak, C.-L. Chang, G. J. Stein, D. Weerawarne, B. Shim, F. X. Kärtner, and K.-H. Hong, "Three-octave-spanning supercontinuum generation and sub-two-cycle self-compression of mid-infrared filaments in dielectrics," Opt. Lett. **40**, 1069-1072 (2015).
8. A. E. Dormidonov, V. O. Kompanets, S. V. Chekalin, and V. P. Kandidov, "Giantically blue-shifted visible light in femtosecond mid-IR filament in fluorides," Opt. Express **23**, 29202–29210 (2015).
9. N. Garejev, V. Jukna, G. Tamošauskas, M. Veličkė, R. Šuminas, A. Couairon, and A. Dubietis, "Odd harmonics-enhanced supercontinuum in bulk solid-state dielectric medium," Opt. Express **24**, 17060–17068 (2016).

10. H. Fattahi, H. Wang, A. Alismail, G. Arisholm, V. Pervak, A. M. Azzeer, and F. Krausz, "Near-PHz-bandwidth, phase-stable continua generated from a Yb:YAG thin-disk amplifier," Opt. Express **24**, 24337–24346 (2016).
11. N. Garejev, G. Tamošauskas, and A. Dubietis, "Comparative study of multioctave supercontinuum generation in fused silica, YAG and LiF in the range of anomalous group velocity dispersion," J. Opt. Soc. Am. B **34**, 88–94 (2017).
12. A. Marcinkevičiūtė, N. Garejev, R. Šuminas, G. Tamošauskas, and A. Dubietis, "A compact, self-compression-based sub-3 optical cycle source in the $3-4\,\mu$m spectral range," J. Opt. **19**, 105505 (2017).
13. S. Ashihara and Y. Kawahara, "Spectral broadening of mid-infrared femtosecond pulses in GaAs," Opt. Lett. **34**, 3839–3841 (2009).
14. M. Liao, W. Gao, T. Cheng, Z. Duan, X. Xue, H. Kawashima, T. Suzuki and Y. Ohishi, "Ultrabroad supercontinuum generation through filamentation in tellurite glass," Laser Phys. Lett. **10**, 036002 (2013).
15. Y. Yu, X. Gai, T. Wang, P. Ma, R. Wang, Z. Yang, D.-Y. Choi, S. Madden, and B. Luther-Davies, "Mid-infrared supercontinuum generation in chalcogenides," Opt. Mater. Express **3**, 1075–1086 (2013).
16. A. A. Lanin, A. A. Voronin, E. A. Stepanov, A. B. Fedotov, and A. M. Zheltikov, "Multioctave, $3-18\,\mu$m sub-two-cycle supercontinua from self-compressing, self-focusing soliton transients in a solid," Opt. Lett. **40**, 974–977 (2015).
17. O. Mouawad, P. Béjot, F. Billard, P. Mathey, B. Kibler, F. Désévédavy, G. Gadret, J.-C. Jules, O. Faucher, and F. Smektala, "Mid-infrared filamentation-induced supercontinuum in As-S and an As-free Ge-S counterpart chalcogenide glasses," Appl. Phys. B **121**, 433–438 (2015).
18. P. Béjot, F. Billard, C. Peureux, T. Diard, J. Picot-Clémente, C. Strutynski, P. Mathey, O. Mouawad, O. Faucher, K. Nagasaka, Y. Ohishi, and F. Smektala, "Filamentation-induced spectral broadening and pulse shortening of infrared pulses in Tellurite glass," Opt. Commun. **380**, 245–249 (2016).
19. B. Zhou and M. Bache, "Multiple-octave spanning mid-IR supercontinuum generation in bulk quadratic nonlinear crystals," APL Photon. **1**, 050802 (2016).
20. Y. Yang, M. Liao, X. Li, W. Bi, Y. Ohishi, T. Cheng, Y. Fang, G. Zhao, and W. Gao, "Filamentation and supercontinuum generation in lanthanum glass," J. Appl. Phys. **121**, 023107 (2017).
21. A. M. Stingel, H. Vanselous, and P. B. Petersen, "Covering the vibrational spectrum with microjoule mid-infrared supercontinuum pulses in nonlinear optical applications," J. Opt. Soc. Am. B **34**, 1163–1168 (2017).
22. A. Marcinkevičiūtė, G. Tamošauskas, and A. Dubietis, "Supercontinuum generation in mixed thallous halides KRS-5 and KRS-6," Opt. Mater. **78**, 339–344 (2018).
23. S. Vasilyev, I. Moskalev, M. Mirov, V. Smolski, S. Mirov, and V. Gapontsev, "Ultrafast middle-IR lasers and amplifiers based on polycrystalline Cr:ZnS and Cr:ZnSe," Opt. Mater. Express **7**, 2636–2650 (2017).
24. S. B. Mirov, I. S. Moskalev, S. Vasilyev, V. Smolski, V. V. Fedorov, D. Martyshkin, J. Peppers, M. Mirov, A. Dergachev, and V. Gapontsev, "Frontiers of mid-IR lasers based on transition metal doped chalcogenides," IEEE J. Select. Topics Quantum Electron. **24**, 1601829 (2018).
25. X. Ren, L. H. Mach, Y. Yin, Y. Wang, and Z. Chang, "Generation of 1 kHz, 2.3 mJ, 88 fs, 2.5 $\mu$m pulses from a $Cr^{2+}$:ZnSe chirped pulse amplifier," Opt. Lett. **43**, 3381–3384 (2018).
26. H. P. Wagner, M. Kühnelt, W. Langbein, and J. M. Hvam, "Dispersion of the second-order nonlinear susceptibility in ZnTe, ZnSe, and ZnS," Phys. Rev. B **58**, 10494–10501 (1998).
27. A. Arie and N. Voloch, "Periodic, quasi-periodic, and random quadratic nonlinear photonic crystals," Laser Photon. Rev. **4**, 355–373 (2010).
28. M. Baudrier-Raybaut, R. Haïdar, Ph. Kupecek, Ph. Lemasson, and E. Rosencher, "Random quasi-phase-matching in bulk polycrystalline isotropic nonlinear materials," Nature **432**, 374–376 (2004).
29. Q. Ru, N. Lee, X. Chen, K. Zhong, G. Tsoy, M. Mirov, S. Vasilyev, S. B. Mirov, and K. L. Vodopyanov, "Optical parametric oscillation in a random polycrystalline medium," Optica **4**, 617–618 (2017).
30. T. D. Krauss and F. W. Wise, "Femtosecond measurement of nonlinear absorption and refraction in CdS, ZnSe, and ZnS," Appl. Phys. Lett. **65**, 1739–1741 (1994).
31. L. Gallais and M. Commandré, "Laser-induced damage thresholds of bulk and coating optical materials at 1030 nm, 500 fs," Appl. Opt. **53**, A186–A196 (2014).
32. M. Durand, A. Houard, K. Lim, A. Durécu, O. Vasseur, and M. Richardson, "Study of filamentation threshold in zinc selenide," Opt. Express **22**, 5852–5858 (2014).
33. O. Mouawad, P. Béjot, F. Billard, P. Mathey, B. Kibler, F. Désévédavy, G. Gadret, J.-C. Jules, O. Faucher, and F. Smektala, "Filament-induced visible-to-mid-IR supercontinuum in a ZnSe crystal: Towards multi-octave supercontinuum absorption spectroscopy," Opt. Mater. **60**, 355–358 (2016).
34. E. A. Migal, F. V. Potemkin, and V. M. Gordienko, "Highly efficient optical parametric amplifier tunable from near- to mid-IR for driving extreme nonlinear optics in solids," Opt. Lett. **42**, 5218–5221 (2017).
35. R. Šuminas, G. Tamošauskas, N. Garejev, V. Jukna, A. Couairon, and A. Dubietis, "Multi-octave spanning nonlinear interactions induced by femtosecond filamentation in polycrystalline ZnSe," Appl. Phys. Lett. **110**, 241106 (2017).
36. A. H. Chin, O. G. Calderón, and J. Kono, "Extreme midinfrared nonlinear optics in semiconductors," Phys. Rev. Lett. **86**, 3292–3295 (2001).
37. G. M. Archipovaite, S. Petit, J.-C. Delagnes, and E. Cormier, "100 kHz Yb-fiber laser pumped 3 $\mu$m optical parametric amplifier for probing solid-state systems in the strong field regime," Opt. Lett. **42**, 891–894 (2017).
38. T. Kanai, P. Malevich, S. S. Kangaparambil, K. Ishida, M. Mizui, K. Yamanouchi, H. Hoogland, R. Holzwarth, A. Pugzlys, and A. Baltuska, "Parametric amplification of 100 fs mid-infrared pulses in $ZnGeP_2$ driven by a Ho:YAG chirped-pulse amplifier," Opt. Lett. **42**, 683–686 (2017).

39. A. A. Lanin, E. A. Stepanov, A. B. Fedotov, and A. M. Zheltikov, "Mapping the electron band structure by intraband high-harmonic generation in solids," Optica **4**, 516–519 (2017).
40. C. B. Marble, S. P. O'Connor, D. T. Nodurft, V. V. Yakovlev, and A. W. Wharmby, "Zinc selenide: an extraordinarily nonlinear material," Proc. SPIE **10528**, 105281X (2018).
41. R. I. Grynko, G. C. Nagar, and B. Shim, "Wavelength-scaled laser filamentation in solids and plasma-assisted subcycle light-bullet generation in the long-wavelength infrared," Phys. Rev. A **98**, 023844 (2018).
42. M. J. Weber, *Handbook of Optical Materials* (CRC Press, 2003).
43. M. Debenham, "Refractive indices of zinc sulfide in the 0.405-13-$\mu$m wavelength range," Appl. Opt. **23**, 2238–2239 (1984).
44. M. Sheik-Bahae, D. C. Hutchings, D. J. Hagan, E. W. Van Stryland, "Dispersion of bound electronic nonlinear refraction in solids," IEEE J. Quant. Electron. **27** 1296–1309 (1991).
45. R. DeSalvo, A. A. Said, D. J. Hagan, E. W. Van Stryland, M. Sheik-Bahae, "Infrared to ultraviolet measurements of two-photon absorption and $n_2$ in wide bandgap solids," IEEE J. Quant. Electron. **32** 1324–1333 (1996).
46. M. Mlejnek, E. M. Wright, J. V. Moloney, and N. Bloembergen, "Second harmonic generation of femtosecond pulses at the boundary of a nonlinear dielectric," Phys. Rev. Lett. **83**, 2934–2937 (1999).
47. G. Valiulis, V. Jukna, O. Jedrkiewicz, M. Clerici, E. Rubino, and P. Di Trapani, "Propagation dynamics and X-pulse formation in phase-mismatched second-harmonic generation," Phys. Rev. A **83**, 043834 (2011).
48. A. K. Dharmadhikari, J. A. Dharmadhikari, and D. Mathur, "Visualization of focusing-refocusing cycles during filamentation in $BaF_2$," Appl. Phys. B **94**, 259–263 (2009).

# A6

# FEMTOSECOND FILAMENTATION, SUPERCONTINUUM GENERATION AND DETERMINATION OF $N_2$ IN POLYCRYSTALLINE SBN

**R. Šuminas**, N. Garejev, A. Šuminienė, V. Jukna,
G. Tamošauskas, A. Dubietis

J. Opt. Soc. Am. B **37**, 1530–1534 (2020)

# Femtosecond filamentation, supercontinuum generation and determination of $n_2$ in polycrystalline SBN

ROSVALDAS ŠUMINAS, NAIL GAREJEV, AGNĖ ŠUMINIENĖ, VYTAUTAS JUKNA, GINTARAS TAMOŠAUSKAS AND AUDRIUS DUBIETIS*

*Laser Research Center, Vilnius University, Saulėtekio Avenue 10, LT-10223 Vilnius, Lithuania*
**audrius.dubietis@ff.vu.lt*

**Abstract:** We demonstrate that polycrystalline strontium barium niobate (SBN) serves as an excellent nonlinear material for supercontinuum generation in the near- and mid-infrared, as pumped by femtosecond pulses in the regions of its normal, zero and anomalous group velocity dispersion. We also show that broadband, octave-spanning planar second harmonic emission generated via random quasi phase matching usefully serves to precisely monitor focusing/refocusing cycles of a filament and to determine position of the nonlinear focus in particular, which was used to estimate the nonlinear index of refraction of the material applying the Marburger's law. The measured $n_2$ values are remarkably large: $44 \pm 7 \times 10^{-16}$ cm$^2$/W at 1.2 $\mu$m, $81 \pm 23 \times 10^{-16}$ cm$^2$/W at 2.0 $\mu$m and $100 \pm 15 \times 10^{-16}$ cm$^2$/W at 2.4 $\mu$m, and thus imply very low energy (below 100 nJ) and power (below 1 MW) thresholds for filamentation and SC generation in the infrared spectral range.



## 1. Introduction

Random quasi phase matching in disordered materials with second-order nonlinearity opens interesting perspectives in broadband frequency conversion of ultrashort light pulses [1]. A possibility to phase match virtually any wavelength that falls into the transparency range of these materials is provided by a natural disorder of orientations and grain-size distribution of individual crystallites [2]. To this end, polycrystalline zinc-blende semiconductors, such as ZnSe and ZnS, which are optically isotropic but possess second-order nonlinearity due to $\bar{4}3$m symmetry, emerge as very attractive nonlinear materials. The frequency conversion processes in these materials become particularly efficient in the femtosecond filamentation regime due to high achieved intensity and localization of the pump, yielding ultrabroadband, multiple octave-spanning supercontinuum, whose short-wavelength side is remarkably extended by overlapping harmonics spectra, right down to the transparency edge [3–9].

Polycrystalline strontium barium niobate (SBN) is another interesting nonlinear material that can be used for various nonlinear optical processes at multiple wavelengths, including second and third harmonic generation without the need of angle or temperature tuning [10]. SBN is ferroelectric negative uniaxial crystal with an energy bandgap of 3.4 eV. The crystal is transparent in the 0.45 – 5.5 $\mu$m wavelength range [11] and has zero group velocity dispersion wavelength at 1.96 $\mu$m [12]. In contrast to polycrystalline zinc-blende semiconductors, polycrystalline SBN consists of birefringent needle-like randomly distributed ferroelectric domains whose widths vary between a few nanometers and a few micrometers and whose lengths are of a few hundreds of micrometers [13]. Broadband second and third harmonic generation in polycrystalline SBN was widely studied regarding harmonic spatial patterns, speckle structure, statistics and polarization properties [14–24]. Eventually, these studies resulted in practical applications, demonstrating adjustment-insensitive techniques for characterization of ultrashort light pulses [25–27]. However,

the nonlinear effects related to the third-order nonlinearity in SBN have not been explicitly addressed so far.

In this Paper we study filamentation and supercontinuum generation in polycrystalline SBN with femtosecond near and mid-infrared laser pulses, whose carrier wavelengths fall into the ranges of normal, zero and anomalous group velocity dispersion (GVD) of the crystal. We show that planar second harmonic generation usefully serves to visualize and monitor precisely filamentation dynamics, allowing to accurately establish the position of nonlinear focus and to determine the nonlinear index of refraction using Marburger's law.

## 2. Material properties and experimental setup

The experiment was performed using near-infrared femtosecond pulses from a commercial optical parametric amplifier (Topas-C, Light Conversion), which was pumped by an amplified Ti:sapphire laser system (Spitfire-PRO, Newport-Spectra Physics) at a 500 Hz repetition rate. The experimental setup is schematically depicted in Fig. 1(a). The beam was focused using a $f = +100$ mm $BaF_2$ lens (L) into the front face of undoped unpoled polycrystalline SBN:61 ($Sr_{0.61}Ba_{0.39}Nb_2O_6$) sample with dimensions of $5 \times 5 \times 5$ mm.

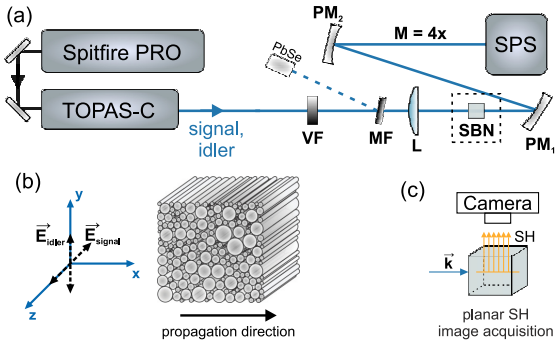


Fig. 1. (a) Experimental setup, see text for details. (b) Orientation of the crystal, its principal axes and pump polarization with respect to propagation direction. (c) Acquisition of planar SH images.

The input pulse energy was adjusted using a variable neutral density filter (VF) and measured with a calibrated PbSe photodetector using a reflection from a metallic filter (MF). The output spectra were recorded with a 4f system consisting of a pair of silver-coated parabolic mirrors $PM_1$ and $PM_2$, which were used to image the output face of the crystal onto the entrance slit of a home built scanning prism spectrometer (SPS) with Ge and InAsSb photodetectors, which allowed to perform spectral measurements in the $0.6 - 5.8$ $\mu$m wavelength region.

In our study we used three different incident wavelengths of 1.2 $\mu$m, 2.0 $\mu$m and 2.4 $\mu$m, which fall into the normal, zero and anomalous GVD regions of the material, respectively. The focal spot sizes of the input beams and corresponding pulse durations were slightly different for the three chosen wavelengths and are listed in Table 1, which also presents the respective refraction indices and GVD coefficients of the crystal. The crystal orientation with respect to the propagation direction of the beam is depicted in Fig. 1(b). In this configuration, the input pulse with a wavelength of 1.2 $\mu$m (the signal wave of the optical parametric amplifier) had an extraordinary polarization, while the input pulses with wavelengths of 2.0 $\mu$m and 2.4 $\mu$m (the idler waves) had ordinary polarizations. Such crystal orientation ensured that second harmonic (SH) is emitted in the direction perpendicular to the incident beam [17]. Images of planar SH

Table 1. Summary of relevant input beam/pulse and material parameters. $\lambda_p$ is the pump wavelength, $\tau$ is the pulse width, $w_0$ is the $1/e^2$ radius of the focal spot at the crystal input, $n$ is the refractive index (note different polarizations), $g$ is the GVD coefficient.

| $\lambda_p$ ($\mu$m) | 1.2 | 2.0 | 2.4 |
|---|---|---|---|
| polarization | e | o | o |
| $\tau$ (fs) | 85 | 95 | 125 |
| $w_0$ ($\mu$m) | 36 | 54 | 53 |
| $n_0$ | 2.216 | 2.211 | 2.198 |
| g (fs$^2$/mm) | +243 | -14 | -180 |

radiation were taken using a Nikon D7200 DSLR camera mounted above the polished top side of SBN crystal, as schematically illustrated in Fig. 1(c).

## 3. Results and discussion

Large nonlinear index of refraction of SBN crystal, $n_2 = 52.4\times10^{-16}$ cm$^2$/W at 1064 nm [28], implies very low (0.14 MW) critical power for self-focusing at that wavelength; $P_{cr} = 3.77\lambda^2/8\pi n_0 n_2$. Indeed, the onset of filamentation was experimentally detected with pump pulse energies less than 100 nJ and sub-MW peak powers: 32 nJ (0.35 MW) at 1.2 $\mu$m, 54 nJ (0.53 MW) at 2.0 $\mu$m and 74 nJ (0.56 MW) at 2.4 $\mu$m, as verified by the onset of spectral broadening and beam filamentation; the latter was visualized by the emergence of intense spot in the planar SH emission from the filament site.

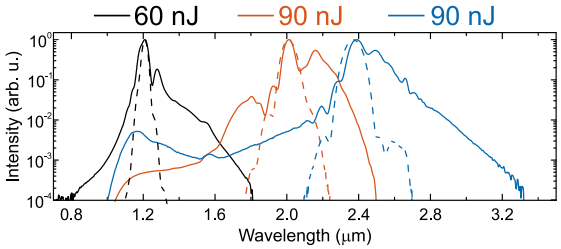


Fig. 2. Supercontinuum spectra generated in SBN using pump pulses with carrier wavelengths of 1.2 $\mu$m (black curve), 2.0 $\mu$m (red curve) and 2.4 $\mu$m (blue curve). The energies of the pump pulses are indicated on the top. The input spectra are depicted by dashed curves.

Figure 2 compares the SC spectra in polycrystalline SBN generated in the ranges of its normal, zero and anomalous GVD. The pump pulse energies were set slightly above the threshold energies for filamentation, where blue-shifted broadenings of the spectra saturate and no refocusing of the filament is observed. Smooth, more than an octave-spanning SC spectra in the wavelength ranges of 0.8 – 1.81 $\mu$m, 1.04 – 2.5 $\mu$m and 1.0 – 3.32 $\mu$m (defined at the $10^{-4}$ intensity level) were obtained using pump pulses with carrier wavelengths of 1.2 $\mu$m, 2.0 $\mu$m and 2.4 $\mu$m, respectively. These results affirm the general consideration that nonlinear polycrystalline materials as well as single crystals with a narrow energy bandgap, such as silicon and mixed thallous halides, usefully

serve for the generation of infrared SC, see e.g. [29] for a review and [30–32] for more recent results.

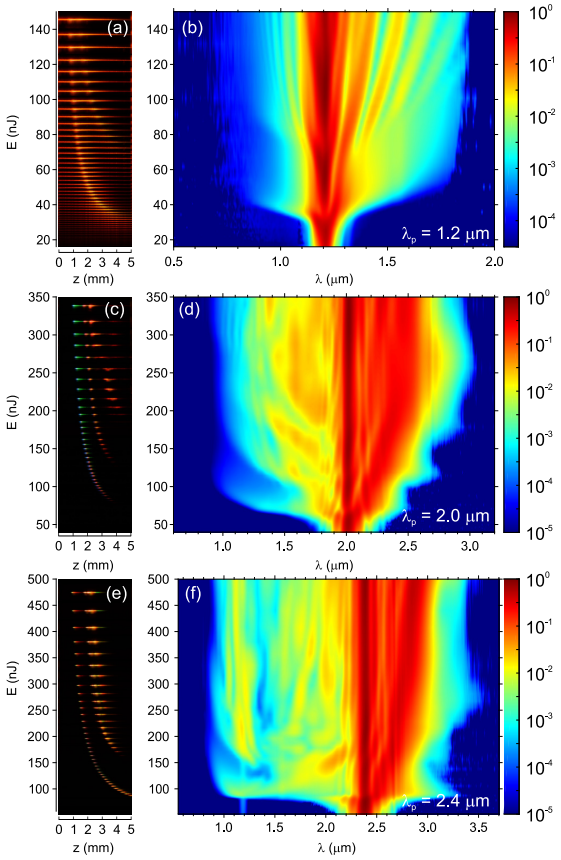


Fig. 3. (a,c,e) Composite images of SH traces and (b,d,f) related dynamics of spectral broadening as functions of the pump pulse energy in the cases of normal (1.2 $\mu$m), zero (2.0 $\mu$m) and anomalous (2.4 $\mu$m) GVD.

Figure 3 shows filamentation and SC generation dynamics in more detail by collation of the images of SH traces and related spectral evolutions as functions of the input pulse energy in the cases of normal, zero and anomalous GVD. The energy ranges for each input wavelength were chosen to preserve a single filament propagation regime and to avoid the occurrence of multiple filamentation. Planar SH generation in pollycrystaline SBN is a well known phenomenon occurring due to the random distribution of the needle-like domains, which provides a continuous set of reciprocal grating vectors that satisfy the phase matching conditions for a wide range of spectral components [10, 17]. The series of SH images depicted in Figs. 3(a), 3(c) and 3(e) reveal that such broadband SH emission closely follows the intensity distribution along the light filament and can be readily used to monitor filamentation dynamics similarly to a more common method of filament visualization based on filament-induced luminescence observed in various single crystals, see e.g. [33–35].

It is very clear that the occurrence of intense planar SH emission manifests the onset of

filamentation, which is also justified by an explosive broadening of the spectrum. The most intense part of the SH trace maps the position of the nonlinear focus, which first appears at the end of the sample and thereafter shifts toward its input face as the energy of the pump pulse increases. The intensity variation along the SH trace also nicely captures filament refocusing at elevated pump pulse energy, which is indicated by the emergence of a secondary intensity peak in the SH trace which correlates with a secondary boost of spectral broadening and the occurrence of interference pattern in the SC spectrum, very clearly visible with 1.2 $\mu$m and somewhat less pronounced with 2.0 $\mu$m and 2.4 $\mu$m pump pulses.

To summarize the observed spectral dynamics presented in Fig. 3, the spectral broadening versus the input pulse energy shows several interesting features, which are quite general from the point of view of underlying physics. First, an apparent shrinking of the SC spectra (especially well-pronounced on the short wavelength side) is observed before the filament refocusing takes place in all investigated cases. This spectral shrinking is attributed to the defocusing and absorption of free electron plasma that push a large portion of the pulse energy out of the propagation axis after the first nonlinear focus, see [35] for details. Second, each refocusing cycle in the cases of zero (2.0 $\mu$m) and anomalous (2.4 $\mu$m) GVD precedes the constant red shift. Such spectral behavior was also observed in various nonlinear media ($CaF_2$ and LiF single crystals and fused silica, see [36]), and was attributed to the periodic breathing of the light bullet, i.e. the self-compressed pulse that emerges due to the interplay between self-phase modulation and anomalous GVD. The same consideration applies also to the case of zero GVD, where the pulse splitting takes place, and the spectrum of the trailing sub-pulse that is responsible for the red shift, falls into the range of anomalous GVD of the crystal.

Notice that no SH emission in the direction of filament propagation is detected, except in the case of 2.4 $\mu$m pumping, see Fig. 3(f), where a very weak SH emission centered at 1.2 $\mu$m is observed before the spectral broadening starts. Almost identical SC spectra and spectral dynamics versus the pump pulse energy (not shown here) were recorded with ordinarily polarized pump pulse at 1.2 $\mu$m and extraordinarily polarized pump pulses at 2.0 $\mu$m and 2.4 $\mu$m, i.e. when the crystal was rotated by 90° in the plane perpendicular to the beam propagation direction, setting needle-like domains vertically; please refer to Fig. 1(b).

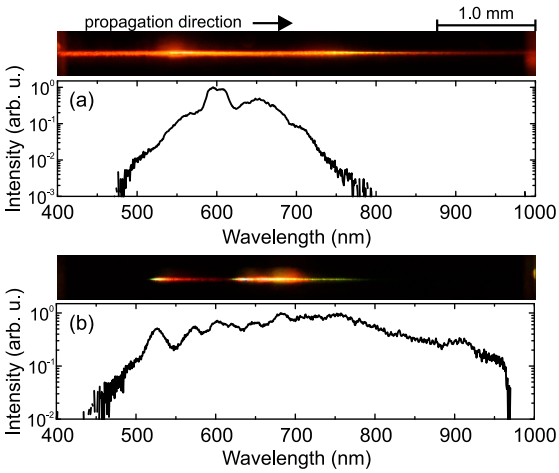


Fig. 4. Photographs of representative SH traces and SH spectra recorded with a fiber spectrometer using (a) 1.2 $\mu$m, 85 nJ and (b) 2.4 $\mu$m, 408 nJ pump pulses.

The SH traces produced by filamentation of the pulses with central wavelengths of 1.2 $\mu$m, 2.0 $\mu$m and 2.4 $\mu$m appear in different colors. Figure 4 compares the spectra of planar SH emissions produced by filamentation of 1.2 $\mu$m and 2.4 $\mu$m pulses and measured with a fiber spectrometer (Ocean Optics QE65000). Figure 4(a) shows the recorded SH spectrum produced with the pump wavelength of 1.2 $\mu$m. The SH spectrum spans the wavelength range from 480 to 800 nm and represents an almost exact replica of the entire SC spectrum with the peak spectral intensity at 600 nm, which is the second harmonic of the pump. With the pump wavelength of 2.4 $\mu$m, the SH spectrum covers the wavelength range from 460 nm to 970 nm, which is the long-wave detection limit of the spectrometer, see Fig. 4(b), attesting that such broadband SH emission is produced by frequency doubling of the blue-shifted part of the SC spectrum. An interesting variation of color along the SH trace indicates the propagation distances at which the particular spectral components of the SC have the highest intensities. This feature is particularly well pronounced in the case of 2.0 $\mu$m pumping, see Fig. 2(c). These spectral measurements demonstrate extremely wide, an octave-spanning conversion bandwidth of SH generation provided by random quasi phase matching.

Series of SH emission traces shown in Figs. 3(a), 3(c) and 3(e) were further exploited in order to determine the nonlinear refractive index of the material. In doing so, each SH trace was converted into greyscale and integrated along the height of the image. The position of the first intensity maximum (that appears closest to the input face of the crystal) was considered to be the nonlinear focal point. Thereafter the retrieved datasets of positions of the nonlinear foci versus the pump energy (power) for each pump wavelength were fitted using Marburger's empirical formula for the position of nonlinear focus [37]:

$$z_{\mathrm{sf}} = \frac{0.367\, z_R}{\sqrt{[(P/P_{\mathrm{cr}})^{1/2} - 0.852]^2 - 0.0219}}, \tag{1}$$

where $z_R = \pi n_0 w_0^2/\lambda$ is the Rayleigh (diffraction) length of the input Gaussian beam with a radius $w_0$, $P$ is the power of the pump and $P_{\mathrm{cr}}$ is the critical power for self-focusing.

The results for the pump wavelengths of 1.2 $\mu$m, 2.0 $\mu$m and 2.4 $\mu$m are summarized in Fig. 5, which shows the retrieved positions of experimental nonlinear foci versus the pump pulse energy and power and the respective best fits using Eq.(1). The fitting procedure was performed taking the radii of input beams and pulse durations from Table 1. However, the best fits were obtained using the radii of the input beams as additional free parameters, yielding $1/e^2$ beam radii of 26 $\mu$m, 43 $\mu$m and 44 $\mu$m for the input beams with carrier wavelengths of 1.2 $\mu$m, 2.0 $\mu$m and 2.4 $\mu$m, respectively. These systematically smaller beam sizes may be attributed to a slightly elliptical shapes of the input beams and unknown amounts of the chirp of the input pulses, which both could slightly alter the position of the nonlinear focus [38]. The best fits yielded the following values of nonlinear refractive indexes: $44 \pm 7 \times 10^{-16}$ cm$^2$/W at 1.2 $\mu$m, $81 \pm 23 \times 10^{-16}$ cm$^2$/W at 2.0 $\mu$m and $100 \pm 15 \times 10^{-16}$ cm$^2$/W at 2.4 $\mu$m.

The obtained $n_2$ value at 1.2 $\mu$m compares favorably with the previously reported value of $52.4 \times 10^{-16}$ cm$^2$/W at 1064 nm [28], however, much larger $n_2$ values obtained at 2.0 $\mu$m and 2.4 $\mu$m look quite surprising. Indeed, these large values appear in stark contrast with what can be expected from a general dispersion law of $n_2$, suggesting the maximum $n_2$ value around the edge of two photon absorption ($\sim$ 730 nm for SBN) and gradual decrease of $n_2$ toward longer wavelengths [28]. This result can not be explained by the contribution of the cascaded nonlinearity due to phase-mismatched SH generation, as the wavevector mismatch for any type of possible three-wave interaction, see [18], for the wavelengths of interest is always positive, so suggesting that the contribution of the cascaded nonlinearity to effective $n_2$ is negative. On the other hand, these large $n_2$ values are confirmed by very low beam powers for filamentation and SC generation thresholds determined experimentally for pump wavelengths of 2.0 $\mu$m and 2.4 $\mu$m.

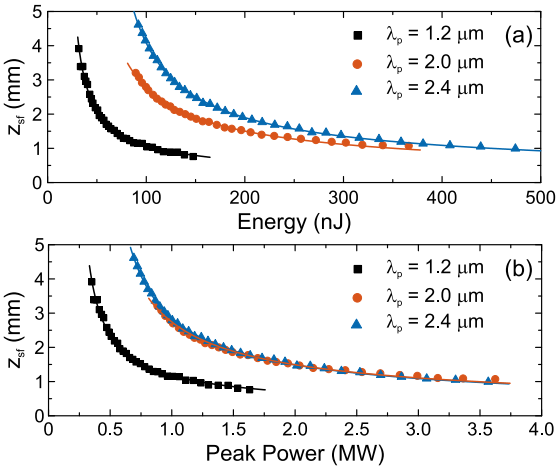


Fig. 5. (a) The positions of the nonlinear foci versus the pump pulse energy (dots) and the best fits using Marburger's formula (curves) for the pump wavelengths of 1.2 $\mu$m (black), 2.0 $\mu$m (red) and 2.4 $\mu$m (blue). (b) the same data represented in terms of a peak power and used for estimation of $n_2$.

## 4. Conclusions

In conclusion, we demonstrated that SBN crystal serves as an efficient nonlinear medium for SC generation in the infrared spectral range. More than an octave-spanning infrared SC spectra were produced with reasonably low pump energies (powers), in the ranges of normal, zero and anomalous GVD of the crystal. We also show that random quasi phase matching in polycrystalline SBN provides an extremely broad, octave-spanning bandwidth for planar SH generation. Moreover, we demonstrate that broadband planar SH emission precisely maps the intensity distribution along the filament of light, and so could be used to visualize the entire self-focusing and filamentation dynamics. This feature was exploited for determination of the nonlinear index of refraction of SBN at 1.2 $\mu$m, 2.0 $\mu$m and 2.4 $\mu$m.

## Funding

This project has received funding from European Regional Development Fund (project No 1.2.2-LMT-K-718-02-0017) under grant agreement with the Research Council of Lithuania (LMTLT).

## Disclosures

The authors declare no conflicts of interest.

## References

1. M. Baudrier-Raybaut, R. Haidar, P. Kupecek, P. Lemasson, and E. Rosencher, "Random quasi-phase-matching in bulk polycrystalline isotropic nonlinear materials," Nature **432**, 374–376 (2004).
2. T. Kawamori, Q. Ru, and K. L. Vodopyanov, "Comprehensive model for randomly phase-matched frequency conversion in zinc-blende polycrystals and experimental results for ZnSe," Phys. Rev. Appl. **11**, 054015 (2019).
3. O. Mouawad, P. Béjot, F. Billard, P. Mathey, B. Kibler, F. Désévédavy, G. Gadret, J.-C. Jules, O. Faucher, and F. Smektala, "Filament-induced visible-to-mid-ir supercontinuum in a ZnSe crystal: Towards multi-octave supercontinuum absorption spectroscopy," Opt. Mater. **60**, 355–358 (2016).

4. R. Šuminas, G. Tamošauskas, G. Valiulis, V. Jukna, A. Couairon, and A. Dubietis, "Multi-octave spanning nonlinear interactions induced by femtosecond filamentation in polycrystalline ZnSe," Appl. Phys. Lett. **110**, 241106 (2017).
5. G. M. Archipovaite, S. Petit, J.-C. Delagnes, and E. Cormier, "100 khz Yb-fiber laser pumped 3 $\mu$m optical parametric amplifier for probing solid-state systems in the strong field regime," Opt. Lett. **42**, 891–894 (2017).
6. R. Šuminas, A. Marcinkevičiūtė, G. Tamošauskas, and A. Dubietis, "Even and odd harmonics-enhanced supercontinuum generation in zinc-blende semiconductors," J. Opt. Soc. Am. B **36**, A22–A27 (2019).
7. K. Werner, M. G. Hastings, A. Schweinsberg, B. L. Wilmer, D. Austin, C. M. Wolfe, M. Kolesik, T. R. Ensley, L. Vanderhoef, A. Valenzuela, and E. Chowdhury, "Ultrafast mid-infrared high harmonic and supercontinuum generation with $n_2$ characterization in zinc selenide," Opt. Express **27**, 2867–2885 (2019).
8. C. B. Marble, S. P. OâĂŹConnor, D. T. Nodurft, A. W. Wharmby, and V. V. Yakovlev, "Eye safety implications of high harmonic generation in zinc selenide," Opt. Express **27**, 2828–2836 (2019).
9. S. Vasilyev, I. Moskalev, V. Smolski, J. Peppers, M. Mirov, A. Muraviev, K. Vodopyanov, S. Mirov, and V. Gapontsev, "Multi-octave visible to long-wave IR femtosecond continuum generated in Cr:ZnS-GaSe tandem," Opt. Express **27**, 16405–16413 (2019).
10. P. Molina, M. de la O. Ramirez, and L. E. Bausa, "Strontium barium niobate as a multifunctional two-dimensional nonlinear "photonic glass"," Adv. Funct. Mater. **18**, 709–715 (2008).
11. M. J. Weber, *Handbook of optical materials* (London: CRC press, 2003).
12. T. Woike, T. Granzow, U. Dörfler, C. Poetsch, M. Wöhlecke, and R. Pankrath, "Refractive indices of congruently melting $Sr_{0.61}Ba_{0.39}Nb_2O_6$," Phys. Status Solidi A **186**, R13–R15 (2001).
13. K. Terabe, S. Takekawa, M. Nakamura, K. Kitamura, S. Higuchi, Y. Gotoh, and A. Gruverman, "Imaging and engineering the nanoscale-domain structure of a $Sr_{0.61}Ba_{0.39}Nb_2O_6$ crystal using a scanning force microscope," Appl. Phys. Lett. **81**, 2044–2046 (2002).
14. E. Y. Morozov, A. A. Kaminskii, A. S. Chirkin, and D. B. Yusupov, "Second optical harmonic generation in nonlinear crystals with a disordered domain structure," JETP Lett. **73**, 647–650 (2001).
15. A. R. Tunyagi, M. Ulex, and K. Betzler, "Noncollinear optical frequency doubling in strontium barium niobate," Phys. Rev. Let. **90**, 243901 (2003).
16. V. Roppo, W. Wang, K. Kalinowski, Y. Kong, C. Cojocaru, J. Trull, R. Vilaseca, M. Scalora, W. Krolikowski, and Y. Kivshar, "The role of ferroelectric domain structure in second harmonic generation in random quadratic media," Opt. Express **18**, 4012–4022 (2010).
17. R. Fischer, S. Saltiel, D. Neshev, W. Krolikowski, and Y. S. Kivshar, "Broadband femtosecond frequency doubling in random media," Appl. Phys. Lett. **89**, 191105 (2006).
18. L. Mateos, P. Molina, J. F. Galisteo-López, C. López, L. E. Bausá, and M. O. Ramírez, "Ultrabroadband generation of multiple concurrent nonlinear coherent interactions in random quadratic media," Appl. Phys. Lett. **103**, 101101 (2013).
19. W. Wang, V. Roppo, K. Kalinowski, Y. Kong, D. Neshev, C. Cojocaru, J. Trull, R. Vilaseca, K. Staliunas, W. Krolikowski, S. M. Saltiel, and Y. Kivshar, "Third-harmonic generation via broadband cascading in disordered quadratic nonlinear media," Opt. Express **17**, 20117–20123 (2009).
20. W. Wang, K. Kalinowski, V. Roppo, Y. Sheng, K. Koynov, Y. Kong, C. Cojocaru, J. Trull, R. Vilaseca, and W. Krolikowski, "Second-and third-harmonic parametric scattering in disordered quadratic media," J. Phys. B **43**, 215404 (2010).
21. F. J. Rodríguez, C. Yao, J. L. Domínguez-Juárez, J. Bravo-Abad, and J. Martorell, "Observation of speckle pattern formation in transparent nonlinear random media," Opt. Lett. **36**, 1347–1349 (2011).
22. C. Yao, F. J. Rodriguez, and J. Martorell, "Controlling the diffused nonlinear light generated in random materials," Opt. Lett. **37**, 1676–1678 (2012).
23. C. Hermann-Avigliano, I. Salinas, D. Rivas, B. Real, A. Mančić, C. Mejía-Cortés, A. Maluckov, and R. A. Vicencio, "Spatial rogue waves in photorefractive SBN crystals," Opt. Lett. **44**, 2807–2810 (2019).
24. M. Ayoub, M. Paßlick, J. Imbrock, and C. Denz, "Controlling the effective second-order susceptibility in random quadratic media," Opt. Express **23**, 33980–33991 (2015).
25. J. Trull, S. Saltiel, V. Roppo, C. Cojocaru, D. Dumay, W. Krolikowski, D. Neshev, R. Vilaseca, K. Staliunas, and Y. S. Kivshar, "Characterization of femtosecond pulses via transverse second-harmonic generation in random nonlinear media," Appl. Phys. B **95**, 609–615 (2009).
26. J. Trull, I. Sola, B. Wang, A. Parra, W. Krolikowski, Y. Sheng, R. Vilaseca, and C. Cojocaru, "Ultrashort pulse chirp measurement via transverse second-harmonic generation in strontium barium niobate crystal," Appl. Phys. Lett. **106**, 221108 (2015).
27. B. Wang, C. Cojocaru, W. Krolikowski, Y. Sheng, and J. Trull, "Transverse single-shot cross-correlation scheme for laser pulse temporal measurement via planar second harmonic generation," Opt. Express **24**, 22210–22218 (2016).
28. M. Sheik-Bahae, D. C. Hutchings, D. J. Hagan, and E. W. Van Stryland, "Dispersion of bound electron nonlinear refraction in solids," IEEE J. Quantum Electron. **27**, 1296–1309 (1991).
29. A. Dubietis, G. Tamošauskas, R. Šuminas, V. Jukna, and A. Couairon, "Ultrafast supercontinuum generation in bulk condensed media," Lith. J. Phys. **57**, 113–157 (2017).
30. A. Marcinkevičiūtė, V. Jukna, R. Šuminas, N. Garejev, G. Tamošauskas, and A. Dubietis, "Femtosecond filamentation and supercontinuum generation in bulk silicon," Opt. Lett. **44**, 1343–1346 (2019).
31. A. Marcinkevičiūtė, G. Tamošauskas, and A. Dubietis, "Supercontinuum generation in mixed thallous halides KRS-5

and KRS-6," Opt. Mater. **78**, 339–344 (2018).
32. K. Liu, H. Liang, S. Qu, W. Li, X. Zou, Y. Zhang, and Q. J. Wang, "High-energy mid-infrared intrapulse difference-frequency generation with 5.3% conversion efficiency driven at 3 $\mu$m," Opt. Express **27**, 37706–37713 (2019).
33. A. Dharmadhikari, J. Dharmadhikari, and D. Mathur, "Visualization of focusing–refocusing cycles during filamentation in $BaF_2$," Appl. Phys. B **94**, 259–263 (2009).
34. D. Kudarauskas, G. Tamošauskas, M. Vengris, and A. Dubietis, "Filament-induced luminescence and supercontinuum generation in undoped, Yb-doped, and Nd-doped YAG crystals," Appl. Phys. Lett. **112**, 041103 (2018).
35. V. Jukna, N. Garejev, G. Tamošauskas, and A. Dubietis, "Role of external focusing geometry in supercontinuum generation in bulk solid-state media," J. Opt. Soc. Am. B **36**, A54–A60 (2019).
36. N. Garejev, G. Tamošauskas, and A. Dubietis, "Comparative study of multioctave supercontinuum generation in fused silica, YAG, and LiF in the range of anomalous group velocity dispersion," J. Opt. Soc. Am. B **34**, 88–94 (2017).
37. J. Marburger, "Self-focusing: theory," Prog. Quantum Electron. **4**, 35–110 (1975).
38. A. Couairon, E. Brambilla, T. Corti, D. Majus, O. de. J. Ramírez-Góngora, and M. Kolesik, "PractitionerâĂŹs guide to laser pulse propagation models and simulation," Eur. Phys. J. Spec. Top. **199**, 5–76 (2011).

NOTES

NOTES

NOTES

Vilnius University Press
Saulėtekio al. 9, LT-10222 Vilnius
e-mail: info@leidykla.vu.lt,
www.leidykla.vu.lt
Print run copies 15